Developments in 2D NMR relaxometry and its application to biological tissue

Thesis submitted for the degree of Doctor of Philosophy

School of biological sciences,
University of East Anglia,
Norwich, Norfolk, UK,
NR4 7TJ

Institute of Food Research,
Norwich Research Park, Colney lane,
Norwich, Norfolk, UK,
NR4 7UA

Joshua Warner

September 2010

Abstract

In this thesis the capability of 2D NMR relaxometry to distinguish between different biological tissues is established using fresh unpreserved samples of lamb's liver and kidney. A novel use of 2D T_1-T_2 relaxation spectra to provide characteristic profiles of specific tissues in specific states of health is proposed and tested in the case of osteoarthritis using human articular knee cartilage obtained from the Norfolk and Norwich University Hospital (NNUH). It is then proposed that 2D relaxation spectra can be used to optimise image contrast, which is an outstanding problem in clinical MRI. Indeed clinical MRI lacks well established and accurate methods for optimising image contrast and fails to exploit much of the potential available to the NMR practitioner. In this thesis two methods for the optimisation of image contrast using 2D T_1-T_2 relaxation spectra are proposed and tested. These are named the Virtual Sample Simulation (VSS) and MRI COntrast Modelling (MRICOM) methods. It is shown that MRICOM is more generally applicable because it exploits the established Object-oriented Development Interface for NMR (ODIN). It is demonstrated that 'in-silico' methods can predict image intensity of specific tissues using specific imaging sequences and use them to optimise contrast between tissues. A newly developed single shot T_1-T_2 sequence named the 'TR method' is proposed and implemented in order to increase the speed of 2D NMR relaxometry by between 2 and 10 times. Its ability to distinguish between different biological tissues is established, again using fresh unpreserved samples of lamb's liver and kidney. Future work is then proposed to combine this faster method with other time reduction methods and volume selective techniques to create the CURE (Clinical Ultrafast RElaxometry) protocol. Methods are also proposed to increase the tissue characterisation and diagnostic capabilities of 2D NMR relaxometry with the use of expert systems and neural networks.

Acknowledgements

I would like to acknowledge the Biotechnology and Biological Sciences Research Council (BBSRC) for my core funding and Plant Bioscience Ltd. (PBL) for my CASE studentship. I would also like to thank Dr Brian Hills for his help and support in his supervisory capacity, as well as his scientific assistance and friendship. I would like to thank Prof Pete Wilde and Prof Peter Belton for their help with the thesis in the difficult time following Brian's death. I would like to thank Dr Simon Donell, Dr Paul Malcolm and Dr Andoni Toms of the Norfolk and Norwich University Hospital (NNUH) for their assistance in procuring samples and their clinical expertise. I would like to thank my lab-mates Ben Piggot, Kevin Wright, Luca Venturi, Chiara Iuliano, Niusa Marigheto, Paola Pani, Maria Furfaro, Marcus Cardoso and any visiting students not specifically named, for their assistance, friendship and occasional language tutoring during my time in the lab. I would especially thank Kevin Wright for his invaluable expertise in MATLAB and other programming languages. Thank you to my friends and family both inside and outside the institute for their friendship and understanding during this time. Special thanks goes to Jess, Rach, Jules, Pedro, Rich, Sam, Mary, Muzz and Copsey for helping me through some tough times, my parents Ken and Jenny for all their support and my nephew James for always making me smile.

Publications

Warner, J., S. Donell, et al. (2010). "The characterisation of mammalian tissue with 2D relaxation methods." Magn Reson Imaging **28**(7): 971-981.

The potential of two-dimensional (2D) relaxometry for characterising mammalian tissue is explored on samples of liver, kidney (cortex, medulla and ureter) as well as cartilage. Significant differences are found between the T(1)-T(2) spectra of healthy and diseased human cartilage which suggests that 2D relaxometry could have potential use in clinical diagnosis. The effect of reducing the recovery delay on the T(1)-T(2) spectrum is explored to try to identify the optimum balance between speed and accuracy. (C) 2010 Elsevier Inc. All rights reserved.

Venturi, L., J. Warner, et al. (2010). "Multisliced ultrafast 2D relaxometry." Magn Reson Imaging **28**(7): 964-970.

By associating each slice in a spatially homogeneous sample with a different inversion-recovery delay time, multislice methods are used to reduce the acquisition times of 2D inversion-recovery T(1)-T(2) relaxation spectra to just a few minutes. The increased speed comes at the expense of reduced signal/noise and this is reflected most noticeably in shifts in the component longitudinal relaxation times. Nevertheless, the major features of the 2D relaxation spectra are reproduced. (C) 2010 Elsevier Inc. All rights reserved.

Wright, K. M., J. Warner, et al. (2010). "MRICOM-MRI COntrast Modelling using 2D T1-T2 correlation spectra and relaxation signatures." Magn Reson Imaging **28**(5): 661-668.

Image contrast is calculated by inputting experimental 2D T1-T2 relaxation spectra into the ODIN software interface. The method involves characterising a magnetic resonance imaging pulse sequence with a "relaxation signature" which describes the sensitivity of the sequence to relaxation and is independent of sample parameters. Maximising (or minimising) the overlap between the experimental 2D T1-T2 relaxation spectra and the relaxation signature can then be used to maximise image contrast. The concept is illustrated using relaxation signatures for the echo planar imaging and Turbo spin-echo imaging sequences, together with in-vitro 2D T1-T2 spectra for liver and cartilage. (C) 2010 Elsevier Inc. All rights reserved.

Contents

Abbreviation list

Abbreviations used in the thesis listed in alphabetical order with their meaning and their page of first appearance. Capital letters in the meaning indicate those used in the abbreviation.

Abbreviation	Meaning	Page
BBSRC	Biotechnology and Biological Sciences Research Council	139
BSA	Bovine Serum Albumin	34
CEST	Chemical Exchange Saturation Transfer imaging	21
CIT	Cold Ischemia Time	58
COSY	COrellation SpectroscopY	10
CPMG	Carr-Purcell-Meiboom-Gill sequence	7
CT	Computed Tomography	2
CURE	Clinical Ultrafast RElaxometry	138
DTI	Diffusion Tensor Imaging	142
EPI	Echo Plannar Imaging	97
FID	Free Induction Decay	5
FIFO	Fast Input Fast Output	106
FLOP	Flipped LOngitudinal Polarisation	105
FSE	Fast Spin Echo	91
HSQC	Heteronuclear Single Quantum Coherence spectroscopy	21
MRI	Magnetic Resonance Imaging	1
MRICOM	MRI COntrast Modelling	95
NECH	Number of ECHoes	26
NMR	Nuclear Magnetic Resonance	1
NNUH	Norfolk and Norwich University Hospital	62
O1	Frequency offset	26
ODIN	Object oriented Development Interface for NMR	86
PCA	Principal Component Analysis	61
PSA	Prostate Serum Antigen	139
PTFE	Polytetrafluoroethylene	25
RAM	Random Access Memory	106
RD	Recycle Delay	104
RG	Receiver Gain	26
ROI	Region Of Interest	22
SF	Spectrometer Frequency	25
SNR	Signal to Noise Ratio	38
SPACE	volume selective sequence (not an acronym)	135
TKR	Total Knee Replacement	63
TR	Time for Recovery (magnetisation recovery time)	105
TSE	Turbo Spin Echo	90
VOI	Volume Of Interest	136
VSS	Virtual Sample Simulation	87

List of Figures

List of Tables

1. Introduction

This chapter will address the need for optimisation in image contrast and the studies already performed in MRI sequence selection. It will then outline the necessary knowledge of the basic science and methodology of NMR and MRI. The problems in the area of contrast optimisation in MRI and tissue characterisation using NMR will be outlined and discussed in order to define the main aims of this thesis.

1.1 The need for optimised image contrast

While Magnetic Resonance Imaging (MRI) is an invaluable tool in the medical profession, there exists the potential to improve clinical practice using a more complete and thorough understanding of the principles underlying the MRI routinely performed. A unique feature of MRI is the almost unlimited variety of pulse sequences (i.e. sequences of radiofrequency and/or gradient pulses) that can be used to create an image. Unfortunately one obstacle to experimenting with modern clinical MRI machines is that access to the underlying code behind these sequences is usually prohibited or requires special permission and licenses. As a result, radiologic images are usually acquired based on standard practice and past experience, without proper optimisation of the sequence selected or the parameters used to acquire the image. The magnetic resonance literature is replete with studies conducted to examine the use of different pulse sequences applied to specific anatomical regions, usually for the examination of specific conditions or injuries, but these are not quantitative studies of the sort common to other physical disciplines. For example, Remplik et al.[1] compared low field MRI with conventional radiography but the study largely consisted of two radiologists examining patients with each technique, without experimentation on parameters. Ku et al[2] looked at the role of MRI in renal trauma but, while they did find it a useful tool, it was simply compared to Computed Tomography with a single parameter set on 12 patients. Pääkkö et al[3] compared high and low field MRI in diagnosis of breast disorders but as before, two radiologists compared scans taken with a single parameter set and the results presented are only measures of agreement. Studies usually consist of a comparison of images acquired using a new technique with images

acquired using a more established MRI pulse sequence or other scanning modality such as Computed Tomography (CT) or arthroscopy (an endoscopic procedure), these being used as a diagnostic gold standard[2, 4-6]. The parameters used are generally stated, if at all, with no indication of selection criteria or optimisation procedures, and this single parameter set is then used to acquire all images, which are then independently reviewed by selected radiologists to reach a series of diagnoses. The new sequence or modality is scored highly when the diagnoses match, providing a vaguely quantitative result, but as the only positive result is a match with the gold standard, any differing diagnosis obtained with the new sequence can be marked as a failure even though it might give a superior diagnosis . There is also an understandable lack of long term follow-up with included patients to confirm the accuracy of diagnoses. This type of experimentation results in useful qualitative indicators for clinical practice, but it does not provide quantitative values for optimising specific sequences, or choosing between them.[4, 5]

1.2 The Basics of NMR

Nuclear Magnetic Resonance (NMR)[7] is possible due to the nuclear magnetic moment of atomic nuclei. In order to possess a nuclear magnetic moment, or spin vector, a nucleus must have non-zero spin, which means it contains the correct number of spin possessing nucleons[8]. Atomic nuclei are made up of differing quantities of protons and neutrons dependent on the chemical element and isotope of the atom. Like electrons, the nucleons of an atom fill orbitals or shells when present in certain quantities (i.e. 2, 8, 20, 28, etc.)[9-11]. As these orbitals are filled, the nucleons pair up in opposing spin states leading to a net spin of zero. When unpaired nucleons are present, the nucleus has non-zero spin and can exhibit nuclear magnetic resonance behaviour. In this thesis we concentrate on ^{1}H (or proton) NMR, in which the single unpaired proton of the nucleus provides the non-zero spin, but other commonly used nuclei include, but are not limited to, ^{2}H (possessing 1 unpaired proton and 1 unpaired neutron) and ^{13}C (possessing 1 unpaired neutron). Both protons and neutrons have spin ½ meaning that the ^{1}H nucleus with its single unpaired nucleon will have a spin of ½ whereas deuterium (^{2}H) with two unpaired nucleons will have a spin of 1. NMR is only possible when the natural abundance of a spin possessing isotope is high enough for detection or in artificially enriched samples.

When placed in a static magnetic field B_0 nuclear magnetic moments align parallel or anti parallel to the magnetic field. In this configuration the parallel alignment is a lower energy state than the anti-parallel alignment. Transitions between these two energy levels are produced by the emission or absorption of a photon at the correct energy, that is, the same as the energy difference between the two levels. The energy of this photon is given by the formula

$$\Delta E = h \nu \quad \textbf{(eq 1.1)}$$

In which ν is the Larmor frequency[12] also referred to as the resonance frequency and h is Plank's constant ($h = 6.626 \times 10^{-34}$ J s). The Larmor frequency of a particle in a magnetic field B_0 is given by

$$\nu = \frac{\gamma B_0}{2\pi} \quad \textbf{(eq 1.2)}$$

In which γ is the gyromagnetic ratio of the particle. This is defined as the ratio of a particle's magnetic dipole moment to its angular momentum. Substituting this into the equation 1.1 we get

$$\Delta E = \hbar \gamma B \quad \textbf{(eq 1.3)}$$

In which $\hbar = h/2\pi$. Via Boltzmann statistics[13] we see that at rest state the ratio of spins in the lower energy level N^1 and higher energy level N^2 is given by

$$\frac{N^2}{N^1} = e^{-E/kT} \quad \textbf{(eq 1.4)}$$

In which k is Boltzmann's constant (1.3805×10^{-23} J/K) and T is the temperature in Kelvin. At room temperature this leaves slightly more nuclei in the lower energy state, producing a net magnetisation M in any room temperature sample. The moments are in fact at a fixed angle θ to the B_0 field but entirely dephased meaning that at this point there is no net

magnetisation transverse to the applied magnetic field (denoted M_x or M_y) and the longitudinal magnetisation (magnetisation parallel to the applied field, denoted M_z) is equal to the total magnetisation at equilibrium M_0. This net magnetisation in a sample, or region of a sample can be thought of as a net magnetisation vector combining the magnetic moments of all nuclei within a volume region (or voxel), with components M_x, M_y and M_z. Using a radio-frequency pulse at the correct frequency ν we can alter the populations of the two energy states and thus, alter the orientation of the net magnetisation vector. By using a long enough pulse to bring the populations of the two energy states to equality, we destroy any magnetisation in the longitudinal direction and leave only magnetisation in the transverse plane as the magnetic moments are now brought into phase. This can be thought of as tipping the magnetisation vector from longitudinal to transverse and is thus referred to as a 90^o pulse. By using a longer duration pulse, we induce more transitions to the higher energy level and thus, further alter the orientation of the net magnetisation vector. A 180^o pulse is one that transfers enough energy to reverse the populations of the upper and lower energy levels, thus reversing the orientation of the magnetisation vector or rotating it 180^o. From this point we continue with the net magnetisation vector model of spin behaviour.

The magnetic moments that the net magnetisation vector is composed of, constantly precess about the static B_0 field[14-16]. Precession, as with a spinning top, is the result of the interaction between the spin nuclear dipole moment and the B_0 field, which generates a torque perpendicular to both, causing the moments to rotate around the axis of the B_0 field at the Larmor frequency ν. As previously stated, during a radio frequency pulse at the correct frequency ν, a torque is applied to the magnetisation vector so as to tip it from its longitudinal alignment. Because they are now in phase with each other, the precessing moments of the magnetisation vector induce an electromagnetic field in a radio-frequency coil, usually the same radio-frequency coil used to generate the radio-frequency pulse, and measurement of the resultant current allows detection of the state of the moments' alignment. The moments continue to precess as the system returns to the equilibrium state with the magnetisation vector back in alignment with the constant field B_0. This return to equilibrium is characterised by the magnetic resonance relaxation times T_1, T_2, and T_{2*}[12].

1.2.1 The T_1 parameter

T_1 is defined as the time taken for longitudinal magnetisation M_z to return to 63% of its equilibrium value after the radio-frequency pulse or, the time taken to restore the Z component of magnetisation by a factor of e. This value is called the longitudinal or spin-lattice relaxation time. This relaxation is caused by the interaction of the static and moving fields returning to the lower energy of the equilibrium state.

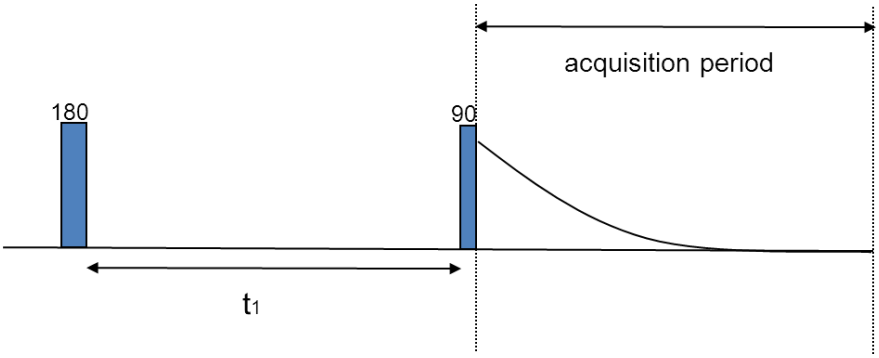

Figure 1.1 The inversion recovery pulse sequence showing pulses in blue separated by the variable recovery time t_1 and the acquisition period during which an FID(Free Induction Decay) is acquired.

T_1 is measured using inversion recovery as shown in figure 1.1 or saturation recovery, which uses a 90 degree starting pulse rather than a 180 degree pulse. During saturation recovery the magnetisation recovers from 0 to M_0 at a rate dictated by the value T_1 as described above. The magnetisation M_z at a given time t can then be shown to be

$$M_z = M_o(1 - e^{-t/T_1}) \quad \textbf{(eq 1.5)}$$

T_1 is more commonly determined using the previously mentioned inversion recovery sequence. In this sequence the magnetisation M_z begins at a value of $-M_0$ following a 180 degree pulse. It then returns to the equilibrium value M_0 as before. In this case the magnetisation M_z at a given time t is given by

$$M_z = M_o(1 - 2e^{-t/T_1}) \quad \textbf{(eq 1.6)}$$

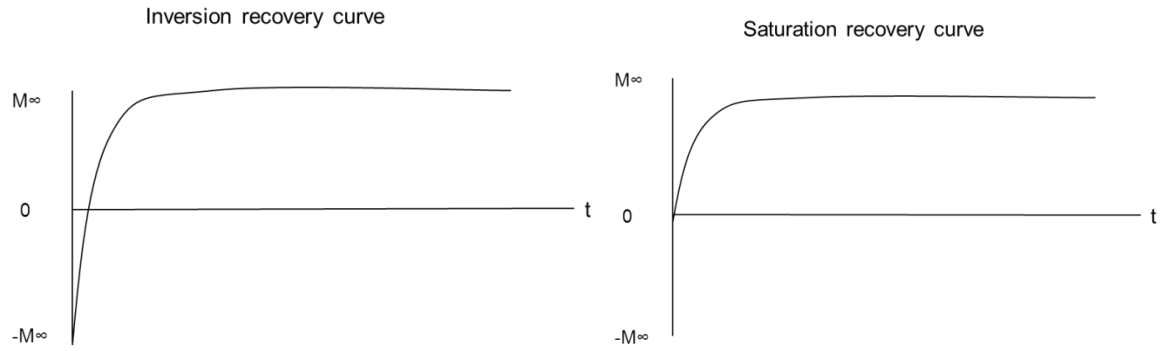

Figure 1.2 Recovery curves of the inversion recovery and saturation recovery pulse sequences showing the recovery of M_z Back to M_∞ from $-M_\infty$ and 0 respectively, following the initial pulse of an inversion recovery or saturation recovery pulse sequence.

Figure 1.2 shows the recovery curves of M_z in both the inversion recovery and saturation recovery situations. In order to find the value of M_z in both cases an FID or free induction decay is induced by using a 90 degree pulse to flip the longitudinal magnetisation into the transverse plane. The precessing moments, now transverse, induce a signal in the radiofrequency coil and its initial magnitude will be the magnitude of M_z at the time of the 90 degree pulse. In this case the sample must return to equilibrium before the experiment is repeated in order to acquire multiple data points and build up a curve.

1.2.2 The T_2 and T_{2*} parameters

T_2 is the time required for the transverse magnetisation to decay via irreversible processes to 37 per cent of its initial value, i.e. to reduce by a factor of e, following the radio-frequency pulse. T_2 is known as the spin-spin or transverse relaxation time and characterises the dephasing of the spins within the sample. The net magnetisation of the sample is made up of many precessing nuclear spins which are in phase following the radio-frequency pulse. They are each in slightly different local magnetic environments and thus have different resonant frequencies. This causes the spins making up the net magnetisation vector to dephase and as spins begin to point in different directions they destructively interfere with each other, reducing the net transverse magnetisation. This process takes place at the same time as the longitudinal recovery and thus T_2 must be equal to or lower than T_1 as the total magnetic magnitude cannot exceed the equilibrium magnitude. In reality the pure T_2 dephasing is also affected by a dephasing due to field inhomogeneities and the combination of this and the pure T_2 dephasing, results in the total

parameter T_2^*. Measurements of the T_2 parameter are carried out using the Carr-Purcell-Meiboom-Gill (CPMG) technique, shown in figure 1.3.

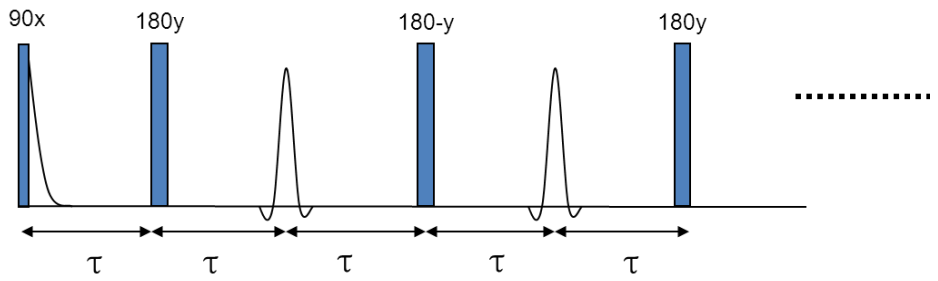

Figure 1.3 The CPMG (Carr-Purcell-Meiboom-Gill) pulse sequence demonstrating the 90-180 pulse separation τ and the 180-180 pulse separation 2τ along with the resultant echoes in transverse magnetisation.

Following a 90 degree pulse and after a time tau, the different spins in the sample have dephased due to precessing at differing frequencies. Using another radio-frequency pulse to flip the spins 180 degrees along the y axis, the spins can be rephased as the slower spins are now placed ahead of the faster spins and, as they continue to precess at the same rate, after another time tau they will have realigned causing a peak in the detected signal. The peak height at this point is the transverse magnetisation reduced only by the pure T_2 dephasing. By repeating this 180 degree pulse after a time 2*tau (as can be seen in figure 1.3) we get a train of peaks and by recording the peak heights we have data points demonstrating only the pure T_2 dephasing of the sample. This decay in the peak amplitude, and so the transverse magnetisation, is characterised by T_2 and the value at time t is given by the formula

$$M_{xy} = M_{xy0}e^{-t/T_2} \qquad \textbf{(eq 1.7)}$$

In which M_{xy} is the transverse magnetisation (magnetisation in the x-y plane) and M_{xy0} is the transverse magnetisation immediately following the 90 degree pulse. As we can see from this equation 1.7, as time t increases, magnetisation M_{xy} decreases towards zero. This can be contrasted with equations 1.5 and 1.6 which show that as time t increases, magnetisation M_z increases towards M_0. If T_2^* is to be examined then a 90 degree pulse from equilibrium to put the magnetisation into the transverse plane will induce an FID which is simply a decay of the transverse magnetisation due to T_2^* effects. T_2^* can then be calculated using the same relationship as with T_2, as shown in equation 1.8

$$M_{xy} = M_{xy0} e^{-t/T_2*} \quad \textbf{(eq 1.8)}$$

1.2.3 Chemical shift

When an atom is placed in a magnetic field its electron orbits change so as to create a small magnetic field at the nucleus, opposing the applied magnetic field[17]. This affects the magnetisation experienced by the nucleus meaning that the effective magnetic field at the nucleus is given by equation 1.9, in which σ is the fraction by which the magnetisation is reduced, also known as the shielding tensor[18].

$$B = B_o (1-\sigma) \quad \textbf{(eq 1.9)}$$

The electron density and arrangement around any particular nucleus will vary based on the surrounding atoms and their chemical bonds and this effect is referred to as chemical shift. The chemical shift parameter δ is the difference between the Larmor frequency of the nucleus ν and the frequency of a reference nucleus ν_{ref} as shown in equation 1.10. A reference is used as the frequency of free nuclei cannot be easily measured.

$$\delta = (\nu - \nu_{ref}) \times 10^6 / \nu_{ref} \quad \textbf{(eq 1.10)}$$

1.2.4 The spectrum of relaxation times in a single dimension

The discussion up to now has assumed that the sample can be characterised by a set of single relaxation times T_1, T_2 and T_2^*. Many examples in the literature treat samples this way, for instance Scholz et al[19] examined the effect of fat and water content on relaxation parameters in samples of hog myocardium. They found an inverse correlation between T_1 and fat content and a positive curvilinear relationship between T_2 and fat content, but by characterising the tissue with only a single T_1 value they were only able to see a weighted average of the T_1 and T_2 values for the water, fat and muscle in the tissue. This would cloud assignment of the cause of any observed effects, for instance water content decreased

at increased fat content so the average would be affected by both. To increase the information content of a sample's relaxation behaviour, many real samples, such as biological tissue, need to be characterised by a continuous distribution of relaxation times, $P(T_1)$, $P(T_2)$ and $P(T_2^*)$ which are the probability distributions of finding a particular T_1, T_2 or T_2^* in the sample[20]. These one dimensional probability distributions are referred to as 1D relaxation spectra. They are defined by the equations

$$M(t) = \int dT_2^{\ *}\ P(T_2^{\ *}\ )e^{-t/T_2^{\ *}} \longleftrightarrow P(T_2^{\ *}\ ) = \int dt\ e^{-t/T_2^{\ *}}\ M(t) \qquad \textbf{(eq 1.11)}$$

FID

$$M\ t\ = \int dT_2 P\ T_2\ e^{-t/T_2} \longleftrightarrow P\ T_2\ = \int dt\ e^{-t/T_2} M(t) \qquad \textbf{(eq 1.12)}$$

CPMG

$$M(t) = \int dT_1 P(T_1)(1 - e^{-t/T_1}) \longleftrightarrow P(T_1) = \int dt(1 - e^{-t/T_1})\frac{M(t)}{M(\infty)} \qquad \textbf{(eq 1.13)}$$

Saturation recovery

$$M(t) = \int dT_1 P(T_1)(1 - 2e^{-t/T_1}) \longleftrightarrow P(T_1) = \int dt(1 - 2e^{-t/T_1})\frac{M(t)}{M(\infty)} \qquad \textbf{(eq 1.14)}$$

Inversion recovery

An example of a T_2 relaxation spectrum is shown in figure 1.4. The integrals in these definitions can be shown to be Laplace transforms and Inverse Laplace transforms. Software for performing these transforms is readily available (e.g. WINDXP[21]). If the relaxation spectrum shows a discrete number of well resolved peaks we say that the relaxation is bi-exponential in the case of 2 peaks, triple in the case of 3 peaks, and so on.

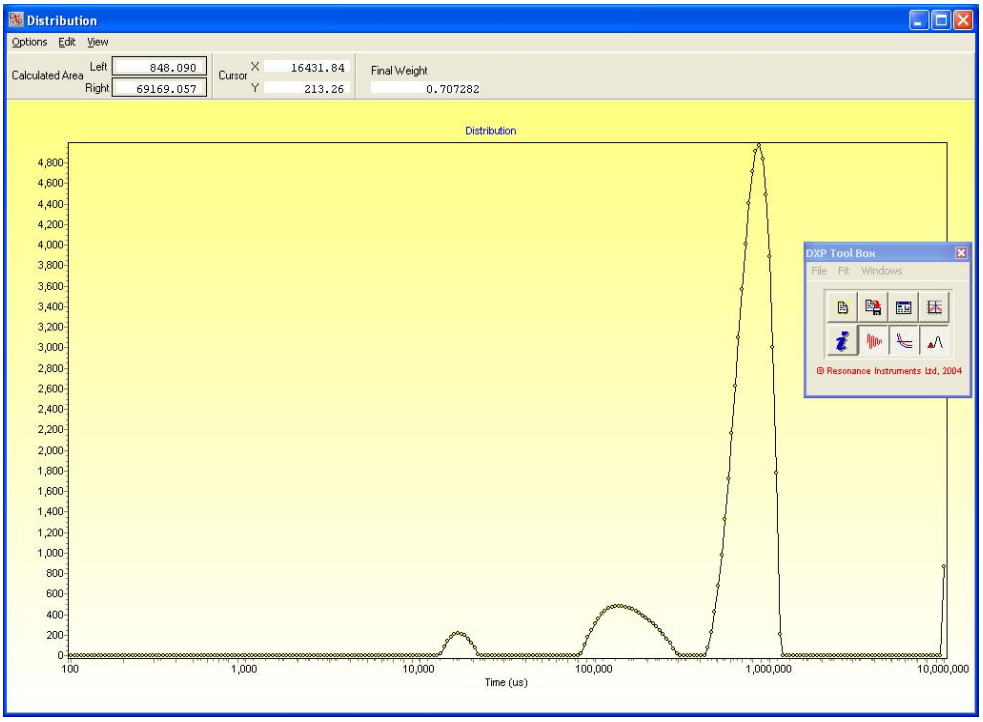

Figure 1.4 An example T_2 relaxation spectrum of a commercial apple acquired at 23.4 MHz demonstrating three well resolved peaks in the sample's T_2.

1.2.5 The spectrum of relaxation in two dimensions

The concept of two dimensional NMR measurements comes originally from high resolution, frequency domain NMR spectroscopy so it is worth, briefly, digressing into this domain. One of the simplest methods is COSY (COrrelation SpectroscopY).

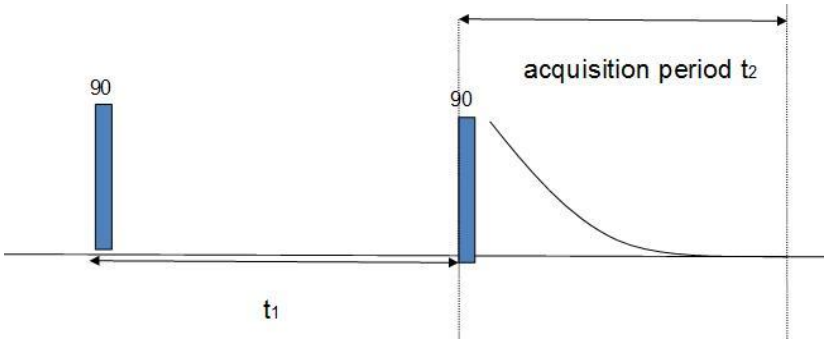

Figure 1.5 The COSY (COrrelation SpectroscopY) sequence showing the variable evolution time t_1 separating the two 90 degree pulses, shown in blue, and the acquisition period t_2 during which an FID is acquired.

COSY[22] uses two 90 degree pulses separated by a time t_1, as shown in figure 1.5. Signal is acquired following the second pulse and this is recorded in a matrix as the t_2 dimension. The t_1 dimension is then filled in by multiple repeats of the sequence using a systematically

increased set of t_1 values (e.g. 0, Δt_1, $2\Delta t_1$, $3\Delta t_1$, ...). This two dimensional time data is then Fourier transformed in both dimensions to give a 2D frequency plot. A simplified example is given in Figure 1.6.

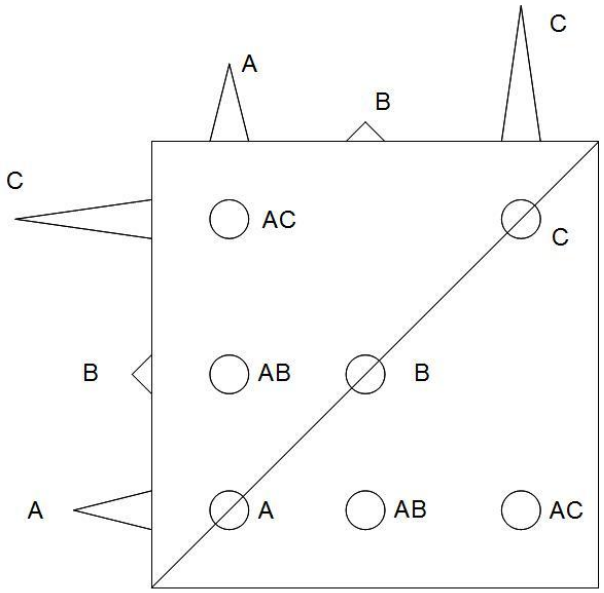

Figure 1.6 A simplified imagining of a possible COSY(COrrelation SpectroscopY) output with T2 peaks A, B and C along the diagonal and projected on the top and left axes of the square. The off diagonal peaks AC and AB are the result of coupling between peaks A and C, and peaks A and B respectively.

In this example an imagined frequency spectrum is shown on the diagonal as well as projected on both axes. In addition to these diagonal peaks, labelled A, B and C, cross-peaks are seen off the diagonal. These peaks result from spin-spin coupling of the nuclei in the diagonal peaks. Spin-spin coupling causes magnetisation transfer between different peaks in the spectrum, and thus nuclei in the sample. Coupling occurs in this example between peaks A and B, as well as peaks A and C. Each of these couplings would result in cross-peaks as shown labelled AB and AC, off the diagonal in line with the two coupled peaks. In this way the COSY sequence provides information on the resonance frequencies and spin-spin couplings of the sample.

In this thesis we will focus exclusively on relaxometry and not on high resolution spectroscopy, but a similar multidimensional concept applies. 2D relaxometry works by introducing two time dimensions in which each time dimension is associated with a particular relaxation time (T_1, T_2 or T_2^*). The simplest example is the Inversion Recovery – CPMG sequence which associates the first time dimension with inversion recovery (T_1) and the second with a CPMG echo decay envelope (T_2)[23].

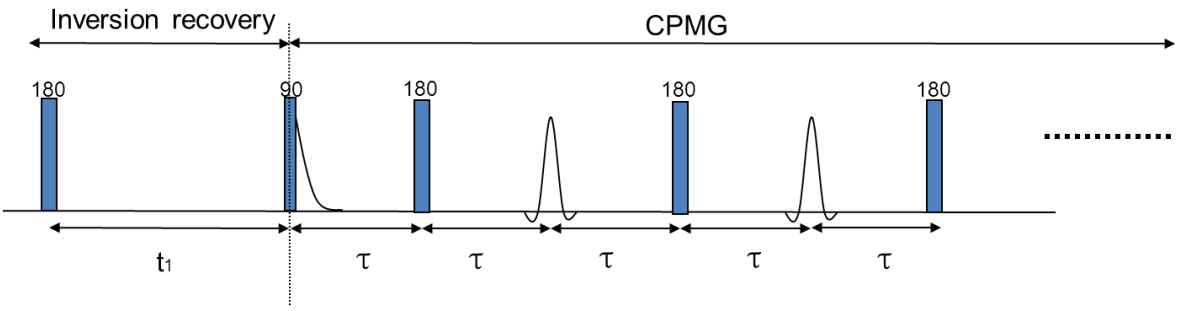

Figure 1.7 The inversion recovery CPMG sequence with variable recovery period t_1 followed by a CPMG train with 90-180 pulse separation τ and 180-180 pulse separation 2τ along with the resultant echoes in transverse magnetisation.

Figure 1.7 shows the pulse sequence for this 2D Inversion recovery CPMG pulse sequence (INVCPMG). As shown, the sequence consists of an inversion recovery step, discussed previously, but instead of using an FID to find the amplitude following the time period t_1, the longitudinal magnetisation is flipped into the transverse plane by the first pulse of a CPMG sequence. By varying t_1 and acquiring CPMGs in this way we can fill in a 2D matrix of timespace data with dimensions t_1 and t_2, where t_1 is the inversion recovery time and t_2 is the echo time for each echo in the CPMG sequence (t_2 =0, 2τ, 4τ, ….N(2τ)). Instead of performing 2D Fourier analysis it is necessary to use Laplace transformation[24]. The 2D Laplace transform algorithm of Song et al[24] performs a least squares fit on two dimensional data with a non-negativity constraint and has been shown to be stable in the presence of noise using a regularisation parameter α set to the correct value. Too small a value will make the results unstable and introduce additional small peaks. Too large a value will remove potentially useful data from the final spectrum. Work done by Nuisa Marigheto[25-27] established the usefulness of an α value of unity in the examination of biological tissues and moist samples, and this is used as standard both within the lab and within this thesis. The 2D data matrix $M(t_1, t_2)$ is related to the T_1-T_2 spectrum $P(T_1, T_2)$ by the 2D Laplace transformation in equation 1.15.

$$M(t_1, t_2) = \int\int dT_1 dT_2 P(T_1, T_2) \exp(\frac{-t}{T_2}) M_\infty [1 - 2\exp(\frac{-t}{T_1})] \quad \textbf{(eq 1.15)}$$

Thus by using 2D inverse Laplace transformation we can obtain the T_1-T_2 spectrum $P(T_1, T_2)$ as can be seen in figure 1.8. The exponential factors in equation 1.15 are called "kernels". The example spectrum in figure 1.8 is from a sample of lamb's liver. Here we can see 7 peaks in the spectrum, resolved in T_1 on the horizontal axis and T_2 on the

vertical. The reasons for 2D T_1-T_2 spectroscopy are now clear as peaks 3, 5 and 7 have very similar T_1 values but can be resolved in T_2, whereas peaks 4 and 5 or peaks 6 and 7 have similar T_2 values but can be resolved easily in T_1.

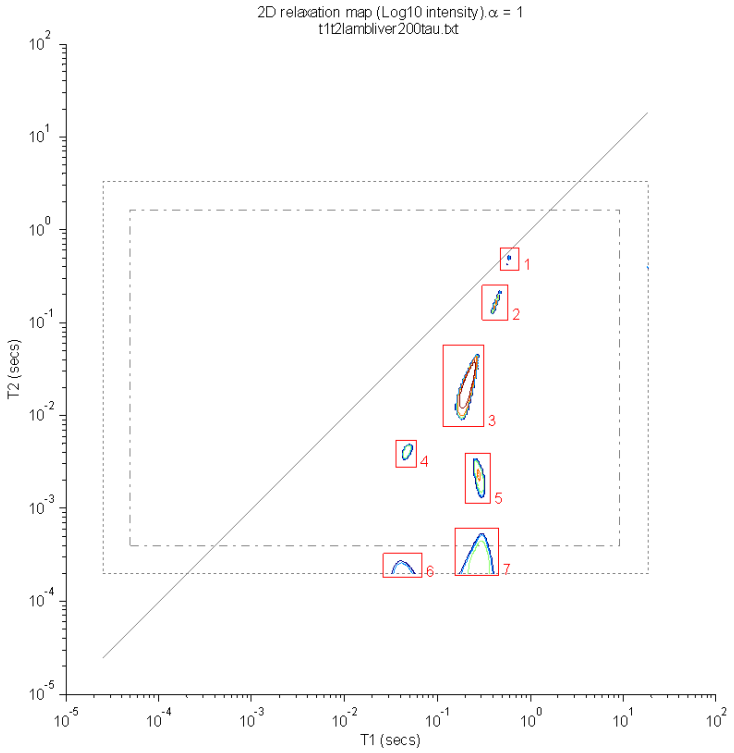

Figure 1.8 T_1 - T_2 relaxation spectrum of fresh lamb's liver acquired at 100 MHz, using inversion recovery.

1.2.6 Volume selection

Previously discussed methods have assumed that an NMR experiment will be performed on a single sample in isolation but, practically, this may not be the case[28, 29]. The sample to be scanned may be contained within a larger mass that cannot be removed, such as when performing spectroscopy on a small region within a living body. In this case the signal must be detected only from the region of interest with extraneous signal being destroyed or ignored. There are many methods of volume selection but most function using multiple slice selective pulse sequence steps[30, 31]. This slice selection is achieved by first applying a longitudinal gradient in the magnetic field along one of the X, Y or Z axes. As shown in equation 1.2, the resonant frequency of the sample is proportional to the applied field B_0 so a longitudinal magnetisation gradient will create a longitudinal gradient in the resonant frequency of the sample. Equation 1.16 shows the resonant frequency of spins under a

static field B_0 with applied gradient G_x in the X direction, at a position x, along the X axis. The position x is determined by rearranging equation 1.16 into equation 1.17. By applying a radio-frequency pulse of the correct frequency during this gradient we affect a slice through the total sample transverse to the gradient axis with a width Δx determined by equation 1.18 below.

$$\nu = \gamma (B_0 + x\, G_x) = \nu_0 + \gamma\, x\, G_x \qquad \textbf{(eq 1.16)}$$

$$x = (\nu - \nu_0) / \gamma\, G_x \qquad \textbf{(eq 1.17)}$$

$$\Delta x = \Delta\nu / \gamma\, G_x \qquad \textbf{(eq 1.18)}$$

By repeating this process in each orthogonal axis (as shown in figure 1.9) and ensuring destruction of magnetisation outside the slice, we can detect magnetisation from a specific volume region and not the bulk sample. Sinc pulses are used as their frequency content is a narrow band of equal intensity and will thus equally excite a narrow region of the sample. This can be shown by Fourier transforming a sinc pulse[32].

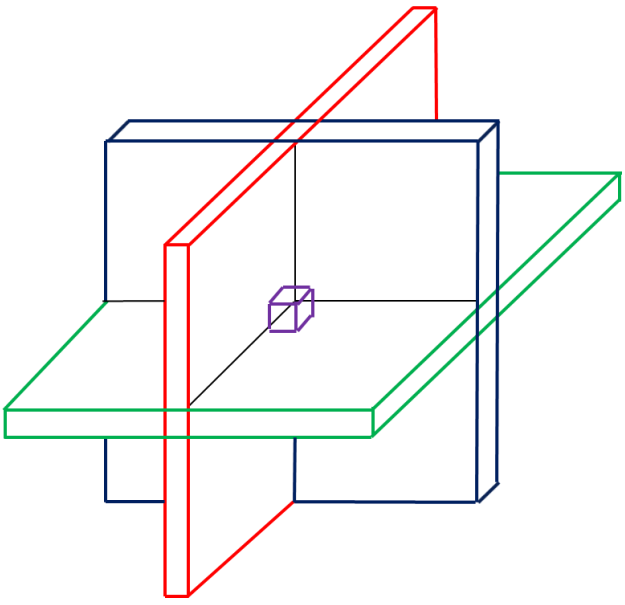

Figure 1.9 Three orthogonal planes in red, blue and green creating a cubic volume of overlap in the centre, shown in purple, with dimensions equal to the width of the orthogonal planes.

1.3 The basics of MRI

MRI uses the properties of NMR to create an image of a scanned object, usually for medical purposes. It uses volume selective methods to differentiate between signal from different regions of the body and converts the information acquired into pixels in an image.

1.3.1 Back projection imaging

Back projection imaging is one of the oldest forms of magnetic resonance imaging[33]. To produce an image in the XY plane we first apply a linear gradient in one direction, such as X, and acquire an NMR spectrum. This sequence is then repeated varying the direction of the linear gradient around a circle in the XY plane. The X and Y gradients can be used to produce an effective gradient at any angle θ in this plane by setting them to values given by equations 1.19 and 1.20 below.

$$G_y = G_f \text{ Sin } \theta \qquad \textbf{(eq 1.19)}$$

$$G_x = G_f \text{ Cos } \theta \qquad \textbf{(eq 1.20)}$$

Where G_f is the necessary frequency encoding gradient. Once these spectra are acquired they can be back-projected as shown in figure 1.10. The background signal is then removed to leave a back projected image in this plane. The back projection scheme is known as the inverse radon transfer[34]. Figure 1.10 shows simulated back projection using only 8 spectra, and thus recreates a distorted 'star-shaped' image of the dots in the original phantom. More spectra provide more exact back projection and thus, better recreation of the phantom in the final image. In order to carry out this back projection procedure we must have first slice selected in the Z direction as explained in the previous section (1.2.6).

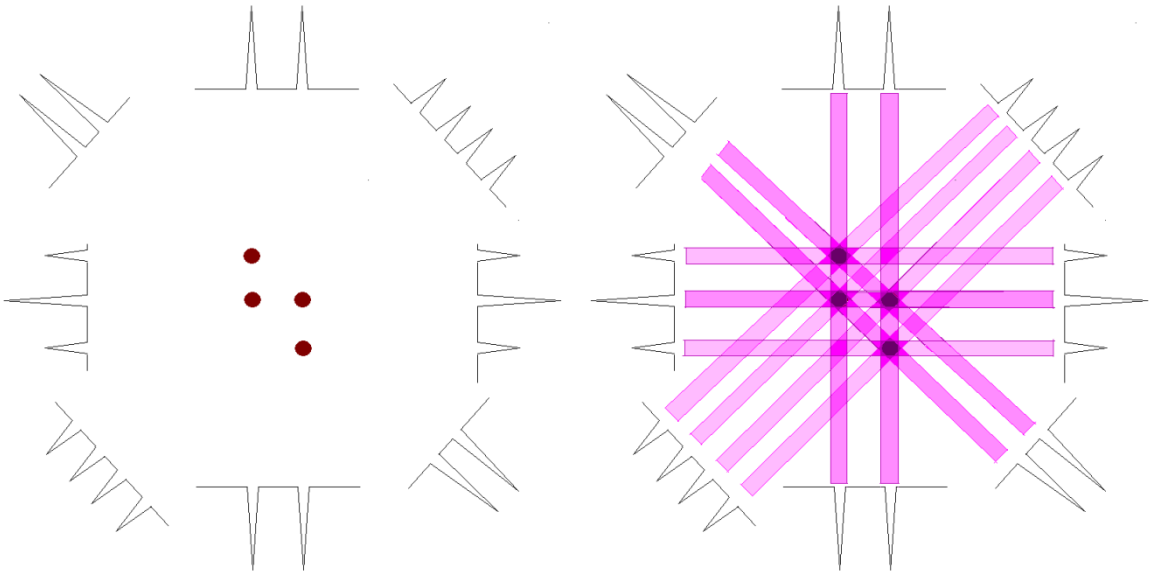

Figure 1.10 Left: A representation of a phantom consisting of four dots of NMR responsive material shown in dark red, within a region of white, non-responsive material. The phantom is surrounded by imagined NMR spectra taken at angles represented by their position around the phantom. Right: the same NMR spectra back projected with darker colour representing increased intensity, showing the resultant image of the phantom obtained via this technique.

1.3.2 Slice selection, frequency encoding and phase encoding

As with volume selected NMR, slice selection in MRI uses a longitudinal gradient to alter the resonant frequency of spins based on their position along a specific axis. Using a sinc pulse during this gradient excites a slice through the object perpendicular to the axis of the magnetic field. This volume selective step could then be repeated in orthogonal dimensions to isolate the received signal from a single voxel, but to create a 3 dimensional image the whole sequence would need to be repeated for each voxel, making the necessary scanning time impractically long. The final 3-dimensional scan will actually be composed of many of these individual slices taken through the region of interest. In order to then differentiate between the voxels contained within the slice selected signal, frequency and phase encoding are used[(35)].

Frequency encoding involves application of a longitudinal gradient during signal acquisition to alter the resonant frequency of spins based on their position along the axis of the field. By altering the frequency at which the spins precess, following their slice selective excitation during the previous step, the spins will be positionally encoded in the

dimension of the applied field based on their frequency. In this way the signal from all voxels can be retained and differentiated.

Phase encoding involves applying a longitudinal gradient during precession of the spins, but not during acquisition. As with frequency encoding, the spins will precess at different rates dependant on position during the gradient and return to their previous precessional frequency following the gradient. Thus there will be a difference in the phase of the spins dependant on position along the axis of the gradient but no difference in frequency.

By applying these techniques orthogonal to each other, positionally encoded phase and frequency information from a single slice through a sample can be acquired. This information can be extracted using Fourier transformation.

1.3.4 Fourier transform tomographic imaging

Figure 1.11 shows a simplified Fourier transform tomographic imaging sequence. The sequence works by using the slice selective, phase encoding, and frequency encoding steps described above and labelled here s, Φ, and f [36, 37]. If we had a single spin-filled voxel located somewhere within our slice through the sample, then a simple one dimensional Fourier transform on the returned signal would yield a single peak with frequency f and phase Φ, corresponding to the position of the voxel.

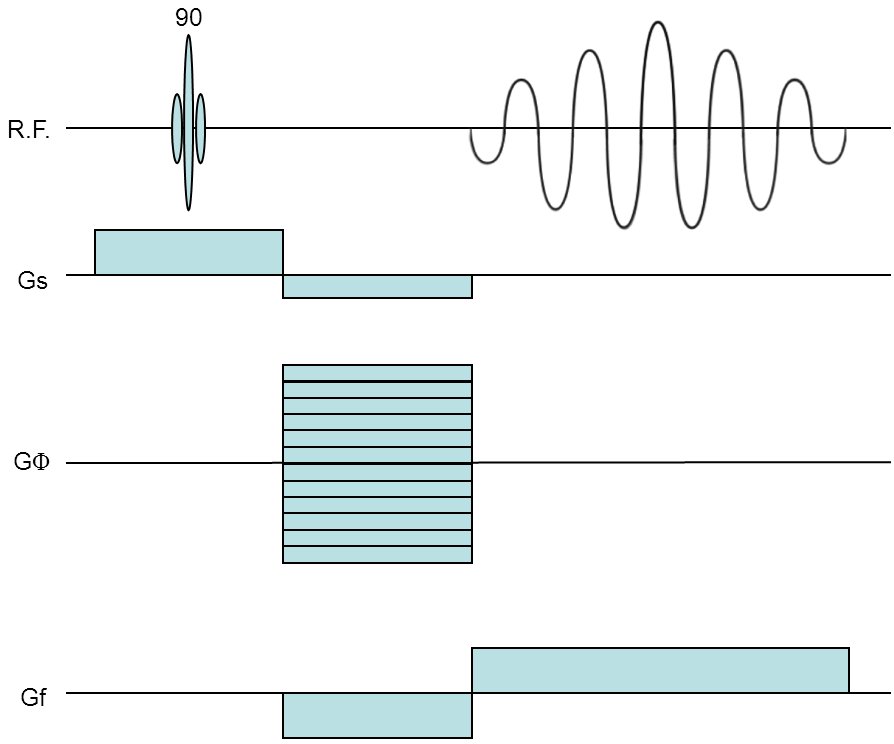

Figure 1.11 Simplified Fourier transform tomographic imaging sequence showing the slice selective radiofrequency sinc pulse during the slice selective gradient G_s, the phase encoding gradient G_Φ and the acquisition during the frequency encoding gradient G_f, represented by the oscillating R.F. line.

In reality any sample worth examining will consist of multiple voxels of different types at different positions. To find all the separate peaks at their specific positions we must repeat the sequence many times at different phase gradient magnitudes in order to build up a 2D matrix of signals. This 2D matrix is referred to as being in k-space[38, 39], thus we can discuss filling in different lines of k-space with each different phase gradient magnitude step. K-space is the term used to describe the reciprocal of the final data set, which is the result of Fourier transforming that data set. When this reciprocal data set is again Fourier transformed, it returns the final data set used to create it. Thus the 2D matrix acquired in k-space must then be Fourier transformed, first in the frequency domain, then in the phase domain, to result in a 2D matrix representing the magnitude and position of all detected spin containing voxels. Showing this matrix as a greyscale image is what gives us the familiar 2D MRI slice which is used to build up the 3D picture of the sample. The Fourier transformed matrix will contain the same number of elements as the acquired signal matrix, so there must be as many repetitions at different phase gradients as the required definition of the final image in the phase encoded dimension.

1.4 The problems to be solved

Having discussed the origin of NMR and MRI processes we now address the aims of the thesis with regard to improving the state of contrast prediction in MRI and tissue characterisation in NMR.

1.4.1 Optimising the parameters determining image contrast

Image contrast is determined by various factors including spin density, T_1, T_2 and T_2* relaxation times, diffusion coefficients and chemical shift (as described previously). Apart from flow imaging, spin density and relaxation times play the dominant role in determining image contrast in MRI. Spin density is a measure of the total available spins per unit volume, which varies according to tissue type. This value determines the maximum possible signal response of a specific tissue and therefore provides one facet of image contrast. However image contrast also depends on the way the magnetisation 'relaxes' in time, that is, changes its magnitude between radio-frequency or gradient pulses. These relaxation processes are usually classified in terms of T_1, T_2 and T_2*, and image contrast can be 'weighted' by these relaxation times, which were discussed previously in this chapter. Here we need only note that they are individually characteristic of the nature of the tissue being imaged. Image contrast can therefore be manipulated by choosing pulse sequences that vary the relative weighting of these relaxation processes. One of the difficulties in developmental MRI is knowing which combination of these relaxation processes is 'optimum' for identifying a particular clinical condition/disease. This choice is made even more difficult because the overall relaxation weighting of image contrast will depend on the plethora of parameters (such as inter-pulse spacing, gradient amplitudes and shapes, etc.) that characterise an MRI pulse sequence.

One of the aims of this thesis is, therefore, to try to rationalise the choice of optimum sequence using 'in silico' methods. This will be discussed in greater detail in chapter 5.

1.4.2 Optimising field strength

The need for optimisation does not end at the choice of sequence and parameters. The magnetic field strength of the scanner itself plays a part in determining image contrast and resolution. Higher field strength induces more polarised magnetisation and therefore gives improved signal to noise in the image. This, in turn, allows higher spatial resolution in the image. For this reason high field scanners predominate the market and the trend is towards increasing field strength[(40)]. While this is a desirable goal, higher field scanners do not necessarily provide the best contrast between tissue types as the higher field strength also affects the relaxation times of the tissue. The T_1 relaxation parameter for different tissues tends to increase and converge with increasing field strength, leading to a reduction of image contrast in T_1 weighted MR images. T_2 values tend to decrease at higher fields, which can cause reduced signal amplitude with some imaging sequences where transverse magnetisation is being manipulated for extended periods. These effects could result in higher field images having reduced contrast between certain tissues and structures and thus potentially cause those tissues and structures to be less clearly distinguishable in clinical images obtained[(40)].

In some countries, such as Japan, the trend towards high field systems is not as evident, as health care reimbursement for MRI scans is capped. This results in more profit from low or mid-field scans than high field ones as these scanners are cheaper to purchase, maintain, and operate[(41, 42)]. Another aim of this thesis is, therefore, to allow identification of the magnetic field strength that gives optimum image contrast while not significantly compromising resolution.

1.4.3 *In vivo* and *in vitro* determination of the NMR parameters

For optimisation of parameters and field strength, proper characterisation of the relaxation behaviour of each tissue type must be conducted. The vast majority of clinical MRI studies merely acquire 'relaxation-weighted' images without ever attempting to measure a tissue T_1 or T_2 value. Even in MRI clinical research where image maps of T_1 or T_2 are acquired, it is usual to assume that the relaxation can be described as a single average exponential[(43)]. Only in a few MRI reports are images characterised with multiple exponential relaxation.

Yet, as we will show, most tissues are characterised by multiple T_1 and T_2 relaxation, and the relaxation is best characterised by the two dimensional T_1 - T_2 cross correlation relaxation spectra described previously. There are only a handful of examples where T_1 - T_2 spectra have been acquired in in-vivo MRI. Another aim of this thesis is, therefore, to show the potential diagnostic value of two-dimensional T_1 - T_2 relaxation spectra in in-vivo MRI.

Examples of clinical relaxation studies where multiple exponential relaxation has been analysed include Zaid Q. Ababneh[44] who examined rat optic nerve in more detail using CPMG sequences and fitted bi-exponential curves to extract two values for T_2 peaks within the sample. This would not allow resolution of peaks with similar T_2 but differing T_1 values and only showed the dominant two peaks, ignoring any additional, but relatively small, peaks. Graham et al.[45] examined human breast tissue using a spatially localised T_2 sequence to extract multicomponent T_2 spectra in vivo but these were not correlated with T_1 values, again losing any additional information about peaks with similar T_2 and differing T_1. Saab et al[46] examined in vivo skeletal muscle assigning multi-component T_2 spectra but, again, these were not correlated with T_1 values. Ping-Chang et al[47] examined cartilage in-vitro examining various NMR constants but, as in previous studies, each was determined separately and then compared. The 2D work they did do, consisted only of looking for clustering when plotting single exponential T_1 and T_2 values against each other along with magnetisation transfer rates and apparent diffusion coefficients. Does and Gore[48] examined rat brain and trigeminal nerve using a 2-dimensional saturation recovery sequence. While this sequence did result in correlated T_1- T_2 values it could only be regarded as preliminary investigation. They found three clusterings in their T_1- T_2 data points (correlating to three likely T_1- T_2 peaks), but their final 2D data set was compiled by summation of all their available data sets. For this reason the results are less instructive than a series of comparable T_1- T_2 profiles, which could be examined for consistency, or contrasted for difference in the case of different tissues or tissue conditions. Ling et al examined bovine cartilage using various NMR spectroscopy methods[49]. Their 2D results consisted of Heteronuclear single quantum coherence spectroscopy (HSQC) which correlates a proton NMR spectrum in one dimension with the chemical shift of a hetero nucleus (another non-proton nucleus, in this case ^{13}C). While this is a 2D technique, it provides information on chemical shift related to a single NMR parameter and does not provide complete T_1-T_2 information. They found results suggesting that spectroscopic

markers of cartilage degradation could be found using techniques such as chemical exchange saturation transfer imaging (CEST), lending weight to the notion that they can be identified using other techniques.[50-52]

1.4.4 Characterisation of tissue with 2D NMR relaxometry

As implied previously, the two dimensional T_1-T_2 relaxation spectrum is a far superior way of characterising the relaxation behaviour of any tissue. Figure 1.12 shows another example of such a spectrum acquired using a laboratory NMR spectrometer 'in-vitro'. Each peak in the spectrum arises from a particular pool of protons with similar T_1-T_2 relaxation behaviour, although it is not always straightforward to assign the peaks to particular sub-cellular water compartments, bio-polymer protons or metabolites.

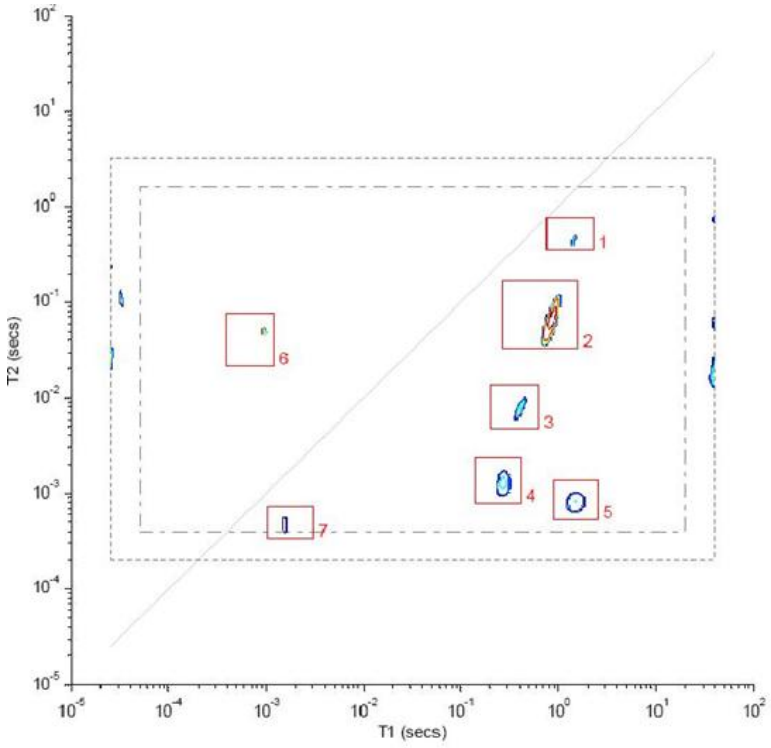

Figure 1.12 The T_1 - T_2 relaxation spectrum of pig kidney cortex acquired at 100MHz, using the inversion recovery pulse sequence, demonstrating a complex spectrum of peaks spread across 2 dimensions.

In the ideal situation it would be desirable to acquire such a T_1-T_2 spectrum from every voxel in an MRI image. However, low signal to noise ratio and/or time constraints make this impractical. Nevertheless it is possible to acquire a 2D T_1-T_2 spectrum from a small region of interest (ROI), although this is at the expense of spatial resolution. It seems,

therefore, that there is a range of choice between high spatial resolution and the degree to which the relaxation is characterised.

In conventional MRI one usually chooses high spatial resolution at the expense of poor characterisation of the relaxation. In this thesis we wish to explore the opposite perspective where we reduce spatial resolution to an ROI but try to maximise information about the relaxation characteristics of the tissue. This is based on the hypothesis that a 2D relaxation spectrum has far greater diagnostic potential than merely relaxation weighted contrast.
The research of the NMR team in Norwich supports this hypothesis, although the studies were mainly limited to cellular plant tissue. For example Marigheto et al[53] used this technique to examine ripening and mealiness in apples. They found differences in the T_1-T_2 spectra of apples in different stages of ripening and freshness, in particular an increase in the T_1 of the T_1-T_2 peak associated with the cell wall in mealy apples. Skinner et al[54] used a similar technique to examine muscle edema in rat limbs. They found that, in scans of rat muscle, artificially induced edema resulted in two well resolved T_1-T_2 peaks in the final spectra. While we focus mainly on T_1 - T_2 relaxation spectra in this thesis, other 2-dimensional methods have been proposed which combine other NMR parameters. Callaghan et al[55] examined a number of these in studies of porous media, highlighting Diffusion-Diffusion and COSY (Correlation Spectroscopy, defined earlier). They found, as with most current 2-dimensional methods, that the time taken to conduct 2D scans was very long, often on the order of hours. This extremely long acquisition time would create an issue in a clinical setting, as in vivo patient scans would necessitate keeping the patient absolutely still for a matter of hours.

1.4.5 The main aims for the thesis

Given this background there is clearly a need to optimise MRI image contrast by optimising the choice of pulse sequence and spectrometer field strength. To do this systematically we require a detailed knowledge of the NMR parameters (T_1, T_2, T_{2*} .....) characterising each type of tissue of clinical interest. As we have shown, the most detailed characterisation is achieved using not 1D, but 2D relaxometry, which includes T_1-T_2, T_2-D and T_2-store-T_2 sequences which will be explained in the next chapter dealing with methodology. Once a 2D relaxation spectrum has been acquired it is then necessary to

develop an 'in-silico' methodology for calculating the image contrast from the 2D relaxation spectrum for any chosen MRI imaging sequence.

As we shall demonstrate, in addition to its use for image contrast prediction, 2D relaxometry offers the potential of acting as a clinical biomarker in its own right. The 2D relaxation spectrum provides good characterisation of the tissue in question and could, with proper refinements, be used to assay the condition of specific anatomical regions and structures in-vivo, without the need for any invasive procedures. Consider, for example, the case of osteoarthritis. Diagnosis is usually reached only after the cartilage has mostly, or completely, worn away, resulting in pain to the individual and the necessity of a replacement joint. Research is under way to find chemical methods to prevent the alterations in structure and composition of the cartilage which allow this degradation and loss to take place. In order for this to be applied in a clinical setting it would necessitate a method for distinguishing between healthy and arthritic cartilage, preferably non-invasively and we will show that a T_1-T_2 spectrum achieves this aim. As well as examination of tissue, in-vivo MRI relaxometry could be used to examine the digestion of food in the GI tract, allowing an examination of the stage at which different nutrients and substances are absorbed.

As mentioned, one of the outstanding problems with 2D relaxometry so far reported in the literature is the very long acquisition times which can be between 20 minutes and several hours, depending on the nature of the tissue and sequence. Reducing the 2D acquisition times will therefore be essential before 2D relaxation methods can be used for routine, in-vivo diagnosis.

In summary, therefore, this thesis has several closely related aims, namely

1. Exploring the application of 2D NMR relaxation methods to a variety of different tissues, specifically liver, kidney, and human cartilage.
2. Testing the clinical diagnostic potential of in-vivo 2D NMR relaxometry, choosing as a specific test example, osteoarthritis of the knee. This will be done in collaboration with a consultant orthopaedic surgeon in the Norfolk and Norwich University Hospital.
3. Developing software for predicting MRI image contrast from the 2D relaxation spectra.
4. Exploring the development of volume selective, fast, 2D NMR relaxation methods suitable for the in-vivo acquisition of 2D relaxation spectra.

2. Materials and Methods

This thesis is based on novel applications of existing 2D NMR relaxometry methods as well as the development of novel methods and simulations. The methods used to acquire results in chapters 3 and 4 are established methods within the lab and are used without modification to acquire data on samples with which they have not yet been used. These existing methods are presented here along with the general experimental set-up required to use the spectrometers available within the lab. Chapters 5 and 6 propose and apply novel methods for contrast simulation and 2D NMR relaxometry. These newly developed methods are discussed in detail in the relevant chapters.

2.1 Experimental set-up

2.1.1 Basic set-up and automatic parameter setting

Lab based experiments were carried out using Maran DRX controlled spectrometers, at 100 or 23.4 MHz, obtained from Oxford Instruments. The experiments are initiated using PC via the RINMR program[56]. Measurements at 100 MHz were conducted using a high power probe with a 5mm horizontally orientated solenoid coil. Measurements at 23.4 MHz were conducted on a bench top scanner with a 10mm vertically aligned solenoid coil. Experiments performed at 2.24 MHz were conducted on an internally developed, home-made spectrometer using similar methods and hardware. All scans were performed on samples contained within non-reactive NMR sample tubes (with diameters of 10 and 5 mm corresponding to the probes coil size) and as much free space as possible was filled with solid blocks of PTFE (Polytetrafluoroethylene) to prevent drying or degradation of samples due to air exposure. Tubes were sealed with appropriately sized caps or putty, outside of the examined sample area, for the same reason. As part of Basic set-up, we first load the FID pulse program in order to use RINMR's built in automatic setup routines[57].

AutoO1 sets the frequency offset required to get the best signal from the sample, i.e. achieve the best resonant frequency. It will only work if the spectrometer frequency (SF)

plus the frequency offset O1 is within 500 kHz of the resonant frequency. AutoRG determines the maximum usable receiver gain (RG, amplification in the receiver) dependent on sample. A sample with a large NMR response will require a low receiver gain as otherwise, the final detected signal for this sample will be "clipped" meaning that the maximum signal detected is at or above the maximum signal level that can be recorded. This would cause a problem as one or more points will be recorded at this maximum level rather than at their true level, causing a flattening of the curve of the detected signal. If the sample has a small NMR response then it will require a high receiver gain to increase the recorded signal. AutoP90 determines the correct radio-frequency pulse duration to induce a 90 degree rotation of the net magnetisation of the specific sample. The automatic routine starts from equilibrium and applies a pulse with a short duration, then acquiring the transverse relaxation following the pulse. The pulse duration is increased steadily and a curve of the acquired magnetisation is plotted. Maximum transverse relaxation occurs when there is a perfect 90 degree pulse, so the routine continues until it reaches a maximum, and then a minimum which correspond to the correct 90 degree pulse duration and the correct 180 degree pulse duration respectively.

All pulse sequences used in this thesis have a CPMG component and so, the tau (90-180 pulse separation) and NECH (number of echoes in the t_2 domain) must be set correctly so as to reach complete transverse magnetisation decay. The CPMGIFR sequence performs a single CPMG experiment (described in section 1.2.2) and displays the resulting decay curve on the screen. Once an appropriate tau value has been selected, the NECH value is increased until full transverse magnetisation decay is achieved. All other parameters are set manually dependent on sample and pulse sequence as described in the following section.

2.1.2 Pulse sequences

2.1.2.1 T_1-T_2 (INVCPMG)

The T_1-T_2 method allows examination of the full relaxation behaviour of the sample rather than simply the T_1 or T_2 profile generated using more common one dimensional methods. As has been demonstrated in figures 1.8 and 1.12, the 2 dimensional profiles obtained by this method allow the distinction of separate peaks that could be amalgamated on those

simpler single dimensional profiles.

The T_1-T_2 method (INVCPMG) is shown in Figure 1.7. It consists of a CPMG sequence with NECH echo acquisition steps, preceded by a period of inversion recovery. NECH and tau are chosen (as described in section 2.1.1) to achieve complete transverse magnetisation decay. The user then creates a list of t_1 values which is designated the D1 list. The pulse program shown is then repeated for each value of D1 and a CPMG decay curve is acquired, thus filling a 2D data matrix. This matrix can then be post-processed as described in section 2.1.3 to achieve a 2D T_1-T_2 relaxation spectrum. Between each iteration of the pulse sequence it is necessary to wait a period of time for the system to return to equilibrium, known as the recovery time. Ideally this should be left as long as possible but to minimise experimental time, a value of at least 5 times the longest T_1 of the sample is used.

2.1.2.2 T_2-store-T_2 (T2T2)

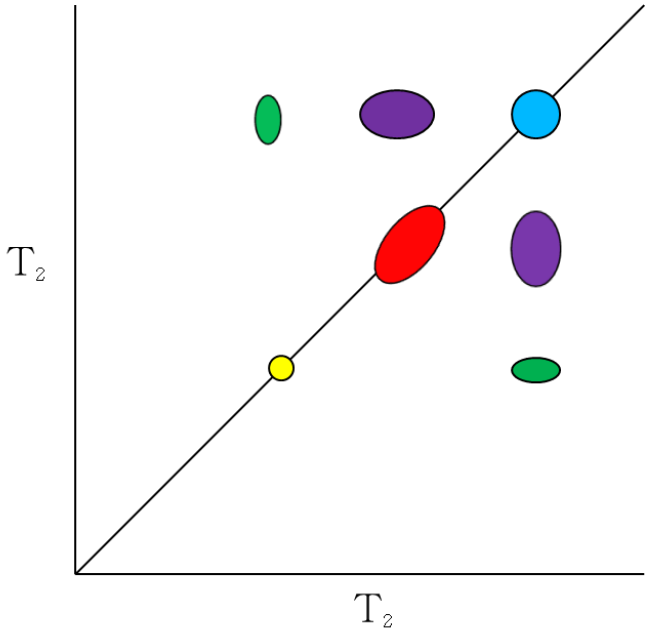

Figure 2.1 An imagined T_2 - store- T_2 spectrum for illustrative purposes. The true T_2 peaks are shown in yellow, red and blue on the diagonal. In this imagined spectrum we see cross peaks between the yellow and blue (shown in green) and cross peaks between the red and blue (shown in purple)

The T_2-store-T_2 sequence allows the identification of additional exchange cross peaks due to magnetisation transfer between different proton pools[(58)]. Figure 2.1 shows an imagined

T_2-store-T_2 spectrum for demonstration of the concept of cross peaks. On a T_2-store-T_2 spectrum the standard peaks from the T_2 spectrum are shown on the diagonal between the two axes. When the store time is comparable to the exchange lifetime between two peaks, cross correlation peaks appear off the diagonal at the same T_2 values as the true peaks, forming a square. This allows these exchange rates to be estimated. Typically the sequence will be run multiple times at different store times to fully examine this behaviour.

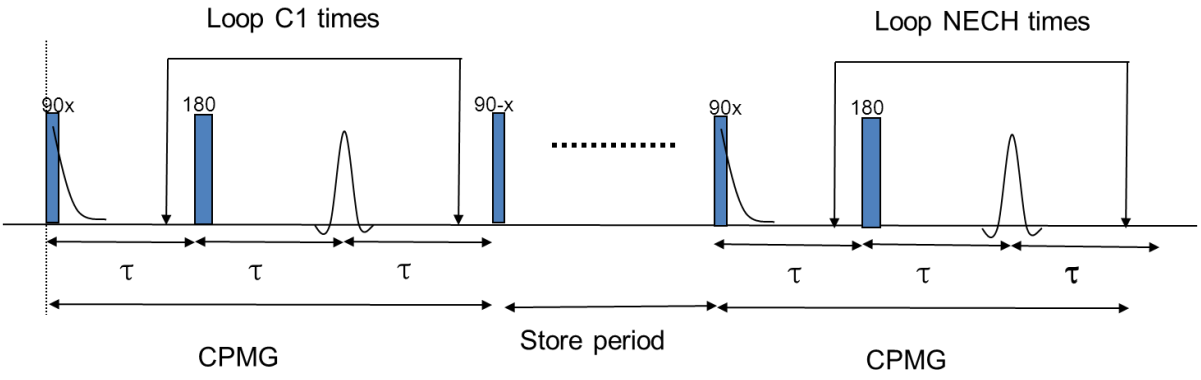

Figure 2.2 The T_2-store-T_2 pulse sequence showing the initial un-acquired CPMG section followed by a period of longitudinal magnetisation storage and then the final, acquired, CPMG section.

The T_2-store-T_2 pulse program is shown in Figure 2.2. The sequence consists of two CPMG sequences separated by a longitudinal store time. NECH, having been calculated as described previously, provides enough time for the transverse relaxation to decay completely. In order to perform the complete 2D experiment we generate a logarithmic list, named C1, of integer values beginning with 1 and ending with NECH. The above sequence is then repeated as many times as there are values in the C1 list, using the current C1 value as the number of echoes in the first, un-recorded, CPMG, waiting for the selected store time (set during experimental set-up) and then acquiring a full CPMG with NECH echoes. In this way we fill in a matrix of values containing the 2D T_2-store-T_2 data which can then be processed as described in section 2.1.3. As with other 2 dimensional sequences, a recovery time of approximately 5 times the longest T_1 of the sample is used.

2.1.2.3 T2-D (CPMGPGSE)

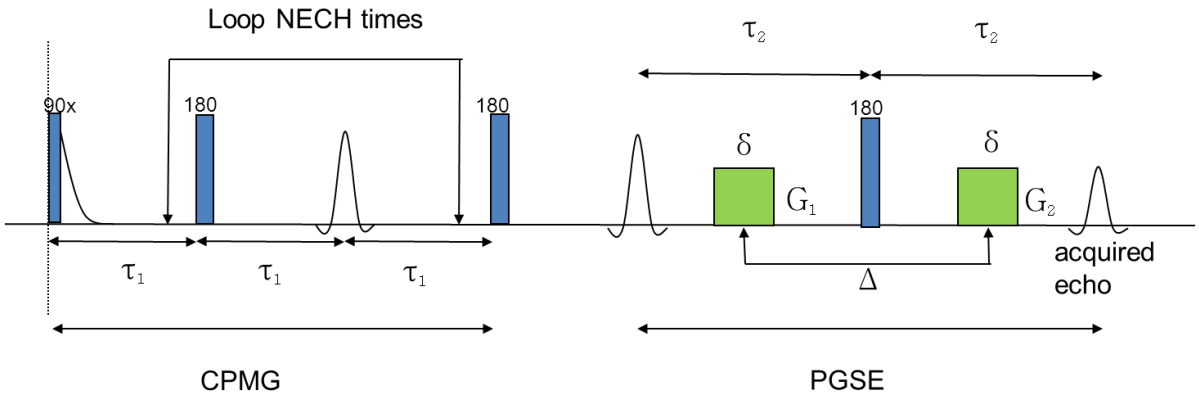

Figure 2.3 The T_2-D pulse program in which τ_1 is CPMG tau spacing and NECH is the number of echoes the CPMG contains. τ_2 is the PGSE tau spacing, δ is the gradient pulse duration, G_1 and G_2 are the amplitudes of the two gradient pulses (shown in green) and Δ is the inter-gradient pulse duration. The acquired echo is shown far right.

A T_2-D spectrum[23, 59] allows examination of diffusivity in the sample and relates it to the sample's T_2 values. As shown in Figure 2.3, it consists first of a CPMG step, followed by a PGSE (pulsed gradient spin echo) step. As in all previously described sequences, NECH and τ_1 must be set so as to give complete transverse relaxation decay. In this case NECH will be a logarithmic integer list starting at 1 and going up to the previously calculated NECH value, so as to achieve full transverse relaxation decay at the maximum value in the list. We then create a logarithmically spaced integer list for the value of G_1. The value of G_2 should be the same as G_1 but in reality it may be necessary to create an expression to calculate G_2 from G_1, in order to account for imperfect pulse shapes etc. that may otherwise affect the position of the acquired echoes. In our lab this is achieved by running a single iteration of the program with a set value of G_1 and adjusting G_2 to centre the acquired echo in the acquisition window. By repeating this at a number of different G_1 values we can generate a linear calibration plot, and fit the data to $y = mx + c$, to determine the value of G_2 at each value of the G_1 list. τ_2 can be independently set but must be longer than τ_1. The values δ and Δ can be set as required by the user so long as they are long enough to make sense with relation to the pulse program. The script can then be run to acquire a 2D matrix of values which can then be post-processed, as described in section 2.1.3, to yield a 2D T_2-D spectrum showing the diffusion of each T_2 peak, assuming the diffusion is large enough to be detected. As with other 2 dimensional sequences, a recovery time of approximately 5 times the longest T_1 of the sample is used.

2.1.3 Post-processing

Analysis of the data matrix $M(T_1, T_2)$ obtained from 2D relaxation spectroscopy is performed using internally developed MATLAB based program routines. Utilising the 2D inverse Laplace transform described in section 1.2.5, the results from other 2D relaxation pulse sequences can be examined by replacing the inversion recovery T_1 kernel ($1-2\exp(-t/T_1)$) and the T_2 kernel ($\exp(-t/T_2)$), as shown in equation 2.1 (repeated from equation 1.15), with the appropriate kernel.

$$M(t_1, t_2) = \int\int dT_1 dT_2 P(T_1, T_2) \exp\left(\frac{-t}{T_2}\right) M_\infty \left[1 - 2\exp\ \frac{-t}{T_1}\ \right] \quad \textbf{(eq 2.1)}$$

(repeat of eq. 1.15)

For example when processing the data from a "T_2-store-T_2" sequence (discussed in section 2.1.2.2) which is composed of two CPMG sequences and examines T_2 in both dimensions, the T_1 kernel is replaced with another T_2 kernel. If performing saturation recovery (discussed in section 1.2.1) rather than inversion recovery the T_1 kernel must be replaced with $1-\exp(-t/T_1)$ the saturation recovery kernel, based on equation 1.13. In the case of the ultrafast variable TR method (to be discussed in the chapter 6), the kernel must be modified to include the additional term $\exp[-(TR+t_1)/T_1]$, as will be described in chapter 6. Kernels can also be derived for mixed relaxation-diffusion sequences such as the T2-D sequence[23, 59], which requires $\exp[-q/D]$ in which D is the diffusion constant to be correlated with the relaxation constant and q is a variable given by equation 2.2, the parameters of which were defined previously in section 2.1.2.3. This allows processing of the obtained 2D data matrices into T_2-D spectra.

$$q = (\gamma\ G_1\ \delta)^2\ (\Delta - \delta)/3 \quad \textbf{(eq 2.2)}$$

3. 2D relaxometry of mammalian tissue

3.1 Introduction

As discussed in previous chapters, acquiring 2D rather than 1D relaxation spectra greatly increases the analytical potential of NMR spectroscopy. Not only do we avoid the 'overlap' problem where peaks with different T_1s but the same T_2 overlap in a one dimensional T_2 spectrum; but we also gain sensitivity through the 'T_1-null' process. By this we mean that there will be a particular T_1 inversion recovery time that nulls the water magnetisation while leaving finite solute or lipid magnetisation. This means that T_1-T_2 spectra contain more peaks from dissolved biopolymers and solutes than a straightforward one-dimensional T_1 or T_2 spectrum.

The superior analytical power of 2D relaxation spectra has led to their use in the examination of various systems such as porous rock, plant tissues, solutes, biopolymer systems and complex foods[24, 53, 60-65]. Some clinical studies have also examined human skeletal muscle and breast, as well as rat brain and trigeminal nerve [43, 45, 48], but these did not take advantage of the most recently developed protocols, based on the 2D Laplace transform algorithm developed by Song et al[24]. There is also little direct comparison of the effects of varying the spectrometer frequency on the relaxation spectra[66].

In this chapter we examine the T_1-T_2 relaxation of a variety of mammalian tissue including liver and kidney (cortex, medulla, and ureter) utilising the INVCPMG T_1-T_2 relaxometry sequence at 100MHz and 23.4 MHz spectrometer frequencies. Examination of these tissues will allow determination of the reproducibility of 2D T_1-T_2 relaxation spectra in the examination of biological tissue, as well as assessing its potential to distinguish between different biological tissue samples.

3.2 Methods

Samples of liver and kidney were obtained from local meat suppliers and examined in as fresh a condition as possible. Using a scalpel, appropriate samples were dissected from the bulk tissue. Care was taken to extract as homogeneous a sample as possible. Samples are then placed in NMR tubes, which are then filled with polytetrafluoroethylene (PTFE) to remove as much remaining air as possible to prevent dehydration of the sample. Samples were kept at 4^{o}C during storage and as cool as possible otherwise so as to further limit the extent of any degradation that may have taken place. Samples were examined using the INVCPMG 2D relaxometry protocol on a 100MHz DRX spectrometer using a high power probe with a 5mm horizontal solenoid coil, using a tau of 200 µs. The 90 and 180 degree pulse widths were automatically determined by the Resonance Instruments software RINMR[*(56)*]. Spectra were acquired with at least 8K (8192) echoes in the t_2 dimension so as to achieve complete transverse magnetisation degradation, at which point the CPMG curve will plateau at zero. At least 80 logarithmically spaced points in the t_1 dimension were used starting at 50 µs and going to at least 15000000 µs (15 s) to ensure adequate time for the longitudinal magnetisation to plateau at its maximum level. Data was then analysed using internally developed MATLAB programs making use of 2D Laplace transform algorithms to obtain a 2-Dimensional cross correlation T_1-T_2 spectrum of the sample. These programs are named InvCpmgEditV3djh, InvCpmgCalcV3djh and InvCpmgResV3djh, each based on InvCpmg Version 12 by Kevin Wright, 20 Jan 2005. The 2.24 MHz T_1-T_2 experiments were performed on a scanner built within the department with similar parameters and processing methods. The 23.4 MHz T_1-T_2 experiments were performed on a commercial DRX bench top scanner, again using similar parameters and post-processing methods. Samples were also examined using the T_2 -D method to aid in peak assignment. These scans were then analysed using the internally developed MATLAB program difft2 to obtain a 2-Dimensional cross correlation T_2- D spectrum of the sample.

3.3 Lamb's liver

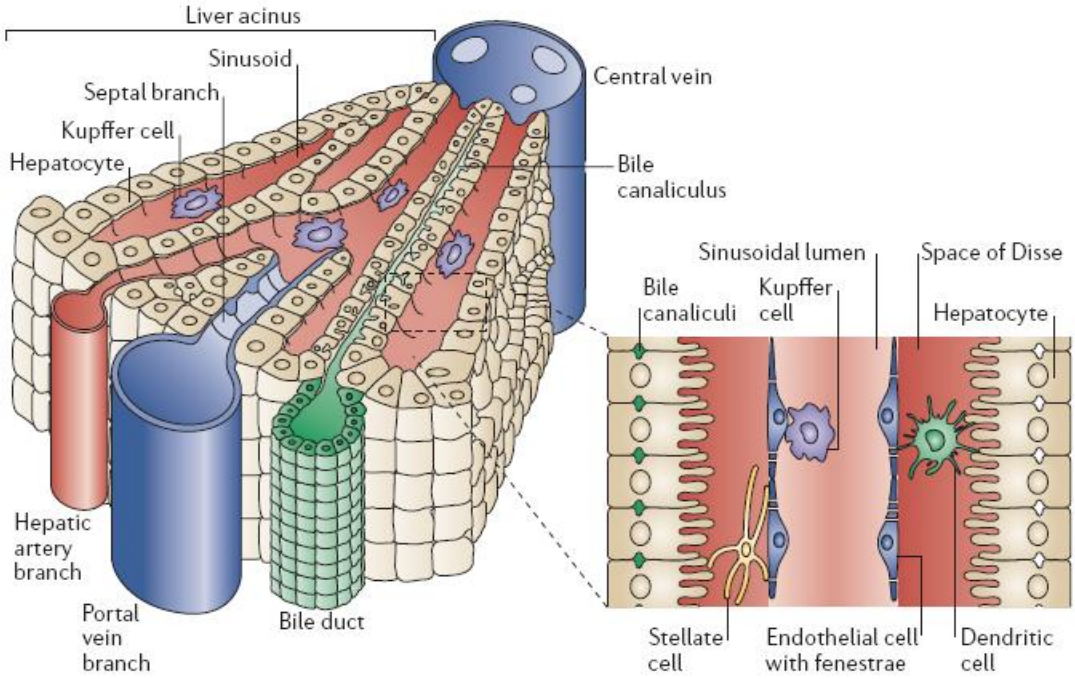

Figure 3.1 Microscopic structure of the liver reproduced from(*67*) with permission

Figure 3.1[(67)] shows the internal structure of liver tissue on a microscopic scale. On a macroscopic scale however, the gross structure of liver is largely homogeneous allowing easy dissection of a sample from a large region of uniform tissue. Care must simply be taken to avoid the large veins and bile ducts running through some parts of the tissue.

3.3.1 Lamb's liver at 100MHz

Figure 3.2 shows a characteristic T_1-T_2 relaxation spectrum taken at 100 MHz with a tau of 200 µs showing 7 peaks, marked as in Figure 3.5 and Figure 3.6. Peaks 1 and 2 have relatively long and similar T_1 and T_2 values which would seem to indicate that they arise from the small amount of relatively free water in the small bile ducts and capillaries running throughout the tissue. This assignment is supported by their low peak intensities. Peak 3 is by far the dominant peak containing in this case 84.9% of the total peak marked signal. This peak, most likely, results from intracellular water in the hepatocyte cells of the liver tissue. To corroborate this provisional assignment a sample of liver was immersed in deuterium oxide (D_2O) for a period of 8 hours prior to experimentation. If the assignment was correct the peak intensity would reduce significantly as D_2O, which is not detected in a proton NMR experiment, would exchange with the intracellular water, reducing its

returned signal. This was found to be true reducing the peak intensity to 55% of the total returned signal. Peak 1 was no longer detectable and peak 2 remained, at heavily reduced intensity (0.3%).

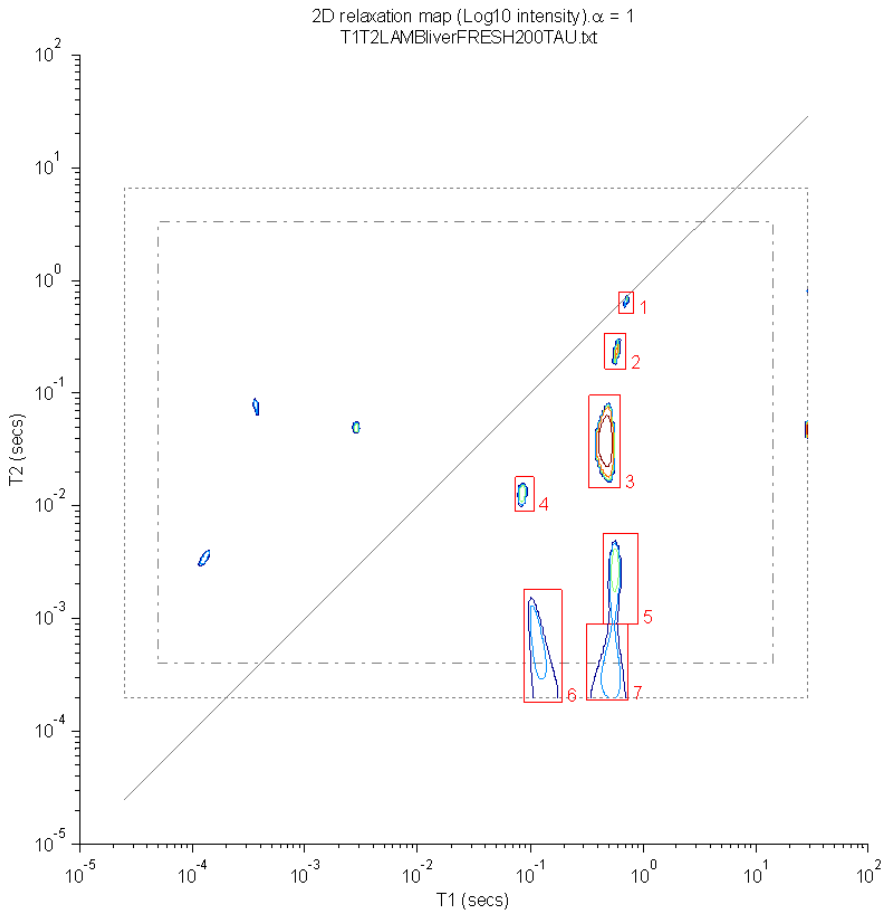

Figure 3.2 A characteristic 2D T_1-T_2 relaxation spectrum performed at 100 MHz on a sample of fresh lamb's liver demonstrating the 7 main peaks

Peak 5 has a relatively low intensity (mean of 5.68%) and a very short T_2 (mean of 2.88 ms). The peak has been provisionally assigned to non-exchanging protons in dissolved mobile proteins and biopolymers for the following reasons. Examination following sample treatment with D_2O showed an increase in relative signal intensity, indicating that it does not arise from water. Previous studies of Bovine serum albumin (BSA) undertaken at 100MHz[68] found corresponding peaks due to non-exchanging protons. Peaks 4, 6 and 7 are not currently assigned in this spectrum though thought has been given to peak 4 arising from sugars, lipids, or small mobile proteins. Further work in this area would be required to assign these peaks with any certainty. The small unmarked regions of signal to the far left of the spectrum are most likely artefacts of the data

processing methods. This assignment is made as they are of low intensity and well within the forbidden region of the spectrum. This forbidden region occurs as the true T_2 value of a peak should not be higher than the T_1. T_1 places a limit on the value of T_2 as the fluctuating molecular fields involved cannot rotate the individual spin polarisations back towards the z axis without causing decoherence in the transverse spin polarisation[(12)]. In a more phenomenological way, T_1 is a measure of the rate at which the magnetisation is restored in the longitudinal dimension and T_2 is a measure of the rate at which magnetisation is lost in the transverse dimension. The magnitude of the total magnetisation of the sample cannot exceed the starting magnetisation M_∞, thus magnetisation must be lost in the transverse plane at least as fast as it recovers in the longitudinal dimension. In typical practice a ratio of $T_2 \leq T_1$ is both expected and found.

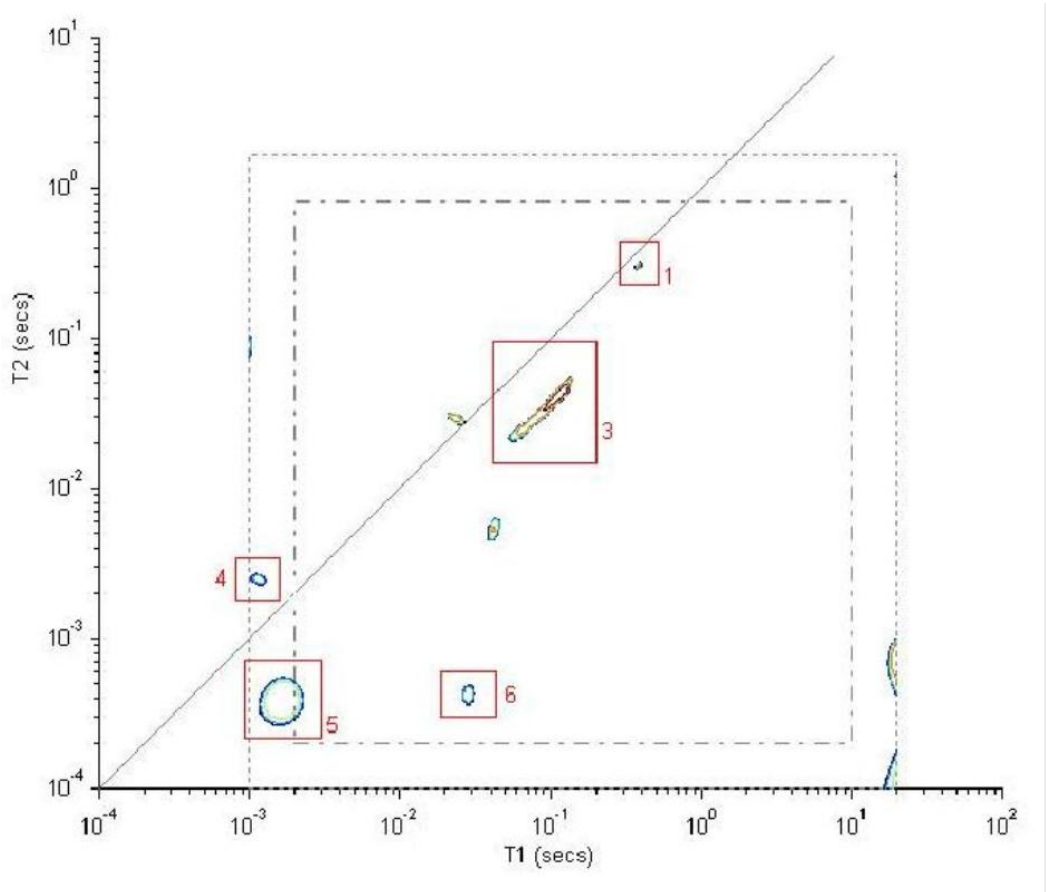

Figure 3.3 The T_1-T_2 profile of lamb's liver conducted using a "home-made" bench-top scanner at 2.24 MHz

Figure 3.3 shows results from an inversion recovery 2D T_1-T_2 profile performed on a sample of liver at the far lower frequency of 2.24 MHz by a colleague as a test of, and during the development of, a 'home-made' low field bench-top scanner. Lower fields allow

the probing of the frequency dependence of T_1-T_2 peaks, as well as aiding in peak assignment. At lower frequencies the peaks arising from non-exchanging protons should show dispersive frequency dependence, shifting to shorter T_1 and T_2 values at lower frequency values. The dominant water peak includes the exchangeable biopolymer protons and will be dominated by proton exchange, leading to an increase in T_2 due to a smaller chemical shift difference between these exchangeable protons and those in the water. Its T_1 will shift to shorter values because of the shorter T_1 of the exchangeable biopolymer protons. By comparison of Figure 3.2 and Figure 3.3 we can see these effects, further confirming our peak assignments of peak 3 as intracellular water and peaks 4 and 5 as non-exchanging biopolymer proton pools. The peaks to the far right are most likely artefacts as they are low intensity and at extremely long T_1 relaxation times.

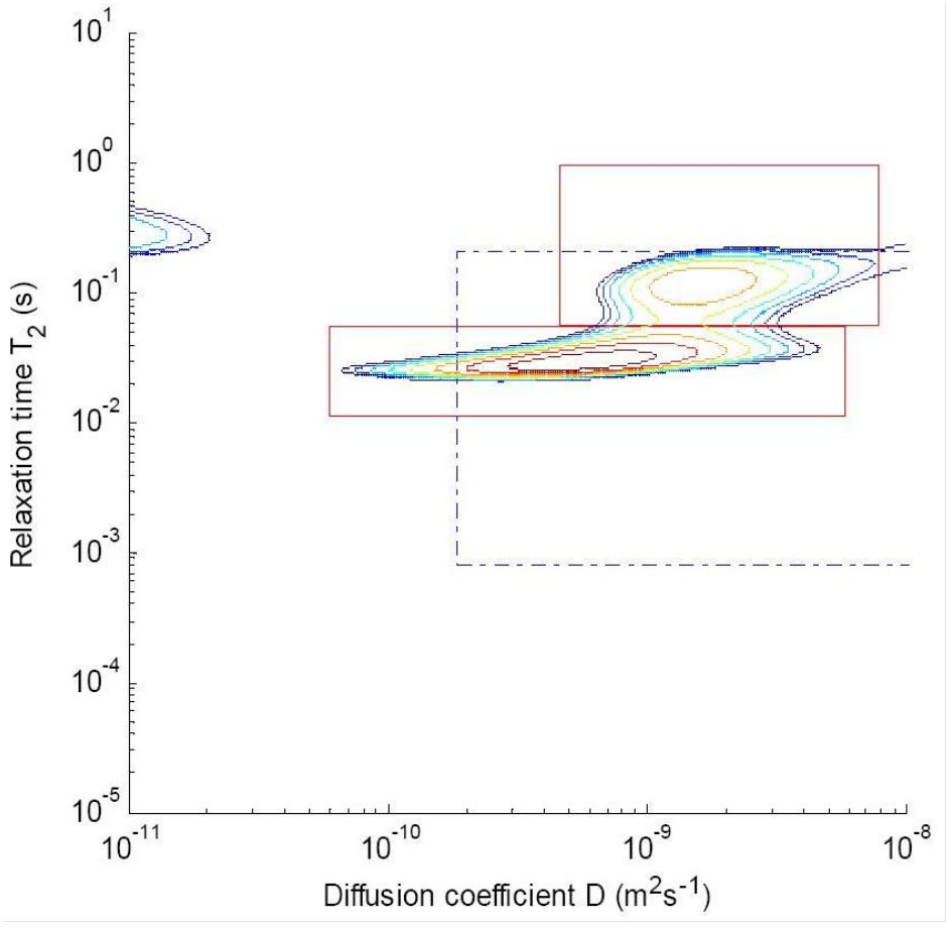

Figure 3.4 two dimensional T2-D relaxation-diffusion spectrum of lamb's liver taken at 100MHz

T_2-D spectra[23, 59] allow examination of diffusivity in the sample and relate it to the T_2 values of the sample. It was performed here to aid in peak assignment in the T_1 - T_2 relaxation spectrum[27]. The T_2-D spectrum of liver confirms the previous assignment, as

lipid and biopolymer proton pools would have too low a diffusivity to show on conventional T_2-D spectroscopy, leading to a loss of peaks 4 and 5. Water in blood vessels and bile ducts would have a slightly higher diffusivity than the bulk water in the hepatocyte cells leading to a high diffusivity peak arising from peaks 1 and 2. This can be seen from the T_2-D spectrum shown in Figure 3.4 acquired on the commercial DRX bench top scanner at 23.4MHz.

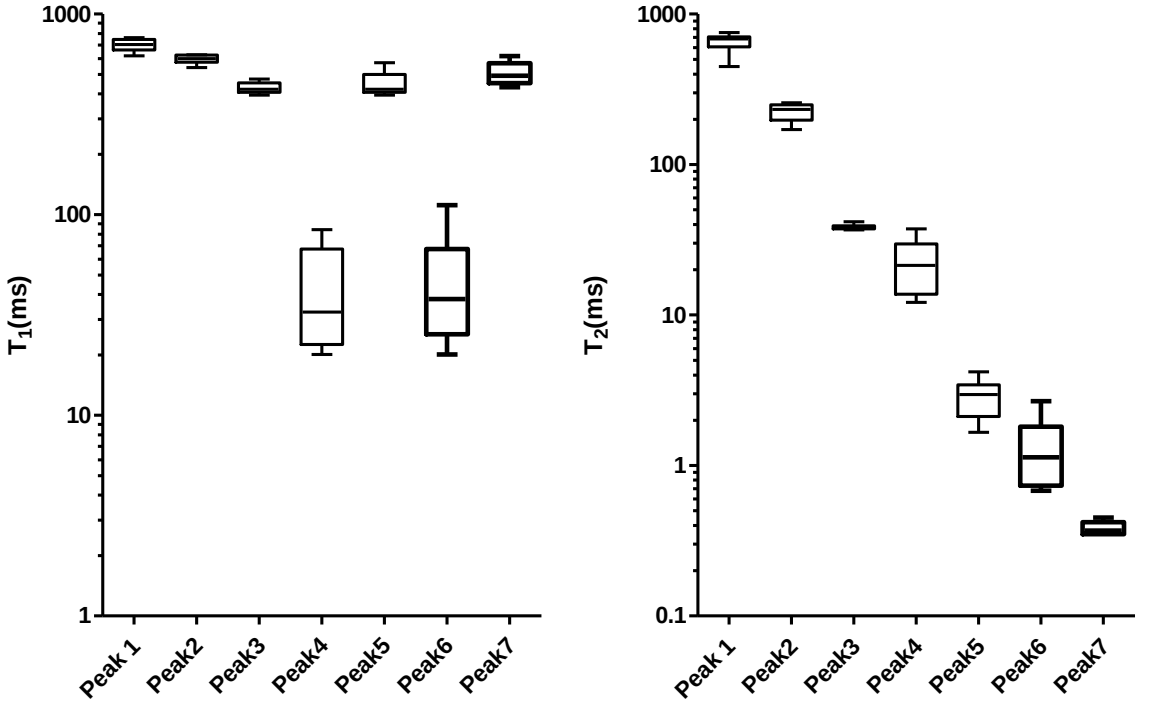

Figure 3.5 The peak positions in T_1(left) and T_2(right) of the 7 peaks obtained from T_1-T_2 relaxometry performed at 100MHz on 8 samples of fresh lamb's liver, demonstrating the consistency in peak positions.

2D T_1-T_2 relaxation spectra are routinely discussed as being characteristic of a tissue type. This designation is used to indicate that there is consistency between spectra from multiple relaxation experiments on the same tissue type, and that the spectrum being discussed is typical of these spectra. Figure 3.5 demonstrates this characteristic nature by presenting boxplots of the peak positions obtained from 8 scans of lamb's liver taken at 100MHz with a tau value of 200μs. It can be seen that there is minimal variation in the positions of peaks 1-7, as marked in Figure 3.2. The dominant peak 3 in particular has almost no variation in either T_1 or T_2. Figure 3.6 shows the peak intensities of these same peaks as a percentage of the total peak-marked area. Again there is little variation in peak intensities with most of the signal (≈84%) contained in the dominant peak 3.

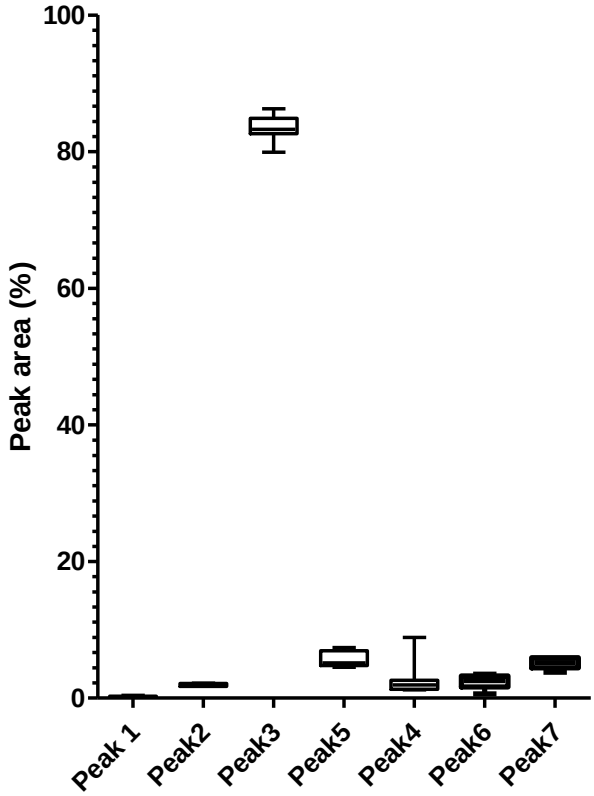

Figure 3.6 The peak intensities, as a percentage of the total peak marked intensity, of the 7 peaks obtained from T_1-T_2 relaxometry performed at 100 MHz on 8 samples of fresh lamb's liver, demonstrating the consistency in peak intensities.

3.3.2 Lamb's liver at 23.4MHz

Directly comparing the two spectra in Figure 3.4 and Figure 3.7, presented here as characteristic, it is immediately apparent that the spectrum taken at 23.4 MHz has fewer peaks than that taken at 100 MHz. This is most likely due to reduced signal to noise ratio (SNR) on the lower frequency equipment, due in large part to the inherent reduction in SNR at reduced spectrometer frequency.

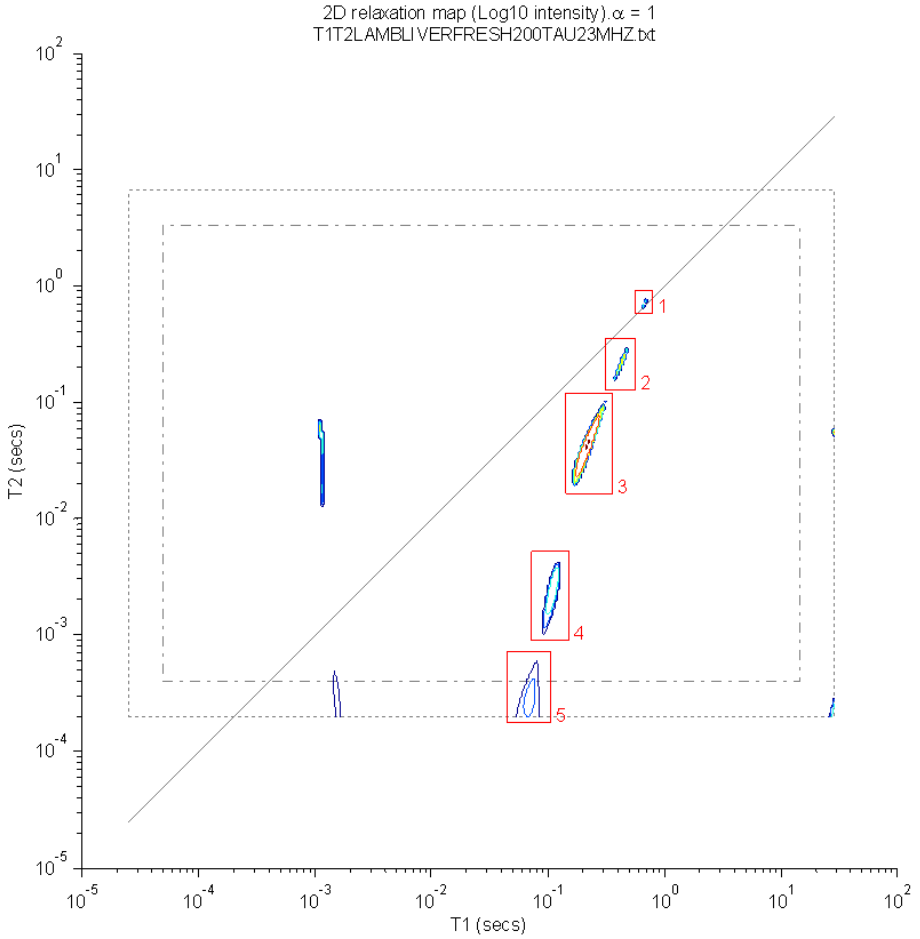

Figure 3.7 A characteristic 2D T_1-T_2 relaxation spectrum performed at 23.4 MHz on a sample of fresh lamb's liver demonstrating the 5 main peaks the additional unmarked peak within the forbidden zone is likely an artefact of the fitting process and the unmarked peaks at the extreme edges of the spectrum are low intensity (<0.5%) and within the outer region of the spectrum, meaning we have reduced confidence in their authenticity.

Peak	Mean area (std. dev.)		Mean T_1 (ms) (std. dev.)		Mean T_2 (ms) (std. dev.)	
	100 MHz	23.4 MHz	100 MHz	23.4 MHz	100 MHz	23.4 MHz
1	0.23% (0.09%)	0.25% (0.21%)	701 (49)	657 (61)	650 (95)	724 (177)
2	1.88% (0.22%)	2.16% (0.56%)	597 (30)	433 (30)	225 (30)	215 (28)
3	83.5% (2.0%)	90.3% (2.6%)	428 (28)	221 (9.3)	38.3 (1.6)	41.0 (1.9)

Table 3.1 The mean values of the peak intensity and position of peaks 1, 2 and 3 taken at 100 MHz and 23.4 MHz, as peak marked in, and figures 3.2 and 3.7 demonstrating the similarities between the peaks. Standard deviation given in brackets next to mean value.

Peaks 1, 2 and 3 in each spectrum are clearly the same with approximately equal intensities and peak positions, as shown in Table 3.1. The T_1 values would be expected to decrease from the 100 MHz to 23.4 MHz due to the dependence of T_1 on the spectrometer frequency[12, 69]. This reduction is seen across these three peaks. Due to the 23.4 MHz

spectrometer's inferior ability to detect smaller peaks, the peaks detected and marked on the lower field machine would contain a greater relative percentage of the total detected signal. This can also be seen in Table 3.1. Assignation of peak 4 in the 23.4 MHz spectrum is less clear. As shown in

Table 3.2, it has values close to those of both peak 4 and peak 5 in the 100 MHz experiment.

Peak	Mean area (std. dev.)		Mean T_1 (ms) (std. dev.)		Mean T_2 (ms) (std. dev.)	
	100 MHz	23.4 MHz	100 MHz	23.4 MHz	100 MHz	23.4 MHz
4	2.73% (2.6%)	5.68% (0.52%)	41.9 (25)	119 (23)	22.5 (9.0)	3.26 (2.0)
5	5.68% (1.2%)		448 (64)		2.88 (0.82)	

Table 3.2 The mean values of the peak intensity and position of peaks 4 and 5 taken at 100 MHz and peak 4 taken at 23.4 MHz, as peak marked in figures 3.2 and 3.7 demonstrating the similarities and differences between the peaks. Standard deviation given in brackets next to mean value.

Peak 5 in the 100 MHz experiment would seem to correspond better as it has far closer peak area and a very similar T_2 value. Assuming this assignment, T_1 values for this peak would typically be significantly higher (mean=448, standard deviation=64) at 100 MHz than at 23.4MHz (mean = 119, standard deviation = 23) but this is not unheard of as a substance's T_1 frequency dependence can cause dramatic T_1 value changes. Fullerton et al.[70] found a linear relationship (T_1 = 1.83 * frequency + 25.0) between T_1 and spectrometer frequency in hydration water examined at frequencies ranging from 5 to 100 MHz. They only took a single T_1 value for an entire sample of biological tissues and assumed that this weighted average included bulk water unaffected by the frequency change and water molecules with reduced mobility hydrated on the surface of macromolecular structures, which caused the frequency dependence.

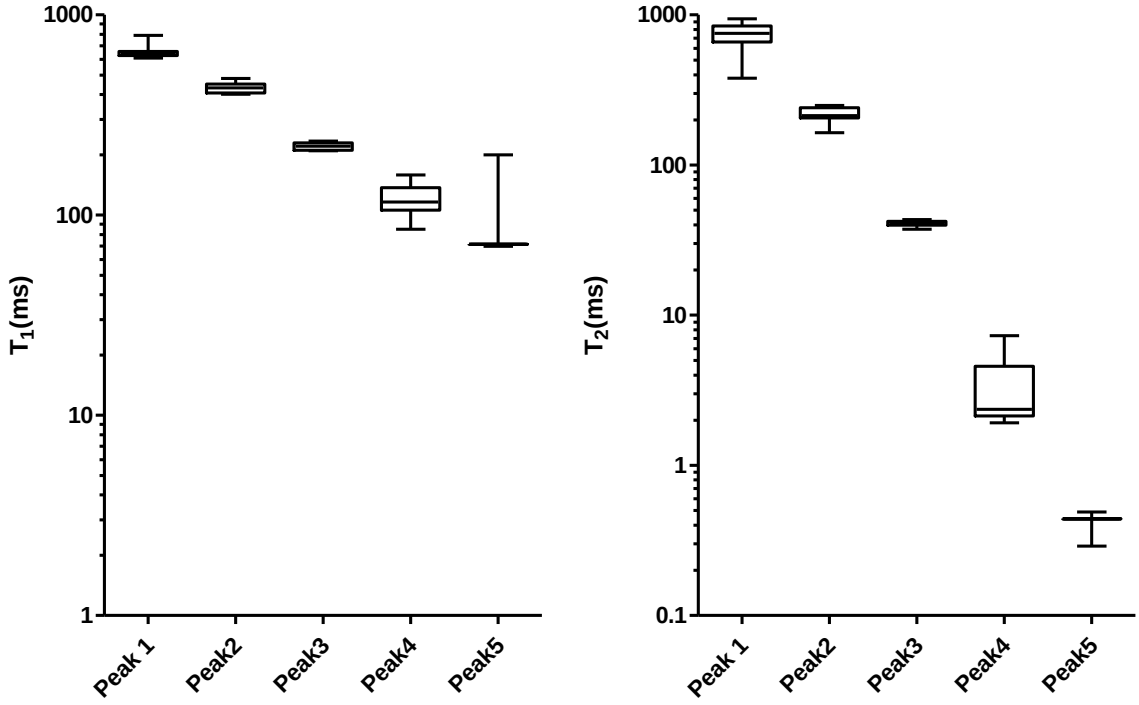

Figure 3.8 The peak positions in T_1(left) and T_2(right) of the 5 peaks obtained from T_1-T_2 relaxometry performed at 23.4 MHz on 8 samples of fresh lamb's liver, demonstrating the consistency in peak positions.

As in the previous section, it is necessary to demonstrate the repeatability of the 2D T_1-T_2 relaxation spectra, this time acquired from 8 samples of lamb's liver taken at 23.4 MHz with a tau value of 200μs. Figure 3.8 shows boxplots of the T_1 and T_2 values of the 5 relevant peaks, marked as in Figure 3.7. As can be seen, there is little variation in either the T_1 or T_2 peak positions. Figure 3.9 shows the peak intensities of these same peaks as a percentage of the total peak-marked area. Again there is little variation in peak intensities with most of the signal (≈90%) contained in the dominant peak 3.

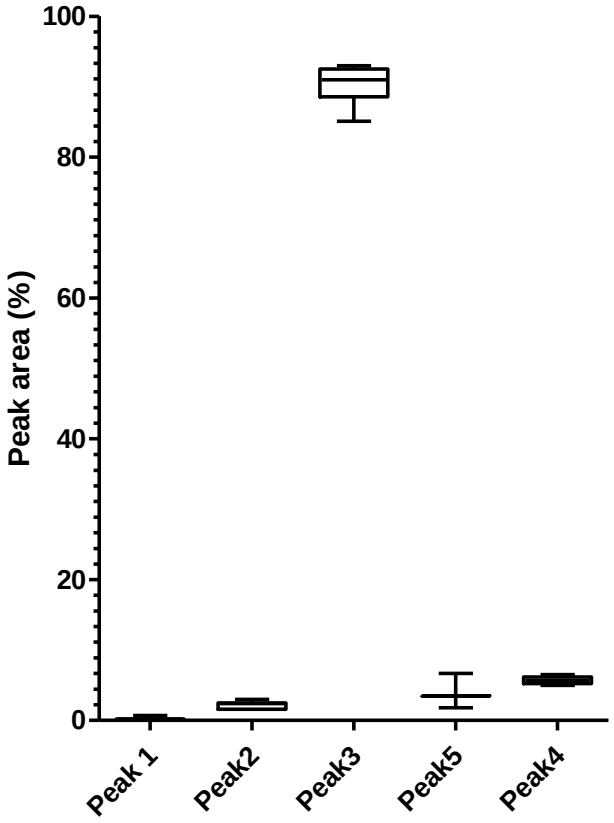

Figure 3.9 The peak intensities, as a percentage of the total peak marked intensity, of the 5 peaks obtained from T_1-T_2 relaxometry performed at 23.4 MHz on 8 samples of fresh lamb's liver, demonstrating the consistency in peak intensities.

3.3.3 Comparison with previous relaxometry studies of the liver

Previous studies have examined the relaxation behaviour in liver but usually only from a single parameter perspective. Studies have examined liver from the perspective of determining viability in transplant organs by T_1 and T_2 relaxation rates, but only acquired a single value, some concluding that relaxometry's ability at this distinction was poor[71]. Others such as Holzmüller et al[72, 73] examined rat liver grafts stored for a range of times and found T_1 to be a good indicator of tissue water content, and therefore graft viability, but as before, only examined T_1 as a single value for each graft. Heye et al[74] used T_1, T_2, and T_2* to examine liver in patients with cirrhosis and concluded that T_1 was a good indicator of liver health but, again, they only characterised the liver samples using a single value for each parameter. Using an average T_1, their value would likely be dominated by the peak in Figure 3.2 labelled peak 3 with a mean T_1 of 428 ms, whereas they found T_1 values of 852 ms for cirrhotic livers and 678 ms for normal controls. There may obviously

be some differences between lamb and human livers which could explain this difference, as well as the possibility that smaller peaks could be affecting the average, but also there is the issue of tissue hydration. As found in studies already discussed above[72, 73], tissue hydration correlates well with T_1 values so the in vivo nature of these measurements may reflect a truer value of the tissue T_1. It may of course be that the correlation with tissue hydration is simply the result of this dominant T_1 - T_2 peak reducing with dehydration (due to its likely identity as intracellular water) and allowing the smaller, and lower T_1, peaks to have a greater relative influence on the average T_1 of the tissue. The paper by Wolf et al[71] examined preserved donor livers over time and although it did not find T_1 to be useful in determining organ viability, it did find T_1 values at the beginning of the storage period of approximately 415 ms (taken from fig 2 in the paper) which is far closer to the dominant peak Figure 3.2 (mean of 428 ms). Hoad et al[75] examined maps of T_1, T_2, and T_2* and concluded that T_1 provided information on fibrosis and T_2* on iron content but, as is typical in quantitative MRI, tissue was characterised using single values per voxel for each parameter. This information, while undeniably useful, falls short of the full relaxation characterisation available with 2D techniques. St Pierre et al[76] examined normal and iron loaded liver and characterised the tissue with bi-exponential T_2 curve fitting but, as can be seen in Figure 3.2, assigning 2 T_2 values would still fall far short of the number of observable peaks in liver tissue. Most studies in this area seek to correlate a single known change in liver state with a single observed relaxation rate change for instance T_1 correlating to water content in transplant organs or T_2 correlating to iron content in iron loaded livers. Liver is typically examined in this way to fulfil the need to determine specific diagnostic criteria that would otherwise require destructive or painful biopsy in order to assess specific tissue conditions and is successful in doing so, despite not fully characterising the tissue as has been attempted here.

3.4 Lamb's kidney

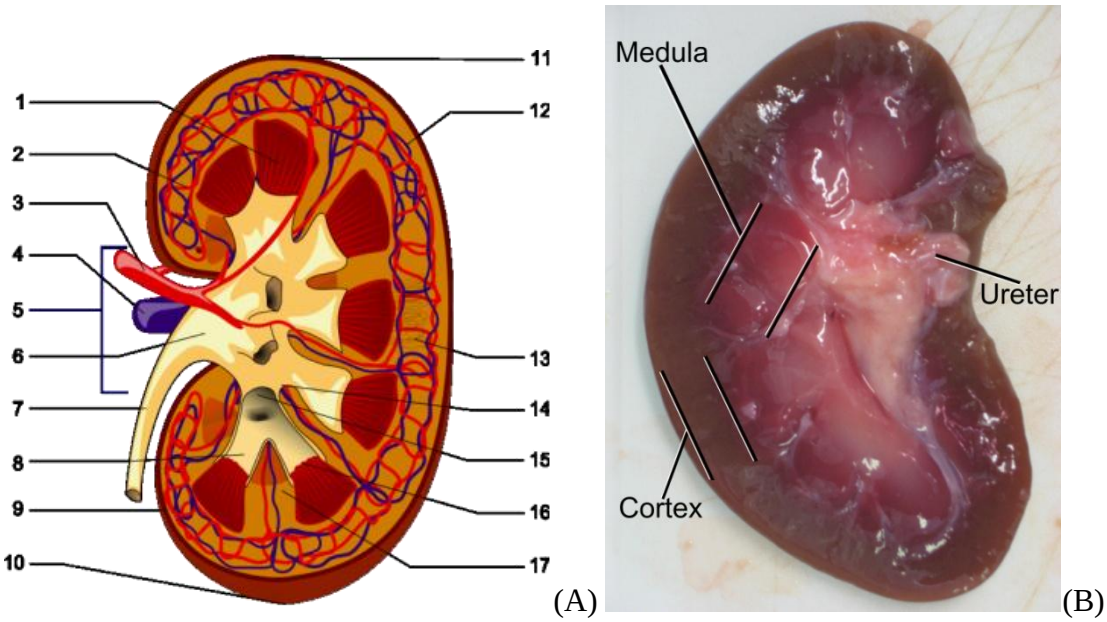

(A) (B)

Figure 3.10

(A) reproduced from (*77*) under creative commons licencing. A diagram of the macroscopic structures of the kidney identified by the following key:

1) Renal pyramid, 2) Efferent artery, 3) Renal artery, 4) Renal vein, 5) Renal hylum, 6) Renal pelvis, 7) Ureter, 8) Minor calyx, 9) Renal capsule, 10) Inferior renal capsule, 11) Superior renal capsule, 12) Afferent vein, 13) Nephron, 14) Minor calyx , 15) Major calyx , 16) Renal papilla, 17) Renal column.

(B) A photograph taken of a lamb kidney prior to dissection of relevant sample, cut in half on the same plane as in the diagram (A). The kidney pictured was typical of lamb kidney size and would be approximately 9cm long weighing 60-90 grams. The cortex is the brown outer region. The ureter is the cartilaginous white structure. The medulla is the pinkish region between them. Examples of each region are indicated on the photograph.

The kidney is composed of various macroscopically distinct tissues as shown in Figure 3.10[(77)]. The three clearly distinguished regions referred to when discussing the kidney are the cortex, medulla and ureter. Each of these regions is examined separately at both 100MHz and 23.4 MHz, allowing tissue characterisation as well as allowing comparison and contrast between these tissues and those of the liver.

3.4.1 Lamb's kidney cortex at 100MHz

The cortex is the outermost region of the kidney, clearly visible as the brown area surrounding the other tissue. As indicated in Figure 3.10(A)[(77)], it contains the efferent artery and the afferent vein although as shown in Figure 3.10(B) neither is clearly visible in the dissected tissue. Also not visible are the small fluid collecting ducts which eventually

lead into minor and major calyx, the renal pyramid and the ureter. This allows exchange of substances between blood in the blood vessels and fluid in the ducts, which is then removed from the kidney. Figure 3.11 shows a characteristic T_1-T_2 relaxation spectrum taken at 100 MHz with a tau of 200 µs showing 6 peaks. Peak 1 has relatively long mean T_1 and T_2 values (1328 ms and 575 ms respectively) which would seem to indicate that it arises from the small amount of relatively free water in the blood vessels and fluid ducts running throughout the tissue. This assignment is supported by its low peak intensity. Peak 2 dominates the spectrum at 90.24% mean peak area and is most likely intracellular water. Peak 4 has a relatively low intensity (mean of 1.87%) and a very short T_2 (mean of 3.94 ms).

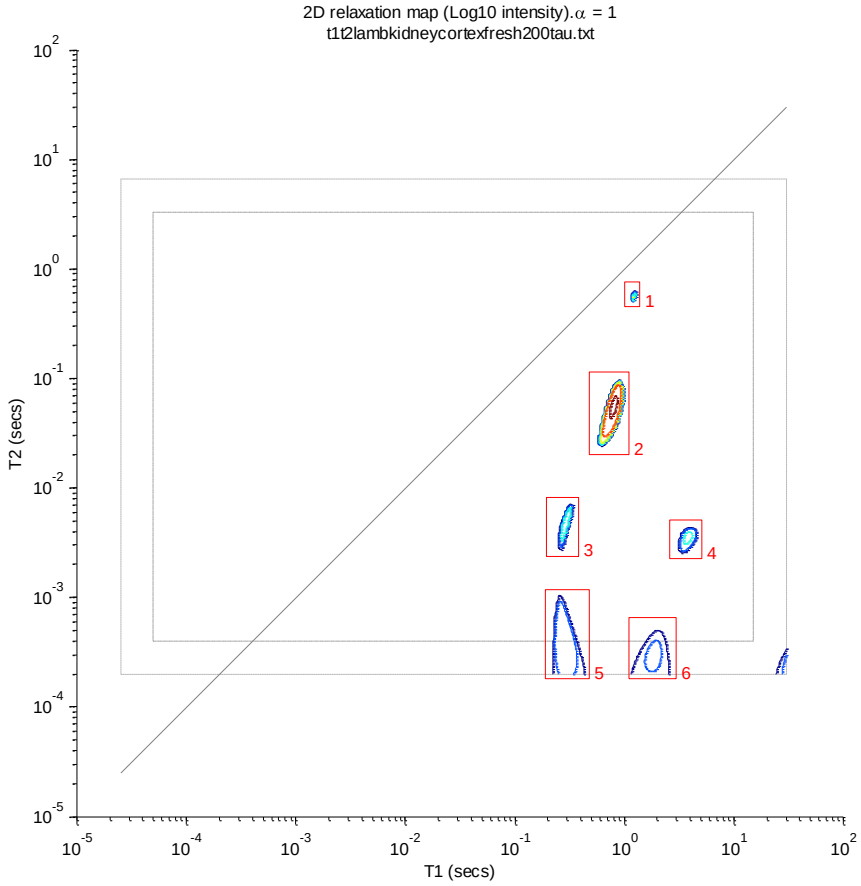

Figure 3.11 A characteristic 2D T_1-T_2 relaxation spectrum performed at 100 MHz on a sample of fresh lamb's kidney cortex demonstrating the 5 main peaks. Peak 6 occurred only in 2 of the 5 spectra but similar peaks have been found in previous similar experiments, the data from which has not been included here as it did not perfectly match the experimental protocol and sample selection criteria used in this round of testing. It is of fairly low intensity (1.8%) and within the outer region of the spectrum meaning we have reduced confidence in its authenticity but due to previous experience it has been retained and marked.

The peak appears to correspond to a similar peak in the liver spectrum, labelled peak 5, and so has been provisionally assigned to the same cause, non-exchanging protons in dissolved

mobile proteins and biopolymers such as globular proteins and enzymes. Peak 3 appears to correspond with peak 4 in the liver spectrum and would thus likely originate from the same substances such as sugars, lipids, or small mobile proteins.

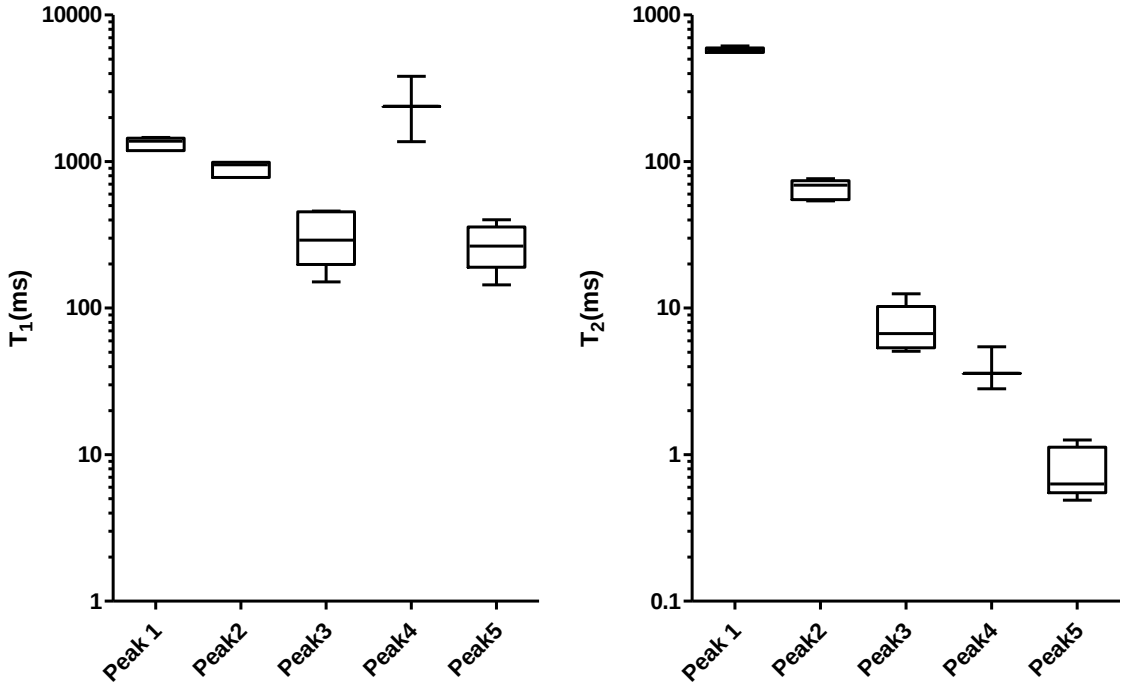

Figure 3.12 The peak positions in T_1(left) and T_2(right) of the 5 main peaks obtained from T_1-T_2 relaxometry performed at 100 MHz on 5 samples of fresh lamb's kidney cortex, demonstrating the consistency in peak positions.

As already discussed, it is necessary to demonstrate the repeatability of the 2D T_1-T_2 relaxation spectra, this time acquired from 5 samples of lamb's kidney cortex taken at 100 MHz with a tau value of 200 µs. Figure 3.12 shows boxplots of the T_1 and T_2 values of the 5 relevant peaks, marked as in Figure 3.11. As can be seen, there is little variation in either the T_1 or T_2 peak positions, especially peaks 1 and 2. Figure 3.13 shows the peak intensities of these same peaks as a percentage of the total peak-marked area. Again there is little variation in peak intensities with most of the signal (≈90%) contained in the dominant peak 2.

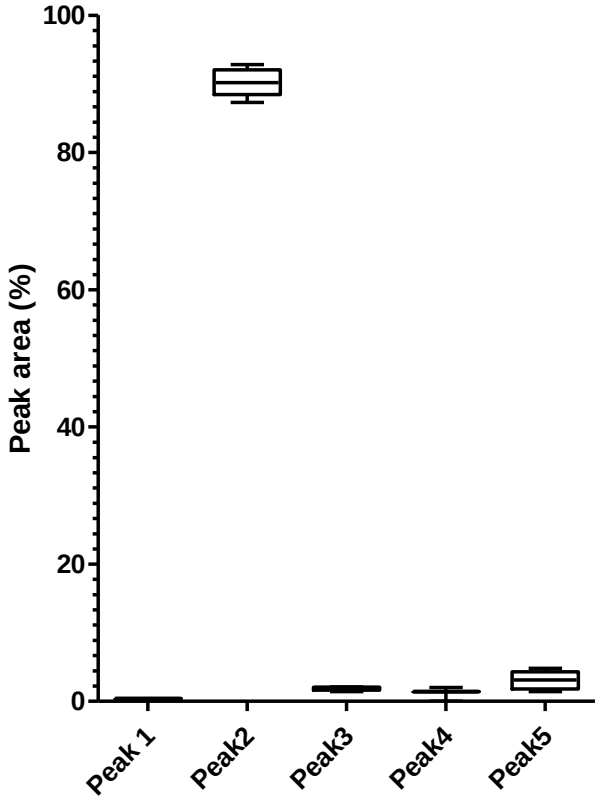

Figure 3.13 The peak intensities, as a percentage of the total peak marked intensity, of the 5 main peaks obtained from T_1-T_2 relaxometry performed at 100 MHz on 5 samples of fresh lamb's kidney cortex, demonstrating the consistency in peak intensities.

3.4.2 Lamb's kidney cortex at 23.4MHz

In the characteristic lamb kidney cortex spectra, peaks 1, 2, 3 and 4 in the 23.4 MHz spectrum (Figure 3.14) line up well to visual comparison with peaks 1, 2, 3 and 5 in the 100 MHz spectrum of the same tissue (Figure 3.11). Table 3.3 shows the peak areas and peak positions in T_1 and T_2 of these peaks for direct comparison. There is a slight increase in the peak areas in the 23.4 MHz spectrum which would be expected as the 4 peaks in the 23.4 MHz spectrum are the only peaks marked and thus contain the total peak-marked area. This is due to the 23.4 MHz spectrometer's inferior ability to detect smaller peaks. The same 4 peaks in the 100 MHz spectrum contain only 94% of the total peak-marked area due to other smaller peaks, not detected at 23.4 MHz. The T_1 values would be expected to decrease from the 100 MHz to the 23.4 MHz due to the dependence of T_1 on the spectrometer frequency[(12)]. This reduction is seen across these 4 peaks. The T_2 values remain approximately equivalent as there is significantly less T_2 frequency dependence at this range. The slight increase in the mean T_2 of peaks 1 and 2 may appear suspect but

taking into account the standard deviation values for each peak (peak 1: 25 at 100 MHz and 84 at 23.4 MHz, peak 2 9.9 at 100 MHz and 9.0 at 23.4 MHz) they are remarkably close.

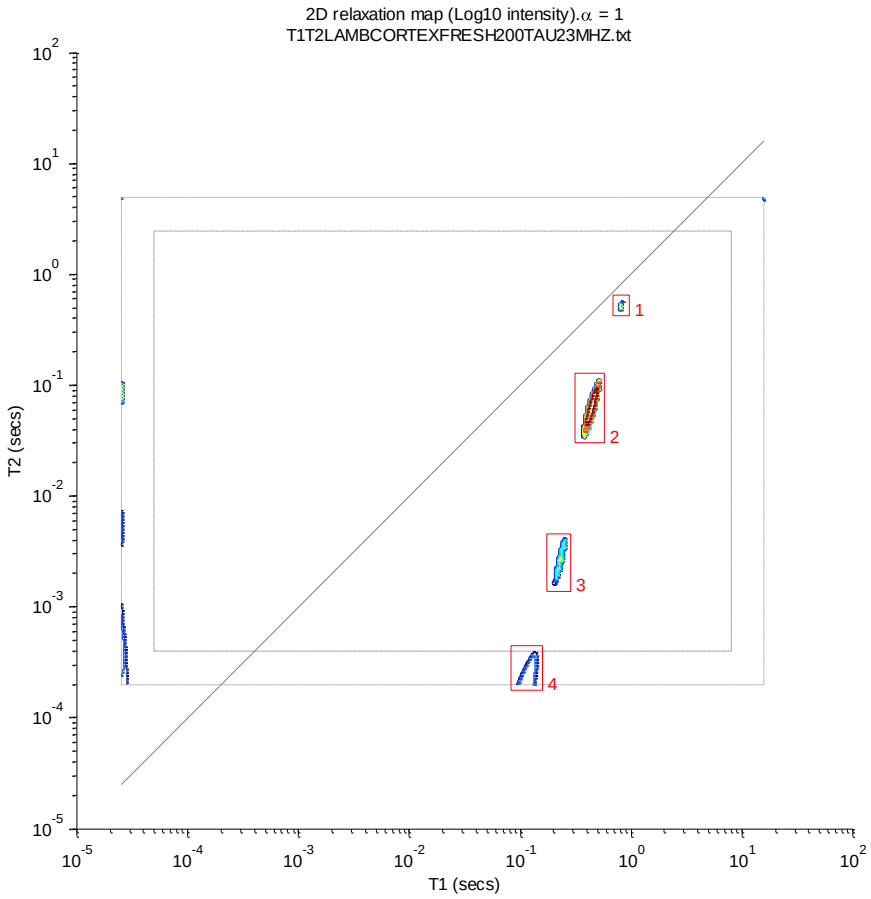

Figure 3.14 A characteristic 2D T_1-T_2 relaxation spectrum performed at 23.4 MHz on a sample of fresh lamb's kidney cortex demonstrating 4 main peaks 1-4.

Peak	Mean area (std. dev.)		Mean T_1 (ms) (std. dev.)		Mean T_2 (ms) (std. dev.)	
	100 MHz	23.4 MHz	100 MHz	23.4 MHz	100 MHz	23.4 MHz
1	0.40% (0.0%)	0.48% (0.08%)	1330 (133)	883 (65)	575 (25)	590 (84)
2	90.2% (2.0%)	95.7% (0.83%)	896 (1.9)	512 (66)	65.3 (9.9)	75.5 (9.0)
3	1.88% (0.28%)	2.56% (0.42%)	319 (133)	276 (60)	7.59 (3.0)	3.40 (0.54)
5/4	3.06% (1.3%)	1.50% (0.0%)	273 (95)	163 (66)	0.796 (0.32)	0.51 (0.38)

Table 3.3 The mean values of the peak intensity and position of peaks 1, 2, 3 and 5 taken at 100 MHz and peaks 1, 2, 3 and 4 taken at 23.4 MHz, as peak marked in figures 3.11 and 3.14 demonstrating the similarities between the peaks. Standard deviation given in brackets next to mean value.

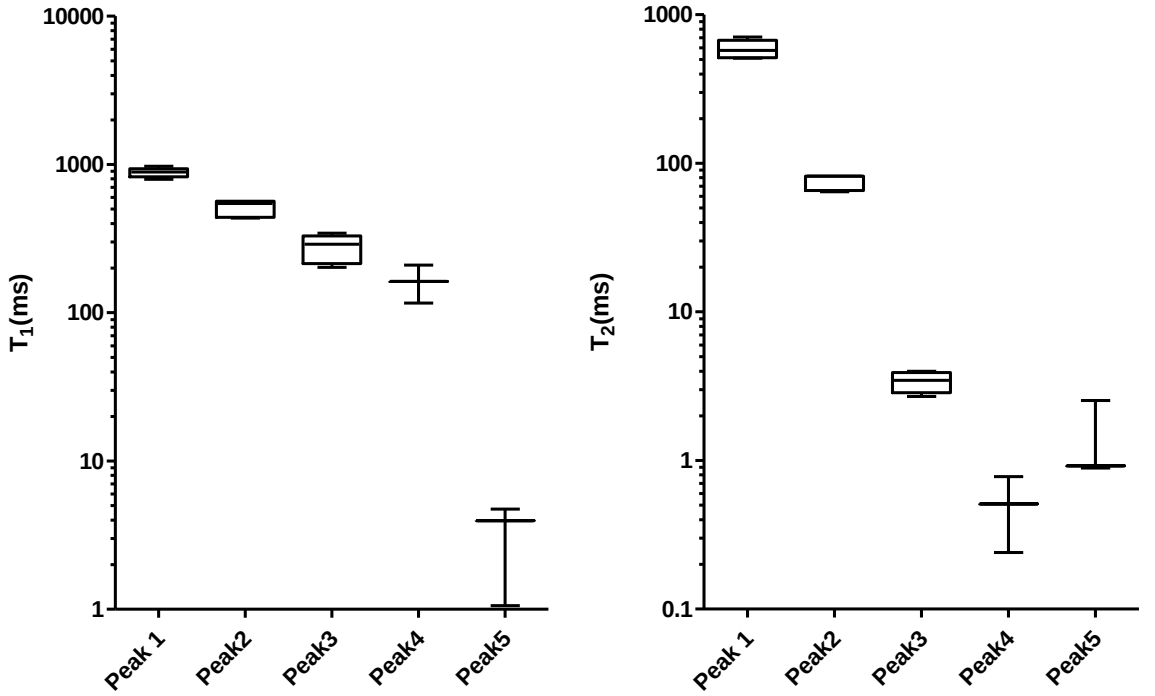

Figure 3.15 The peak positions in T_1(left) and T_2(right) of the 5 main peaks obtained from T_1-T_2 relaxometry performed at 23.4 MHz on 5 samples of fresh lamb's kidney cortex, demonstrating the consistency in peak positions.

As already discussed, it is necessary to demonstrate the repeatability of the 2D T_1-T_2 relaxation spectra, this time acquired from 5 samples of lamb's kidney cortex taken at 23.4 MHz with a tau value of 200 μs. Figure 3.15 shows boxplots of the T_1 and T_2 values of the 5 relevant peaks, marked as in Figure 3.14. Peaks 4 and 5 each appear in only half the spectra but remain similar in both T_1 and T_2 where present. As can be seen, there is little variation in either the T_1 or T_2 peak positions of peaks 1, 2 and 3. Figure 3.16 shows the peak intensities of these same peaks as a percentage of the total peak-marked area. Again there is little variation in peak intensities with most of the signal (≈95%) contained in the dominant peak 2.

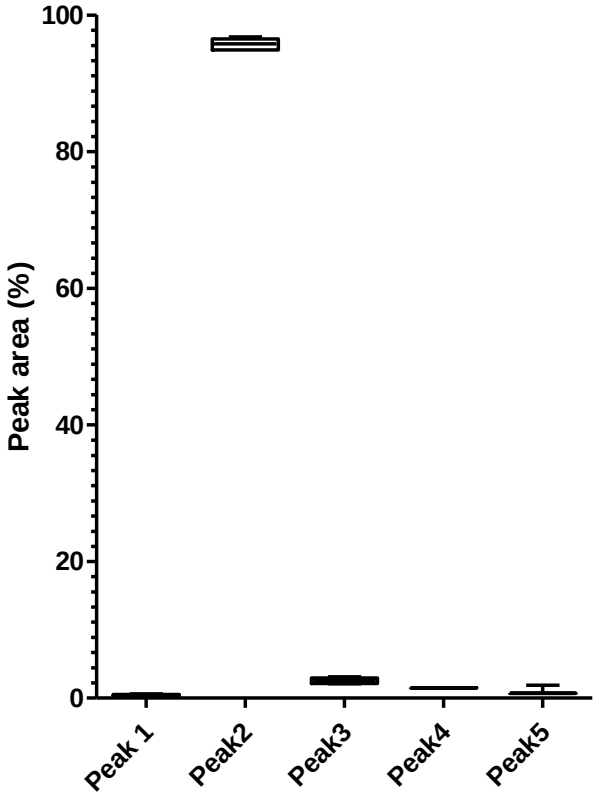

Figure 3.16 The peak intensities, as a percentage of the total peak marked intensity, of the 5 main peaks obtained from T_1-T_2 relaxometry performed at 23.4 MHz on 5 samples of fresh lamb's kidney cortex, demonstrating the consistency in peak intensities.

3.4.3 Lamb's kidney medulla at 100 MHz

As can be seen in Figure 3.10(A), the medulla is the region of the kidney between the cartilaginous fluid channels of the kidney (ureter, renal pelvis and the major and minor calyx) and the brown outer region named the cortex. As can be seen from Figure 3.10(A)[77], it is principally composed of a number of renal pyramids. The renal pyramid can have a striped or ridged appearance as it is composed of many parallel aligned nephrons running from the base of the pyramid, by the cortex, to the 'point', by the cartilaginous centre of the kidney. Nephrons are the main functional unit of the kidney, filtering the blood to regulate the concentration of water and dissolved substances, retaining what is needed and excreting the rest in the urine.

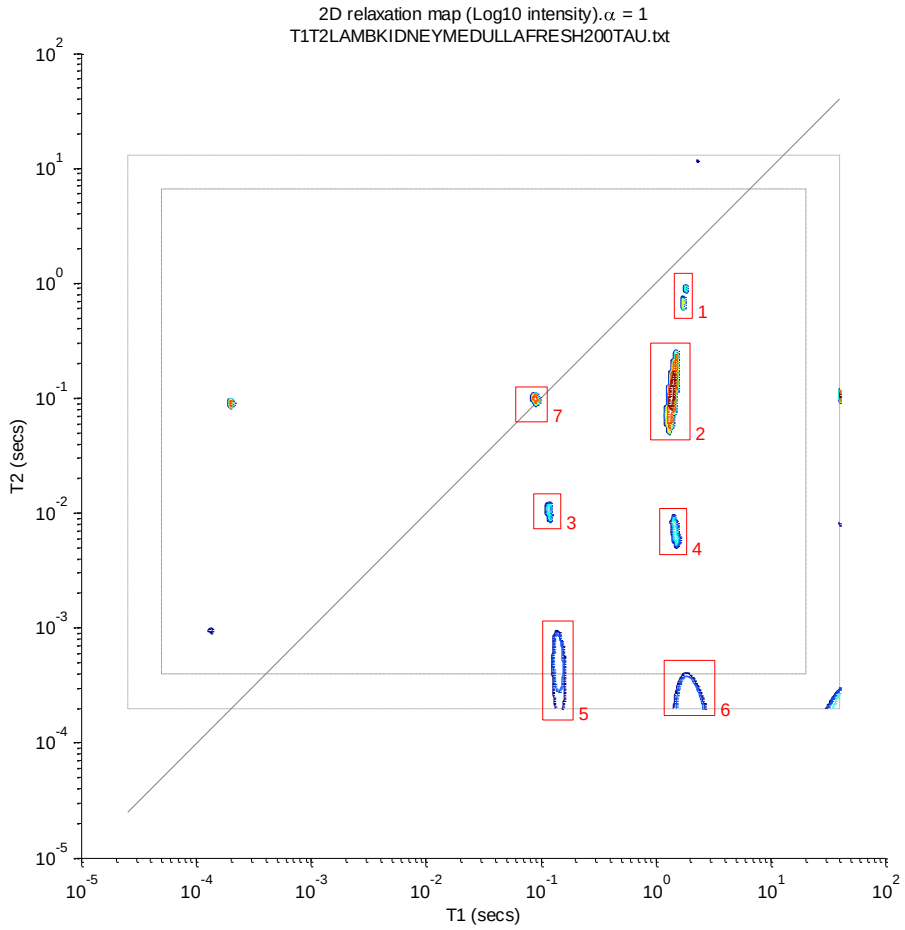

Figure 3.17 A characteristic 2D T_1-T_2 relaxation spectrum performed at 100 MHz on a sample of fresh lamb's kidney medulla showing the 7 main peaks.

Figure 3.17 shows a characteristic 2D T_1-T_2 relaxation spectrum performed at 100 MHz on a sample of fresh lamb's kidney medulla demonstrating the 7 main peaks. Peak 1 has a high mean T_1 value of 1920 ms and a high mean T_2 value of 804 ms indicating that it arises from the relatively free water in the glomeruli, other small capillaries and fluid channels of the medulla. The dominant peak 2 (≈92%) is almost certainly intracellular water. Peak 4 has a relatively low intensity (mean of 1.50%) and a very short T_2 (mean of 5.06 ms). The peak appears to correspond to a similar peak in the liver and cortex spectra, labelled peak 5 and 4 respectively, and so has been provisionally assigned to the same cause, non-exchanging protons in dissolved mobile proteins and biopolymers such as globular proteins and enzymes. Peak 3 appears to correspond with the peak marked as 4 in the liver spectrum and as 3 in the cortex spectrum, thus it would likely originate from the same substances. Possible candidates include sugars, lipids, or other small mobile proteins, although this has not been determined with confidence. Peak 7 occurs in only two spectra

with fairly distinct peak intensities of 0.3% and 5.1%. Further work would be needed to establish its identity as a true peak or an artefact and, if real, identify its cause.

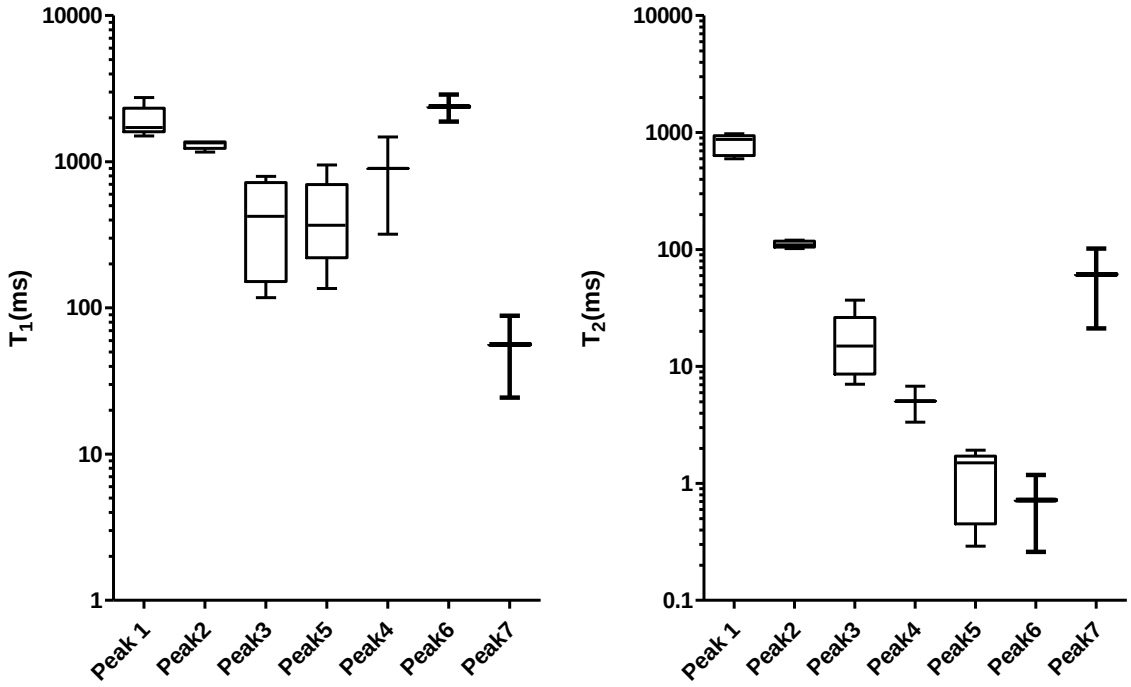

Figure 3.18 The peak positions in T_1(left) and T_2(right) of the 7 main peaks obtained from T_1-T_2 relaxometry performed at 100 MHz on 5 samples of fresh lamb's kidney medulla, demonstrating the consistency in peak positions.

As before, it is necessary to demonstrate the repeatability of the 2D T_1-T_2 relaxation spectra, this time acquired from 5 samples of lamb's kidney medulla taken at 100 MHz with a tau value of 200 µs. Figure 3.18 shows boxplots of the T_1 and T_2 values of the 7 relevant peaks, marked as in Figure 3.17. Peaks 4, 6 and 7 each appear in only half the spectra but remain similar in both T_1 and T_2 where present. As can be seen, there is little variation in either the T_1 or T_2 peak positions particularly peaks 1 and 2. Figure 3.19 shows the peak intensities of these same peaks as a percentage of the total peak-marked area. Again there is little variation in peak intensities with most of the signal (≈92%) contained in the dominant peak 2.

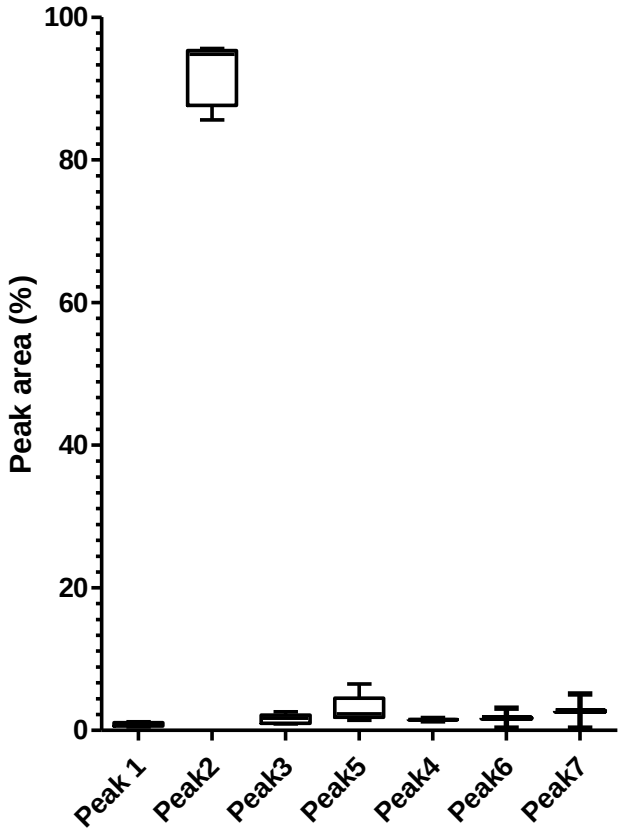

Figure 3.19 The peak intensities, as a percentage of the total peak marked intensity, of the 7 main peaks obtained from T_1-T_2 relaxometry performed at 100 MHz on 5 samples of fresh lamb's kidney medulla, demonstrating the consistency in peak intensities.

3.4.4 Lamb's kidney medulla at 23.4MHz

Peaks 1, 2, and 3 in the 23.4 MHz spectrum (Figure 3.20) line up well to visual comparison with peaks 1, 2, and 3 in the 100 MHz spectrum of the same tissue (Figure 3.17). Peak 4 at 23.4 MHz appears to correspond to peak 5 at 100 MHz. Table 3.4 shows the peak areas and peak positions in T_1 and T_2 of these peaks for direct comparison.

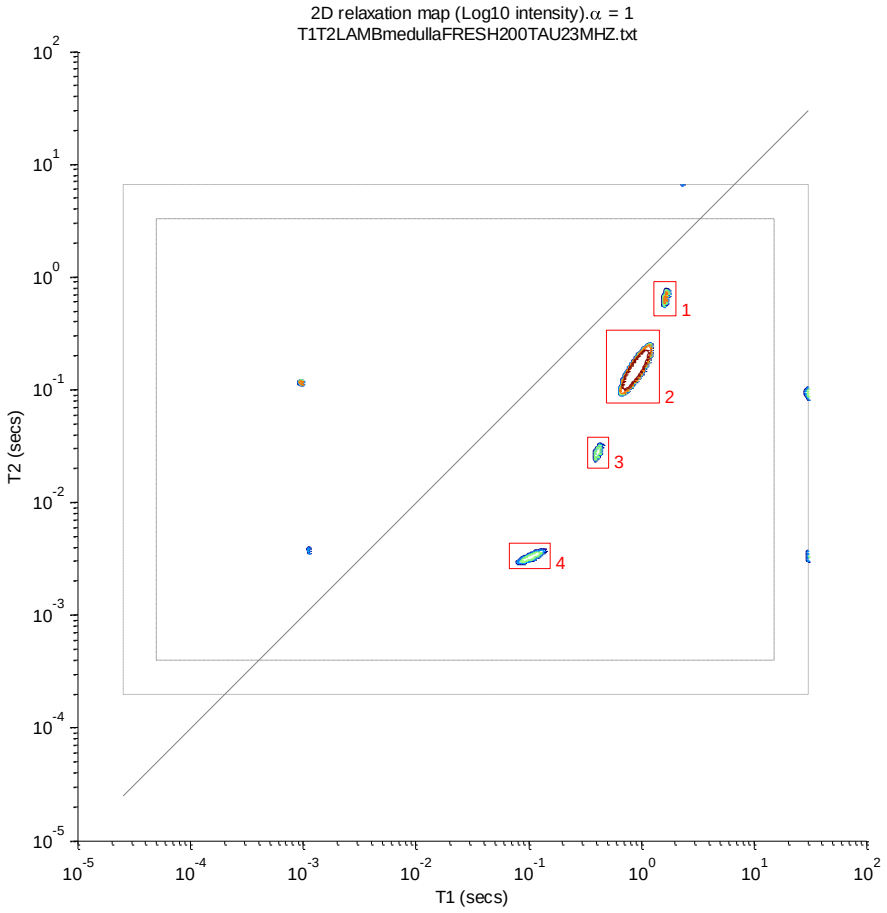

Figure 3.20 The peak intensities, as a percentage of the total peak marked intensity, of the 4 main peaks obtained from T_1-T_2 relaxometry performed at 23.4 MHz on a sample of fresh lamb's kidney medulla. The additional unmarked peaks within the forbidden zone are likely an artefact of the fitting process and the unmarked peaks at the extreme right edge of the spectrum are low intensity and barely visible within the outer region of the spectrum, meaning we have vastly reduced confidence in their authenticity.

Peak	Mean area (std. dev.)		Mean T_1 (ms) (std. dev.)		Mean T_2 (ms) (std. dev.)	
	100 MHz	23.4 MHz	100 MHz	23.4 MHz	100 MHz	23.4 MHz
1	0.88% (0.28%)	1.65% (0.68%)	1920 (490)	1477 (160)	804 (162)	747 (70)
2	92.1% (4.4%)	94.8% (1.1%)	1310 (85)	864 (43)	111 (7.2)	151 (9.8)
3	1.60% (0.66%)	1.43% (0.05%)	433 (291)	428 (102)	16.9 (12)	34.5 (22)
5/4	3.00% (2.0%)	1.45% (0.41%)	441 (307)	180 (88)	1.16 (0.68)	4.19 (1.94)

Table 3.4 The mean values of the peak intensity and position of peaks 1, 2, 3 and 5 taken at 100 MHz and peaks 1, 2, 3 and 4 taken at 23.4 MHz, as peak marked in figures 3.17 and 3.20 demonstrating the similarities between the peaks. Standard deviation given in brackets next to mean value.

There is a slight increase in the peak areas of peaks 1 and 2 in the 23.4 MHz spectrum which would be expected as the 4 peaks in the 23.4 MHz spectrum are the only peaks marked and thus contain the total peak-marked area. This is due to the 23.4 MHz spectrometer's inferior ability to detect smaller peaks. The areas of peaks 3 and 4 in the

23.4 MHz spectrum seem to have reduced when compared with peaks 3 and 5 in the 100 MHz spectrum. This may be due to a single result included in the 100 MHz data which was obtained from a sample stored a few days longer than the rest. When this result is remove the 100 MHz peak averages reduce to 1.35% for peak 3 and 2.13% for peak 5, which are closer to the expected values. The T_1 values would be expected to decrease from the 100 MHz to the 23.4 MHz due to the dependence of T_1 on the spectrometer frequency[12, 69]. This reduction is seen across these 4 peaks. The T_2 values remain approximately equivalent as there is significantly less T_2 frequency dependence at this range. The slight increase in the mean T_2 of peaks 3 and 4 may appear suspect but taking into account the standard deviation values for each peak (peak 3: 12 ms at 100 MHz and 22 ms at 23.4 MHz, peak 4 0.68 ms at 100 MHz and 1.94 ms at 23.4 MHz) they are remarkably close, as would be expected.

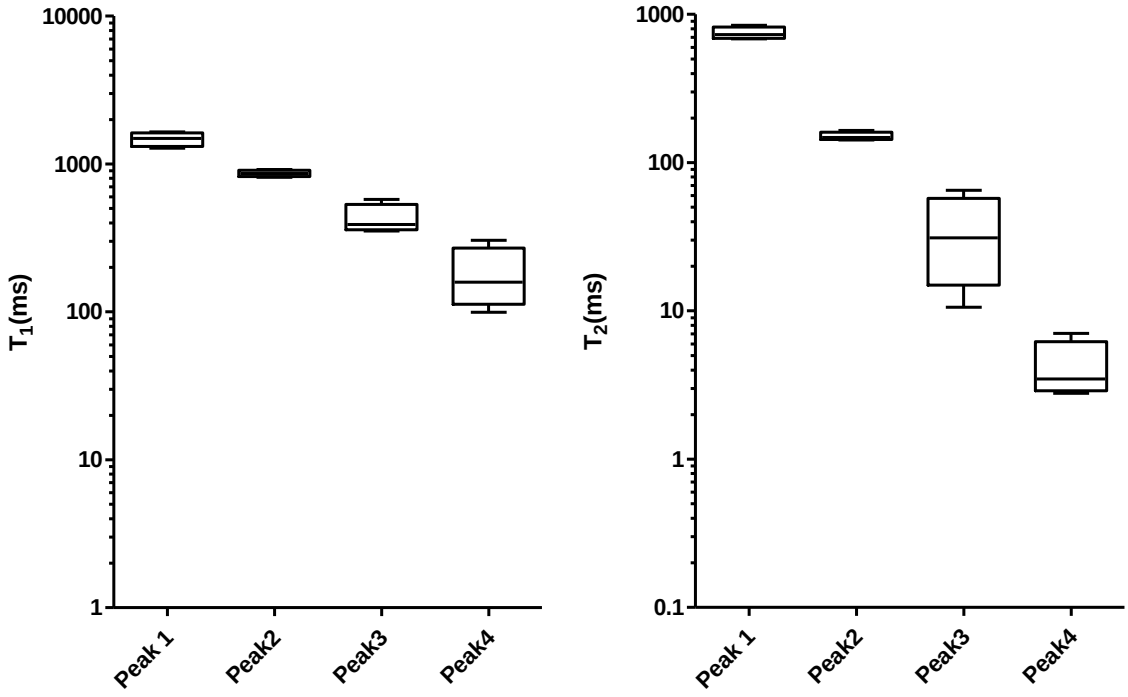

Figure 3.21 The peak positions in T_1(left) and T_2(right) of the 4 main peaks obtained from T_1-T_2 relaxometry performed at 23.4 MHz on 4 samples of fresh lamb's kidney medulla, demonstrating the consistency in peak positions.

Repeatability of the 2D T_1 - T_2 relaxation spectra is now demonstrated, this time acquired from 4 samples of lamb's kidney medulla taken at 23.4 MHz with a tau value of 200 µs. Figure 3.21 shows boxplots of the T_1 and T_2 values of the 4 relevant peaks, marked as in Figure 3.20. As can be seen, there is little variation in either the T_1 or T_2 peak positions

particularly peaks 1 and 2. Figure 3.22 shows the peak intensities of these same peaks as a percentage of the total peak-marked area. Again there is little variation in peak intensities with most of the signal (≈95%) contained in the dominant peak 2.

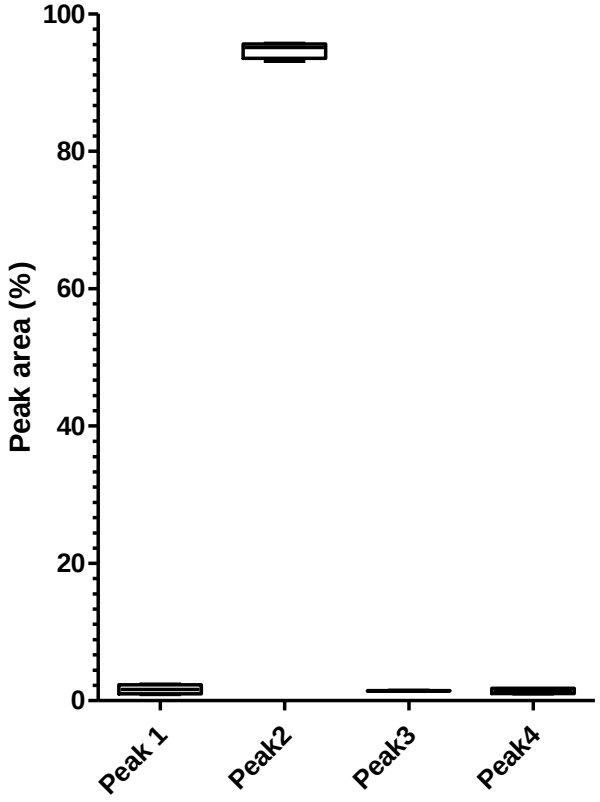

Figure 3.22 The peak intensities, as a percentage of the total peak marked intensity, of the 4 main peaks obtained from T_1-T_2 relaxometry performed at 23.4 MHz on 4 samples of fresh lamb's kidney medulla, demonstrating the consistency in peak intensities.

3.4.5 Lamb's kidney ureter

The ureter is the duct through which fluid is removed from the kidney. The ureter consists of a flexible tube containing a fibrous outer layer, an inner mucous membrane and three layers of muscle (external longitudinal as well as circular and longitudinal inner layers). Figure 3.23 shows the T_1 T_2 relaxation spectrum of lamb kidney ureter acquired at 100 MHz. As can clearly be seen the spectrum consists mainly of 2 greatly spread out peaks, most likely from water protons, covering 2 orders of magnitude in both transverse and longitudinal dimensions.

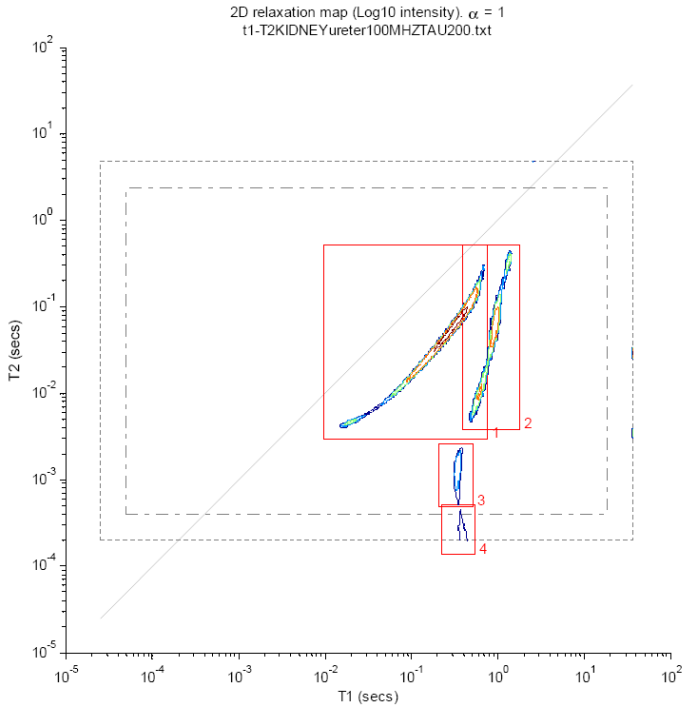

Figure 3.23 A 2D T_1-T_2 relaxation spectrum performed at 100 MHz on a sample of lamb's kidney ureter. Attempts at properly peak marking this spectrum have failed due to the square box peak marking tool and the extended nature of peaks 1 and 2.

As can be seen in Figure 3.23 the spectrum is difficult to peak mark properly due to the shape of the main peaks and their placement close to each other. This very different spectrum is likely due to the very different structure and composition of the ureter when compared to the cortex and medulla, as well as potential issues that the effect of extended storage may have on this kind of tissue. There may also be issues with the orientation of the tissue. The ureter is such a thin tissue that, to reach a useable volume in the sample tube, a large area of the tissue was extracted and packed into the tube, leading to a large range of tissue orientations in the examined sample. Further examination of this tissue was not conducted as the potential for discovery was outweighed by the issues raised above.

3.4.6 Comparison with previous relaxometry studies of the kidney

As in studies of liver, kidney relaxometry studies largely focus on correlating a single average T_1 or T_2 value for a tissue, with a single known change in tissue content or condition. The hydration level of donor organs as an indicator of tissue condition was examined by van der Hoeven et al[78] in porcine kidney with T_1 and T_2 relaxometry. Only single values were acquired but they found time dependent changes with different results

for the cortex and medulla. They found significant correlation between single average T_1 in the cortex and cold ischemia times (CIT). There was non-significant reduction in single T_2 values in the cortex and no significant difference in T_1 or T_2 of the medulla. They concluded that MR relaxometry could be a valuable technique in assessing donor kidney quality but missed out on potentially improved diagnostic value from the full characterisation available through 2D T_1 - T_2 relaxometry. Sievers et al[79] examined single values of T_1 in the kidneys of patients with known renal failure in vivo. They found T_1 to be a good, non-invasive indicator of over hydration but, as discussed already, missed on additional characterisation from 2D techniques. Wolff et al[80] looked at magnetisation transfer from one proton pool (a peak in the T_1 - T_2 spectrum) arising from free water to another proton pool with restricted motion. They found that this exchange was tissue specific and suggested that this pathway is a major determinant of water proton relaxation behaviour in vivo. Huang et al[81] used relaxometry to examine single T_1 values of cortex and medulla for native and transplanted kidneys and found higher T_1 values in transplanted kidney cortex (1183 ± 136 ms) than native kidney cortex(1057 ± 94 ms) . This average T_1 would likely be dominated by the main peak marked as peak 2 in Figure 3.11. This peak only has a T_1 value of 896 ms but is from lamb cortex rather than human (in the Huang et al study) so some difference is to be expected. There may also be a reduction in the T_1 value due to reduction in tissue hydration after storage, as was shown in the studies already discussed above[78, 79]. The Huang et al[81] study was conducted at 1.5T *in vivo*, thus at body temperature, whereas the 2D spectrum was acquired at room temperature on our 100 MHz (≈ 2.34T) spectrometer, which would each also affect the T_1 value. A slight increase in spectrometer frequency should increase the T_1 value, which is not seen here, but the effect of temperature change on T_1 is more complex, so it may be playing a part in the difference here observed. A study by Parker et al[82] found T_1 to vary linearly with 1/T in samples of blood whereas Lui et al[83] and Birkl et al[84] found T_1 to vary linearly with T in human brain tissue. T_1 is expected to decrease with increasing temperature (increased molecular motion) as the rate of molecular motion approaches the rate of spin lattice exchange, and then to increase after this point.[85] Biological tissues are made up of various substances with varying rates of molecular motion and so temperature effects will affect them based on their composition and may increase or decrease their overall T_1 value. In the case of the kidney, the tissue would likely be closer to that of the brain and have slower rates of molecular motion, thus the slight temperature increase in the tissues examined by Huang et al[81] may account for their tissues' increased T_1 values.

3.5 Pig hyaline cartilage

Figure 3.24 shows a 2D T_1-T_2 relaxation spectrum performed at 100 MHz on a sample of pig hyaline cartilage. As with the ureter spectrum (shown in Figure 3.23) the main peak is thin and spread out over multiple orders of magnitude. At this point it was decided that cartilaginous structures such as this would require immediate sampling and experimentation to ensure useful results. Both the ureter used to acquire Figure 3.23 and the hyaline cartilage used to acquire Figure 3.24 are stored by commercial distributers for at least 2 days before becoming available for study and so further study of these tissues was not conducted. As with the ureter, extraction of a large enough sample necessitated removal of many thin layers of cartilage to be compiled into a single sample so tissue orientation was not consistent and may have led to the stretching of the detected peaks.

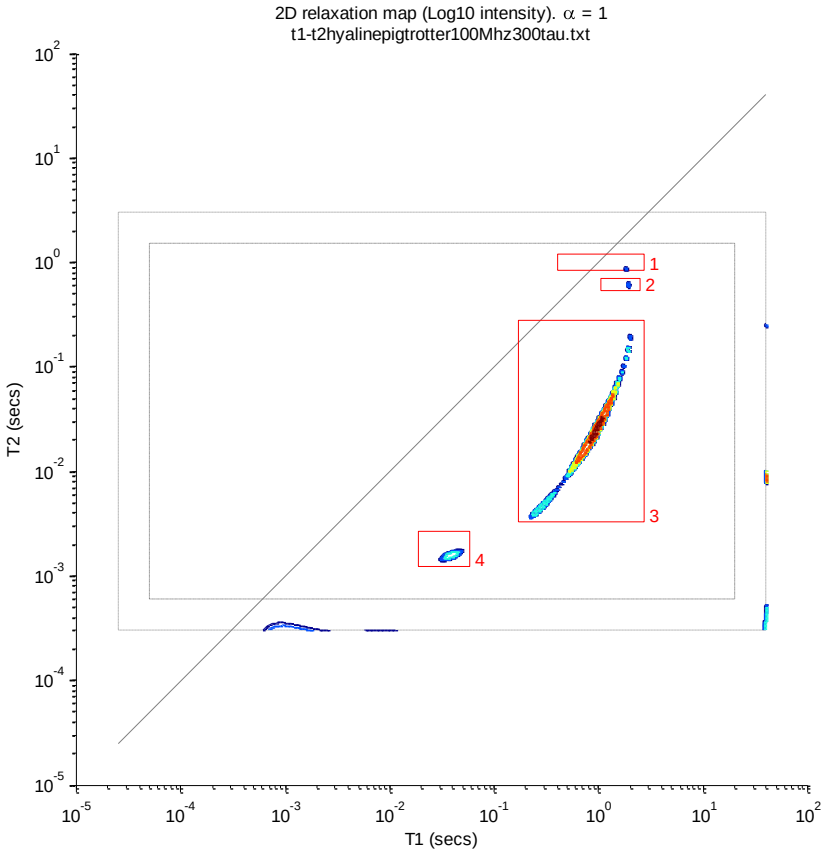

Figure 3.24 A 2D T_1-T_2 relaxation spectrum performed at 100 MHz on a sample of pig hyaline cartilage demonstrating the long thin nature of the dominant peak, stretching across 2 orders of magnitude in T_2 and 1.5 orders in T_1.

3.5 Conclusions

At this point it would seem obvious that the T_1-T_2 relaxation spectra of mammalian tissue provide information about the structure and composition of the tissues themselves as well as a way of distinguishing between different tissue types.

Main Peak	Tissues compared at 100 MHz		P-value
Area	Kidney Medulla	Kidney Cortex	0.40
Area	Kidney Medulla	Liver	<0.01
Area	Kidney Cortex	Liver	<0.01
T_1	Kidney Medulla	Kidney Cortex	<0.01
T_1	Kidney Medulla	Liver	<0.01
T_1	Kidney Cortex	Liver	<0.01
T_2	Kidney Medulla	Kidney Cortex	<0.01
T_2	Kidney Medulla	Liver	<0.01
T_2	Kidney Cortex	Liver	<0.01

Table 3.5 P-values obtained from two tailed statistical t test on the main peak's area, T_1 and T_2 in different mammalian tissues at 100MHz showing significant differences between each data set other than between the areas of the main peak in the kidney cortex and medulla.

Table 3.5 shows the result of statistical t-tests on the area, T_1 and T_2 of the main intracellular water peak in the different examined mammalian tissues at 100 MHz. We see clearly significant differences between each of the peak's characteristics in the different tissue types, excluding its peak area when compared between the kidney medulla and cortex. Typically a p-value of 0.05 or less is considered significant and the p-value in this case (0.40) falls far short of this. While additional experiments on these tissues may improve any observed difference between these two data sets to a significant level, they may also further clarify the lack of difference between them. Therefore, we cannot make any definitive statements about the relationship between these two tissues with regards to intracellular water peak area. The T_1 and T_2 of this peak, however, show clear difference between these two tissues and so, they are still distinguishable by 2D T_1 - T_2 relaxometry at 100 MHz. Each of the comparisons in Table 3.5 was performed separately to examine whether a difference could be found and has not been corrected for multiple comparisons.

Main peak	Tissues compared at 23.4 MHz		P-value
Area	Kidney Medulla	Kidney Cortex	0.18
Area	Kidney Medulla	Liver	0.01
Area	Kidney Cortex	Liver	<0.01
T1	Kidney Medulla	Kidney Cortex	<0.01
T1	Kidney Medulla	Liver	<0.01
T1	Kidney Cortex	Liver	<0.01
T2	Kidney Medulla	Kidney Cortex	<0.01
T2	Kidney Medulla	Liver	<0.01
T2	Kidney Cortex	Liver	<0.01

Table 3.6 P-values obtained from two tailed statistical t test on the main peak's area, T_1 and T_2 in different mammalian tissues at 23.4 MHz showing significant differences between each data set other than between the areas of the main peak in the kidney cortex and medulla.

Table 3.6 shows the result of statistical t-tests on the area, T_1 and T_2 of the main intracellular water peak in the different examined mammalian tissues at 23.4 MHz. Significant differences are present between each of the peak's characteristics in the different tissue types, excluding its peak area when compared between the kidney medulla and cortex. As already discussed, a p-value of 0.05 or less is considered significant and the p-value in this case (0.18) falls short of this, as with the same comparison at 100 MHz. As before, additional experiments on these tissues may improve, or confirm the lack of, the significance of any observed difference between the two data sets. In the light of this we cannot make any definitive statements about the relationship between these two tissues with regards to intracellular water peak area. The T_1 and T_2 of this peak show significant difference between the two tissues meaning that, as with the data at 100 MHz, they are distinguishable by 2D T_1 - T_2 relaxometry at 23.4 MHz. Again, as with the 100MHz data, each comparison was performed separately and has not been corrected for multiple comparisons. Examining the p-values in Table 3.5 and Table 3.6 it is clear that the 2D T_1 - T_2 relaxometry technique can differentiate between different tissue types, in some cases using only a single parameter from a single peak. It has also been shown that spectra are reproducible within the set of a single tissue. In situations where tissue identification is key, the various parameters of each consistent peak could be combined to form a unique fingerprint for each tissue. These tissue fingerprints could be used with statistical or probabilistic classification methods[86-88] such as principal component analysis (PCA)[89-91] to identify tissue types from a library of possibilities.

Chapter 4 will further examine 2D T_1 - T_2 relaxometry's ability to differentiate tissue and identify its constituents by examining Human articular knee cartilage in both a healthy and osteoarthritic state at 100 MHz and 23.4 MHz spectrometer frequencies.

4. 2D relaxometry of human articular cartilage

4.1 Introduction

MRI, when used in standard clinical practice, consists mainly of weighting an imaging sequence towards either T_1 or T_2 and generating a grey scale image based on the intensity of signal received from each voxel (a single volume element) [92]. The contrast arising from the different proton environments in the various organs and tissues provides a 3D representation of the physical locations and conditions of these various tissues and allows for diagnosis of many conditions and disorders. While this is a useful and effective diagnostic tool, it fails to take advantage of the opportunities provided by the many and varied sequences and methods available to the NMR practitioner.

In some cases the relaxation is quantified in the form of a T_1 or T_2 map. This is obtained by acquiring the image with several different inversion recovery or echo times (typically 10-12) then fitting the data with a single effective T_1 or T_2 exponential which is then associated with that voxel. In this way high spatial resolution and large field of view is achieved at the cost of low resolution in the relaxation time domain[93, 94].

In this chapter we examine the application of 2D relaxation techniques, as described in previous chapters, to achieve high relaxation time resolution in a small region of interest. The aim is to characterise the 2D relaxation spectrum of the tissue in question, in order that the healthy state could be distinguished from one or many diseased states, allowing the 2D relaxation spectrum to be used as a clinical biomarker. As previously discussed this requires the development of both ultrafast and volume selective techniques but in order to be of use at all it must be demonstrated that, for at least one disease state, it is possible to distinguish healthy and diseased tissue with some degree of confidence. For the purposes of this investigation potentially osteoarthritic human articular knee cartilage has been selected, due to its availability from a local hospital (NNUH, Norwich, UK) in both healthy and diseased forms, as well as for the huge potential for NMR as a clinical biomarker in this area. Articular cartilage covers the face of bones at joints in the skeleton. It provides a low friction surface at the joints, allowing easy and pain free articulation of

the joint.

Current diagnostic techniques in osteoarthritis tend to come in too late to provide any effective management of osteoarthritis. Patients usually present with severe joint pain and upon examination are found to have lost most of their articular cartilage in the joint or joints in question. At this point the only available option is surgical replacement of the joint with one of many available artificial implants. Work is now under way to develop a medicinal treatment to slow, halt, or perhaps in milder, early cases even reverse damage to the cartilage itself. It is thought that chemical changes occur within the cartilage itself prior to its degradation and loss, which impair its effectiveness as a near frictionless mechanical surface, leading to wear and damage to the surface and body of the cartilage layer. In order to implement treatments such as this the alteration to the chemical composition of the cartilage layer must be detected before any serious damage occurs, preferably via non-invasive means, allowing the screening of at risk groups without causing damage arising from invasive biopsies etc. Thus we attempt to demonstrate the potential of 2 dimensional relaxometry for use as a clinical biomarker in distinguishing healthy and arthritic articular knee cartilage. T_1 and T_2 are frequency dependent [40, 95]. As discussed in chapter 1, the T_1 relaxation parameter for different tissues tends to increase and converge with increasing field strength. T_2 values tend to decrease at higher fields. Any distinguishable characteristics of healthy and diseased tissue may be shifted by alterations in spectrometer frequency, and comparisons to find difference and similarity between spectra may be enhanced or impaired by these shifts.

4.2 Methods

Samples were obtained from the Norfolk and Norwich University Hospital during total knee replacement (TKR) and trochleoplasty. TKR[96, 97] is performed to completely replace the articular surface in the knee. The end of the bone is removed and replaced with an artificial version, leaving the removed bone free for sample dissection and ideally allowing a return to normal pre-operative use after a period of recovery and rehabilitation. While most of the articular cartilage is usually worn away (necessitating the operation itself) there is usually an area of cartilage remaining that, whilst now in an osteoarthritic state, has not worn away due to its location out of the normal wear pattern of the joint. Trochleoplasty[98,

[99] is performed to correct a luxating patella, in which the knee cap dislocates. The cause is usually a congenital defect although in rarer cases it can be caused by blunt force trauma. During trochleoplasty the surface of the femur is reshaped and secured with a surgical screw, necessitating the removal of a plug of articular cartilage for the screw and potentially a region of articular cartilage from the surface itself to allow the reshaping. This provides our healthy sample, as the cartilage is removed due to physical necessity rather than because of its own condition.

In both cases the sample is taken from the operating theatre as soon as it is removed from the patient and placed in 5 mm and 10 mm NMR tubes, which are then filled with polytetrafluoroethylene (PTFE) to remove as much remaining air as possible to prevent dehydration of the sample. The samples are kept chilled (approximately 4°C) to slow any degradation and immediately scanned using a 100 MHz DRX spectrometer using a high power probe with a 5 mm horizontal solenoid coil. Experiments are conducted using a tau of 200-400 µs dependant on the sample and 90 or 180 degree pulse lengths automatically calculated by the Resonance Instruments RINMR software[56, 57]. The 23.4 MHz scan was performed on a commercial DRX bench top scanner using similar parameters with a 10 mm vertical solenoid coil. T_1 - T_2 experiments were performed using the existing 2D inversion recovery CPMG sequence (INVCPMG) using 4K (4096) or more of echoes in the T_2 dimension and 80 or more logarithmically spaced inversion recovery steps in the T_1 dimension taking upwards of 90 minutes (usually closer to 2-3 hours) to complete the experiment. Data was then analysed using internally developed MATLAB programs making use of 2D Laplace transform algorithms to obtain a 2-Dimensional cross correlation T_1-T_2 spectrum of the sample. These programs were named InvCpmgEditV3djh, InvCpmgCalcV3djh and InvCpmgResV3djh, all based on InvCpmg Version 12 by Kevin Wright, 20 Jan 2005). Samples were also examined using the T_2-store-T_2 method at store times 500 µs, 2 ms, 12 ms and 50 ms to aid in peak assignment by allowing the examination of magnetisation transfer cross peaks in the sample. These scans were then analysed using the internally developed MATLAB programs CPMGCPMGEdit, CPMGCPMGCalc and CPMGCPMGRes to obtain a 2-Dimensional cross correlation T_2 - T_2 spectrum of the sample. Again for use in peak assignment, samples of purified proteoglycan and collagen from bovine sources were analysed using the T_1 - T_2 sequence. Samples were delivered dry and rehydrated to 60-70% with deionised water in order to correspond to biologically present hydration levels [100]. These samples were examined

using similar protocols and parameters to the human cartilage samples in order to provide accurate references of their T_1 - T_2 spectra.

4.3 Healthy and diseased human articular knee cartilage

Samples were initially divided into two groups labelled healthy and diseased based on the operation in which they were extracted, either trochleoplasty or TKR respectively. During extraction and discussion with the lead operating surgeon it was decided that this was too rigid a distinction as, during some of the trochleoplastys, the cartilage of the knee was judged as being in the early or more advanced stages of osteoarthritic degradation, this state having potentially contributed to the need for the operation itself. Thus some of the trochleoplasty samples were ruled out of the healthy group and included within the overall data set appropriately labelled as being from early stage patients. In this section we discuss the examination and comparison of characteristic healthy and diseased samples as well as attempting peak assignment[27].

4.3.1 Healthy human articular knee cartilage at 100 MHz

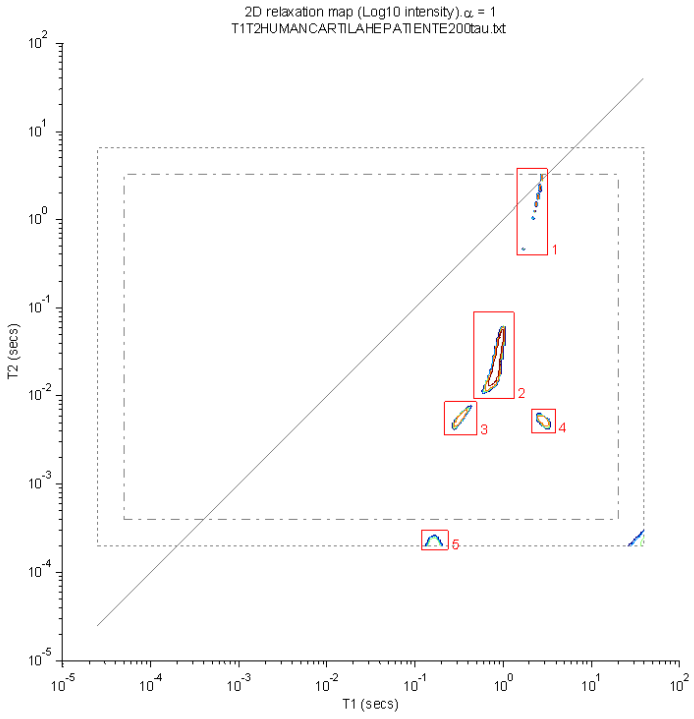

Figure 4.1 Characteristic T_1 - T_2 spectrum of a healthy human articular knee cartilage sample, taken at 100 MHz with a tau of 200 µs with 5 marked peaks. The signal region to the bottom right at extremely high T_1 and low T_2 is likely an artefact as it is in the outer region of the spectrum, in which we have reduced confidence, and has an unreasonable 40 second T_1.

Figure 4.1 shows a characteristic T_1 - T_2 spectrum of a healthy cartilage sample acquired at 100 MHz with a tau value of 200 µs. The peaks marked 2, 3 and 4 are arranged in a triangle formation with a dominant peak presenting with two smaller peaks below and to either side. This formation is consistent throughout the cartilage samples and in most biological samples such as the liver and kidney described in chapter 3. Typically there is also a fourth peak present above this triangle formation, in this case labelled peak 1. Peak 1 appears to be composed of many smaller peaks which may be due to digitisation of the spectrum due to the limited number of T_1 steps and the small total peak intensity of 3.5%. Its long T_1 and T_2 relaxation times are suggestive of something close to bulk water. Peak 2 takes up 81.5% of the total spectrum and is certainly due to water in the sample. Peaks 3 and 4 (7.6% and 5.6% respectively) cannot currently be assigned with confidence but likely candidates have been suggested as compartmentalised water and mobile non-exchanging biopolymer proteins such as those in proteoglycan. Peak 5 is at the limit of detection but is, as with the kidney spectra in chapter 3, suggestive of the more rigid proteins of the cartilage fibres. The signal region with extremely high T_1 and low T_2 is most likely an artefact as it is in the outer region of the spectrum, in which we have reduced confidence. This assignment is confirmed by its unreasonable T_1 value upwards of 40 seconds.

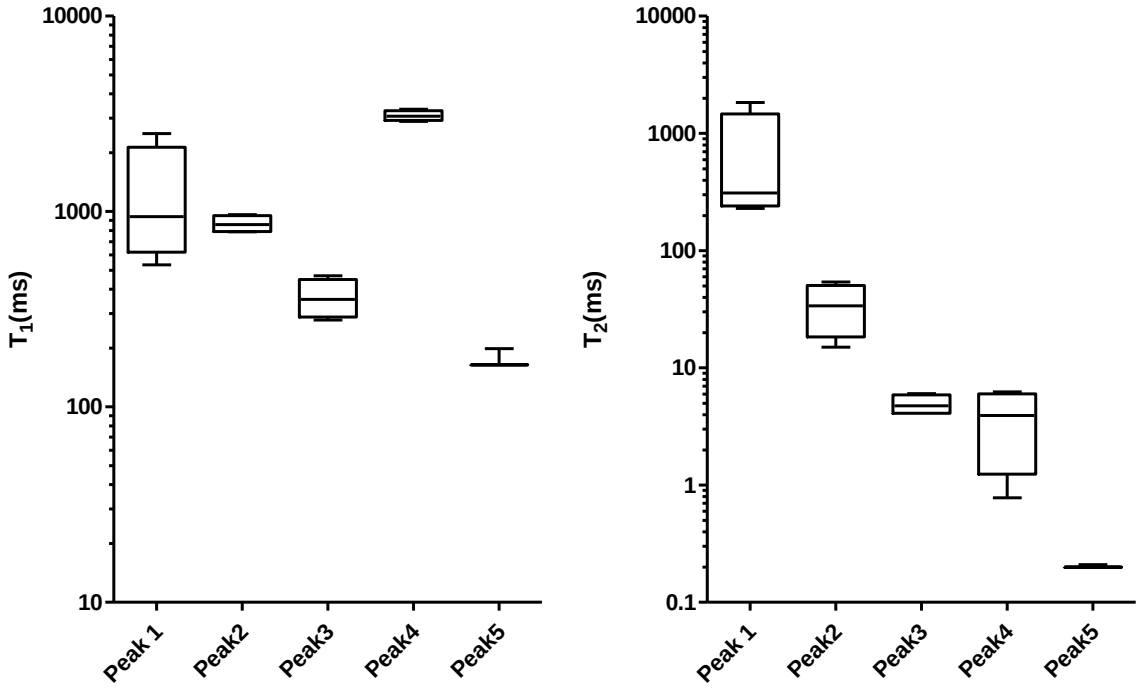

Figure 4.2 Boxplots of the peak positions in T_1(left) and T_2(right) of the 5 peaks obtained from T_1-T_2 relaxometry performed at 100 MHz on 4 samples of healthy human articular knee cartilage, demonstrating the consistency in peak positions.

Figure 4.2 shows the T_1 and T_2 peak positions of the 4 healthy sample spectra acquired at 100 MHz. Peak 1, as discussed previously and shown in Figure 4.1, is a low intensity peak which appears to be made of many smaller peaks, likely due to digitisation of the spectrum from the limited number of T_1 steps. It is not then surprising that it is the most variable of the peaks marked here. The more significant peaks (2, 3 and 4) making up the triangle formation in the spectrum are far more consistent in peak position.

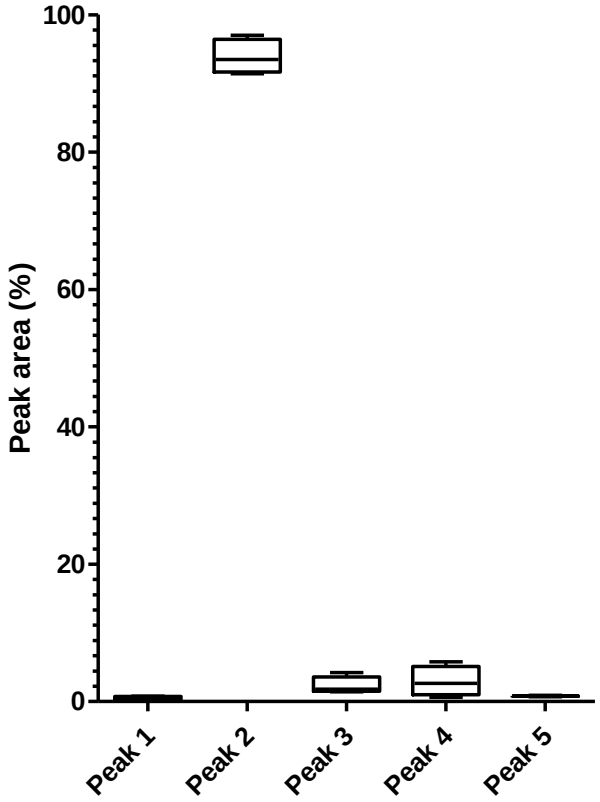

Figure 4.3 Boxplot of the peak areas, as a percentage of the total peak marked intensity, of the 5 peaks obtained from T_1-T_2 relaxometry performed at 100 MHz on 4 samples of healthy human articular knee cartilage, demonstrating the consistency in peak areas.

Figure 4.3 shows the peak intensities of these same peaks as a percentage of the total peak-marked area. There is little variation in peak intensities with most of the signal (mean 85.02% std. dev. 3.42%) contained in the dominant peak 2.

4.3.2 Osteoarthritic human articular knee cartilage at 100 MHz

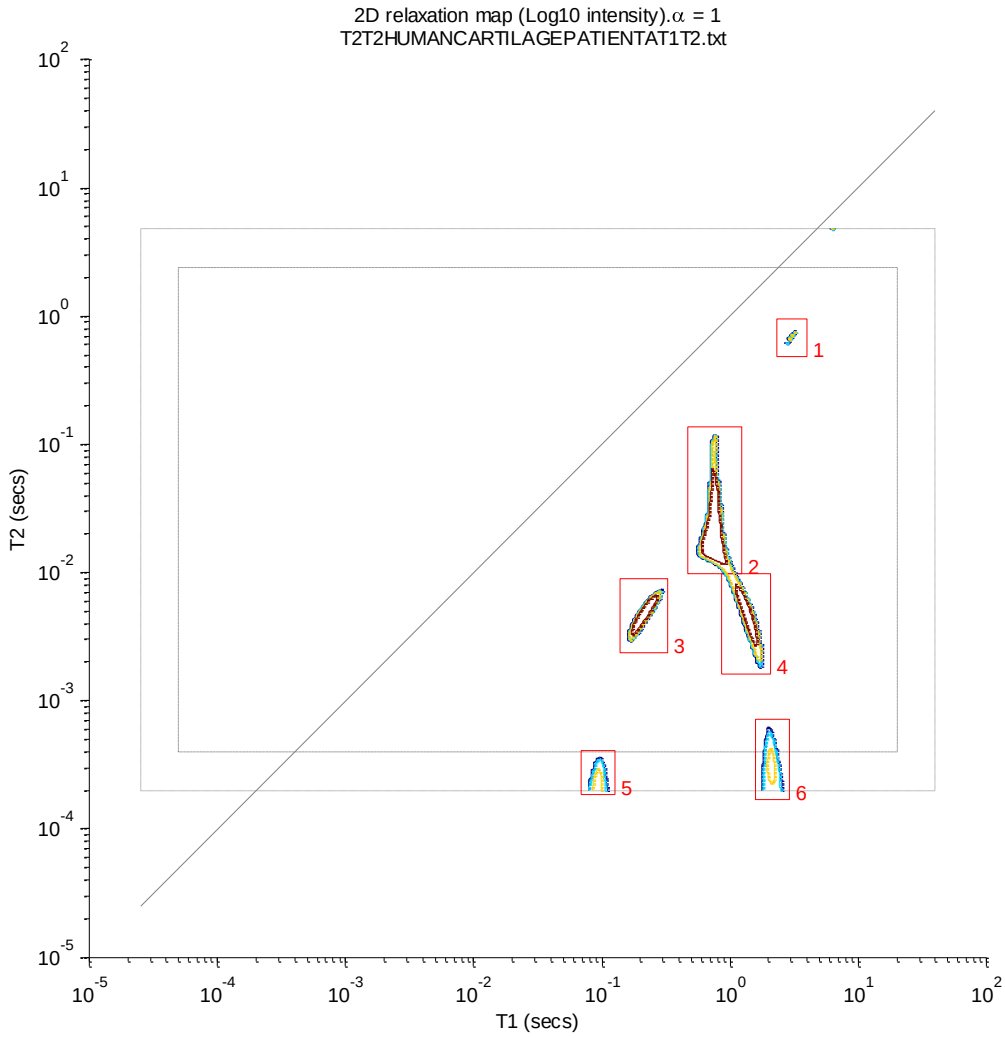

Figure 4.4 Characteristic T_1 - T_2 spectrum of an osteoarthritic human articular knee cartilage sample, taken at 100 MHz with a tau of 200 µs with 6 marked peaks.

Figure 4.4 shows the characteristic spectrum of a diseased sample. As with the healthy cartilage sample, the triangle peak formation (peaks 2, 3 and 4) can be seen along with the other major peaks of the spectrum (peaks 1 and 5). Peak 6 occurs only in two of the 7 available spectra, so will not yet be discussed with confidence. Table 4.1 contains the peak areas of the 3 major peaks making up the triangle formation (2, 3 and 4) in both the healthy and arthritic samples. The arthritic samples have been subdivided into two groups labelled A and B. From the values in the table it would seem clear that this subdivision is necessary

when examining and interpreting the arthritic data set. While the healthy group has a stable peak 2 intensity with mean 85% and standard deviation 3.4%, the arthritic group has two clear distinct peak 2 intensities with group A having a mean of 61.6% (std. dev. 5.3%) and group B having a mean of 93.9% (std. dev. 2.5%). Peaks 3 and 4 have shifted to larger values in group A, indicative of significant signal loss in the main water peak. Group B has shifted the other way, greatly decreasing the peak areas of 3 and 4, consistent with the rise in relative signal intensity in its peak 2.

Tissue type	peak 2	peak3	peak4
healthy	84.2%	9.7%	4.2%
healthy	81.5%	7.6%	5.6%
healthy	84.7%	6.9%	4.6%
healthy	89.7%	6.6%	3.3%
arthritic A	56.0%	16.5%	20.5%
arthritic A	62.3%	10.9%	15.5%
arthritic A	66.6%	9.9%	19.2%
arthritic B	94.6%	1.4%	3.1%
arthritic B	97.0%	1.8%	0.6%
arthritic B	91.4%	1.8%	5.8%
arthritic B	92.4%	4.2%	2.2%

Table 4.1 Peak intensities of the main peaks in the triangle formation (2, 3 and 4) taken from T_1 - T_2 spectra of human articular knee cartilage samples taken at 100 MHz with a tau of 200 µs, divided into healthy and arthritic (from patients suffering from osteoarthritis). The arthritic group is subdivided into groups A and B due to significant divergence in peak intensities.

The arthritic samples are all taken from TKR patients and then handled and processed using the same methods so this discontinuity is not an expected result. Assuming no significant experimental error, which seems unlikely, some speculation as to the cause has suggested the possibility of two different disease states or perhaps a shift in disease state during progression of osteoarthritis.

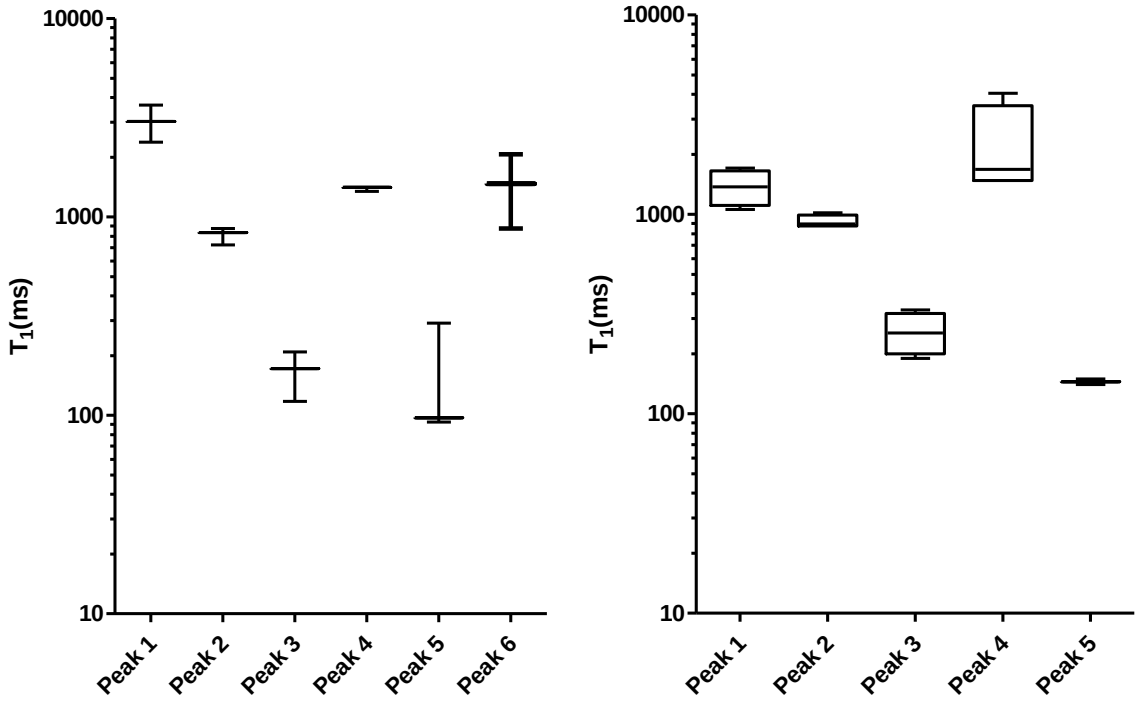

Figure 4.5 Boxplots of the peak positions in T_1 of the peaks obtained from T_1-T_2 relaxometry performed at 100 MHz on samples of human articular knee cartilage extracted during total knee replacement (TKR) due to osteoarthritic nature of tissue. This disease group referred to as group A is to the left and contains 3 samples. The disease group referred to as B is to the right and contains 4 samples.

Figure 4.5 directly compares the T_1 values for the two arthritic groups A and B. We see here that peak 6 occurs only in group A. There also appears to be a significant shift in the T_1 of peak 1 to lower values in the second group (p value= 0.0053). Shifts in peaks 2 and 3 seem present but less significant (p values of 0.10 and 0.085). The other peaks do not appear to demonstrate any significant difference in T_1. Figure 4.6 directly compares the T_2 values for the two arthritic groups A and B. In the T_2 values we see a reduction in peak 1 (p value =0.047) and in peak 4 (p value = 0.016). There is a less significant increase in peak 2 (p value =0.13) and decrease in peak 3 (p value =0.089). It is important to note that these differences were not previously predicted but found by calculating the p value between the A and B group for each peak. Further investigation would be required to determine whether they are real or simply the result of fishing for difference.

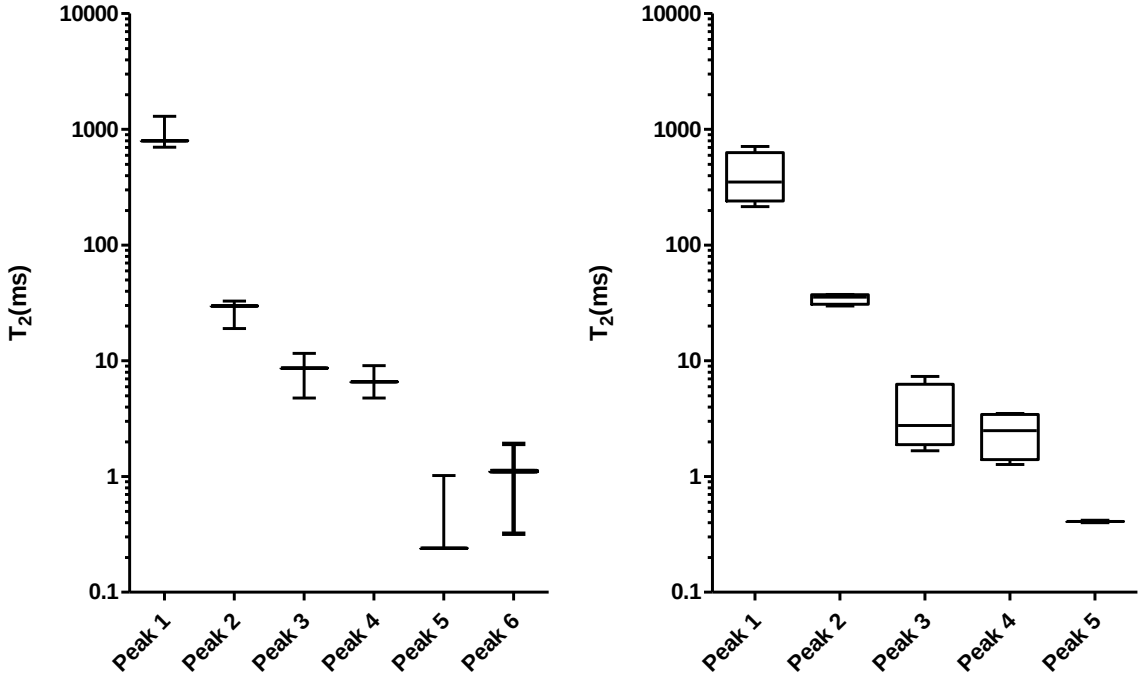

Figure 4.6 Boxplots of the peak positions in T_2 of the peaks obtained from T_1-T_2 relaxometry performed at 100 MHz on samples of human articular knee cartilage extracted during total knee replacement (TKR) due to osteoarthritic nature of tissue. This disease group referred to as group A is to the left and contains 3 samples. The disease group referred to as B is to the right and contains 4 samples.

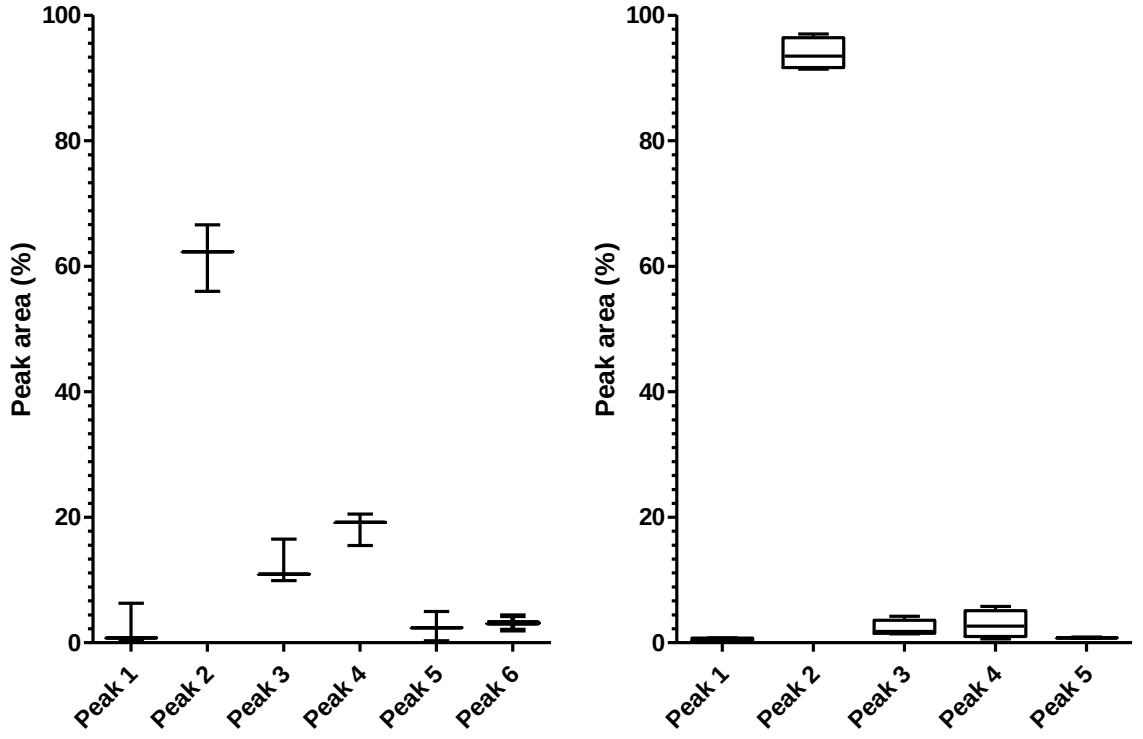

Figure 4.7 Boxplots of the peak areas of the peaks obtained from T_1-T_2 relaxometry performed at 100 MHz on samples of human articular knee cartilage extracted during total knee replacement (TKR) due to osteoarthritic nature of tissue. This disease group referred to as group A is to the left and contains 3 samples. The disease group referred to as B is to the right and contains 4 samples.

Figure 4.7 directly compares the peak areas for the two arthritic groups A and B. We see clearly the significant differences in peaks 2, 3 and 4 (p values of 0.00011, 0.0030 and 0.00035 respectively). The other peaks show no significant difference.

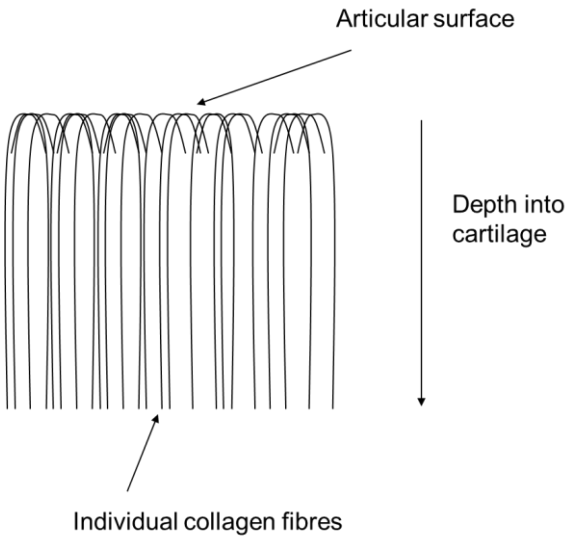

Figure 4.8 A basic diagram of the macroscopic arrangement of collagen fibres in articular knee cartilage tissue

The main constituents of cartilage are collagen, water and proteoglycans. As shown in Figure 4.8, the collagen fibres form a macroscopic matrix varying in arrangement dependant on depth into the articular surface. To aid in peak assignment, samples of collagen and proteoglycan were obtained and restored to 60-70% hydration as is typical in articular cartilage[100] . Figure 4.9 and Figure 4.10 show the T_1 - T_2 spectra of collagen and proteoglycan.

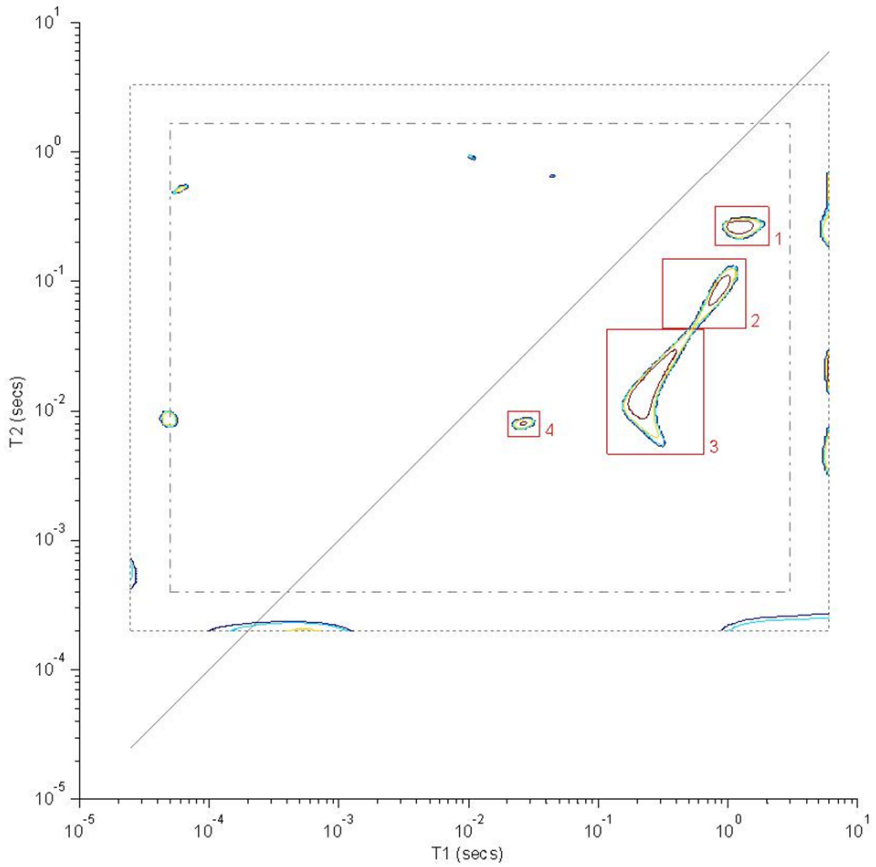

Figure 4.9 The T_1 - T_2 relaxation spectrum of collagen acquired at 100 MHz. The collagen was delivered dry and rehydrated to 60-70% with deionised water in order to correspond to biologically present hydration levels [100]

As can be seen, collagen has no peaks below a T_2 of 10 ms, probably because its more rigid fibrous structure gives non-exchanging CH proton relaxation times of only a few hundred microseconds, which is lower than the tau value (the CPMG echo spacing), which would prevent them showing on this spectrum[27].

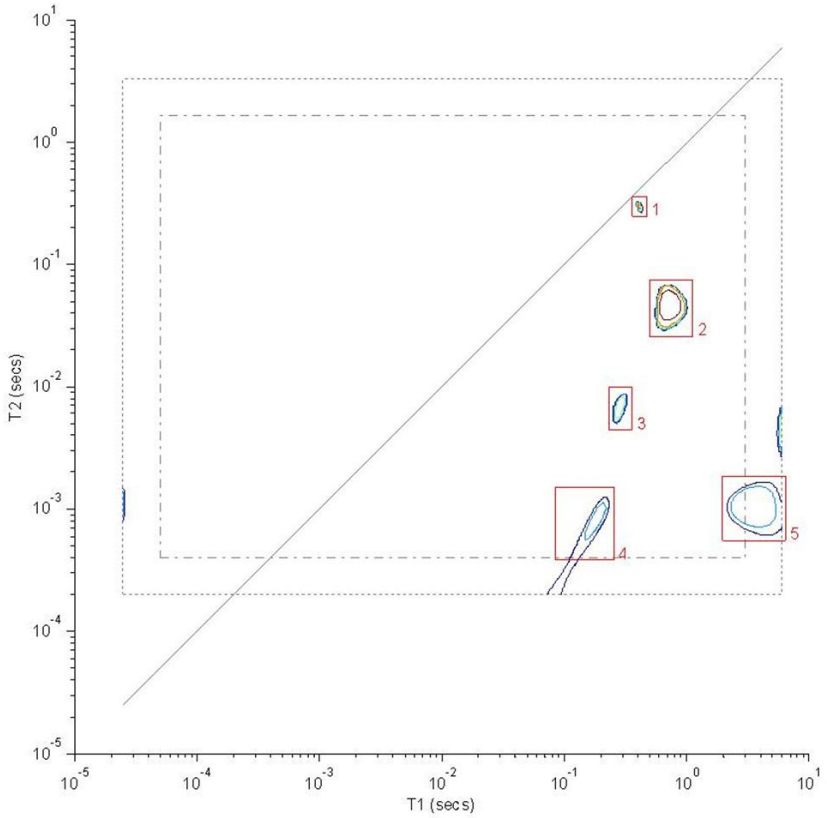

Figure 4.10 The T_1 - T_2 relaxation spectrum of proteoglycan acquired at 100 MHz. The proteoglycan was delivered dry and rehydrated to 60-70% with deionised water in order to correspond to biologically present hydration levels (*100*)

As the proteoglycan (Figure 4.10) is a more flexible hydrophilic molecule, its non exchanging CH values lie closer to those for mobile proteins and therefore give characteristic peak T_2s of about 10 ms. As has been previously noted, the relative water peak of the diseased samples seems to fall into two groups at either ~90% or ~60% both of which differ from the healthy average of ~84%. Work done elsewhere on the binding of water in cartilage has shown that a decrease in proteoglycan is associated with a 9% rise in water content, which would seem consistent with one group of samples but not the other. Again, this is an area which warrants further inquiry into possible reasons for this result. T_2-store-T_2 examination of human articular knee cartilage can provide further insight into possible peak assignments. The T_2-store-T_2 sequence allows the identification of additional exchange cross peaks due to magnetisation transfer between different proton pools. On a T_2-store-T_2 spectrum the standard peaks from the T_1 - T_2 spectrum are projected onto the diagonal between the two axes and when the store time is comparable to the exchange lifetime between two peaks, two cross correlation peaks appear off the diagonal at the same T_1 and T_2 as the true peaks, forming a square. This allows these exchange rates to be estimated.

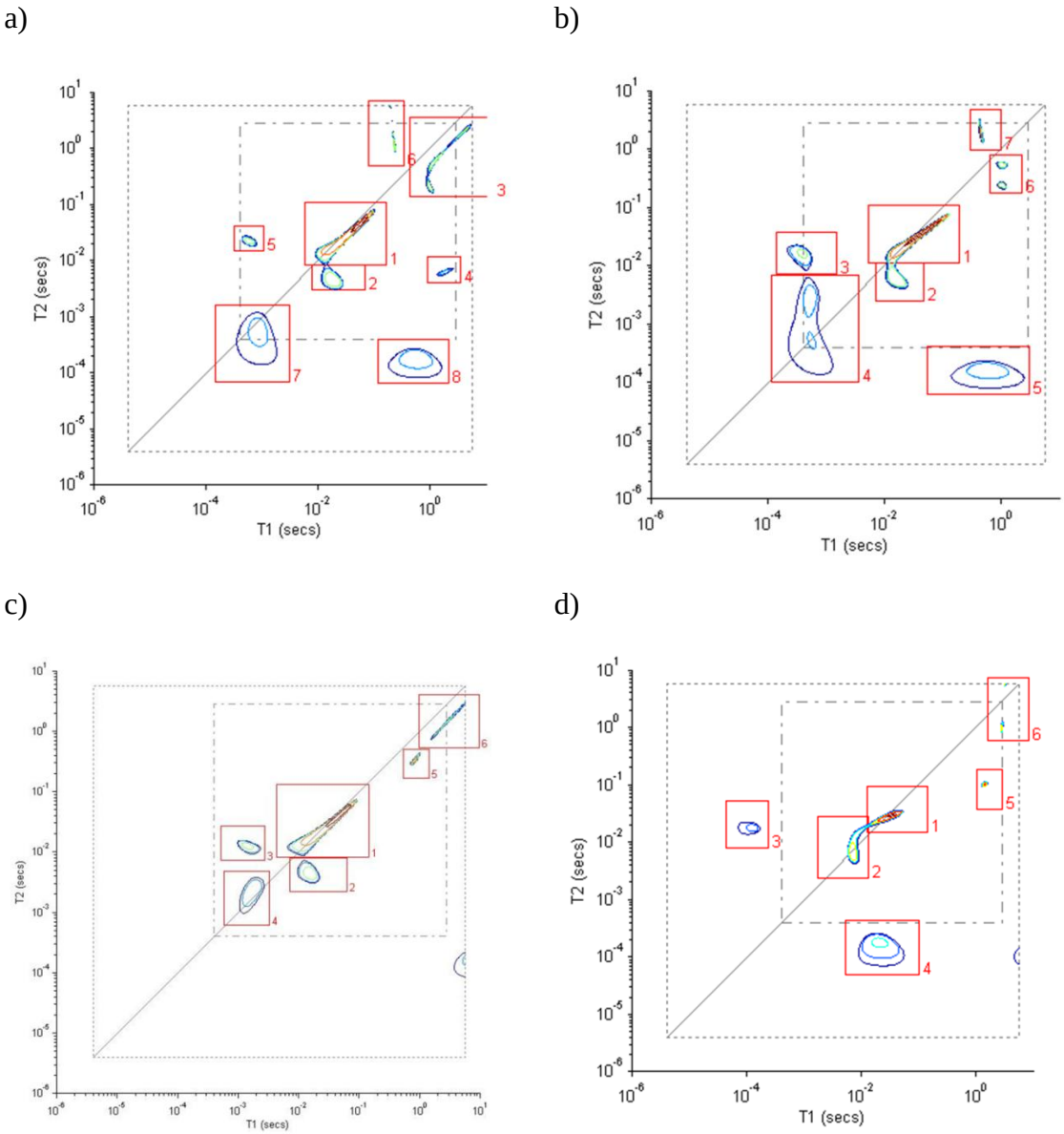

Figure 4.11 The T_2 - T_2 relaxation spectrum of osteoarthritic human articular knee cartilage acquired using the T_2-store-T_2 method at 100 MHz, using a store time of a) 500 µs b) 2 ms c) 12 ms d) 50 ms. Peaks on the diagonal are real peaks originating from proton pools visible on a T_1-T_2 relaxation spectrum. Peaks off the diagonal are the additional exchange cross peaks due to magnetisation transfer between different proton pools[58]. Axis labels are auto-generated by in house software but should read T2 (secs) on both axes.

Figure 4.11 a to d (acquired at 500 µs, 2 ms, 12 ms and 50 ms) show the T_2-store-T_2 spectra of diseased human cartilage acquired at 100 MHz showing the waning and waxing of cross peaks at different store times. Closer examination of Figure 4.11c showing the spectrum acquired at a store time of 12 ms gives us some additional information about our sample. Peaks 2 and 3 from Figure 4.1 and Figure 4.4 are close enough that they are superimposed into a single peak on the T_2-store-T_2 spectrum, labelled as peak 1. In Figure 4.11c cross peaks appear between peak 4 at ~1 ms and the combined peak 1. It is unlikely

that direct proton magnetisation exchange would take place between two different biopolymers so it is likely that one of the two peaks combined into peak one originates from compartmentalised water. Of the two, that labelled as peak 4 in Figure 4.1 has the longest T_1 and can be provisionally assigned to water in the proteoglycan gel matrix. This would then leave peak 3 as most likely originating from non-exchanging CH protons in the flexible proteoglycan molecules.

4.3.3 Healthy human articular knee cartilage at 23.4 MHz

As mentioned in the introduction to this chapter, T_1 and T_2 are frequency dependant so to fully characterise a tissue and optimise the ability to compare and contrast we examine tissue at different spectrometer frequency. Here, tissue is examined at the lower frequency of 23.4 MHz.

At 100 MHz the sample required is approximately 1 cm in length filling a tube with a 5 mm diameter. This requires that the volume of sample for use in the 5 mm horizontal sample tube of the 100 MHz spectrometer is $\pi r^2 h = \approx 0.2\ cm^3$ where r is the radius (0.25 cm) and h the sample length (1 cm). For the 23.4 MHz spectrometer with its 10 mm vertical sample tube the sample must again be approximately 1 cm long so, ignoring the curved tube base, the required sample volume is $\pi r^2 h \approx 0.79\ cm^3$ where r is the radius (0.5 cm) and h the sample length (1 cm). In reality this sample is slightly smaller than is ideal, so a sample of $\approx 1\ cm^3$ is preferred. The larger sample size necessary for use in the 23.4 MHz scanner means that not every surgical extraction would provide enough high quality homogenous cartilage tissue to make up a usable sample. The 23.4 MHz spectrometer also has reduced signal to noise ratio (SNR) due in large part to the inherent reduction in SNR at reduced spectrometer frequency, meaning some data was unusably noisy. As a result, only 4 healthy and 4 diseased samples are presented at this lower frequency and the division in the peak intensities within the diseased group shown at 100 MHz can not be reproduced with the current data set at 23.4 MHz. One sample displays the decreased main peak (62.6%) and increased minor peaks present in arthritic group A, the other three having arthritic group B's higher main peak (mean = 96.9%) values but without further repetition no conclusion can currently be drawn as to the reality of these separate groups at 23.4 MHz.

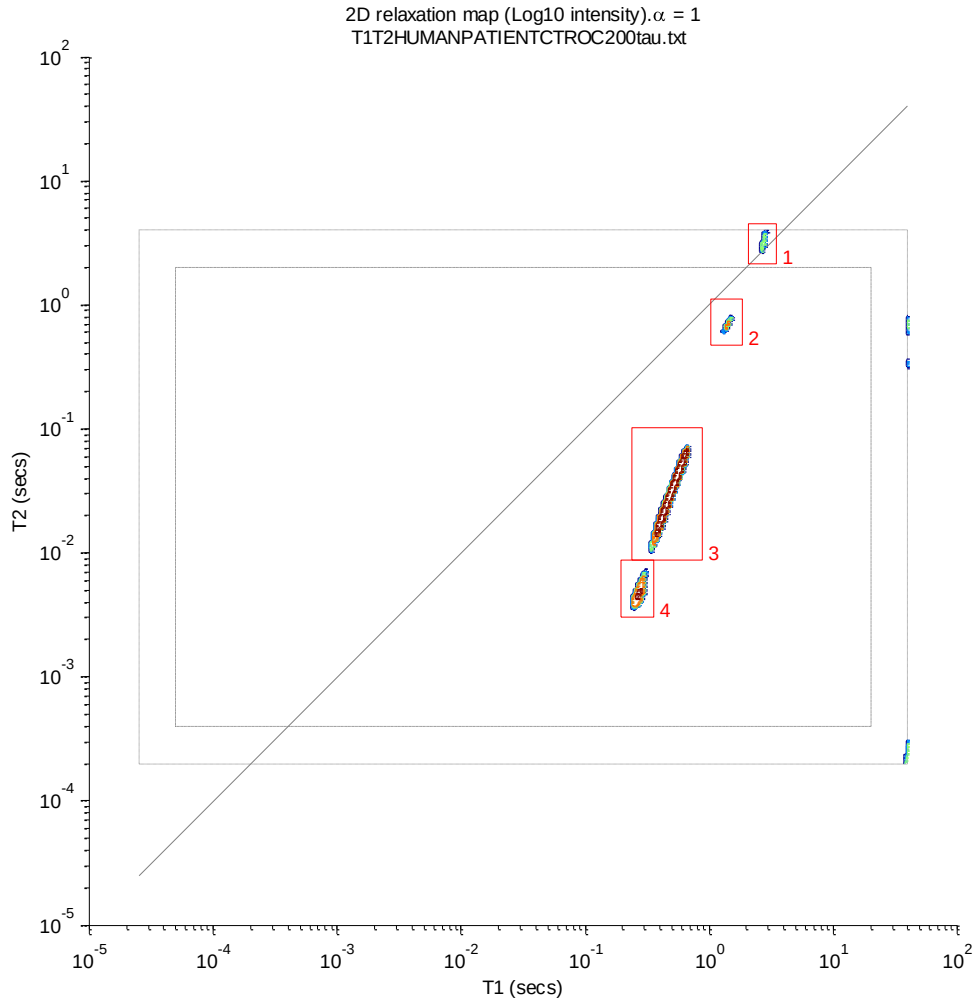

Figure 4.12 Characteristic T_1 - T_2 spectrum of a healthy human articular knee cartilage sample, taken at 23.4 MHz with a tau of 200 µs with 4 marked peaks. On one spectrum in the healthy group peaks 3 and 4 are amalgamated into a single longer peak covering the area of both. The area of this peak is not included in calculations of the mean peak areas, etc. It should be noted that the peak intensity of this combined peak is of equivalent peak intensity to the total area of both peaks (3 and 4).

Figure 4.12 shows a characteristic T_1 - T_2 spectrum of a healthy cartilage sample acquired at 23.4 MHz with a tau value of 200 µs. Comparing with Figure 4.1, the same tissue spectrum acquired at 100 MHz, we see that peaks 1 and 2 in the 23.4 MHz spectrum both fall within the range of values of peak 1 in the 100 MHz spectrum. Table 4.2 compares the mean values of peak area, T_1 and T_2 for tissue at each spectrometer frequency. Here we see that the mean values for peak 1 at 100 MHz seem to match better with peak 2 at 23.4 MHz but comparing the range of values for each, shown in Figure 4.2 and Figure 4.13, appears to confirm the conclusion from visual comparison of the spectra in Figure 4.1 and Figure 4.12 that both peaks at 23.4 MHz are contained within peak 1 at 100 MHz. Their long T_1 and T_2 relaxation times are suggestive of something close to bulk water.

Peak no.		Area (%) (std. dev)		T_1 (ms) (std. dev)		T_2 (ms) (std. dev)	
100 MHz	23.4 MHz	100 Mhz	23.4 Mhz	100 Mhz	23.4 Mhz	100 Mhz	23.4 Mhz
-	1		2.6 (2.1)		2480 (460)		1910 (1000)
1	2	1.08 (1.6)	1.4 (0.5)	1230 (870)	1340 (430)	671 (780)	316 (240)
2	3	85.0 (3.4)	80 (5.1)	866 (88)	499 (80)	34.2 (17)	35.5 (12.43)
3	4	7.7 (1.4)	15 (1.9)	364 (83)	235 (28)	4.90 (0.97)	5.28 (0.8)
4	-	4.43 (0.95)		3100 (187)		3.71 (2.5)	
5	-	1.73 (0.12)		176 (20)		0.203 (0.005)	

Table 4.2 Mean values of peak area, T_1 and T_2 for healthy articular cartilage at 100MHz and 23.4MHz spectrometer frequency. Numbered peaks are aligned to indicate likely peak matches based on all three parameters. Standard deviation given in brackets next to mean value.

Peak 2 at 100 MHz and peak 3 at 23.4 MHz seem consistent (at 85% and 80% respectively) and arise due to water in the sample. Peak 4 at 23.4 MHz appears to correspond to peak 3 at 100 MHz. This peak has not currently been assigned with certainty but analysis of the T_2-store-T_2 spectra in Figure 4.11 in the previous section suggested that this peak most likely originates from non-exchanging CH protons in the flexible proteoglycan molecules of the cartilage.

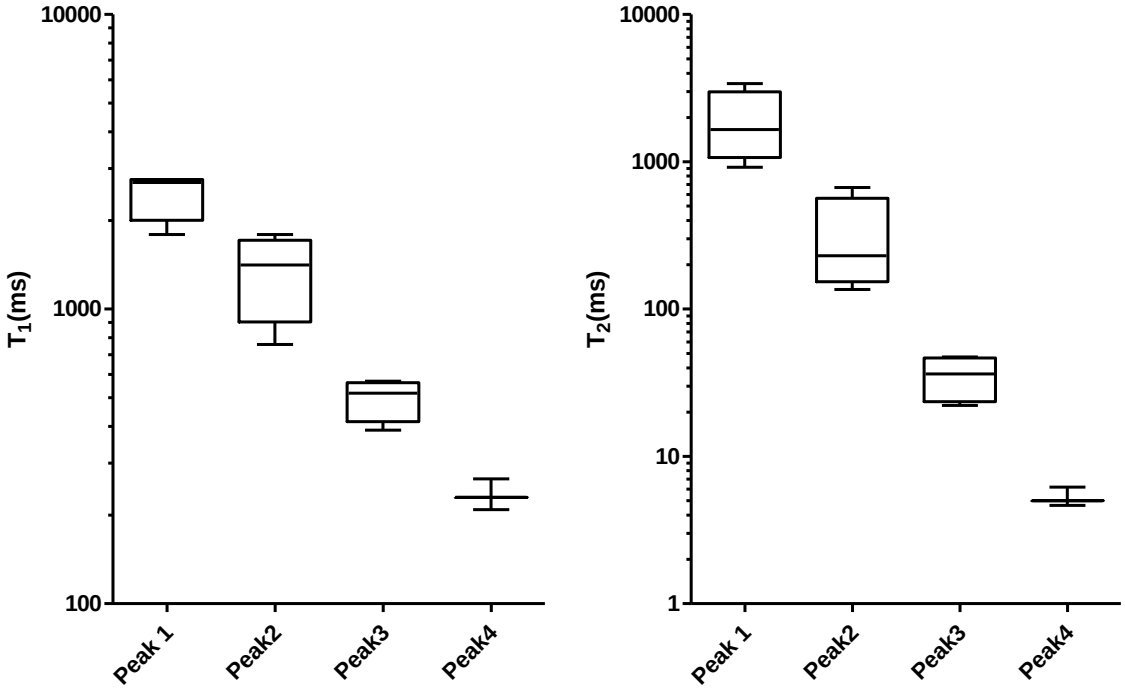

Figure 4.13 Boxplots of the peak positions in T_1(left) and T_2(right) of the 4 peaks obtained from T_1-T_2 relaxometry performed at 23.4 MHz on 4 samples of healthy articular cartilage, demonstrating the consistency in peak positions.

Figure 4.13 shows the T_1 and T_2 peak positions of the 4 healthy sample spectra acquired at 23.4 MHz. The ranges of peaks 1 and 2 do not overlap but do meet. As previously discussed they cover the same range as peak 1 in the 100 MHz spectra and likely originate from the same source. There is significantly less variation in peaks 3 and 4. Figure 4.14 shows the peak areas of each peak, showing the consistency between them. As is typical in biological tissue, the spectrum is dominated by the main peak, here labelled peak 3, representing water contained in the tissue.

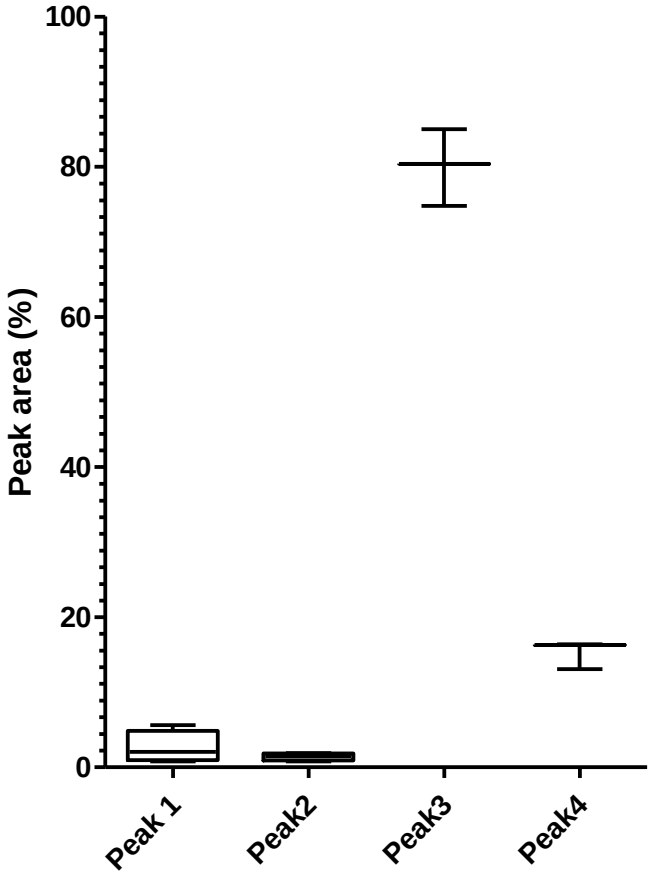

Figure 4.14 Boxplot of the peak areas, as a percentage of the total peak marked intensity, of the 4 peaks obtained from T_1-T_2 relaxometry performed at 23.4 MHz on 4 samples of healthy human articular cartilage, demonstrating the consistency in peak areas.

4.3.4 Osteoarthritic human articular knee cartilage at 23.4 MHz

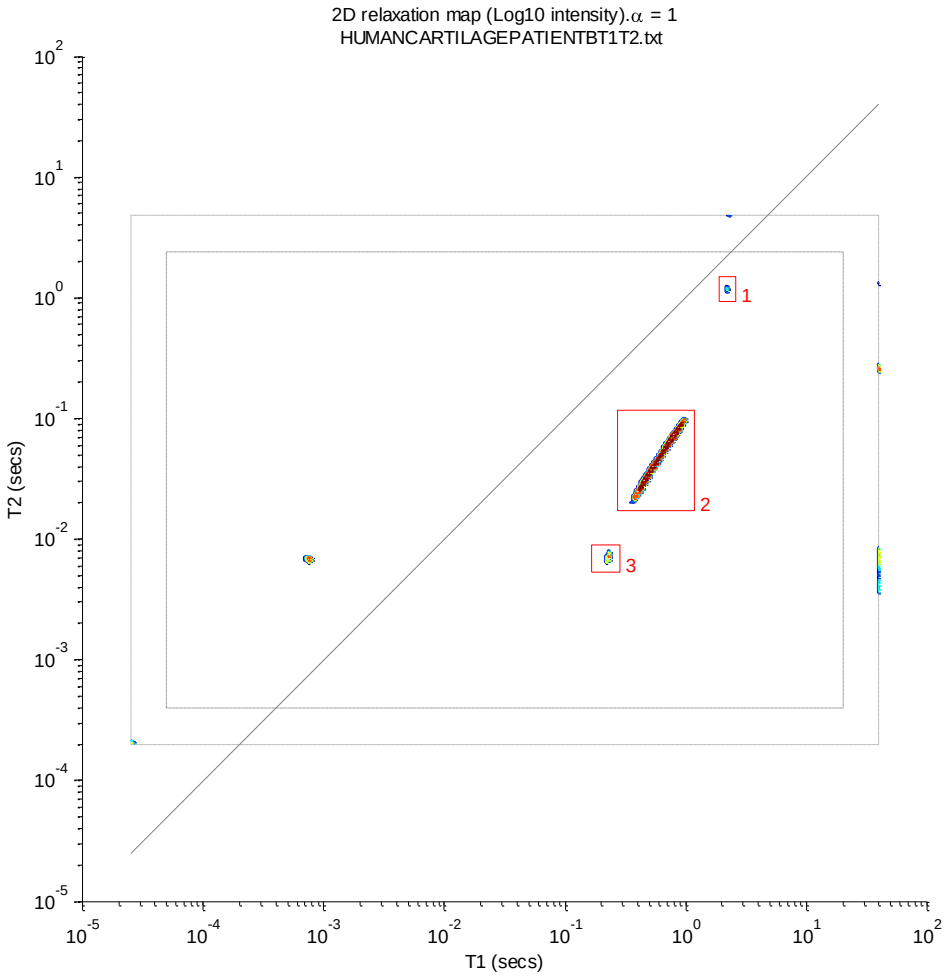

Figure 4.15 Characteristic T_1 - T_2 spectrum of an osteoarthritic human articular knee cartilage sample, taken at 23.4 MHz with a tau of 200 µs with 3 marked peaks. On one spectrum in the diseased group peaks 2 and 3 are amalgamated into a single longer peak covering the area of both. The area of this combined peak is of equivalent peak intensity to the total area of both peaks (2 and 3) in the other spectra (mean = 97.38% std. dev. = 3.08%).

Figure 4.15 shows a characteristic T_1 - T_2 spectrum of an osteoarthritic human articular knee sample taken at 23.4 MHz. Only three peaks are visible in the diseased cartilage spectrum which, comparing with Figure 4.4, appear to correspond well with peaks 1, 2 and 3 in the 100 MHz spectra, although peak areas suggest that peak 3 at 23.4 MHz may in fact be made up of peaks 3 and 4 at 100 MHz. This attempted peak matching can be seen in Table 4.3. Only 3 of the 4 available spectra have been used in Table 4.3 to calculate the mean values for diseased cartilage at 23.4 MHz. These values are then compared to the diseased group labelled B in the 100 MHz analysis. This is because 1 sample has drastically different peak areas fitting well with the expected values for the diseased group A at 100 MHz, while the rest fit well with the expected values of group B.

Peak		Area (%) (std. dev)		T_1 (ms) (std. dev)		T_2 (ms) (std. dev)	
100 MHz-B	23.4 MHz	100 MHz-B	23 Mhz	100 MHz-B	23 Mhz	100 MHz-B	23 Mhz
1	1	0.5 (0.25)	0.13 (0.06)	1380 (280)	1990 (630)	407 (210)	1080 (350)
2	2	93.9 (2.5)	96.9 (3.6)	922 (68)	579 (190)	34.5 (3.6)	46.5 (23)
3	3	2.3 (1.3)	4.5 (3.5)	257 (61)	247 (25)	3.64 (2.5)	7.55 (0.58)
4		2.9 (2.2)		2220 (1200)		2.44 (1.1)	
5		0.8 (0.14)		145 (6.6)		0.41 (0.014)	

Table 4.3 Mean values of peak area, T_1 and T_2 for osteoarthritic human articular knee cartilage at 100 MHz and 23.4 MHz spectrometer frequency. Only the results for diseased group B are included in the 100 MHz numbers as this seems the most likely match for the 23.4 MHz results. Numbered peaks are aligned to indicate likely peak matches based on peak area, T_1 and T_2 parameters. Standard deviation given in brackets next to mean value.

While this is indicative of the presence of the 2 groups, A and B, at 23.4 MHz as well as 100 MHz, 1 spectrum is insufficient to confirm the presence of group A with any certainty. This spectrum is included in Table 4.4 along with the mean values for diseased group A for comparison but is not included in Figure 4.16 or Figure 4.17 showing the range of peak areas and positions at 23.4 MHz.

Peak		Area (%) (std. dev)		T_1 (ms) (std. dev)		T_2 (ms) (std. dev)	
100 MHz-A	23.4 MHz	100 MHz-A	23 Mhz	100 MHz-A	23 Mhz	100 MHz-A	23 Mhz
1	1	2.47 (3.3)	1.2	3030 (640)	1410	931 (320)	48.9
2	2	61.6 (5.3)	62.6	811 (79)	407	27.2 (7.2)	19.7
3	3	12.4 (3.6)	36.3	166 (46)	278	8.34 (3.4)	7.14
4		18.4 (2.6)		1390 (38)		6.81 (2.2)	
5		2.57 (2.4)		161 (110)		0.50 (0.45)	
6		3.15 (1.6)		1470 (840)		1.12 (1.1)	

Table 4.4 Mean values of peak area, T_1 and T_2 for diseased group A from samples of osteoarthritic human articular knee cartilage at 100 MHz spectrometer frequency. Standard deviation given in brackets next to mean value.Only the results for a single osteoarthritic sample spectrum at 23.4 MHz are shown. This sample is thought to correspond with diseased group A at 100 MHz but cannot be assigned with confidence using the available data set. Standard deviation given in brackets next to mean value.

Figure 4.16 shows the T_1 and T_2 peak positions of the 3 osteoarthritic human articular knee cartilage sample spectra acquired at 23.4 MHz. As discussed, the ranges do not include the values for the single spectrum which appears to correlate with group A in the diseased sample spectra taken at 100 MHz. Excluding this spectrum, there is minimal variation in any of the visible peaks. Figure 4.17 shows the peak areas of each peak, showing the consistency between them. As is typical in biological tissue, the spectrum is dominated by the main peak, here labelled peak 2, representing water contained in the tissue. Again, only peaks from the three consistent spectra are shown.

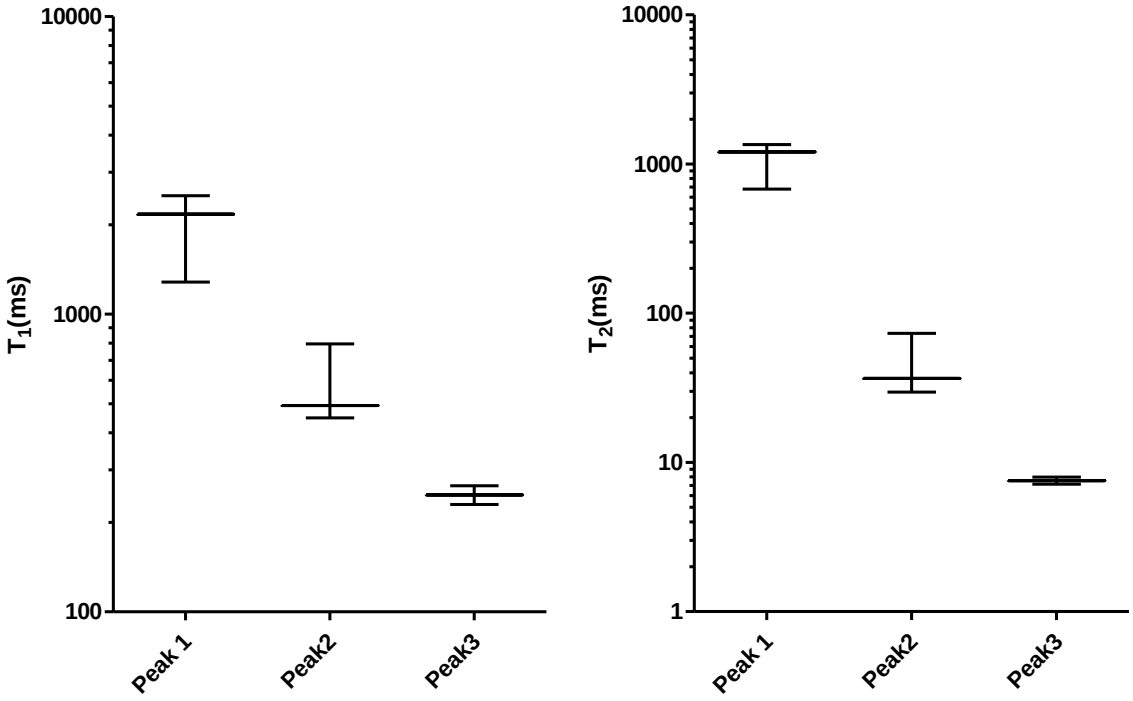

Figure 4.16 Boxplots of the peak positions in T_1(left) and T_2(right) of the 3 peaks obtained from T_1-T_2 relaxometry performed at 23.4 MHz on 3 samples of osteoarthritic articular cartilage, demonstrating the consistency in peak positions.

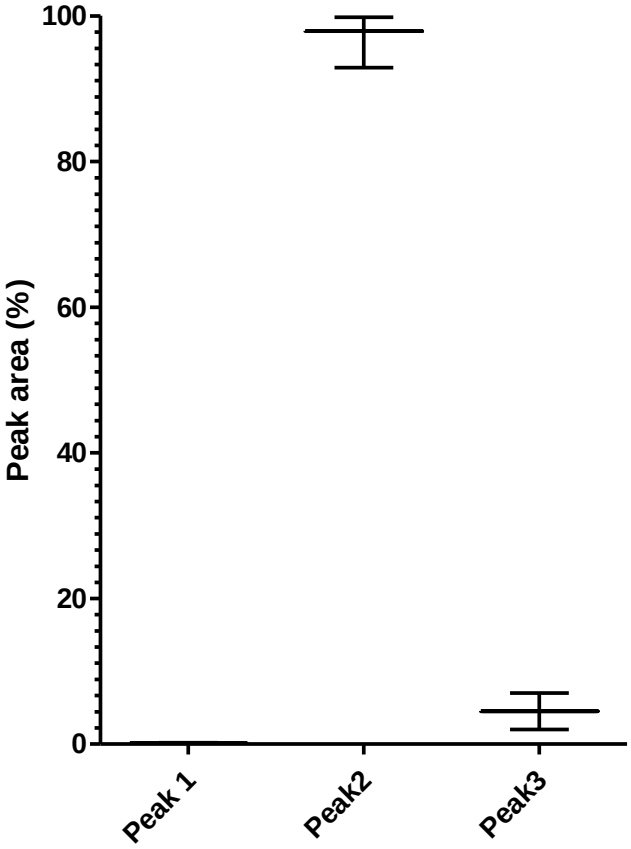

Figure 4.17 Boxplot of the peak areas, as a percentage of the total peak marked intensity, of the 3 peaks obtained from T_1-T_2 relaxometry performed at 23.4 MHz on 3 samples of diseased human articular cartilage, demonstrating the consistency in peak areas. The values of peak 1 are hard to see as they do not rise above 0.2%.

4.5 Discussion

Carballido-Gamio et al[101] gathered maps of T_2 and $T_{1\rho}$ (discussed in chapter 7) from 6 people but only to create a library of these and other characteristic parameters for comparison to other tissues for use in examining the changes which occur in osteoarthritis. As with other papers in this area, only an average T_2 value was gathered from each voxel. Another paper by Carballido-Gamio et al[102] gathered specific T_2 values (although still a single value). Their results gave values of 28.38 ± 2.66 ms for healthy and 34.78 ± 8.36 ms for arthritic tissue. The value would likely be dominated by the peak marked as peak 2 in the T_1 - T_2 relaxation spectrum (Figure 4.1) which has an intensity of 85.0% (std. dev. = 3.4) and a mean T_2 of 34 ms (std. dev. = 17) in healthy tissue. In osteoarthritic tissue group B, the intensity has risen to 93.9% (std. dev. = 2.5) but retains a T_2 value of 34.5 ms (std. dev. = 3.6). I would propose that the reason for the reduced average T_2 found in their healthy samples, is due to the influence of peaks 3 and 4 in Figure 4.1. In healthy tissue the average is reduced by these peaks which have relative intensities of 7.7% (std. dev. = 1.4) and 4.43% (std. dev. = 0.95) as they have lower T_2 values and would therefore lower the average single value T_2 given in the paper. In the osteoarthritic group however the main peak completely dominates the spectrum meaning that the average single value of the tissue would rise to ≈34 ms, that of the main peak. This corresponds well to the values found in the Carballido-Gamio et al[102] study.

A recent review by Binks et al[103] examines the use of quantitative MRI and relaxometry in articular cartilage. Within it was discussed a paper by Nissi et al[104] in which they correlated the mechanical properties of cartilage and its T_1 and T_2 values. As with most studies in this area, only single T_1 and T_2 values are acquired for each voxel examined so full characterisation of the tissue is not achieved. A paper by Julkunen et al[105] indicates that the reason for the observed correlation between mechanical properties and T_2 may lie with proteoglycan content rather than collagen architecture. Again, the study attempted to characterise articular cartilage and did so with excellent spatial resolution but not the spectral resolution available with 2D T_1 - T_2 relaxation. A study by Wiener et al[106] correlated depth of cartilage with changing T_1 value and gave specific values for different regions of the cartilage in the knee. The dominant peak 2 in the T_1 - T_2 relaxation spectrum of healthy cartilage (Figure 4.1) gave a T_1 of 866 ms (std. dev. = 88) which is significantly

higher than those found in the Wiener study (between 702 ± 68 ms and 594 ± 74 ms). Difference in T_1 is correlated to change in proteoglycan levels here which would make sense with the 2D data acquired in this thesis, assuming that the higher T_1 of peak 2 is reduced by the lower T_1 peaks to give the average T_1 found in the study[106]. Variation in the quantity of proteoglycan, thus the amount by which the average value is shifted, would then account for the varying single T_1s found in different cartilage regions.

The same review[103] then separately discusses T_2 which further highlights the current state of research, dealing almost exclusively with single separate values of T_1 and T_2. Having discussed the work by Carballido-Gamio et al[101, 102], further work is addressed conducted by Dunn et al[107]. In the Dunn study, cartilage was assigned a single T_2 value of 32.1 ms to 35 ms in healthy subjects and 34.4 ms to 41.0 ms in arthritic patients. For the same reasons as with the Carballido-Gamio et al[102] work these values fit well with values obtained within this thesis, although it should be noted that the values found by Dunn are slightly higher than both those presented here and those reported in that paper[102]. Another paper by Stehling et al[108] showed even higher T_2 values in middle aged subjects (45-55 years old) and identified variation based on levels of physical activity (45.8 ± 3.93 ms in sedentary subjects and 48.7 ± 4.35 ms in active subjects). Active subjects were found to exhibit far more damage in the form of cartilage abnormalities. This lends credence to the idea that a rise in average T_2, correlates with various forms of damage, both activity induced and osteoarthritic. As discussed before this may be due to the loss of substances such as proteoglycan which are responsible for the smaller peaks in the T_1 - T_2 relaxation spectrum.

By comparison with similar studies it would appear that the loss of proteoglycan, which is likely the cause of peaks marked as 3 and 4 in the T_1 - T_2 relaxation spectrum (Figure 4.1), can be associated with an increase in single average tissue T_2 values. A mechanism for this reduction, by reduction of the influence of peaks 3 and 4, is here proposed as a possible reason for this decrease in T_2. Further work would be useful to clarify the situation by acquiring more T_1 - T_2 relaxation spectra, potentially shifting 2D relaxometry to be performed in vivo (discussed further in chapter 7).

4.4 Conclusions

T_1 - T_2 relaxometry shows promise as a technique for distinguishing clinical biomarkers for use in examination of osteoarthritic articular knee cartilage. As shown in Table 4.1, distinction can be made between healthy and diseased cartilage at 100 MHz using the intensities of the 3 main peaks. It even seems to have shown a difference in disease states within the osteoarthritic group. This differentiable disease state may be replicated at 23.4 MHz but further work would be required to establish this. P values for comparisons of the main peak, demonstrating that the healthy, diseased A and diseased B groups are separate populations are included in Table 4.5. There is clearly a significant difference (p-value ≤ 0.05) between each of the groups.

Tissues compared at 100 MHz		P value
Healthy	Diseased A	<0.01
Healthy	Diseased B	<0.01
Diseased A	Diseased B	<0.01

Table 4.5 The p value for comparisons between the main peak area of the 3 distinguishable tissue types found by T_1 - T_2 relaxometry of human articular knee cartilage samples at a spectrometer frequency of 100 MHz

This work suggests that T_1 - T_2 relaxometry has potential in differentiating other tissues in diseased and healthy states, although this would need to be further examined and require 2D T_1 - T_2 relaxation studies of each tissue in each disease state. Not all tissues which require differentiation will necessarily have a single clearly defined difference in a single parameter. Principal component analysis (PCA)[89-91] could allow differentiable tissue states in less clearly segregated sets of spectra by including the peak area, T_1 and T_2 of all the conserved peaks. In essence, principal component analysis converts data with many possibly variables into just a few linearly uncorrelated principal components. When plotted on a 2D x-y plot these principal components may display clustering around certain values, indicating commonalities between those data points within a cluster and differences between those data points in different clusters. Which peaks are chosen will obviously depend on tissue types and conditions being examined. Once differentiable tissue states have been identified, statistical or probabilistic classification methods[86-88] such as the already discussed principal component analysis[89-91] could be used to indicate the tissue type and state from T_1 - T_2 relaxation spectra of unknown tissue samples to aid in medical

diagnosis (e.g. identifying tissue in biopsies).

More general discussion of 2 dimensional relaxometry will be conducted in a chapter 7, but suffice to say the examination of T_1 - T_2 and T_2 - store - T_2 sequences has barely scratched the surface of the information that can be obtained from clinical samples via use of the many 2 dimensional relaxation methods available to the NMR practitioner.

5. Contrast simulation

5.1 Introduction

As has been previously discussed, current clinical practice in MRI tends to focus on high field spectrometers and be based on a best practice method, often established by local staff. Research often focuses on comparisons of a single, newly developed or implemented sequence with the currently established protocol[1-6]. The aim is usually to choose an MRI pulse sequence and sequence parameters that optimise image contrast so that key clinical features can be identified. Contrast in an MRI image is dependent on T_1, T_2, T_{2*} and spin density, all of which feed into the pulse sequence used and the parameter set chosen. Relaxation behaviour is dependent on the tissue being examined and the condition that tissue is in. Most medical studies assume single T_1 and T_2 values for the tissue in question and thus miss out on the more complete characterisation of tissue relaxation behaviour available in 2D T_1 - T_2 relaxation spectra[109]. The information provided by the relaxation spectra must then be used in conjunction with a measure of the effects of specific pulse sequences on the final signal intensity obtained in an MRI examination. The final contrast obtained from a specific tissue with a specific imaging sequence will be dependent on the parameter set used. Varying the time period between radiofrequency pulses in a pulse sequence will affect the final image intensities based on the condition of the spins during these time periods and the tissues spin condition dependent relaxation behaviour.

In this chapter we demonstrate two methods in which 2D relaxation spectra can be used to simulate image contrast and thereby provide an 'in-silico' method for contrast optimisation[110]. The first method implemented was developed entirely within the lab using MATLAB to simulate virtual samples and run a simulation of the effects of a pulse sequence on them. It examines the complete behaviour of a simulated sample of tissue and provides an image of the expected signal output of an MRI scan performed on it with a specific parameter set.

The second method involves a novel use of the ODIN (Object-oriented Development Interface for NMR) platform available to the public. By using a 2D T_1 - T_2 relaxation

spectrum, in place of the simulated sample for which the interface is designed, full sample image information is sacrificed to provide more complete, relaxation based, contrast information about a single simulated voxel of a specific tissue under examination with a specific imaging sequence and parameter set.

5.2 Virtual sample simulation (VSS)

5.2.1 1D Stimulated echo[111]

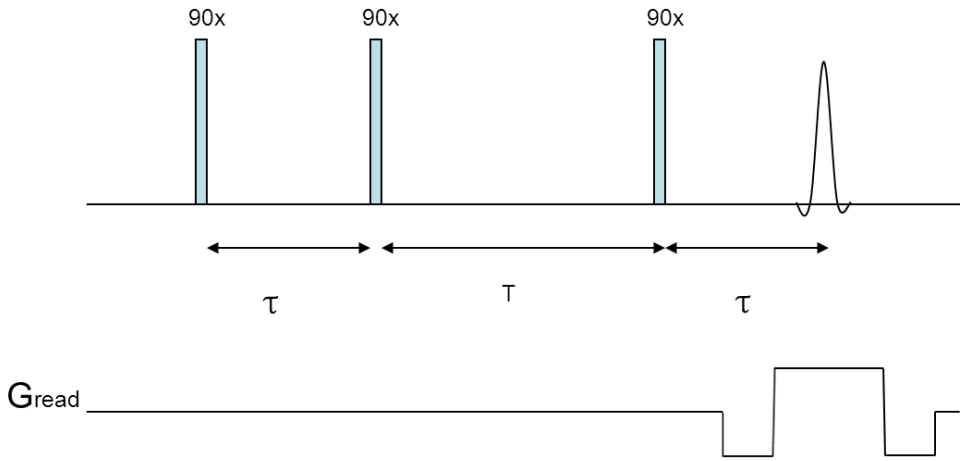

Figure 5.1 Simulated stimulated echo imaging pulse sequence for use with simulated 1D sample. The first 2 90 degree pulses are separated by a time τ as are the final 90 degree pulse and the peak of the acquired echo. The second and third 90 degree pulses are separated by a different time period T.

The first method implemented to examine how relaxation affected image contrast involved the simulation of a virtual sample consisting of virtual voxels with fixed position and an orientable spin. It was therefore called the "Virtual Sample Simulation" (VSS) method. The first pulse sequence simulated with this method was the 1 dimensional stimulated echo imaging sequence with a simulated 1D phantom. The full MATLAB code for this simulation is included with explanation and annotation in appendix 5.2.1. The phantom used in the simulation consisted of a 1D array of voxels containing vectors which could be given any magnitude and orientation required. Relaxation was to be applied according to the full 2D T_1-T_2 relaxation spectrum of one or more tissue types. For efficiency of simulation this information was kept separate from the phantom, to be applied based on a voxels position in the simulated phantom rather than saving the full relaxation behaviour information in each voxel. As can be seen in Figure 5.1 the stimulated echo imaging pulse

sequence begins with the material at equilibrium. The spins are then excited with a 90 degree radio-frequency pulse leaving the magnetisation in the transverse plane. After a time period tau another 90 degree pulse flips the magnetisation back towards the longitudinal axis. After a store time labelled T we use another 90 degree pulse to return the spins to the transverse plane, creating the equivalent of a 180 degree flip using these final two 90 degree pulses. At a time tau after this last pulse the spins will re-phase resulting in the stimulated echo. The received signal can be regarded as a single line of k-space which would normally be multidimensional, were it not for the 1D nature of the simulated sample. This echo in k-space is then Fourier transformed to return the initial phantom sample whose contrast is now weighted by relaxation.

In the simulation each pulse is simulated by affecting the vector in each voxel with a simulated radiofrequency field with set amplitude and for a time, long enough to produce the appropriate rotation, in this case 90 degrees. During the period between pulses each voxel undergoes simulated relaxation. This was achieved by affecting the individual spins in the phantom by transverse or longitudinal relaxation for the correct simulated time and rotating them as they would rotate during free procession, adding a random offset to the standard rate for each spin to simulate T_{2*} effects over the entire phantom. The rate of longitudinal and transverse relaxation is determined by the vectors orientation during the relaxation period and according to the relaxation values for the tissue being simulated, determined by the 2D relaxation spectrum. Imaging sequences require the use of gradients to positionally encode the spins excited by the pulse sequence. In the simulation the 90 degree pulses in the sequence are applied under simulated gradients and shaped as sinc pulses so as to be slice selective. Simulated gradients could also be applied during other periods of rotation as required using a positionally varying offset in the rate of that rotation.

In order to create a simulated phantom consisting of a small sample within our area of interest, a region in the centre of the simulated phantom was filled with voxels of spin intensity 2 and the area to either side with voxels of intensity 0 (shown by the dotted line in Figure 5.2). So as to compare the contrast between two different tissues, the relaxation values applied to the voxels on one half of the sample were set to the those of one tissue type, and the values applied to the other side to those of another. To better approximate the sort of conditions in real life scans, the simulation was run repeatedly using slice selective

simulated pulses so as to only receive signal from a slice of the sample. In the simulation each voxel is affected by the full sequence individually with appropriate transverse and longitudinal relaxation and the final signal is obtained by summing the transverse magnetisation from each voxel. Following Fourier transformation the image profiles obtained from each of the slices can then be reassembled into a final intensity profile for our sample and sequence.

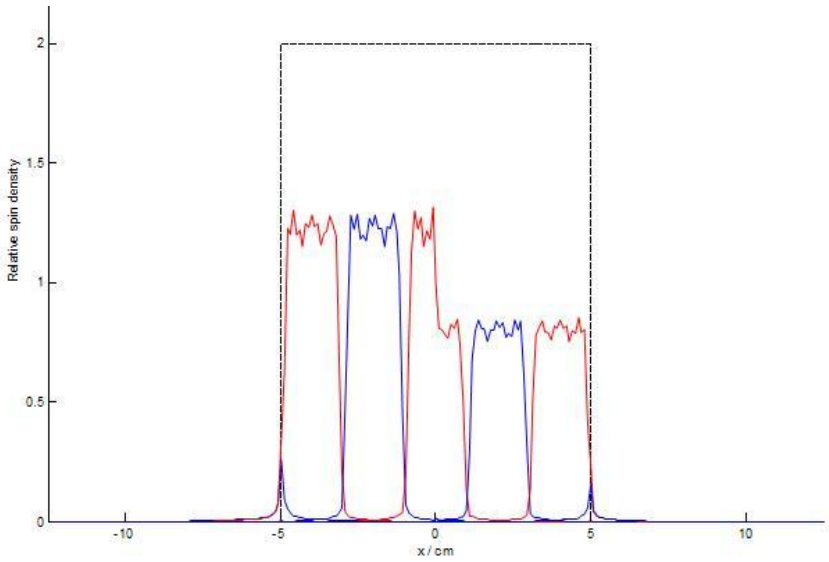

Figure 5.2 1D simulated image. The dotted line shows the position and intensity of the original simulated phantom. The output from simulated slice selective pulses is shown alternating between red and blue. The voxels within the simulated phantom experienced different relaxation behaviours dependent on which side of the phantom they were on, divided in two at 0 on the x axis. The difference in final signal intensity between the two sides is clearly visible, transitioning from one to the other during the central slice. The returned signal intensity is all contained within the region of the original simulated phantom, except for a slight tail either side of the output from each slice selective step, due to it not being a perfect top hat function.

Using conventional relaxation methods utilising only single observed average relaxation times for each voxel, no observable relaxation difference could be obtained, but by using our more information rich 2D relaxation profiles good levels of contrast were shown between different tissues and between similar tissues at different frequencies. Figure 5.2 shows the results of the slice selective pulses, alternating from red to blue. As can be clearly seen, there is no signal outside the area containing simulated spins (shown by the dotted line) other than a trailing off of the waveform within, due to each waveform not being a perfect step function. Within the simulated sample the Fourier transformed simulated echoes generate position accurate slices of intensity with matching values based on which side of the sample, and therefore which simulated tissue, they belong to. In the centre of the sample we see a clear discontinuity within a single slice at the border of the

two tissue types. The values of each side of this discontinuity line up with those of the rest of the sample. For demonstration purposes Figure 5.2 shows the results of one of the more easily delineated tissue pairings, with values of intensity varying from tissue type to tissue type.

Using this simulation output a quantifiable value for the contrast between these two areas of signal intensity can be obtained from the equation below (eq 1.1).

$$C = | I_1 - I_2 | / [I_1 + I_2] \quad \textbf{(eq 5.1)}$$

Where I_1 is the observed final intensity of one tissue type and I_2 is that of the other.

In the simulation the intensities were calculated by taking the average of the Fourier transformed signal across the width of the tissue type within the sample.

Frequency	Tissue 1	Tissue 2	Contrast
100 MHz	Cartilage A (A)	Cartilage B (A)	0.165
23.4 MHz	Cartilage A (A)	Cartilage B (A)	0.173
100 MHz	Cartilage B (A)	Cartilage D (A)	0.098
100 MHz	Cartilage C (H)	Cartilage E (H)	0.003
23.4 MHz	Cartilage C (H)	Cartilage E (H)	0.033
100 MHz	Cartilage C (H)	Cartilage B (A)	0.058
100 MHz	Cartilage E (H)	Cartilage A (A)	0.177
23.4 MHz	Cartilage E (H)	Cartilage A (A)	0.005

Table 5.1 Tissue contrast comparisons performed using the VSS method and using relaxation profiles obtained at 23.4 MHz and 100 MHz. Cartilage labelled as (H) is from the healthy group. Cartilage marked with an (A) is from the arthritic group.

Table 5.1 shows tissue comparisons performed using the VSS method and using relaxation profiles taken at different frequencies, obtained from human cartilage samples. These early comparisons seem to show that there is little intensity difference and therefore contrast (due to relaxation) between different healthy tissue samples (labelled H). The arthritic (labelled A) samples however, have a greater range of intensities leading to a wider range of contrast values both between different arthritic samples and also between the healthy and arthritic groups. As discussed in previous chapters, it is possible that arthritic tissue undergoes various changes during progression of the condition and may be in different stages of degradation upon extraction. It was also noted that the arthritic group seemed to show a noticeable difference in signal intensity between scans taken at 23.4 and 100 MHz while the value of the healthy group remained fairly constant.

5.2.2 Turbo Spin Echo[92, 111-113]

The Turbo Spin Echo (TSE) imaging sequence was the next to be tackled with the VSS method. The full MATLAB code for this simulation is included with explanation and annotation in appendix 5.2.2. The Turbo Spin Echo also called the Fast Spin Echo (FSE) sequence is used in a clinical setting to acquire a 2D image of a slice taken through the sample, often an entire person. The sequence can then be repeated on different slices to produce a 3D map of the entire sample.

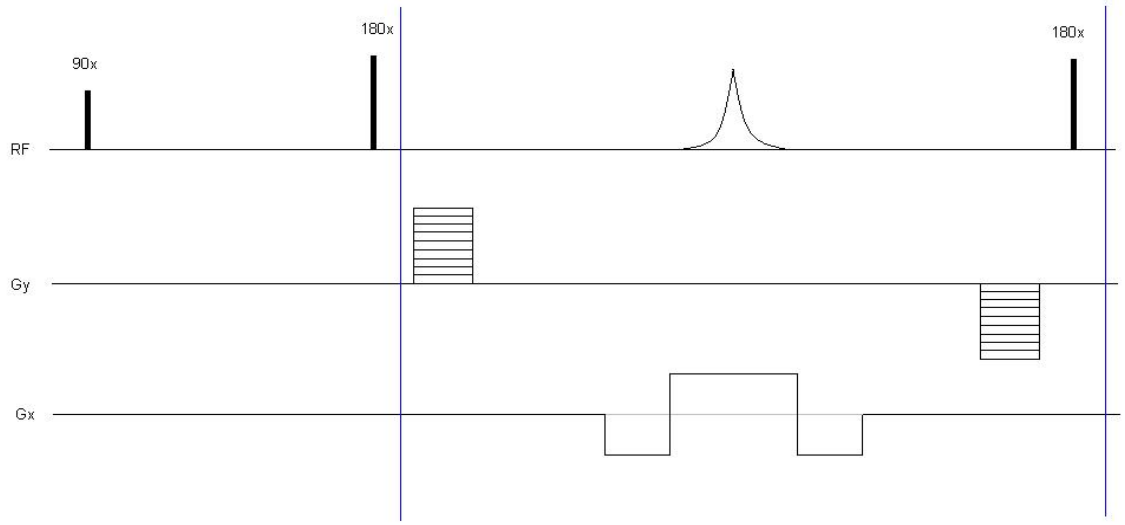

Figure 5.3 The Simulated Turbo-Spin Echo (TSE) or Fast-Spin Echo (FSE)pulse sequence. The section enclosed by blue lines is repeated using different phase encoding gradients to obtain a different line of 2D k-space. The pulse spacing between the 90 degree and 180 degree pulses, as well as that between the 180 degree pulses and the peak of the acquired echo is the same time τ.

The sequence is basically a Hahn echo sequence, but with an additional phase encoding step, as shown in Figure 5.3. This G_y phase encoding alters the line in 2 dimensional k-space[38, 39] represented by the received echo. As previously discussed, k-space is the Fourier transform of the final image. Data acquired is acquired in 2D k-space with dimensions of frequency and phase. The section enclosed by blue lines is repeated with different phase encoding each time to obtain a different line of k-space. This allows many lines of k-space to be filled in with each excitation, increasing the speed of the MRI scan often by as much as 8 times, as there is no longer a need to wait for the sample magnetization to return to equilibrium between every acquired line. The only real limit is the gradual relaxation of the spins over the entire time period of excitation, which is why clinical scans tend to be limited to around 8-10 repetitions per excitation[92, 114, 115],

although greater numbers of excitations can be achieved depending on the tissue being examined and the specific methods used[4, 116, 117]. The 2D k-space built up in this way is then Fourier transformed to return the 2D image of the sample or slice through it.

Using the Stimulated echo simulation as a starting point, the TSE simulation was programmed from scratch, beginning with a Hahn echo and working up to the full sequence. The first results showed that there was a problem with the formation of rotary echoes in the simulation. Rotary echoes are simulation artefacts which arise when the modelled spins are too far apart, so that the applied gradient causes adjacent spins to differ in phase by a full 2π rotation and so re-align. The result is additional echoes that would not occur in real life. This is because in real life the spins are separated by molecular distances whereas, for speed of calculation, the simulation is used with relatively few spins in the examined area. Even simulating a million spins can take 20-40 minutes, but this hardly approaches the numbers actually present, which involve multiples of Avogadro's constant (6.0221415×10^{23} mol^{-1}). To solve this problem a test for rotary echoes was included in the simulation so that it would stop and give the user the chance to change the parameters in the event that they were occurring. The sequence was then tested to see if a reasonable image could be returned from a phantom sample.

a) b)

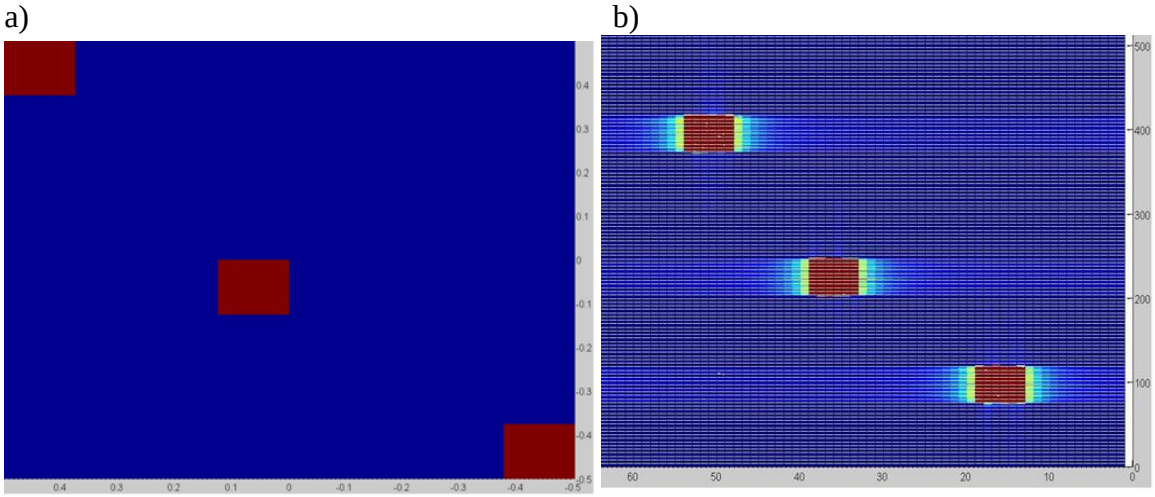

Figure 5.4 (a) A visual representation of a 2D numerical phantom in which the red squares are areas with active spins and the blue region contains no spins. (b) Final simulated image acquired by running the phantom in Figure 5.4a through the VSS TSE simulation. The returned signal intensity varies from high signal intensity (shown in red) to zero signal intensity (shown in blue). As can be seen, the image is a good representation of the original phantom.

Figure 5.4a shows a 2D numerical phantom containing three areas with active spins (red boxes) surrounded by blank regions (blue area). Figure 5.4b shows the final simulated

image profile of the phantom calculated with the simulation, with the intensity of the signal ranging from high (red) to zero (blue). As can be seen, a very good replication of the original phantom is obtained in the final, Fourier transformed signal. Increased resolution can be obtained in the final image by increasing the number of echoes (y resolution) or the number of points taken over each echo (x resolution), but at a cost of an increase in total simulation time.

The above TSE simulation did not include the effects of relaxation in the simulated sample. As has been previously stated, the TSE sequence allows for increased acquisition speed by filling in more than one line of k-space per excitation. In this initial simulation we acquired 128 lines of k-space in a single iteration of the sequence because there is no loss of signal intensity during each repetition of the gradient encoding and acquisition regions of the sequence. In reality relaxation effects cause loss of signal intensity each time and thus, limit the number of gradient encoded steps that can be taken from a single initial excitation. The number of steps taken, and thus lines of k-space acquired, is known as the turbo factor which in this simulation is taken to be 8. This means that for each period of excitation, and subsequent recovery time, we can fill in 8 lines of k-space reducing the total experimental time to approximately one eighth its initial value.

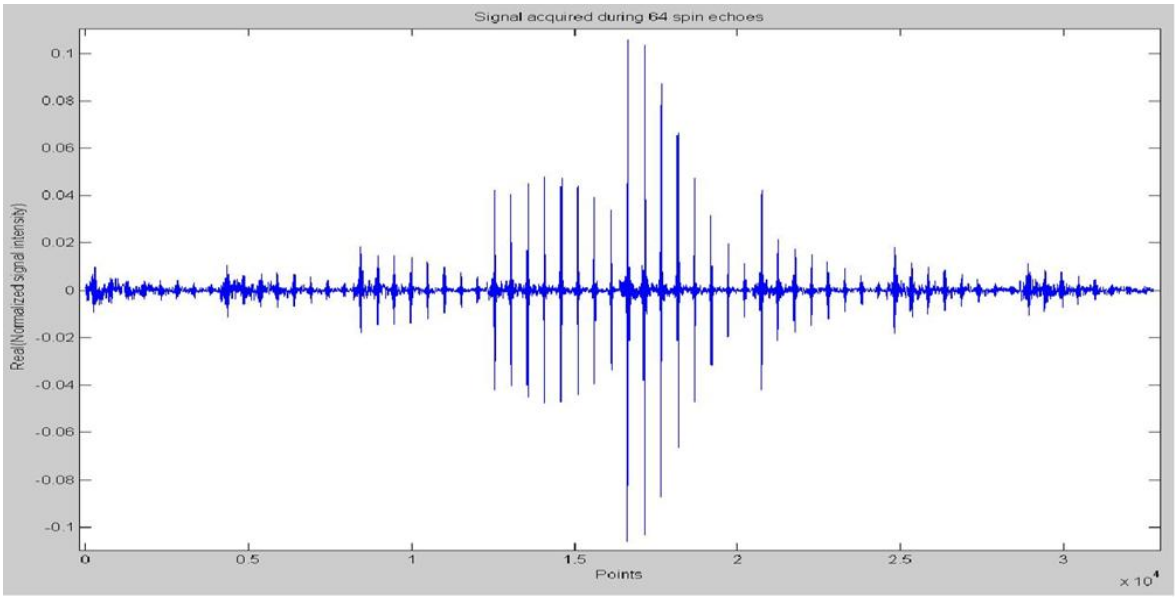

Figure 5.5 Echo train acquired by VSS simulation of a circular phantom containing two tissue types, one with a long and one with a short relaxation time using a turbo factor of 8 to simulate the acquisition of 64 echoes. The lines of k-space are shown end to end in a single dimension, as they would be acquired by the radio frequency coil before being split up and put into a 2D data matrix. This is done so as to observe the effect of the turbo factor. As can be seen, the expected increase in signal intensity towards the centre is present, as well as a tendency for signal intensity to reduce over the course of the 8 echoes within each simulated excitation.

Figure 5.5 shows the train of echoes acquired by simulating a circular phantom containing two tissue types, one half of the circle having a longer relaxation time than the other half. In the echo train the lines of k-space are shown end to end in a single dimension, as they would be acquired in reality by the radio frequency coil before being split up and put into a 2D data matrix. A turbo factor of 8 was used so as to simulate the acquisition of 64 echoes in 8 groups of 8. These groups can be clearly seen as the expected increase in intensity towards the centre of the total experiment has a trend to decrease towards the end of each group superimposed upon it. In order to obtain our initial phantom the signal is processed as before, by separating each individual echo and using it to fill in a line of k-space. This 2D profile is then Fourier transformed to produce the final 2D intensity map of the sample. As can be seen from Figure 5.6 a and b (the same output from a different angle) the circular phantom has been reproduced with high intensity on one side, and low on the other, as we would expect.

a) b)

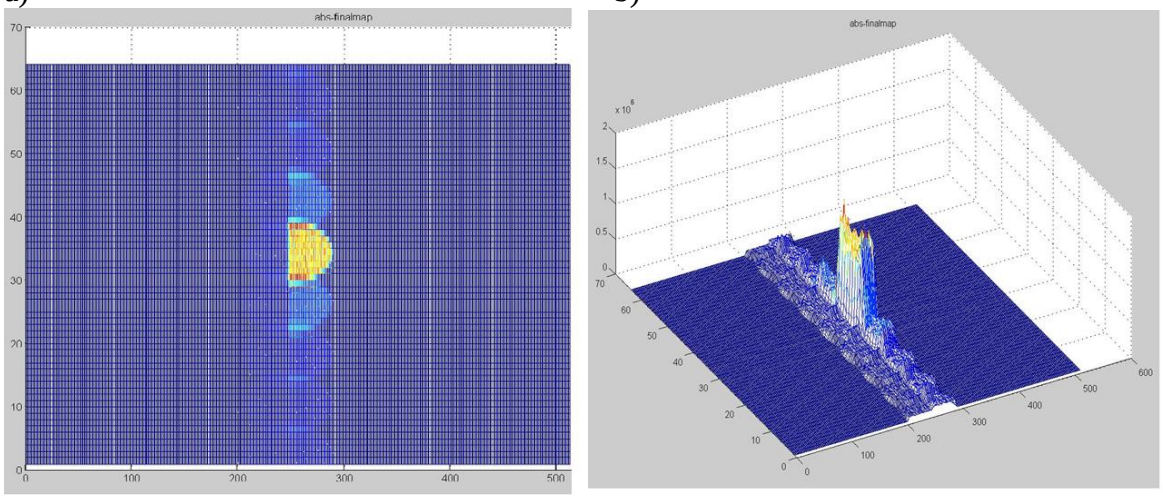

Figure 5.6 The VSS TSE recreated 2D phantom acquired by simulation of a circular phantom containing two tissue types, one with long and one with short relaxation times using a turbo factor of 8 to simulate the acquisition of 64 echoes, viewed from a) above and b) an angle to more clearly show the returned image. A ringing artefact is clearly visible emanating from the true image in the centre along both directions in the frequency dimension.

What might not be expected is the ringing artefact in which lower intensity images of the final sample results are produced emanating away from the true image, in the centre, along the frequency dimension. While this ringing artefact was initially thought to be an error in the simulation, further research showed it to be an inevitable consequence of the truncating of the Fourier series, in this case due to finite data sampling. This is a problem which occurs in real world MRI practice[(118-120)] implying a degree of accuracy in the simulation.

While the VSS method provides useful information and accurate modelling of the effects and outputs of an MRI sequence, even down to real world artefacts, it requires individual modelling of each sequence taking into account each step and the effects of relaxation on it. The VSS method is, therefore, very labour intensive. What is needed is a more general method that can be easily implemented on any imaging sequence and yet still give image intensity, and therefore contrast, so that image contrast in the clinical setting can be more easily optimised. Continuation of this work was then achieved by incorporating experimental 2D relaxation spectra into the ODIN (Object-oriented Development Interface for NMR) platform in use by Kevin Wright.

5.3 MRICOM (MRI COntrast Modelling)

Programming on the ODIN platform was conducted by Kevin Wright. All experiments were run using relaxation profiles acquired by myself on the lab's spectrometers.

5.3.1 The MRICOM methodology

ODIN[110, 121] is used to run MRI experiments on real world hardware but also includes a simulation facility in which various pulse programs and their associated parameters can be simulated using digital phantoms. In conventional ODIN the sample is characterised by four matrices specifying the spin density, T_1, T_2 and chemical shift for each voxel in a digital phantom. These are saved as text files and combined with information of the samples morphology to form a single binary file that can then be input into ODIN. This is performed using an ODIN DOS program named Gensample. However this conventional use of ODIN fails to exploit the full relaxation information contained in an experimental T_1-T_2 relaxation spectrum. We have therefore modified ODIN to exploit 2D relaxation signatures for calculation of image contrast. The new package is called MRICOM. MRICOM uses ODIN in a novel way to generate what we call a relaxation signature. As shown in Figure 5.7 we assign all voxels to uniform density and zero chemical shift. We then create a gradient of T_1s and T_2s across the sample in the x and y dimensions respectively. These gradients are set to the form $\log_{10}[T_1(j,k)]=a*j + b$ and $\log_{10}[T_2(j,k)]=c*k + d$ so as to achieve a logarithmically spaced set of values in order to get

a more useful spread of data points across the sample. In this way each voxel is labelled with a unique pair of T_1 -T_2 values and uniform spin density, referred to here as the uniform phantom. Appropriate allocation of a, b, c and d values allows the T_1 and T_2 ranges to correspond with those of our experimentally acquired T_1 -T_2 spectra. This uniform phantom can then be run through the ODIN simulation, taking care to use realistic parameters and sufficiently high gradients so as to prevent line broadening causing information leakage from one voxel to the next. In this manner rather than a recreated phantom image, each voxel of the final output is a simulation of the effect of that pulse program and parameter set on a sample with that voxel's specific T_1 -T_2 values. This means that the final output of the simulation provides a map of the sequence and parameter response across a range of T_1 -T_2 values.

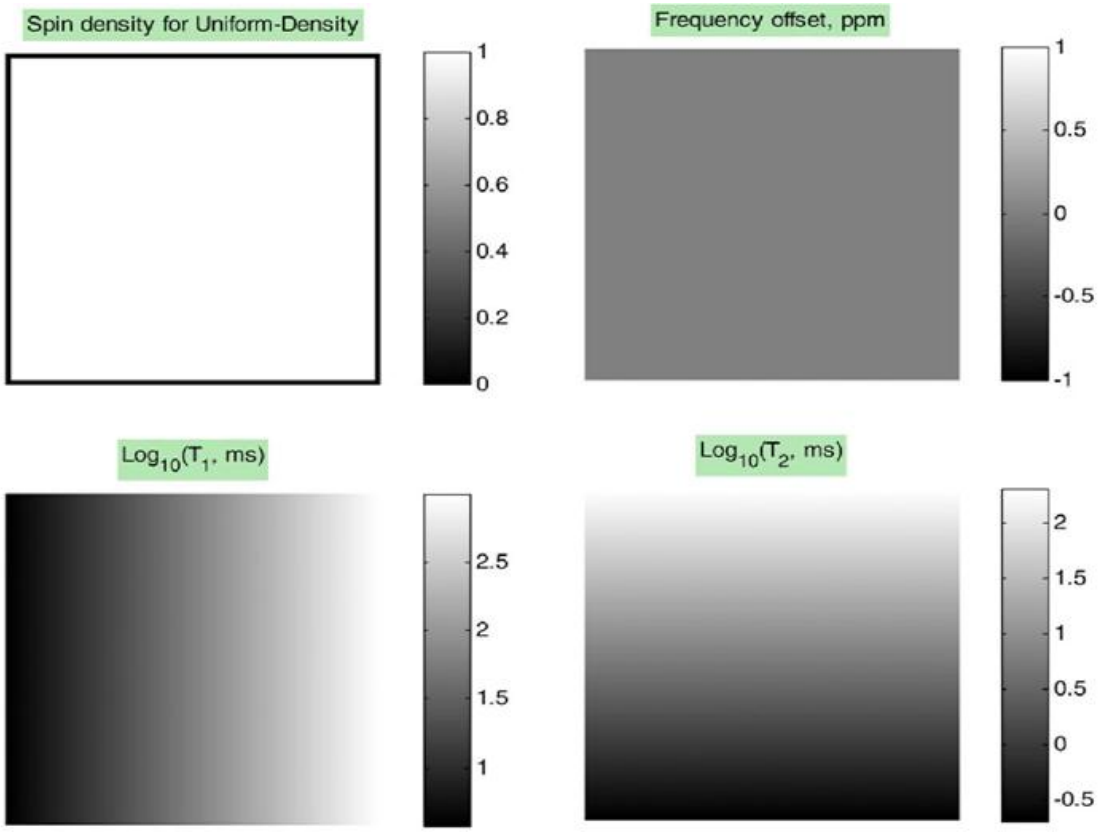

Figure 5.7 A uniform ODIN phantom characterised by four matrices specifying uniform spin density, a gradient of T_1s and T_2s across the sample in the x and y dimensions respectively set to the form $\log_{10}[T_1(j,k)]=a*j + b$ and $\log_{10}[T_2(j,k)]=c*k + d$ and zero chemical shift.

As the ODIN simulation, Fourier transform and other data processing don't scale their output to produce a unit intensity image from a unit spin density sample, it is necessary to properly scale the final image using a calibration phantom. This is achieved by setting a single voxel in the centre of the image to unit spin density and all others to zero.

Relaxation is removed by setting all T_1 -T_2 values to over-large numbers (~10^{12} ms) and chemical shift is set to zero in all voxels. When run through the same protocol as the uniform phantom, this provides a single peak, whose integrated volume provides a calibration constant based on how ODIN scales its outputs. The results of the uniform phantom can then be divided down by this calibration constant to provide a properly scaled measure of the frequency response of the protocol in question, previously referred to as the relaxation signature. Figure 5.8 shows the relaxation signature of both the TSE (Turbo-Spin Echo) and EPI (Echo Planar Imaging) sequences. By examining this signature we can discover how much signal loss due to relaxation will occur during this sequence for a specific T_1 -T_2 pairing, i.e. if signal loss at a certain T_1 -T_2 will be 75% then the intensity of the relaxation signature at that point will be 0.25 indicating that only 25% of the signal will remain. Visual examination of the relaxation signatures can tell us what kind of sample is likely to give the best response simply by making sure that the major T_1 -T_2 peaks are in a region of the signature without significant signal loss.

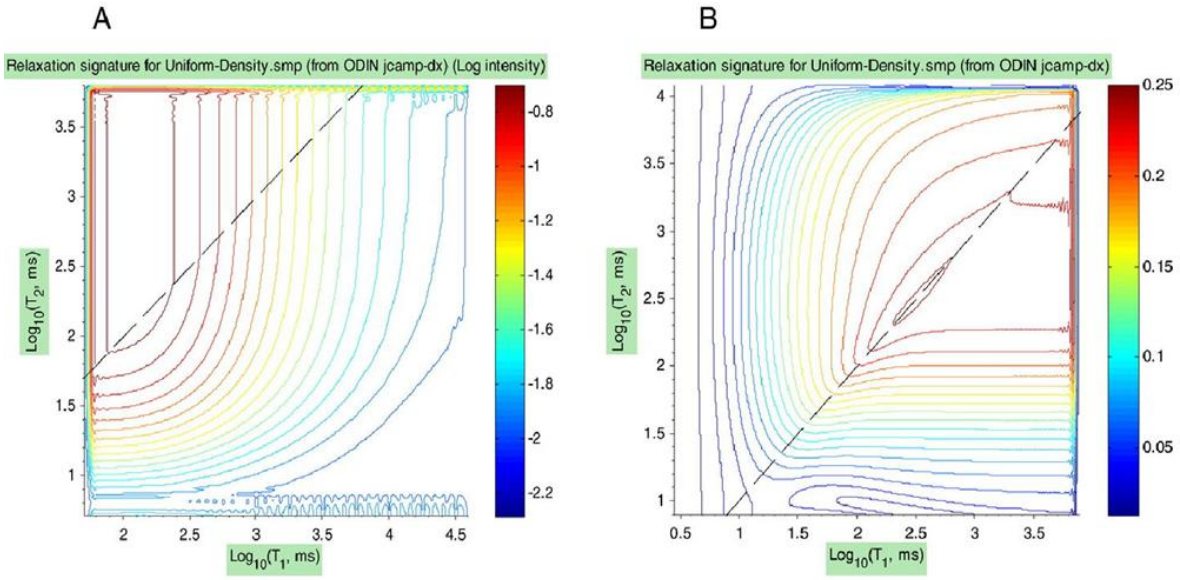

Figure 5.8 The relaxation signature of the A) Turbo spin echo (TSE) and B) Echo Planer Imaging (EPI) sequences

Similarly if one wishes to maximise or minimise the response of a sample or samples so as to increase image contrast then one need only find the relaxation signature which includes the samples main peaks in its high or low signal intensity regions respectively. The relaxation signatures calculated are entirely sample independent and characterise a single sequence and parameter set, thus a library of relaxation signatures can be built up in order to allow the best sequence to be chosen for a specific set of circumstances. In order to get a

quantifiable parameter for comparison of final signal intensities we first calculate the MRI-weighted T_1 -T_2 profile. This involves using our previously calculated T_1 -T_2 relaxation profiles which must be checked to ensure that they are normalised using the integrated intensity so that each value is the fraction of the sample's spins with that specific T_1 -T_2 value. Each point in the normalised T_1 -T_2 profile is now multiplied with its corresponding point in the relaxation signature to achieve a final profile showing the retained signal intensity arising from each point of the T_1 -T_2 profile of the sample, thus the integrated intensity of the final image will correspond to the intensity of a voxel of that sample when run through that specific imaging sequence. To achieve better image contrast between two tissues, as defined earlier, it would be necessary to find a sequence that maximises the difference in the final intensities of the two sample types.

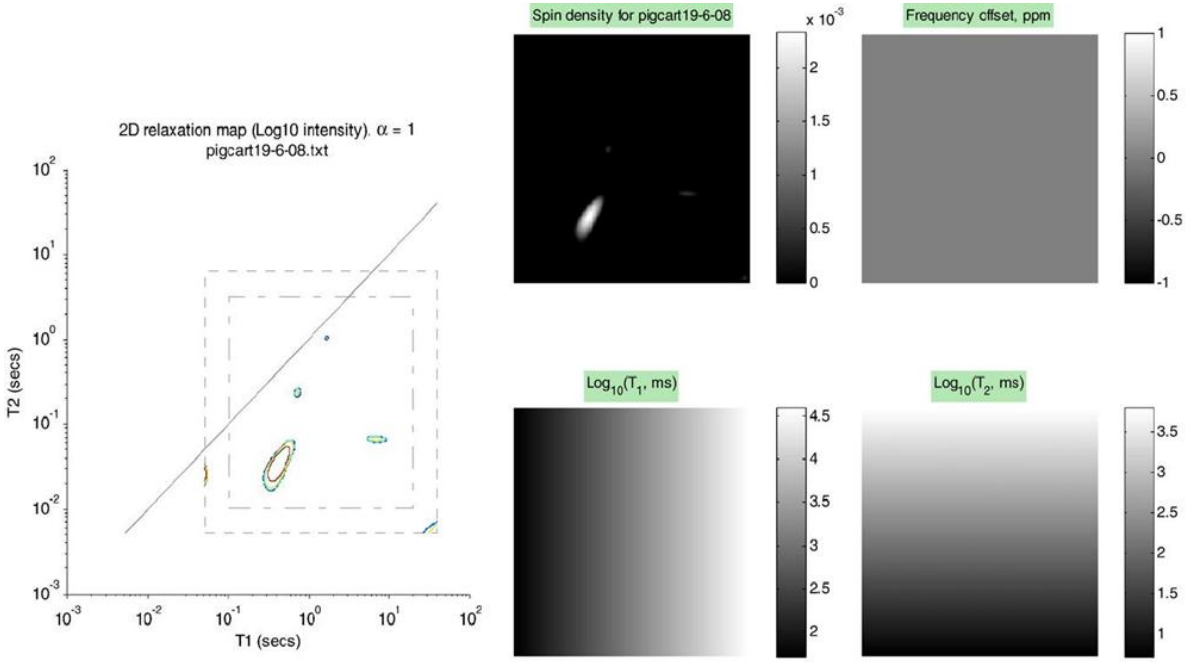

Figure 5.9 An ODIN phantom consisting of a uniform phantom with spin densities set to the normalised T_1 -T_2 profile of pig cartilage.

As can be seen from the above method, a more direct pathway can be used to calculate the MRI-weighted T_1 -T_2 profile. As can be seen in Figure 5.9, the system is set up as with the uniform phantom, but instead of setting all spin densities to 1, the spin densities are set to those of the normalised T_1 -T_2 profile of the sample, taking care to set the parameters of the T_1 and T_2 lists so that they correspond to the axes of the normalised T_1 -T_2 profile. This output would then need to be scaled using a calibration phantom as before, and should then give the same final output as the relaxation signature method. Any small difference in the

outputs will be due to information leakage between voxels due to line broadening, truncation of the free induction decay (FID), simulated noise and other fine details of the simulation methods. In-house testing (described later) found close agreement in intensities, usually within 10% which can be seen as a confirmation of the overall consistency of the calculations. While this method is a useful test of some of the general principles of the procedure, in practice the relaxation signature method is to be preferred as the simulation step is the more time consuming and so the construction of a relaxation signature library requires that each sequence and parameter set be simulated only once, for later use with many different samples. The visual nature of the library also allows for more intuitive user inspection by taking advantage of the human aptitude for visual pattern recognition[122] to find a good fit between relaxation profile and relaxation signature. By altering the initial parameters of the sequence, the high intensity area of the relaxation signature can be shifted so as to maximise the overlap between the sample and sequence, further increasing image intensity. The relaxation profile of the sample itself can be altered by changing the conditions under which it was acquired. Of course this would mean more significant changes to the final clinically chosen protocol as one of the major methods for altering the profile acquired is to change the spectrometer frequency[27]. T_1's in biological samples show a dispersive dependence in spectrometer frequency, leading to a decrease at lower frequencies. The T_2 value of the water and exchangeable proton peak is typically dominated by chemical exchange and so, decreases with increasing spectrometer frequency due to the larger frequency differences between chemically exchanging protons. T_2 values can be decreased by extending the echo spacings due to faster dephasing. Relaxation profiles can also be affected through the use of contrast agents[123, 124], common in clinical settings.

In practice another factor will affect the final intensity, and thus the contrast, of imaged samples. In the above instance we have assumed equivalent spin density in each sample but, in reality there may be differences. Thus, in order to properly optimise image contrast, the contrast parameter must be adapted slightly as shown below (eq 5.2).

$$C = \frac{|\ \rho_1 I_1 - \rho_2 I_2\ |}{\rho_1 I_1 + \rho_2 I_2} \qquad \textbf{(eq 5.2)}$$

Where ρ_i represents the spin density of sample i with intensity I_i. In this way any spin density differences can be used to further aid the final image contrast by reducing the intensity of the lowest spin density tissue and increasing that of the highest. Without taking these spin densities into account the user may find themselves reducing contrast rather than maximising it by, for instance, increasing an intensity that would have been naturally lower than that of a neighbouring tissue.

5.3.2 Testing MRICOM using pig cartilage spectra

We first demonstrate how MRICOM can be used to choose which imaging protocol gives the best contrast. We limit ourselves to a comparison of two pulse sequences, namely TSE and EPI in the examination of pig cartilage. The spectrum of pig cartilage, as shown in Figure 5.9, was multiplied by the relaxation signatures of the TSE and EPI sequences, as shown in Figure 5.8, to calculate the final integrated intensity I for the two sequences. A basic qualitative comparison of the profile and signatures would seem to suggest that the TSE sequence has the greatest peak overlap, which is confirmed by the final calculated intensities of 0.06 for EPI and 0.12 for the TSE sequence. At this stage further optimisation could be achieved by varying the input parameters of the sequence to achieve the optimal overlap.

5.3.3 MRICOM maximisation of image contrast

As a second demonstration of MRICOM we use the experimental T_1-T_2 relaxation spectra of healthy and diseased human articular cartilage to predict the image contrast between them when imaged with the EPI sequence at 100 MHz. As shown in Figure 5.10, when multiplied by the relaxation signature for EPI the healthy cartilage sample resulted in an image intensity of $2.67e^{-2}$ whereas the diseased sample resulted in an I value of only $0.81\ e^{-2}$. This would provide an image contrast of 0.535 indicating that the tissues should be easily distinguishable in the greyscale images typical of clinical MRI practice. This example is carried out irrespective of tissue spin densities, but it would seem that this is a reasonable simplification as, when tested independently, spin densities of three available samples were shown to be 3006 (healthy tissue), 3052 (diseased) and 2880 (diseased) taken in arbitrary units of signal intensity per cm^3.

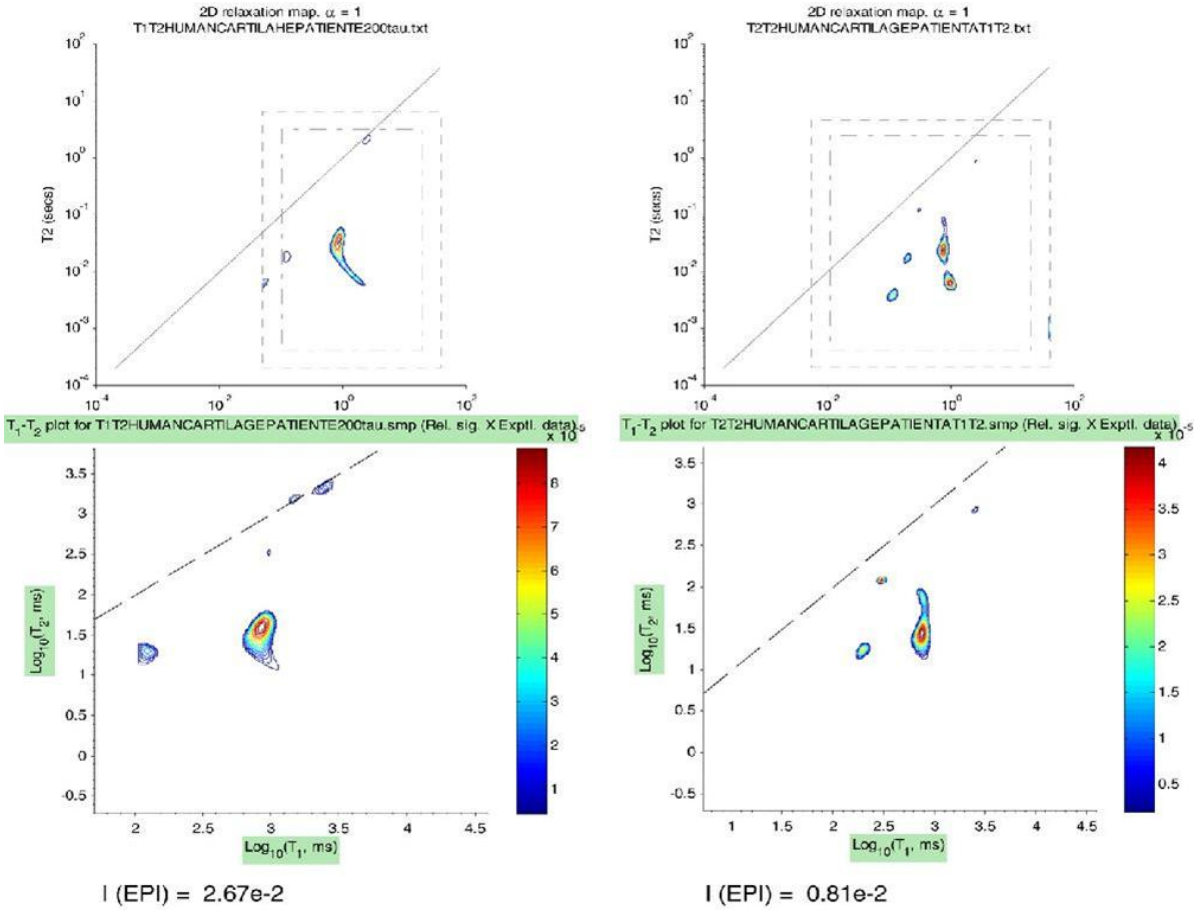

Figure 5.10 The normalised T_1 -T_2 profile of healthy (left) and diseased (right) human articular cartilage are presented as required to be used in MRICOM. Below each is their calculated MRI-weighted T_1 -T_2 profiles obtained using the EPI relaxation signature, as well as their final integrated intensity I, demonstrating the difference in intensity between healthy and diseased human articular cartilage.

This process would need to be repeated for each MRI protocol in order to determine the available image contrast, including a range of pulse programs and input parameters.

5.3.4 MRICOM optimisation of spectrometer frequency

As has been discussed previously, spectrometer frequency is not often optimised and is generally limited to the available frequencies of local equipment. This typically consists of the highest available field strength, within budgetary constraints, at the time the equipment was acquired. This situation means that comparing sequence performance at varying frequencies is rare and difficult to co-ordinate, as it would involve imaging identical samples under similar conditions at multiple institutes.

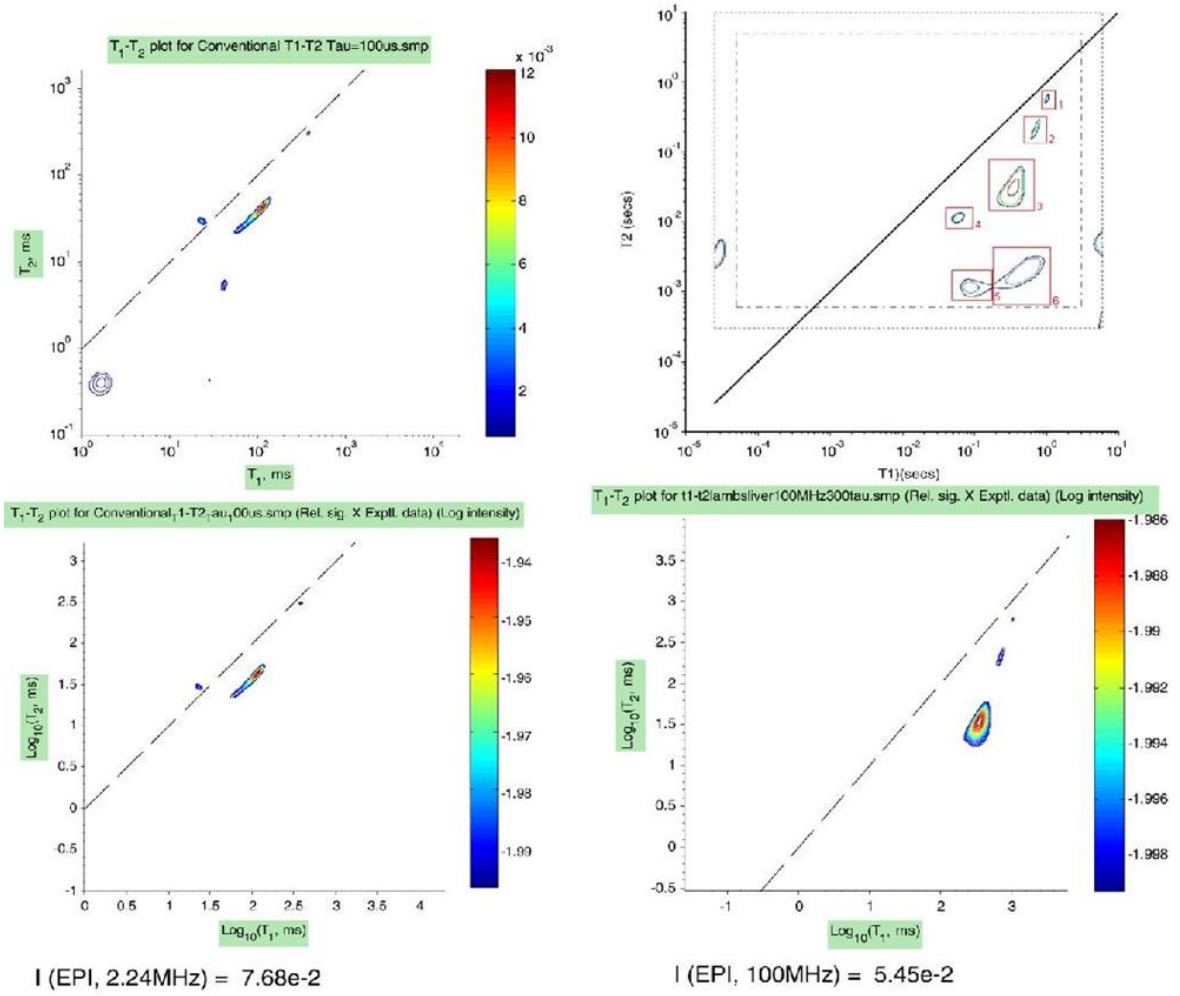

Figure 5.11 The T_1 -T_2 relaxation spectra of lamb's liver taken at 2.24 MHz (left) and 100 MHz (right) on lab based spectrometers. Below each is their calculated MRI-weighted T_1 -T_2 profiles, acquired using the EPI sequence simulation, as well as their final integrated intensity I, demonstrating the difference in intensity obtained from the same tissue at different spectrometer frequency.

The MRICOM methodology provides a way around this problem, as the only requirement is the availability of experimental T_1 -T_2 relaxation spectra at the frequencies to be examined. Figure 5.11 shows the T_1 -T_2 relaxation spectra of lamb's liver taken at 2.24 and 100 MHz on lab based spectrometers, as well as their calculated MRI-weighted T_1 -T_2 profiles using the EPI sequence. As can be seen from the integrated signal intensities shown below each graph, the final signal intensity is actually higher at 2.24 MHz ($7.68e^{-2}$) than at the higher 100 MHz field ($5.45e^{-2}$). In order to optimise image contrast, the other tissue to be imaged would need to be scanned and its MRI-weighted T_1 - T_2 profiles simulated so as to find the final intensities at each frequency and thus the image contrast obtained. The work done so far would seem sufficient to demonstrate that increasing spectrometer frequency is not a guarantee of increased signal return and certainly not of increased image contrast.

5.4 MRICOM vs. VSS

While the Virtual Sample Simulation (VSS) method presented at the beginning of the chapter can be used to simulate specific images and view the final intensities of the tissues involved, much of the information generated is superfluous when interested only in image contrast. It is also highly time consuming, both to program for each sequence and to run, once programs are completed. Therefore, it would seem that the MRICOM-ODIN methodology provides the most time efficient way of calculating final image contrast for a specific condition, as well as providing the opportunity to create a library of relaxation signatures and relaxation spectra which could be quickly referred to, so as to properly select appropriate imaging protocols in the future. All that would be required would be to find in the library, or acquire, the appropriate 2D T_1-T_2 relaxation spectrum for each tissue being imaged and multiply it by the calibrated relaxation signature. Acquiring reliable relaxation spectra using the standard INVCPMG inversion recovery sequence is time consuming and requires extraction of a sample to be examined in-vitro. To address these issues, chapter 6 will address methods of speeding up T_1-T_2 relaxation spectrum acquisition, while volume selective in-vivo spectrum acquisition will be discussed in chapter 7.

6. Development of Ultra-fast 2D relaxometry

6.1 Introduction

The T_1 - T_2 techniques described in previous chapters use a combination of an inversion recovery step, followed by a CPMG sequence as shown in figure 2.7. One problem with this sequence is the very long acquisition time required to obtain a 2D matrix of spin echoes, $M(t_1,t_2)$, where t_1 is the set of inversion recovery times and t_2 is the set of spin echo times [24, 53, 60-64]. The reason for this long acquisition time becomes clear when we consider in detail the way in which the 2D matrix is acquired. Each iteration of the standard T_1 - T_2 sequence involves waiting for an inversion recovery time taken from a list, followed by the time to complete the CPMG sequence, and a recovery time to allow the sample to return to equilibrium (Typically 5 times the longest T_1 of the sample). This whole process is then repeated for each t_1 step (typically t_1 has about 80 steps) and is also repeated 4 times to achieve phase cycling of the NMR signal. Phase cycling is performed to reduce or cancel out artefacts that may arise in the received signal from tip angle imperfections in the 90 and 180 degree radio-frequency pulses which may, in reality, deviate from those angles. By alternating the phase of the 90 and 180 degree pulses and adding or subtracting the NMR signals within the receiver these tip angle artefacts can be cancelled. In this case the 90 degree pulse is applied at X, -X, Y, and -Y, necessitating the 4 steps. Due to limitations of the hardware and software it is necessary to define a single fixed time between the start of one acquisition step and the beginning the next (the recycle delay, RD), meaning that RD must be set to accommodate the longest experiment time needed. This means the longest inversion recovery delay, t_1, must be used to calculate RD. All of these factors combine, meaning that even if the time for each step is kept to a low value such as 15 seconds, each step repeated 4 times will take a minute and the total experimental time will be at least 80 minutes, if not longer. In some tissues 3-4 hours is not uncommon.

While this may cause some delays in a lab setting, it is completely unacceptable in the context of a medical test, where a patient will be required to remain stationary throughout and could not be reasonably expected to maintain their position for longer than 15 minutes. It is therefore necessary to develop a new T_1 - T_2 technique that can work with and around

the limitations of both hardware and software while still providing an accurate profile in a medically acceptable time of around 15 minutes or less. Attempts have been made elsewhere[94, 125, 126] and to this end three new methods have been proposed and implemented by our lab group.

The TR method[127] was developed by me to optimise the timing of an inversion recovery sequence and allow experimentation with a specific definable recovery time, TR. This allows examination of a tissue from saturation T_1 recovery through to full Inversion T_1 recovery to observe differences in the obtained spectra. It also means the minimum possible time can be taken to execute each repeated step of the sequence rather than waiting for the same total experimental time for each repeated step, labelled the recycle delay on the spectrometer.

The Multi-slice method[128], developed principally by Dr Luca Venturi with input from myself, seeks to improve acquisition speed by slice selecting within a homogeneous sample and running different inversion recovery steps on each selected slice simultaneously. This allows a speed increase by a factor of as many slices as can be selected.

The FLOP[129, 130] method was developed and implemented by Dr Venturi and Dr Brian Hills to exploit the phenomenon of steady state magnetisation. It acquires multiple T_2 profiles under different steady state magnetisations and calculates a T_1 for each T_2 peak rather than measuring it directly. Each of these methods is presented with discussion of their merits and limitations.

6.2 The TR method[127]

Most of the necessary steps in this sequence are the same as those in the standard sequence, but they are implemented in a more efficient and controllable way, allowing the possibility of varying the recovery time (TR, the time left to allow a return to equilibrium following the CPMG sequence) rather than the recycle delay (RD, the time for the total experiment). The basic idea of this new sequence is to carefully time each step in the process, including the final TR period, so that no time is wasted. The limitations of the

experimental setup make this impossible when used to acquire each step individually as in previous programs, so it is necessary to acquire the entire data set in a single long sequence, referred to as a "single shot" sequence (see Figure 6.1). The Turbo Pascal pulse program composed to implement this sequence is included with explanation and annotation in appendix 6.2 along with the MATLAB program from which it is launched and in which the data is gathered, put into a data matrix and saved ready for processing.

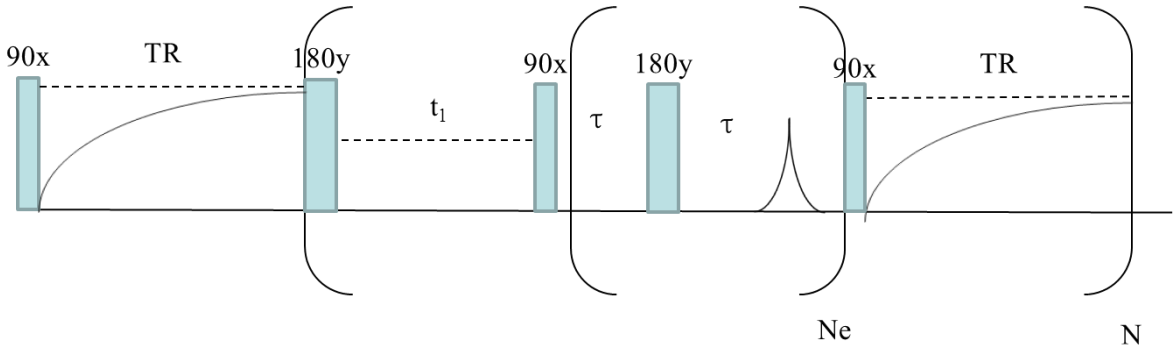

Figure 6.1 Single shot inversion recovery-CPMG sequence in which Ne is the repeating unit of the CPMG sequence and N is the overall repeating unit of the sequence. TR is the recovery time between iterations of N. t_1 is taken from the list of t_1 values making up the t_1 dimension (changing with each iteration of N) and 2τ is 180^o pulse spacing in the CPMG echo train.

When looking at the effects of varying TR it is necessary to establish the same conditions before the first acquisition as will be present following each acquisition with regards to sample magnetisation recovery. In order to achieve this, a 90x pulse is applied and the time TR is waited in order to put the magnetisation into the same state as it would be following the TR recovery period of the main sequence. This step is only performed at the start of the sequence and not repeated. After this step a 180 degree pulse is applied and followed by a period of longitudinal recovery for a time t_1, taken from a predefined list. This is then followed by a CPMG sequence after which all transverse magnetisation is gone and any remaining longitudinal component is destroyed with a 90 degree pulse. In the previous sequence we would now wait until the set experiment time RD had elapsed, transfer the signal from RAM in the pulse programmer to memory via the FIFO (Fast Input Fast Output) unit, and begin again at the next t_1 step. However, in the TR method we wait a defined time TR and immediately begin the next t_1 step with a 180 degree inversion pulse. After all steps are complete the single 1 dimensional signal, made up of that from each step, is transferred from RAM to memory and can then be divided into each individual step in post-processing. This means that only the bare minimum of time is waited and also allows TR to be varied.

As before, the data is then stored as a 2D matrix of spin echo amplitudes $M(t_1,t_2)$ which, at $TR \geq 5T_1$, is related to the T_1 - T_2 spectrum $P(T_1,T_2)$ by the 2D Laplace transformation below (eq 1.1), as with the standard inversion recovery sequence.

$$M(t_1,t_2) = \iint dT_1 dT_2 P(T_1,T_2)\exp(-t/T_2)M_\infty[1-2\exp(-t/T_1)] \quad \textbf{(eq 6.1)}$$

The final spectrum $P(T_1,T_2)$ is thus obtained from the data matrix $M(t_1,t_2)$ by 2D inverse Laplace transformation.

In order to experiment with values of $TR < 5T_1$ of the peak with longest T_1, we must examine the behaviour of the system when not allowed to fully return to equilibrium. Longitudinal magnetisation following the CPMG sequence will be negligible if the pulse spacing 2τ is much less than the shortest T_1, otherwise it should be destroyed with a 90x pulse to achieve this condition. In this case the magnetisation following the recovery period TR can be characterised by the following formula (eq 6.2)

$$M(TR) = M_\infty[1-\exp(-TR/T_1)] \quad \textbf{(eq 6.2)}$$

Following this recovery the magnetisation will be flipped by the 180 degree pulse to begin the next inversion recovery step and, following an inversion recovery time of t_1, would be characterised by

$$M(t_1) = M_\infty + [-M(TR) - M_\infty]\exp(-t/T_1) \quad \textbf{(eq 6.3)}$$

Which, substituting for M(TR) gives

$$M(t_1) = M_\infty\{1 - 2\exp(t_1/T_1) + \exp[-(TR+t_1)/T_1]\} \quad \textbf{(eq 6.4)}$$

This shows that the kernel of the 2d inverse Laplace transform, given earlier, must now include the extra term $\exp[-(TR+t_1)/T_1]$. This replaces the simpler kernel and means we can alter TR and investigate the effect of varying TR on the 2D T_1-T_2 spectrum.

The sequence was tested using a highly and moderately doped sample of water, which should each have a single peak with equal values for T_1 and T_2, when examined with a TR of $5T_1$. As can be seen in Figure 6.2 the first peaks T_1 value was 257 ms and the T_2 value was 232 ms while the second peaks values were 1.28 ms and 4.29 ms respectively, agreeing well with expected outcomes.

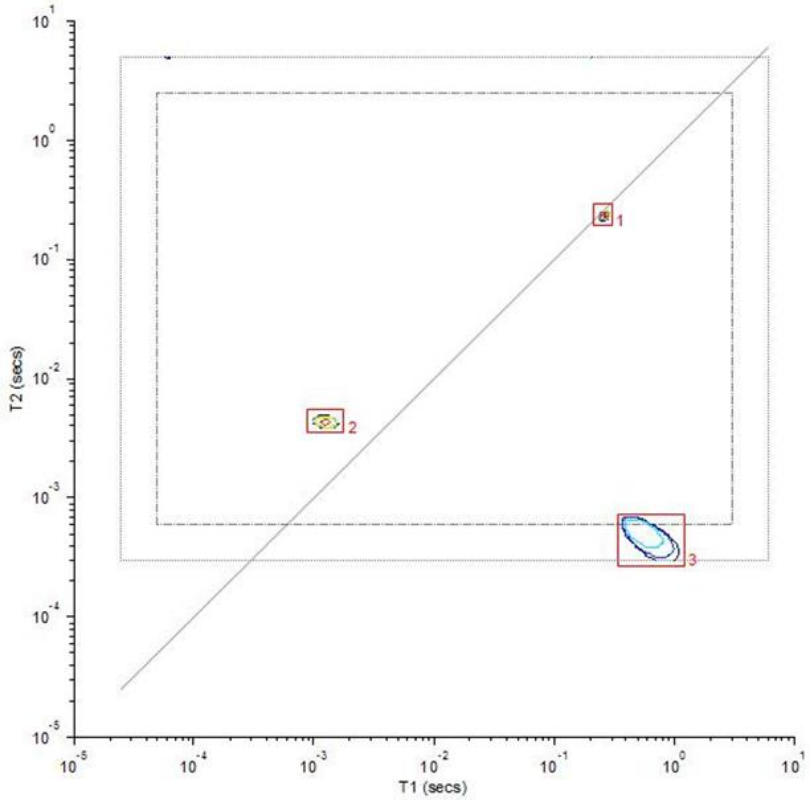

Figure 6.2 T_1-T_2 of highly and moderately doped water samples contained within the same sample area. As expected, two major peaks are present with approximately equal T_1 and T_2. The additional peak at the far right is likely an artefact due to its limited intensity and position in the outer region of the examined area, leading to reduced confidence in its authenticity.

6.3 Saturation recovery T_1 - T_2 spectra (TR = 0)

Saturation recovery is achieved by setting the TR recovery period to zero. When this occurs, the magnetisation of the sample has no time to recover and starts at a value of zero, rather than at $-M_\infty$ in the standard inversion recovery sequence. This increases the speed but, as seen earlier in Figure 1.2, the magnetisation in the sequence begins at zero and initial values are lost in the noise of the signal. This can be partially corrected by dividing the sequence into two sections to acquire the first and second parts of the profile. The first

part can then be acquired multiple times with increased receiver gain, so as to increase the signal to noise of the accumulated signal. This can cause problems as we then have to match the accumulated signal from the first part to the signal acquired with a different number of accumulations and receiver gain in the second part. Otherwise the complete signal has a break between the two parts. This break needs to be removed in post-processing, complicating the fitting process. It also increases the time taken to acquire the scan, although as the initial acquisitions have far shorter t_1 values the experimental time is not simply multiplied by the total number of acquisitions. Application of saturation recovery to liver tissue will be examined in section 6.6.1.

6.4 The Multi-slice method[(128)]

As mentioned before, a large proportion of the total experimental time in a T_1-T_2 acquisition is taken up with waiting for the sample to return to equilibrium. The multi slice method is an entirely different approach to the problem of reducing this time constraint which involves a novel use of volume selective methods. In conventional clinical MRI a magnetic field gradient is applied longitudinally to the sample, causing a longitudinal gradient in the resonance frequency. This allows for slice selection (specific excitation of a single slice through the sample), transverse to the direction of the applied magnetic field gradient. Similar methods of slice selection through a homogeneous sample have been trialled for speed enhancement purposes already with some success[(60, 126, 131)].

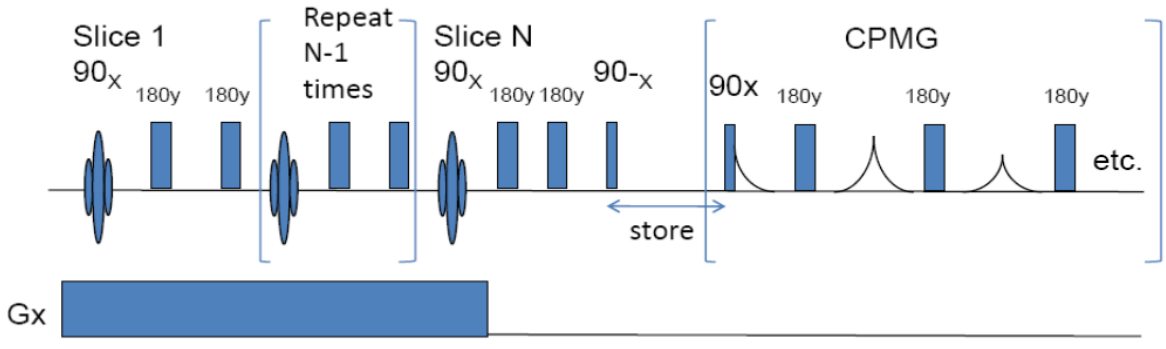

Figure 6.3 Multislice 2D inversion recovery-CPMG sequence for acquiring T_1-T_2 relaxation spectra from multiple slices of a homogeneous sample using gradient Gx.

The Multi slice method proposes to reduce the total sequence time by running each t_1 iteration of the experiment on a separate slice of the sample. The pulse program to achieve

this is shown in Figure 6.3. In theory with a large enough homogeneous sample, the standard 80 points in the t1 dimension could be acquired from 80 separate slices reducing the necessary time to that of a single experimental step without the recovery period.
In practice, factors such as available magnetic field gradients, sample size and signal to noise ratio limit the total number of excitable slices, leading to a reduction in the speed increase of the sequence. If only 10 slices can be excited within the sample then further points in the T_1 dimension must be acquired in batches. If 80 is still the desired target then each slice can be excited to acquire the first 10 steps and then allowed to recover before the next batch of 10 are acquired. In this manner, the total experiment time is reduced by a factor of the number of excitable slices. Perhaps the major limitation of the multislice method is the reduced signal to noise, due to a reduction in the sample size for each experiment. Signal is now acquired from a single slice through the sample, rather than the entire sample. This provides an additional constraint to the total number of slices a sample can be divided into. Given the small size of the homogeneous regions that would be examined in a medical context, this may mean as few as 2 or 3 slices can be separately excited.

While this alone would not provide enough of a reduction in total sequence time to achieve a clinically acceptable experiment time, work is under way to combine the TR and Multi-slice methods to further reduce the total experimental time. This would mean that some of the longer duration TR experiments could be speeded up to the point of being comfortably within acceptable clinical time frames.

6.5 The Flipped Longitudinal Polarisation (FLOP) sequence[129, 130]

The Flipped Longitudinal Polarisation sequence (developed by L. Venturi and B. Hills[129, 130]) exploits steady state longitudinal magnetisation to obtain a T_1-T_2 profile of a sample far faster than was possible with the above methods. A periodically repeating pattern of 180 degree pulses will eventually result in a steady state in which the longitudinal magnetisation periodically returns to some value M_s. In this state all information about the initial state is lost and the spin is now considered at equilibrium at a new spin temperature. Using a train of equally spaced 180 degree pulses the samples magnetisation eventually enters this steady state with a sawtooth pattern of inversion and recovery back to M_s. The

magnetisation in this steady state can be calculated using the standard recovery equation (eq 6.5)

$$M(t) = M_\infty + [M(0) - M_\infty]\exp(-t/T_1) \quad \textbf{(eq 6.5)}$$

With M_∞ being the equilibrium magnetisation of the sample. Consider a steady state created with a train of pulses with separation t_e. After a time of t_e following a 180 degree inversion, the magnetisation $M(t_e)$ is

$$M(t_e) = M_\infty - [M_s - M_\infty]\exp(-t_e/T_1) \quad \textbf{(eq 6.6)}$$

At this point the magnetisation is flipped by the next 180 degree pulse and after another period t_e recovers to a magnetisation given by,

$$M(2t_e) = M_\infty + [2M_\infty + (M_s + M_\infty)\exp(-t_e/T_1)]\exp(-t_e/T_1) \quad \textbf{(eq 6.7)}$$

But in the steady state $M(t_e) = M(2t_e)$ so by equating the two equations we get,

$$m = [1 - \exp(-t_e/T_1)] / [1 + \exp(-t_e/T_1)] \quad \textbf{(eq 6.8)}$$

with m equal to M_s/M_∞.

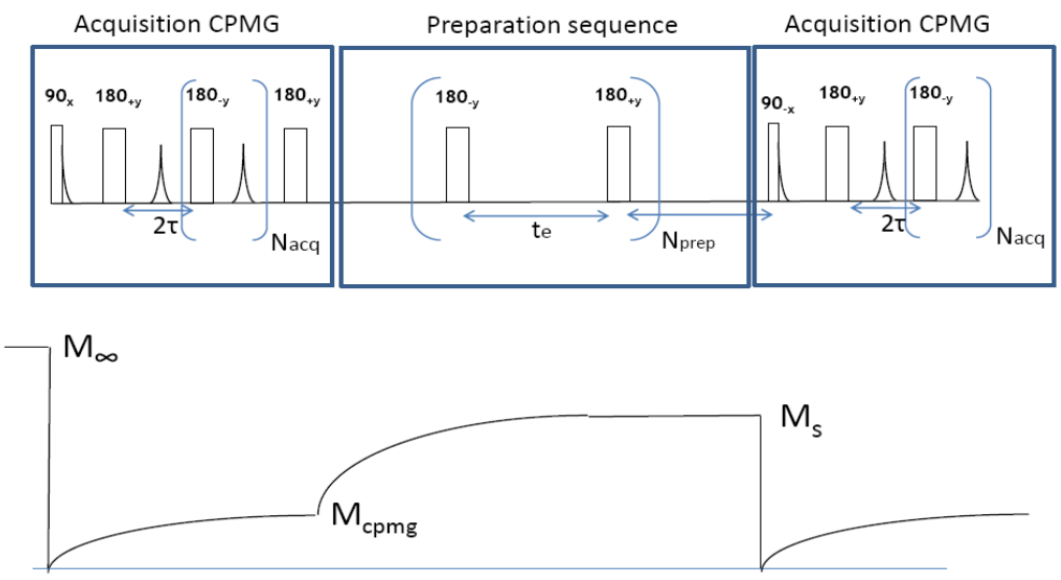

Figure 6.4[130] A Basic T_1 - T_2 FLOP sequence showing the pulse sequence above with the longitudinal magnetisation during each stage shown below.

This steady state situation can be used to acquire a T_1-T_2 profile via the method shown in Figure 6.4. A standard CPMG sequence, itself a train of 180 pulses, is first used to acquire an echo train down to the baseline. This leaves some steady state longitudinal magnetisation but with typical values of τ this value is small enough to be neglected. Then a train of 180 pulses is run with separation t_e without acquiring any signal to establish a steady state magnetisation M_s. Another CPMG sequence is run with the same parameters (τ, NECH, etc.) and a second echo train is acquired. Analysing both the CPMG acquisitions results in two one dimensional T_2 spectra with discrete peaks. The peaks in each spectra should have the same T_2 peak positions but will likely differ in area, as the first was acquired starting with equilibrium magnetisation and the second with steady state magnetisation. Because of this the ratio of the two peak areas is a direct measurement of m, allowing the T_1 of each peak to be calculated (eq 6.8). As can be seen from this equation, the steady state magnetisation for a peak with very long T_1 values will be severely suppressed and require a far longer t_e to get a measurable peak area. This may then necessitate repetition of the sequence with increasingly long values of t_e, which can be built into the standard sequence and run in a single shot by inserting extra preparation steps with longer t_e values each followed by additional CPMG acquisition windows until all desired CPMG signals are acquired. This property can also be of use in samples where the spectra are dominated by large peaks with large T_1 values, which will be preferentially suppressed allowing better examination of smaller, short T_1 peaks. If there are 2 peaks with

the same T_2 but different T_1 values then measurements at two different t_e values are necessary so that a pair of simultaneous equations can be solved to obtain the two different T_1 values. This and more advanced FLOP techniques were developed by Luca Venturi and Brian Hills and are described in the original papers[129, 130].

While the FLOP method does allow fast acquisition of a 2D T_1-T_2 relaxation spectrum, each T_2 peak calculated has only a single T_1 value, meaning that information about the shape etc. of relaxation spectra peaks is lost. As described in the original papers[129, 130], many of the FLOP methods lose sensitivity of either T_1 or T_2 peaks with short relaxation times, which may mean a loss of useful information. The loss of peaks and peak shape information would restrict the utility of the obtained T_1-T_2 relaxation spectra, particularly with reference to the contrast simulation and prediction methods examined in chapter 5. Thus the Fast TR method potentially combined with the multi-slice method is the currently preferred ultrafast acquisition mode and will be the focus of further work, both within this thesis and beyond.

6.6 Examination of mammalian tissue at 100 MHz with the TR method

As before, samples of liver and kidney were obtained from local meat suppliers and examined in as fresh a condition as possible, without prior freezing or other preservation besides refrigeration. Appropriate samples were dissected using a scalpel from the bulk tissue. Care was taken to extract as homogeneous a sample as possible. Samples are then placed in NMR tubes, which are then filled with polytetrafluoroethylene (PTFE) to remove as much remaining air as possible so as to prevent dehydration of the sample. Samples were kept at 4°C during storage and as cool as possible otherwise so as to further limit the extent of any degradation that may have taken place. Samples were examined using the INVCPMGSS 2D relaxometry protocol (referred to as the TR method) on a 100 MHz DRX spectrometer using a high power probe with a 5 mm horizontal solenoid coil, using a tau of 200 µs. The 90 and 180 degree pulse widths were automatically determined by the Resonance Instruments software RINMR[56]. Spectra were acquired with as few echoes in the t_2 dimension as possible while still achieving complete transverse magnetisation degradation at which point the CPMG curve will plateau at zero echo amplitude. This was

typically 8K (8192). 64 logarithmically spaced points in the t_1 dimension were used starting at 100 µs and typically going up to 10-20 seconds to ensure adequate time for the longitudinal magnetisation to plateau at its maximum level. Phase cycling is not currently implemented with this method and will slow it down if implemented. Data was analysed using internally developed MATLAB programs making use of 2D Laplace transform algorithms to obtain a 2-Dimensional cross correlation T_1-T_2 spectrum of the sample. These programs are named InvCpmgEditV3djh, InvCpmgCalcSSjfw and InvCpmgResV3djh, each based on InvCpmg Version 12 by Kevin Wright, 20 Jan 2005. InvCPMGSSjfw was adapted by me from InvCpmgCalcV3djh to include the additional post processing term in the kernel used by the 2D Laplace transformation, as described in section 6.2

6.6.1 Liver

As described in chapter 3, liver tissue is largely homogeneous on a macroscopic scale[(132)]. Samples were dissected from the bulk tissue taking care to avoid large fluid channels running through the tissue.

6.6.1.1 Liver at equilibrium

Equilibrium recovery occurs when the final recovery period TR is approximately 5 times the longest T_1 value of the sample. Experiments run with grossly overlong TR periods of 20 seconds have shown the longest T_1 of lamb liver recorded with this sequence to be approx. 430 ms, so to achieve equilibrium a T_1 value of at least 2.15 seconds (5 times the longest T_1) was used. Figure 6.5 shows a characteristic 2D T_1-T_2 relaxation spectrum performed at 100 MHz on a sample of fresh lamb's liver using the TR method at equilibrium recovery. Peak 5 in this spectrum was not present in any other equilibrium spectra, but this absence is likely due to necessary steps in data processing to overcome dropped points in the 2D data matrix which give a value of zero where data points should be. Values below a certain t_2 value had to be cropped to avoid unusable matrix regions at low t_1 and t_2, meaning that in the final processed spectra, the minimum detectable T_2 value was higher than originally intended as the range over which peaks are displayed is determined by the minimum and maximum t_1 and t_2 values in the recovery curves.

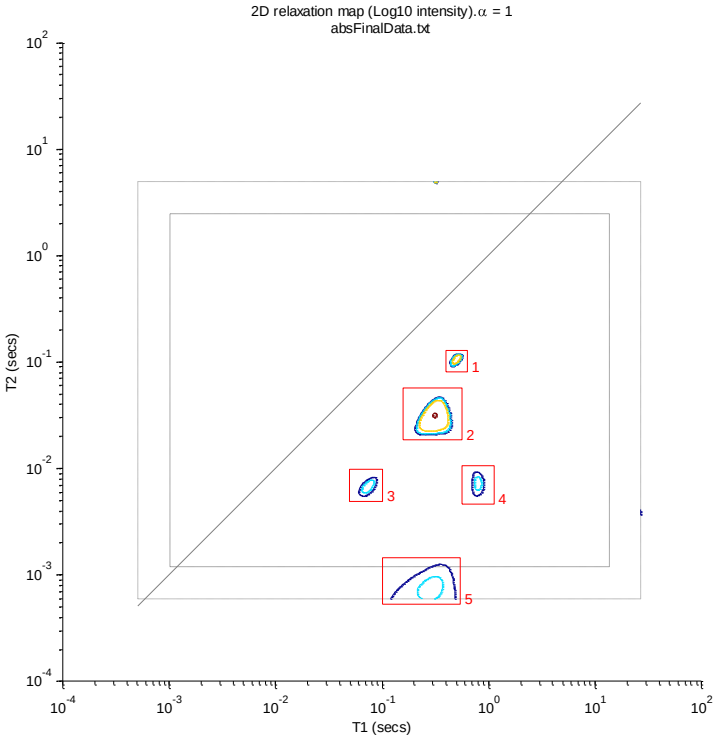

Figure 6.5 A characteristic 2D T_1-T_2 relaxation spectrum performed at 100 MHz on a sample of fresh lamb's liver using the TR method at equilibrium recovery demonstrating the 4 main peaks, labelled 1-4. Peak 5 was not present in any other equilibrium spectra. Reasons for its inclusion here and absence in the other spectra are discussed in the text.

Confidence in the authenticity of peak 5 is based on the presence of similar peaks in spectra acquired at different TR times and using the slower inversion recovery technique. Peaks 1 to 4 were clearly present in the equilibrium recovery spectra and appear to line up well with peaks found using the slow T_1-T_2 inversion recovery sequence (discussed in chapter 3). These comparisons are shown in Table 6.1.

Liver peak slow/fast	slow Area (std. dev.)	fast Area (std. dev.)	slow T_1 (ms) (std. dev.)	fast T_1 (ms) (std. dev.)	slow T_2 (ms) (std. dev.)	fast T_2 (ms) (std. dev.)
1	0.23% (0.09%)		701 (49)		650 (95)	
2/1	1.88% (0.22%)	4.35% (0.84%)	597 (30)	473 (24)	225 (30)	110 (6.0)
3/2	83.5% (2.0%)	84.8% (3.5%)	428 (28)	325 (14)	38.3 (1.6)	30.4 (1.6)
4/3	2.73% (2.6%)	5.61% (4.4%)	41.9 (25)	108 (88)	22.5 (9)	5.49 (3.8)
5/4	5.68% (1.2%)	5.48% (1.6%)	448 (64)	827 (278)	2.88 (0.82)	4.72 (1.8)
6	2.34% (0.98%)		49.9 (30)		1.32 (0.71)	
7	5.18% (0.86%)		508 (70)		0.38 (0.04)	

Table 6.1 Mean peak intensity, T_1, and T_2 values for lamb's liver acquired at 100 MHz using both the slow and fast T_1-T_2 acquisition methods examining 8 samples with the slow sequence and 7 with the fast sequence. Peaks have been lined up to indicate probable correspondence between spectra acquired using the different methods. Standard deviation given in brackets next to mean value.

Fewer peaks are detected with the faster TR method which may be due to reduced signal to noise arising from the single scan used in the faster method, compared to the 4 phase cycled scans used in the slower method. As previously mentioned the "field of view" in the final T_1-T_2 spectra had to be reduced to remove dropped points from the data matrix, which may also be remedied by the addition of phase encoding in the sequence. Due to the lower number of peaks, the peak intensities as a percentage of the total peak marked signal would be expected to rise. This seems to occur in peaks 1 to 3 but not in peak 4. While there are significant differences in the precise T_1 and T_2 values of the peaks between the two methods, comparison of Figure 6.5 and Figure 3.2 would seem to confirm the correlations shown in Table 6.1. As can be seen from Figure 6.6 the T_1 and T_2 values of peaks 1 and 2 have very narrow ranges. The standard deviation of peak 1's T_1 and T_2 are 24 ms and 6 ms respectively whereas peak 2's are 14 ms and 1.6 ms respectively. Peaks 3 and 4 are far less consistent however. Assignment of peak numbers is a process requiring a significant amount of judgement and experience which could impair accuracy of pattern assignment. When looking at the numerical data, peak 3 was briefly considered to potentially contain two separate groups which were found to give statistically significant p values between their peak intensity, T_1, and T_2 values. This concept was abandoned, however, upon examination of the spectra themselves, each clearly showing the standard peak arrangement shown by peaks 1 to 4 in Figure 6.5. Care must be taken when assigning peak markings in spectra to avoid artificial distinction due to errors of judgement or an overreliance on statistical tests. In this case the cause for the apparent division in the values of peak 3 has not been identified. Figure 6.7 shows the peak intensities as a percentage of the total peak marked area. It shows the peak intensities to be fairly consistent and peak 2 dominating the spectrum with a mean of 84.8%.

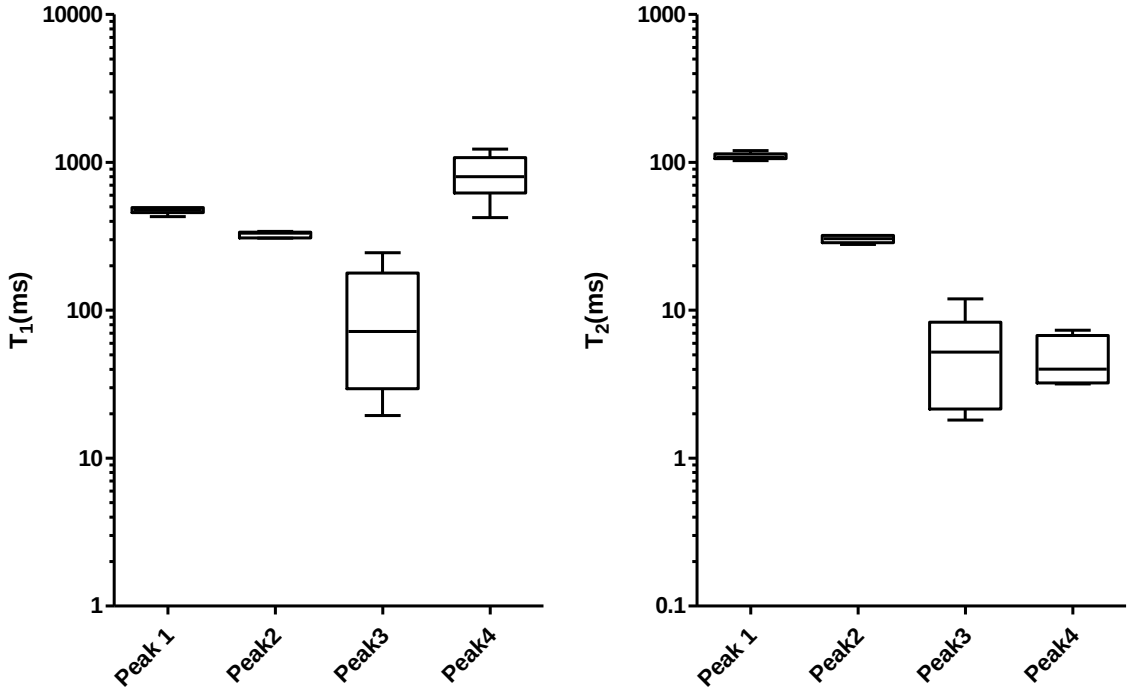

Figure 6.6 The peak positions in T_1(left) and T_2(right) of the 4 peaks obtained from T_1-T_2 relaxometry performed at 100 MHz on 7 samples of fresh lamb's liver using the TR method at equilibrium recovery, demonstrating the consistency in peak positions.

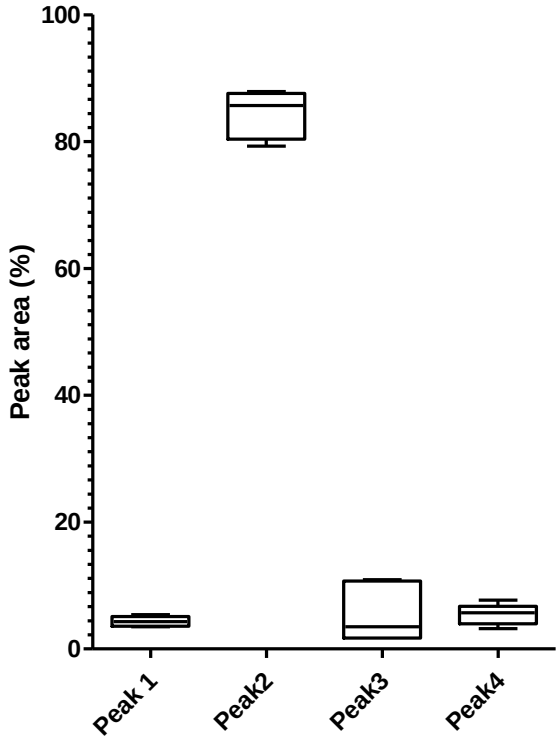

Figure 6.7 The peak intensities, as a percentage of the total peak marked intensity, of the 4 peaks obtained from T_1-T_2 relaxometry performed at 100 MHz on 7 samples of fresh lamb's liver using the TR method at equilibrium recovery, demonstrating the consistency in peak intensities.

6.6.1.2 Liver at intermediate recovery

Intermediate recovery occurs when the final recovery period TR is between 5 times the longest T_1 value of the sample and zero. As previously stated, experiments run with long TR periods have shown the longest T_1 of lamb liver recorded with the TR method to be approx. 430 ms, so to achieve intermediate recovery a T_1 value of 1.075 seconds (2.5 times the longest T_1) was used. Figure 6.8 shows a characteristic profile of intermediate recovery performed using the TR method at 100 MHz.

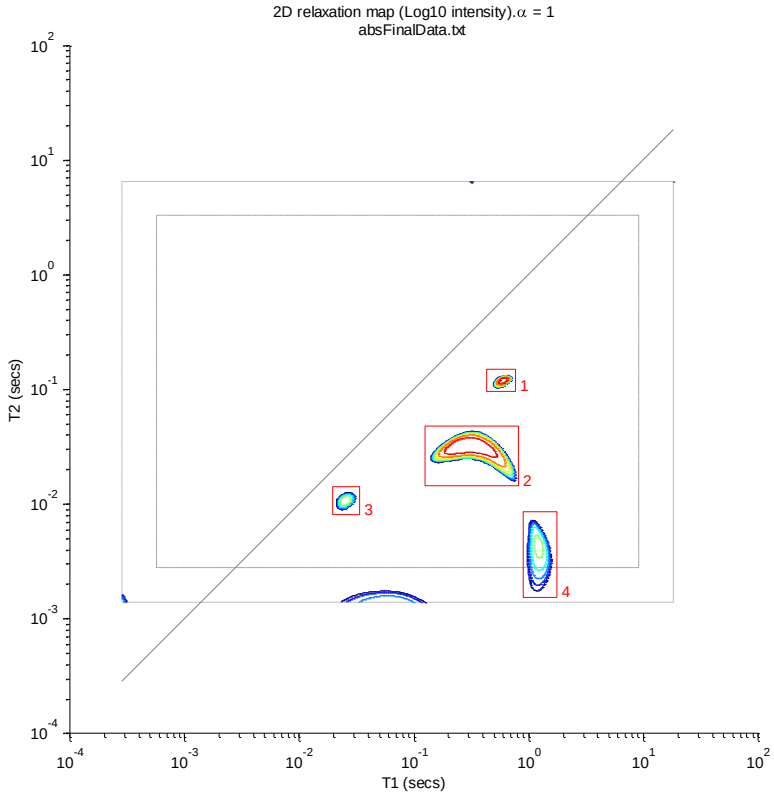

Figure 6.8 A characteristic 2D T_1-T_2 relaxation spectrum performed at 100 MHz on a sample of fresh lamb's liver using the TR method at intermediate recovery demonstrating the 4 main peaks

Peaks 1 to 4 appear marked as, and comparable to, the peaks in the equilibrium recovery spectrum (Figure 6.5). The unmarked peak at the mid T_1 and low T_2 region appears to correspond well with the peak marked as 5 in Figure 6.5, lending credence to that peaks authenticity. The position of the main 4 peaks is shifted slightly. The extent to which the spectrum is distorted is presented in Table 6.2, which compares equilibrium, intermediate and saturation recovery, and is discussed in more detail in section 6.6.1.4. As with the spectra acquired at equilibrium recovery, Figure 6.9 shows that the T_1 and T_2 values of

peaks 1 and 2 have very narrow ranges. The standard deviation of peak 1's T_1 and T_2 are 75 ms and 8.5 ms respectively whereas peak 2's are 25 ms and 1.4 ms respectively. Peaks 3 and 4 are, as before far less consistent however. Figure 6.10 shows the peak intensities as a percentage of the total peak marked area. It shows the peak intensities to be fairly consistent and peak 2 dominating the spectrum with a mean of 83.9%.

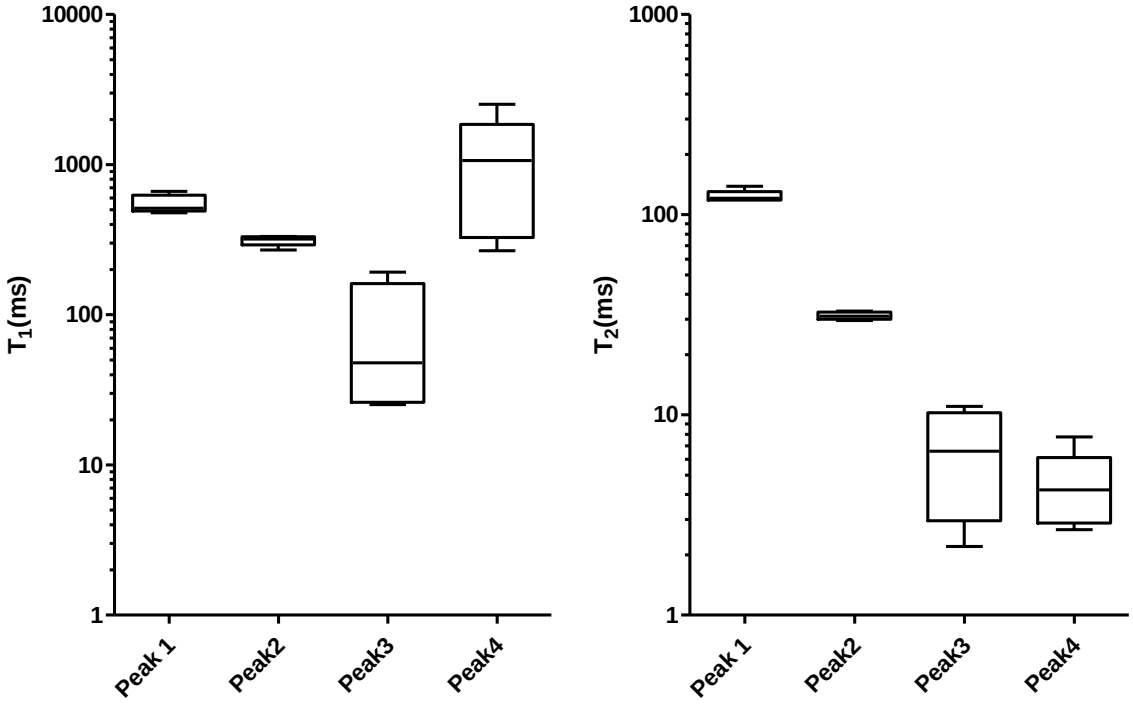

Figure 6.9 The peak positions in T_1(left) and T_2(right) of the 4 peaks obtained from T_1-T_2 relaxometry performed at 100 MHz on 5 samples of fresh lamb's liver using the TR method at intermediate recovery, demonstrating the consistency in peak positions.

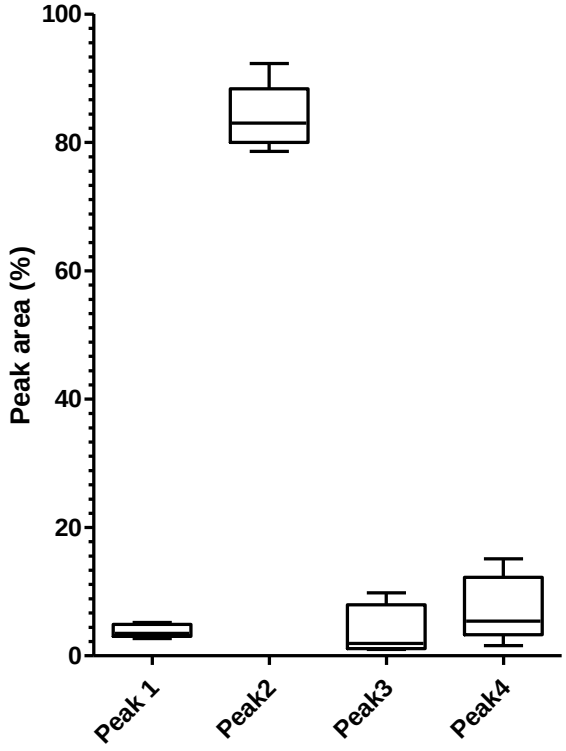

Figure 6.10 The peak intensities, as a percentage of the total peak marked intensity, of the 4 peaks obtained from T_1-T_2 relaxometry performed at 100 MHz on 5 samples of fresh lamb's liver using the TR method at intermediate recovery, demonstrating the consistency in peak intensities.

6.6.1.3 Liver at saturation recovery

Saturation recovery occurs when the final recovery period TR is at or as close as possible to zero. Figure 6.11 shows a characteristic profile of saturation recovery performed using the TR method at 100 MHz. Peaks 1 and 2 appear marked as, and comparable to, the peaks in the equilibrium recovery spectrum (Figure 6.5). Peak 3 would appear to correlate with peak 4 in Figure 6.5 whereas the peak marked as 3 on that spectrum is no longer visible on this one. The peak marked here as 4 was present in all saturation recovery spectra and appears to correlate well with the questionable peak marked as peak 5 in Figure 6.5. As discussed in section 6.3, saturation recovery begins with zero longitudinal magnetisation. Because of this, the issue of dropped points does not apply. Any dropped data point would be indistinguishable from a genuine data point in this region, meaning that no cropping of the data set is necessary and full characterisation of the low T_2 region of the spectrum is possible.

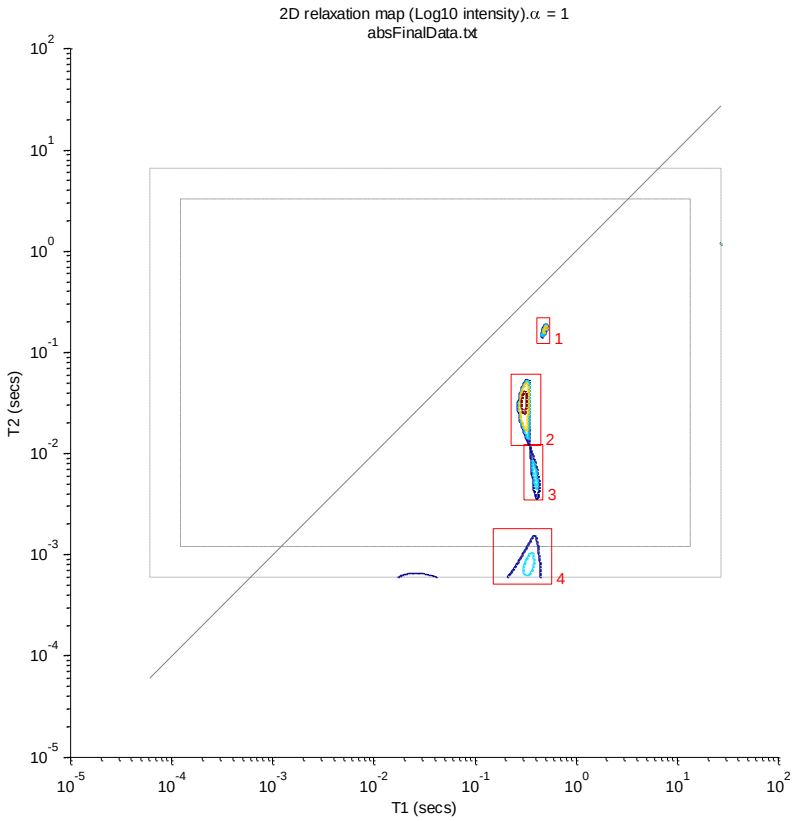

Figure 6.11 A characteristic 2D T_1-T_2 relaxation spectrum performed at 100 MHz on a sample of fresh lamb's liver using the TR method at saturation recovery demonstrating the 4 main peaks

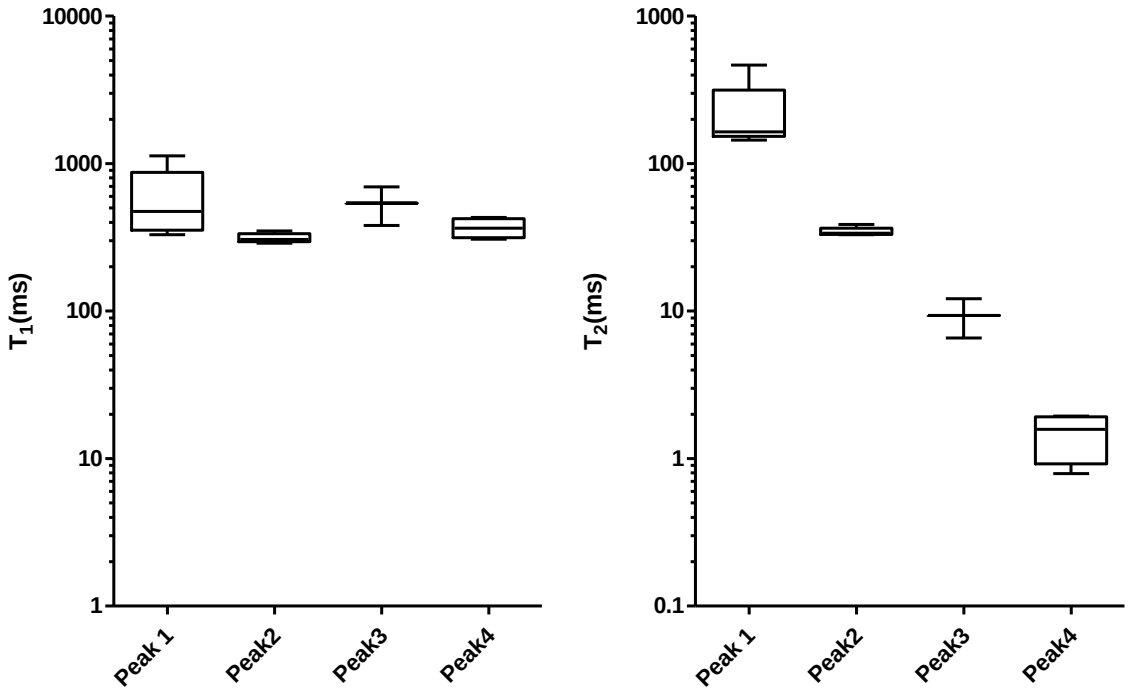

Figure 6.12 The peak positions in T_1(left) and T_2(right) of the 4 peaks obtained from T_1-T_2 relaxometry performed at 100 MHz on 5 samples of fresh lamb's liver using the TR method at saturation recovery, demonstrating the consistency in peak positions.

Figure 6.12 shows the peak positions in T_1 and T_2 of the peaks marked 1 to 4 in Figure 6.11 shown as boxplots obtained from 5 samples of lamb's liver taken at 100 MHz with a tau value of 200 µs. The dominant peak 2 in particular has almost no variation in either T_1 or T_2. Figure 6.13 shows the peak intensities of these same peaks as a percentage of the total peak-marked area. Again there is little variation in peak intensities with most of the signal (≈80.9%) contained in the dominant peak 2.

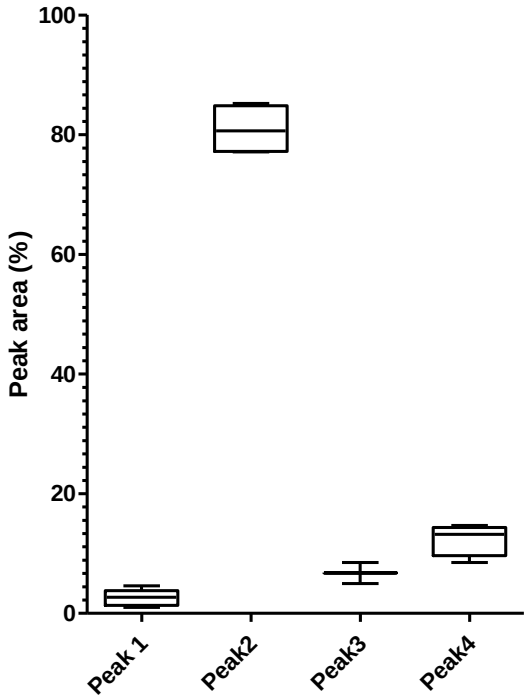

Figure 6.13 The peak intensities, as a percentage of the total peak marked intensity, of the 4 peaks obtained from T_1-T_2 relaxometry performed at 100 MHz on 5 samples of fresh lamb's liver using the TR method at saturation recovery, demonstrating the consistency in peak intensities.

6.6.1.4 Comparison of the TR method at equilibrium, intermediate and saturation recovery at 100 MHz in lamb's liver.

A comparison of the TR method at equilibrium, intermediate and saturation recovery is necessary for determination of which recovery time to use in further experiments and tissue characterisation in general. At a total experiment time of 7 minutes, the saturation recovery sequence is, as would be expected, the fastest followed by intermediate recovery at 8 minutes and equilibrium recovery at 9 minutes. Saturation recovery has no recovery period and so its time of 7 minutes is also the time required for the acquisition of the active

phase of the total experiment time. In this case this is the time required to perform a CPMG with 8192 echoes with a spacing of 400 µs (2 x tau of 200 µs) following each t_1 period. This time itself could be further reduced by reducing the number of echoes or the tau value, taking care to ensure that the CPMG echo train returns to equilibrium. While it is faster, the saturation recovery method loses 1 of the smaller peaks (labelled peak 3 in Figure 6.5 and Table 6.2). This loss may be due to the larger problem of the "null point", which is reached in full inversion recovery but not in saturation recovery. The "null point" is the time at which, during inversion recovery, the magnetisation of the bulk water or dominant peak in the sample goes through from negative, through zero, to positive magnetisation. At this point the magnetisation from smaller peaks is more easily detectable. In Figure 6.11 and Table 6.2 it can be seen that the T_1 values of all peaks have become remarkably similar. This distortion of the saturation recovery spectra may still allow their use in tissue classification, but would prevent their use in determining the simulated tissue contrast using the methods discussed in Chapter 5. It also appears to have a problem with "lost signal" in the noise. When spectra are obtained during data processing they are peak marked manually, the user defining what is and is not a peak. The peak intensities are calculated as a percentage of the total peak marked area, but their intensities as a percentage of the total signal are also available. These values are typically within a few per cent of each other, indicating that a small percentage of the total signal is being lost as noise or in unmarked artefacts. In the case of saturation recovery, with the current sequence and experimental set-up, the second value is typically around half the first (i.e. peak 2 in Figure 6.11, 77.6% peak marked signal, 39.5% total signal). This means that around half the signal is contained in noise, between the well resolved peaks.

Liver peak	equil area (std. dev.)	inter area (std. dev.)	sat area (std. dev.)	equil T_1 (ms) (std. dev.)	inter T_1 (ms) (std. dev.)	sat T_1 (ms) (std. dev.)	equil T_2 (ms) (std. dev.)	inter T_2 (ms) (std. dev.)	sat T_2 (ms) (std. dev.)
1	4.35% (0.84%)	3.88% (1.0%)	2.60% (1.4%)	473 (24)	549 (75)	586 (320)	110 (6.0)	124 (8.5)	220 (140)
2	84.8% (3.5%)	83.9% (5.1%)	80.9% (4.2%)	325 (14)	313 (25)	313 (23)	30.4 (1.6)	31.3 (1.4)	34.6 (2.4)
3	5.61% (4.3%)	3.68% (4.1%)		108 (88)	78 (78)		5.49 (3.8)	6.60 (3.8)	
4	5.48% (1.6%)	7.30% (5.2%)	6.75% (2.5%)	827 (280)	1090 (900)	539 (220)	4.72 (1.8)	4.44 (2.0)	9.35 (3.9)
5	16.70%	6.00%	12.40%	286.91	239.20	367.32	0.76	1.12	1.47

Table 6.2 Mean peak intensity, T_1, and T_2 values for lamb's liver acquired at 100 MHz using the TR method at equilibrium recovery (TR = 2.15 seconds, labelled equil) with 7 samples, intermediate recovery (T = 1.075 seconds, labelled inter) with 5 samples and saturation recovery (TR = 0 seconds, labelled sat) with 5 samples. Peaks have been lined up to indicate probable correspondence between spectra acquired using the different TR recovery periods. Standard deviation given in brackets next to mean value. Peak 5 appeared only once in each processed data set but is included here for comparison. Necessary cropping of recovery curves during data processing of some spectra may account for its absence in those spectra as the range over which peaks are displayed is determined by the minimum and maximum t_1 and t_2 values in the recovery curves.

At 8 minutes the intermediate recovery experiments performed are only a minute faster than the full equilibrium recovery experiments. In tissues with shorter times required for the CPMG acquisition phase of the experiment this may be more significant but in this case represents only an 11% speed increase. Theoretically in a tissue with extremely short T_2s and long T_1s it would provide far more significant speed increases as the equilibrium recovery time of 5 times the longest T_1 would become the dominant factor in total experiment time. Another issue with the intermediate experiment is the way in which different peaks would be affected differently based on their T_1 value. At a TR period of 1.075 seconds, as used here, any peaks above 215 ms (a fifth the TR period length) will be affected to a greater extent the higher the T_1, while those below this level will be unaffected. In tissue not yet characterised this may lead to significant peaks being distorted and shifted in T_1 and T_2, which may then necessitate reacquiring the data. In mammalian tissues such as this, typical T_1 values are low enough to render the speed increase from TR reduction extremely limited. Due to the various issues raised in this comparison section, it seems foolish to sacrifice potential accuracy and utility in the final $T_1 - T_2$ spectrum to save 1 or 2 minutes out of a total time of 8 minutes. Therefore it would seem that, for the purpose of tissue characterisation, the full equilibrium recovery TR method is to be preferred.

6.6.2 Kidney cortex

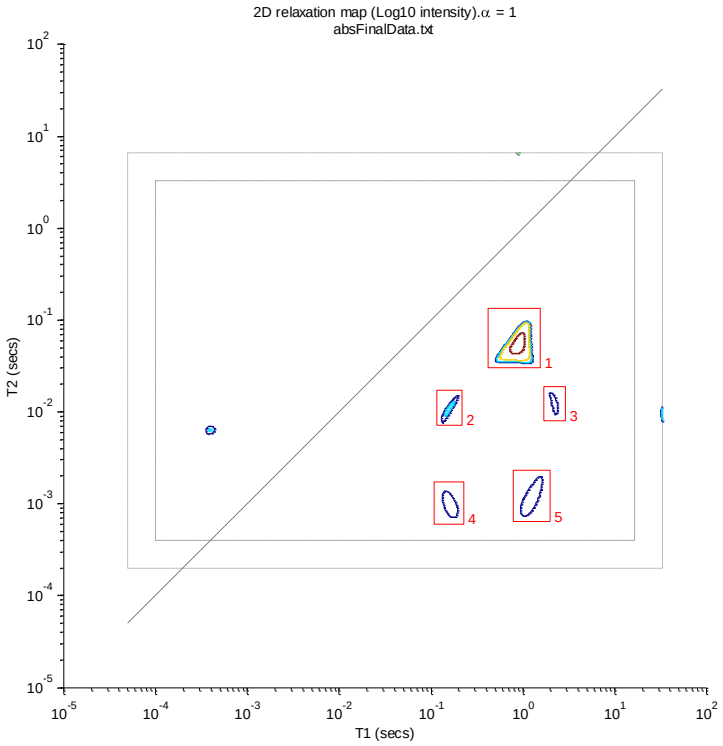

Figure 6.14 A characteristic 2D T_1-T_2 relaxation spectrum performed at 100 MHz on a sample of fresh lamb's kidney cortex using the TR method at equilibrium recovery demonstrating the 5 main peaks

Figure 6.14 shows a characteristic 2D T_1-T_2 relaxation spectrum performed at 100 MHz on a sample of fresh lamb's kidney cortex using the TR method at equilibrium recovery. Peaks 1 to 5 were clearly present in the kidney cortex spectra and appear to correspond with peaks found using the slow T_1-T_2 inversion recovery sequence (discussed in chapter 3). These comparisons are shown in Table 6.3.

Kidney cortex peaks slow/fast	slow area (std. dev.)	fast area (std. dev.)	slow T_1 (ms) (std. dev.)	fast T_1 (ms) (std. dev.)	slow T_2 (ms) (std. dev.)	fast T_2 (ms) (std. dev.)
1	0.40% (0.0%)		1330 (133)		575 (25)	
2/1	90.2% (2.0%)	89.0% (2.2%)	896 (1.9)	918 (62)	65.3 (9.9)	66.4 (14)
3/2	1.88% (0.28%)	2.30% (1.4%)	319 (133)	342 (105)	7.59 (3.0)	13.0 (11)
4/3	1.14% (1.0%)	1.77% (1.1%)	2520 (1240)	2100 (644)	3.94 (1.4)	15.9 (9.7)
5/4	3.06% (1.3%)	2.60% (1.5%)	273 (95)	275 (113)	0.80 (0.32)	1.81 (1.4)
6/5	2.40% (0.85%)	5.02% (1.5%)	1400 (583)	2210 (873)	0.53 (0.32)	1.75 (0.77)

Table 6.3 Mean peak intensity, T_1, and T_2 values for lamb's kidney cortex acquired at 100 MHz using both the slow and fast T_1-T_2 acquisition methods examining 5 samples with each sequence. Peaks have been lined up to indicate probable correspondence between spectra acquired using the different methods. Standard deviation given in brackets next to mean value.

The very small peak 1 in the spectrum of the slower sequence Figure 3.11 is not present in Figure 6.14 but at a mean peak intensity of 0.4% this is likely due to the slightly reduced signal to noise ratio due to the lack of multiple signal averaging in the faster sequence. The other peaks are present and replicated well using the faster sequence despite the lack of phase cycling. Figure 6.15 shows the peak positions in T_1 and T_2 of each peak as boxplots of the complete data set. As can be seen, the peaks are well replicated within the data set, particularly the dominant peak 1. Other peaks are clearly resolved by differences in either T_1 or T_2. Figure 6.16 shows boxplots of the peak areas of the dataset, showing a good replication of each peak in the spectrum, which is dominated by peak 1 (89%).

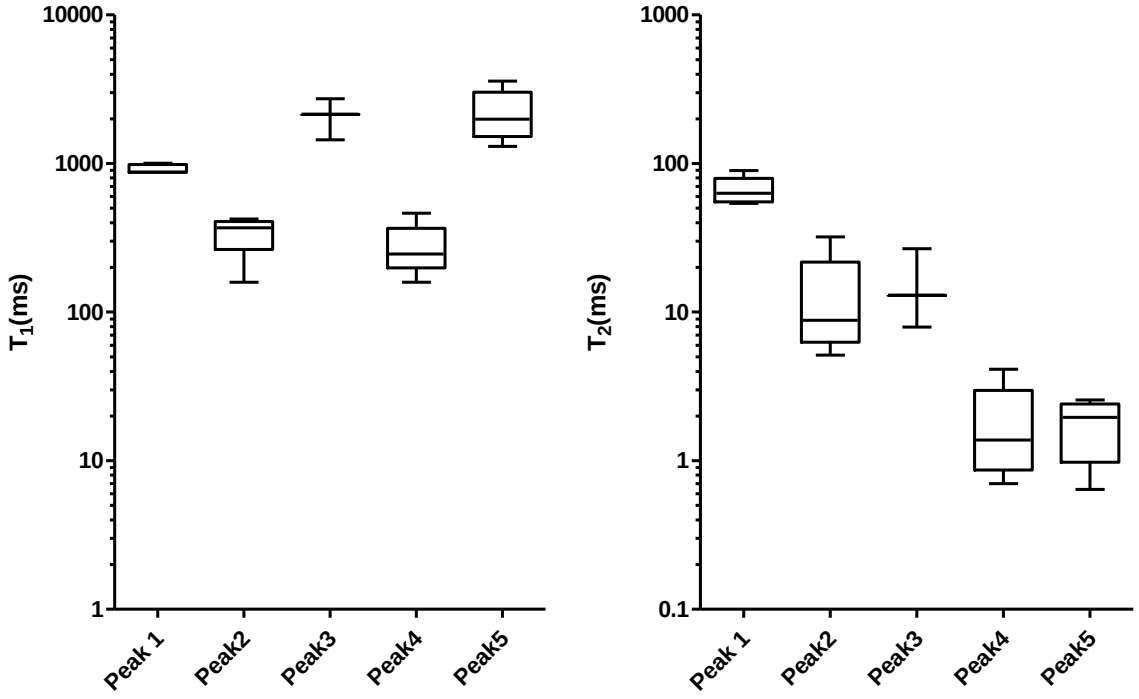

Figure 6.15 The peak positions in T_1(left) and T_2(right) of the 5 peaks obtained from T_1-T_2 relaxometry performed at 100 MHz on 5 samples of fresh lamb's kidney cortex using the TR method at equilibrium recovery, demonstrating the consistency in peak positions.

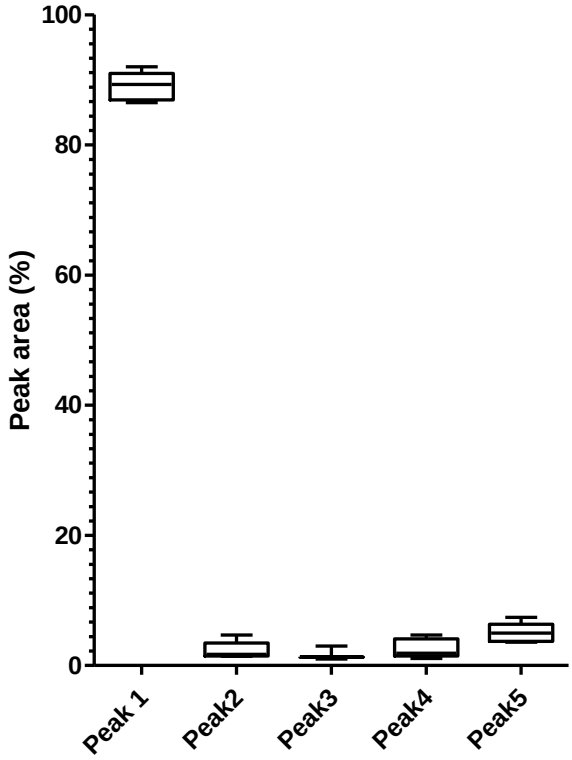

Figure 6.16 The peak intensities, as a percentage of the total peak marked intensity, of the 5 peaks obtained from T_1-T_2 relaxometry performed at 100 MHz on 5 samples of fresh lamb's kidney cortex using the TR method at equilibrium recovery, demonstrating the consistency in peak intensities.

Experiments with overlong TR periods determined that a TR of at least 10 seconds was necessary for equilibrium recovery of lamb kidney cortex tissue, as the longest T_1 detected was approximately 2 seconds. As discussed in section 3.4.1, this peak likely originates from non-exchanging protons in dissolved mobile proteins and biopolymers such as globular proteins and enzymes. The more significant time saving abilities of the TR method come into play with a sample like this. In order to ensure that the T_1 behaviour of the sample is properly characterised, shown by the inversion recovery curve reaching a stable equilibrium, a sufficiently long maximum t_1 value must be used. In this case that value was 20 seconds, as can be seen in Figure 6.17.

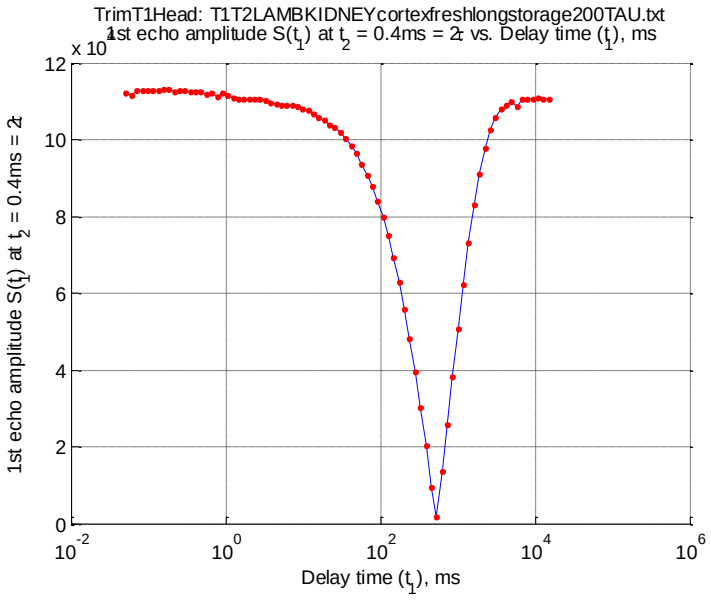

Figure 6.17 The t_1 dimension of the returned signal from a 2D T_1-T_2 relaxation experiment performed at 100 MHz on a sample of fresh lamb's kidney cortex. The signal is transferred to the data processing program as a magnitude and must be inverted before the minimum point to return the correct data set. The t_1 dimension is shown on a logarithmic scale with the maximum t_1 point at 20seconds (20000ms).

What can also be seen is the large number of points at the lower values of t_1 which must be acquired to build up a well characterised recovery curve. The time required to perform a traditional T_1-T_2 relaxation experiment on this sample is given by the formula below (eq 6.9).

$$t_{total} = [\ (2\tau * NECH) + t_1 \text{ longest} + \text{recovery time}]\ * \text{no. phase steps} * \text{no. } t_1 \text{ steps} \qquad \textbf{(eq 6.9)}$$

In which NECH is the number of echoes in the CPMG, no. phase steps is the number of phase encoding repeats and no. t_1 steps is the number of points acquired in the t_1 dimension. Using typical values of these parameters gives a minimum experimental time of just under 3 hours (177.48 minutes). Even by optimising the parameters to those used in the TR method and removing phase cycling, we get a total experiment time of 35.5 minutes. This time is significantly bloated by the requirement to wait the longest t_1 even for the large number of experimental steps acquired with far shorter t_1 values. Using the TR method we no longer have to wait any longer than the minimum necessary time for each step. In the case of the lamb kidney cortex sample the TR method experimental time was only 17 minutes, at least a twofold speed increase over the older sequence.

6.6.3 Kidney medulla

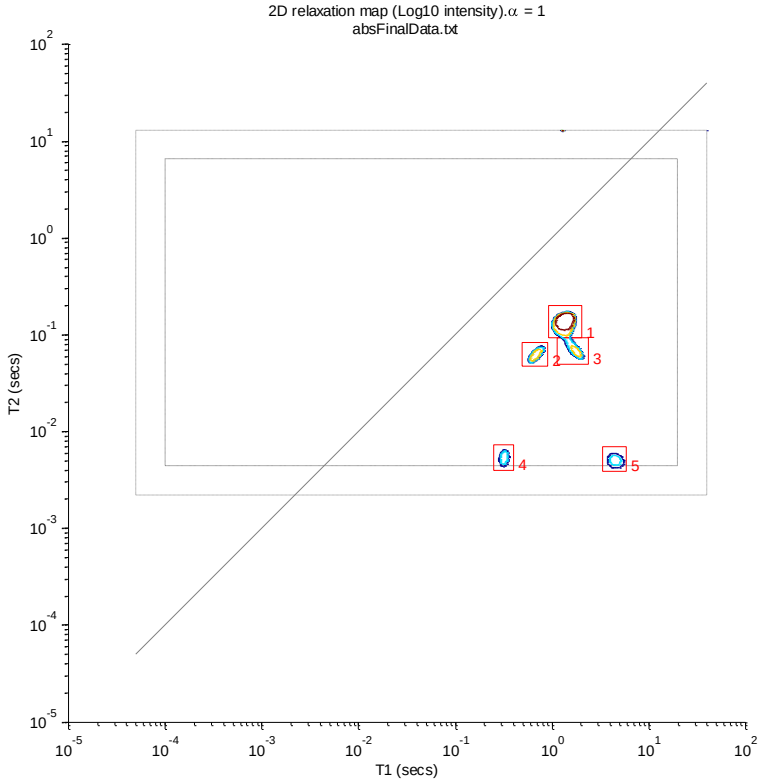

Figure 6.18 A characteristic 2D T_1-T_2 relaxation spectrum performed at 100 MHz on a sample of fresh lamb's kidney medulla using the TR method at equilibrium recovery demonstrating the 5 main peaks

Figure 6.18 shows a characteristic 2D T_1-T_2 relaxation spectrum performed at 100 MHz on a sample of fresh lamb's kidney medulla using the TR method at equilibrium recovery. Peaks 1 to 5 were clearly present in the kidney medulla spectra and appear to correspond with the well established peaks found using the slow T_1 - T_2 inversion recovery sequence (discussed in chapter 3). These comparisons are shown in Table 6.4.

Kidney medulla peaks slow/fast	slow area (std. dev.)	fast area (std. dev.)	slow T_1 (ms) (std. dev.)	fast T_1 (ms) (std. dev.)	slow T_2 (ms) (std. dev.)	fast T_2 (ms) (std. dev.)
1	0.88% (0.28%)		1920 (490)		804 (160)	
2/1	92.1% (4.4%)	84.2% (4.6%)	1310 (85)	1320 (90)	111 (7.2)	125 (30)
3/2	1.60% (0.66%)	5.86% (1.5%)	433 (290)	501 (110)	16.9 (12)	53.6 (8.2)
4/3	1.50% (0.42%)	7.93% (2.2%)	900 (820)	1750 (240)	5.06 (2.4)	58.0 (15)
5/4	3.00% (2.0%)	1.73% (0.83%)	441 (310)	232 (59)	1.16 (0.68)	6.21 (1.8)
6/5	1.70% (2.0%)	2.75% (1.1%)	2390 (710)	3400 (810)	0.72 (0.65)	5.77 (1.7)

Table 6.4 Mean peak intensity, T_1, and T_2 values for lamb's kidney medulla acquired at 100 MHz using both the slow and fast T_1-T_2 acquisition methods examining 5 samples with each sequence. Peaks have been lined up to indicate probable correspondence between spectra acquired using the different methods. Standard deviation given in brackets next to mean value.

As in other tissues, the very small peak 1 in the spectrum of the slower sequence (Figure 3.17) is not present in Figure 6.18. As before, the mean peak intensity of 0.88% indicates that this is likely due to the slightly reduced signal to noise ratio due to the lack of multiple signal averaging in the faster sequence. The other peaks are present and replicated well using the faster sequence despite the lack of phase cycling.

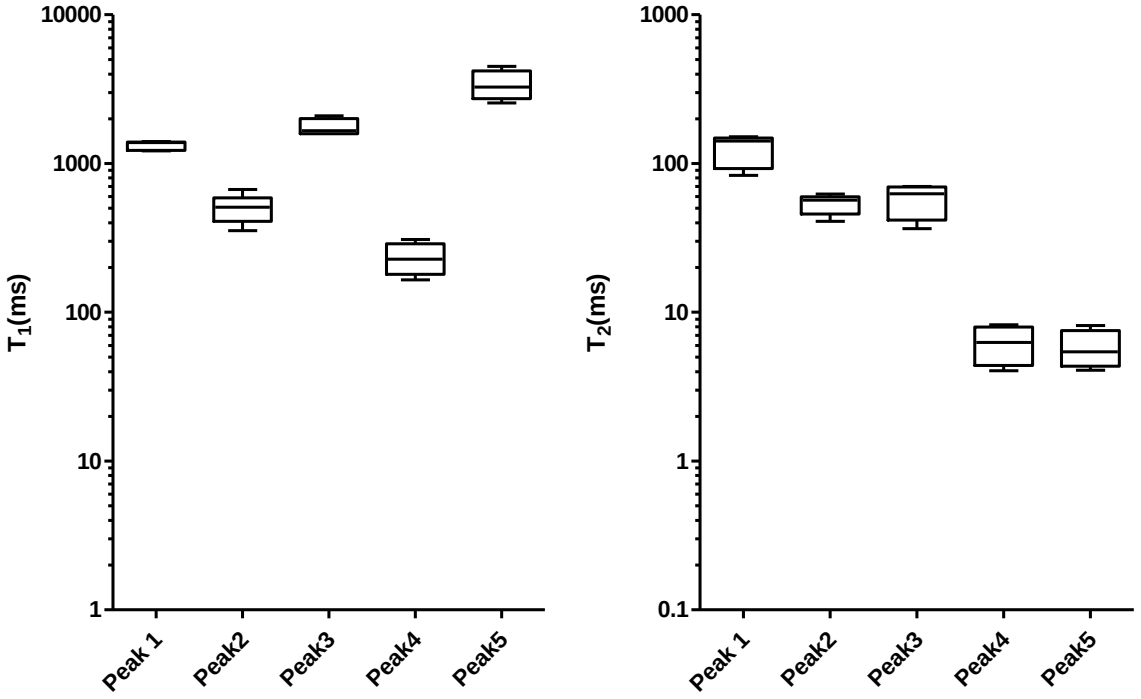

Figure 6.19 The peak positions in T_1(left) and T_2(right) of the 5 peaks obtained from T_1-T_2 relaxometry performed at 100 MHz on 5 samples of fresh lamb's kidney medulla using the TR method at equilibrium recovery, demonstrating the consistency in peak positions.

Figure 6.19 shows boxplots of the peak positions in each peak in the complete data set. There is little variation in the peak positions in either T_1 or T_2 of any peak and each is resolvable in either 1 or both of these dimensions. Figure 6.20 shows boxplots of the peak areas of the dataset, showing a good replication of each peak in the spectrum, which is dominated by peak 1. Peak 1's standard deviation is 4.6 which is higher than would be ideal but is still only a fraction (5.5%) of its value.

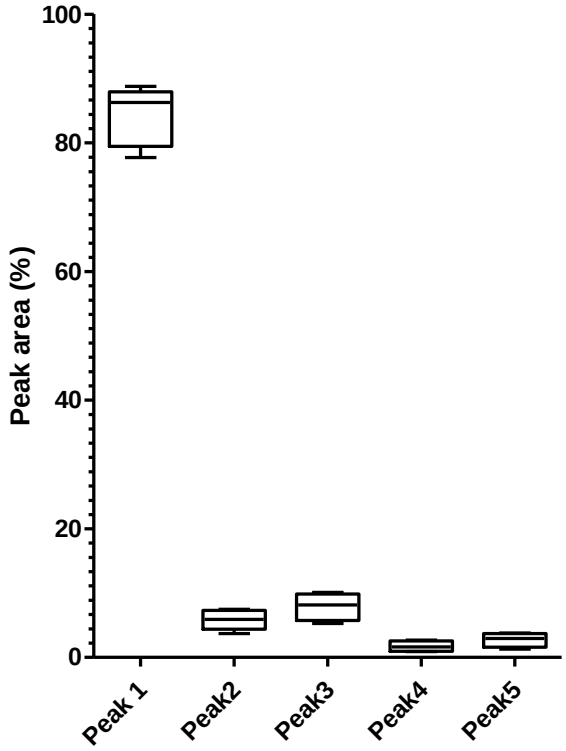

Figure 6.20 The peak intensities, as a percentage of the total peak marked intensity, of the 5 peaks obtained from T_1-T_2 relaxometry performed at 100 MHz on 5 samples of fresh lamb's kidney medulla using the TR method at equilibrium recovery, demonstrating the consistency in peak intensities.

Scans of lamb's kidney medulla could be acquired with 8k of echoes (8192) in the CPMG and 10 seconds of longitudinal recovery time TR, as with the lamb's kidney cortex. Therefore, as with the kidney cortex, using the slower T_1-T_2 relaxometry sequence on this sample using typical parameters would take just under 3 hours (177.48 minutes) and with parameters optimised for speed increase would take 35.5 minutes. Again as with the cortex, the total experiment using the fast TR method and this parameter set is only 17 minutes.

6.7 Conclusions

The TR method allows at least a halving of the required experimental time to acquire 2D T_1-T_2 relaxation spectra. In practice it is currently 10 times faster than the established T_1-T_2 acquisition protocols (slow sequence 177 minutes, fast sequence 17 minutes). This speed increase will be reduced by modifications to increase spectrum quality such as phase cycling or an increase in the number of t_1 values, to increase resolution in that dimension of the final spectrum.

Main peak	Tissues compared using TR method		P-value
Area	Kidney Medulla	Kidney Cortex	0.02
Area	Kidney Medulla	Liver	0.26
Area	Kidney Cortex	Liver	0.06
T1	Kidney Medulla	Kidney Cortex	<0.01
T1	Kidney Medulla	Liver	<0.01
T1	Kidney Cortex	Liver	<0.01
T2	Kidney Medulla	Kidney Cortex	<0.01
T2	Kidney Medulla	Liver	<0.01
T2	Kidney Cortex	Liver	<0.01

Table 6.5 P-values obtained from two tailed statistical t test on the main peak's area, T_1 and T_2 in different mammalian tissues at 100 MHz acquired using the TR method showing significant differences between each data set other than between the areas of the main peak in the liver and kidney medulla.

Table 6.5 shows the result of statistical t-tests on the area, T_1 and T_2 of the main intracellular water peak (as identified in chapter 3) common to each of the different mammalian tissues, examined at 100 MHz using the TR method at equilibrium recovery. We clearly see significant differences between the main peak's characteristics in the different tissue types, excluding its peak area when compared between the liver and the kidney medulla. Typically a p-value of 0.05 or less is considered significant and the p-value in this case (0.26) falls short of this. The p-value between the liver and the kidney cortex is also just slightly outside the typically desired level of statistical significance. It is important to note that this is the opposite of what was observed in the peak area comparisons using the slower T_1-T_2 relaxometry sequence in chapter 3. This should seriously reduce the confidence of any conclusions we may draw at this time from the main peak area with regards to tissue characterisation. Further experimental work would be necessary, possibly with improvements to the TR pulse program such as phase cycling, in order to draw definitive conclusions based on peak area. As with the slower sequence, the T_1 and T_2 values of this peak show clear and significant differences between the different tissues.

This would indicate that, even without further improvement to the TR method, tissue distinction is possible using this method of fast T_1-T_2 relaxometry. It has also been shown that spectra are fairly reproducible using the current TR method within the set of a single tissue type. This reproducibility will likely be improved by the phase cycling improvements already suggested. As discussed in chapters 3 and 4, in situations where tissue identification is not possible through single peak comparisons the various parameters of each consistent peak could be combined to form a unique fingerprint for each tissue.

These tissue fingerprints could be used with statistical or probabilistic classification methods[86-88] such as principal component analysis (PCA)[89-91] to specifically identify spectra from a library of potential matches.

In this thesis so far it had been demonstrated (in chapter 3) that 2D T_1 - T_2 relaxation methods can be used to acquire characteristic 2D relaxation spectra. It was shown that these spectra are conserved within a tissue and vary from tissue to tissue, opening the possibility of using them to distinguish between tissue types. The data gathered here is shown to fit within the framework of other studies of the same or similar tissues, despite those studies being conducted with a focus on high image resolution and low spectral resolution (usually acquiring only single T_1 or T_2 values).

Using similar methods it has also been shown (in chapter 4) that discrimination between healthy and diseased tissue, in this case human articular cartilage, can be achieved through 2D T_1 - T_2 relaxation methods. As before, the data acquired here has been compared to, and fits well with, the wider framework of similar studies, although this comparison is plagued by the same lack of high spectral resolution data acquired by others with this tissue.

Contrast simulation methods have been demonstrated (chapter 5) to make use of these characteristic T_1 - T_2 relaxation spectra in predicting image contrast in MR imaging sequences, with the potential for this to be expanded into standard MRI practice discussed.

Finally, in this chapter methods of accelerating the speed of acquisition have been presented and the TR method tested on the same sample types as those used in chapter 3. In this chapter it has been shown that, even in its current state, the TR method provides tissue specific and differentiable T_1 - T_2 relaxation spectra and methods of improvement have been presented.

7. Summary and Future Direction

Optimising MRI image contrast provides the opportunity to improve the day to day use of medical MRI technologies. Optimising the choice of pulse sequence, spectrometer frequency and parameter set requires first that we acquire a detailed knowledge of the NMR parameters (T_1, T_2, T_2* .....) characterising each tissue type to be examined by the clinical practitioner. A more thorough characterisation of these tissues is achieved using not 1D, but 2D relaxometry, which can include but is not limited to T_1 - T_2, T_2 - D and T_2-store-T_2 sequences. Making use of these 2D relaxation spectra for the purpose of MRI contrast prediction requires the implementation of 'in-silico' computer based contrast prediction methods which allow experimentation with different tissue types, spectrometer frequencies, MRI pulse sequences and parameter sets. Beyond their use as contrast prediction data, 2D T_1 - T_2 relaxation spectra provide the potential for use in identifying and differentiating a multitude of tissue types. The superior tissue characterisation properties of 2D T_1 - T_2 relaxation spectra show potential for use in differentiating not just different types of tissue, but different states of disease and health within a tissue type. To this end it must be shown that 2D T_1 - T_2 relaxation spectra are characteristic of a tissue type or disease state and vary to a sufficient extent to allow differentiation between different healthy tissues or different disease states within a single tissue. To be used in a clinical setting it must also be shown that 2D T_1 - T_2 relaxation spectra can be acquired fast enough to be used in practice with patients. Experimental times measured in hours rather than minutes could be a barrier to entry into the clinical setting and so methods to reduce the acquisition time of a 2D T_1 - T_2 relaxation spectrum are a necessary step in its implementation in this field.

To this end, in chapter 3 we examine the characterisation of healthy mammalian tissue from samples of the lamb's liver, kidney cortex and kidney medulla, using 2D T_1 - T_2 relaxometry at 100 MHz and 23.4 MHz. At both spectrometer frequencies we establish by direct spectral comparison and statistical t-tests, that each of the tissues can be clearly distinguished (with typical p values < 0.01), even when considering only a single parameter of a single peak. We also establish via box plots a good degree of replicability between 2D T_1 - T_2 relaxation spectra acquired from a single tissue type.

In chapter 4 the concept of 2D T_1-T_2 relaxometry as a designator of tissue condition in health and disease is examined, using as an example the case of potential osteoarthritic degradation in human articular knee cartilage. It is clearly demonstrated that not only can the healthy cartilage be distinguished from the unhealthy, but that there may be two distinguishable stages of disease progression within the diseased group. These differences may be due to different stages of the disease, or different underlying causes of the disease. Using only the peak intensity of the main peak, statistical t-tests give p values of < 0.006 for comparisons of these three tissue conditions indicating statistical significance to these results.

In order to allow optimisation of the choice of pulse programs and parameters in MRI practice, chapter 5 presents 2 possible methods of simulating contrast in MRI pulse programs using 2D T_1-T_2 relaxation spectra. The first (VSS) is developed to simulate, from the individual spin voxels up, the behaviour of a complete sample undergoing an MRI pulse sequence with fully characterised T_1-T_2 relaxation behaviour during it. It provides a final image of the initial sample and can be programmed to contain different tissues (by affecting different voxels with different 2D relaxation spectra) in order to provide a visual and numerical representation of predicted image contrast. The second method takes advantage of the fully characterised T_1-T_2 relaxation behaviour of a tissue and combines it with an existing MRI pulse program simulation suite (ODIN[(121)]) to determine final image intensity of a single voxel of a specific tissue type, which can then be compared to others acquired with different relaxation behaviour but the same simulated sequence and parameters to determine final image contrast between two or more tissues. In evaluating the potential application of each method it is demonstrated that the second is superior for the purpose of contrast simulation as it provides the opportunity to establish a library of 'relaxation signatures' (discussed fully in section 5.3.1) which could quickly be used in conjunction with a 2D T_1-T_2 relaxation spectrum to determine the image intensity of a tissue. The first method simulates a significant amount of unnecessary information and is labour intensive with regards to programming new MRI pulse sequence simulations as well as time intensive with regards to re-simulating each sequence with each parameter set and T_1-T_2 relaxation spectrum. Additional work to acquire the T_1-T_2 relaxation spectra of more tissues would allow a greater range of tissues to be simulated, providing the ability to determine image contrast between any tissues in which it is required, such as between

healthy organ tissue and lesions or tumours within that organ.

One of the key issues of this type of relaxometry is the long acquisition time. In chapter 6 methods were developed to increase the speed of acquisition of the 2D T_1-T_2 relaxation spectra vital to the characterisation, differentiation and contrast simulation work so far performed. Three methods proposed and developed in the group were discussed and the TR method (developed by me) was implemented and used on the same samples as those in chapter 3, namely lamb's liver, lamb's kidney cortex and lamb's kidney medulla. Spectra acquired with this method were examined in the same manner as those acquired in chapter 3 using the slow technique. By direct spectral comparison and using statistical t-tests of the main peaks intensity, T_1 and T_2, it is demonstrated that each of the tissues can be clearly distinguished (with typical p values < 0.02), even when considering a single parameter of the main peak. The peak intensity values are not as easily distinguished as the relaxation times (T_1 and T_2) and will require further experimentation to more clearly determine their difference or similarity with certainty. The additional time savings offered by saturation and intermediate recovery experiments are discussed with reference to the loss of spectral quality versus speed increase and it is determined, for these tissues with the current program and data set, that full inversion recovery provides adequate speed increase (between 2 and 10 fold) without greatly sacrificing spectrum quality. Potential improvement to the sequence, such as phase cycling, is proposed but the current program is determined to provide adequate spectrum reproducibility and quality.

These approaches demonstrate the information available with current 2D relaxometry techniques in the laboratory and medical field as well as the potential for newly developed techniques for use in a clinical setting. Further work would be required to implement these techniques out of the laboratory setting. Some further ideas for future development are presented below.

7.1 Volume selective 2D NMR spectroscopy

The advent of ultrafast, volume selective 2D relaxometry could potentially provide entirely new clinical diagnostic techniques[20, 110, 127, 128, 133]. While the ultrafast and volume selective aspects have been developed and tested separately in vitro within the department,

the challenge remains to combine them into a single sequence for in vitro testing before implementing it on clinical MRI scanners. For volume selection the SPACE (not an acronym)[134] sequence has been selected and implemented in our lab to acquire 2D T_1 - T_2 relaxation spectra. The SPACE sequence localises the signal obtained to that of the VOI (volume of interest) by refocusing the magnetisation within the VOI as a spin echo and restoring it to longitudinal magnetisation while converting the magnetisation outside the VOI into transverse magnetisation, which is then destroyed using a spoiler gradient.

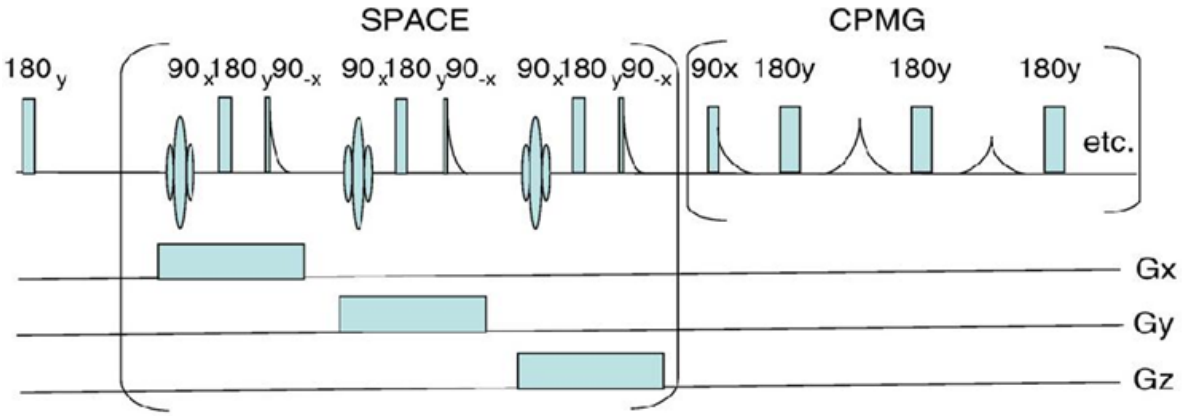

Figure 7.1 reproduced from (*133*). The inversion recovery- SPACE-CPMG pulse sequence. The standard inversion recovery – CPMG sequence has been modified with the addition of a volume selective SPACE sequence within the period of longitudinal recovery, just before the CPMG section.

Figure 7.1[133] shows how SPACE can be concatenated with the 2D T_1-T_2 sequence to provide acquisition of a 2D relaxation spectrum from a specific volume of interest. To avoid recovery of the magnetisation outside the VOI, the SPACE sequence is inserted at the end of the inversion recovery step. The inversion recovery and CPMG sequences will only yield signal response from the VOI and allow a 2D signal matrix to be acquired and analysed as normal in order to obtain a full T_1 - T_2 relaxation spectrum of the VOI. Figure 2.14 produced by Venturi and Hills[133] shows 2D T_1 - T_2 relaxation profiles obtained from signals acquired using this sequence, but selecting a slice rather than a single volume element, on a 10 mm wide NMR tube containing a layer of water resting on top of a layer of agarose. As can be seen, slice selection at specific heights in the tube is achieved by varying the frequency of the slice selective pulses, allowing acquisition of signal response from layers above, below, and straddling the boundary between agarose and water.

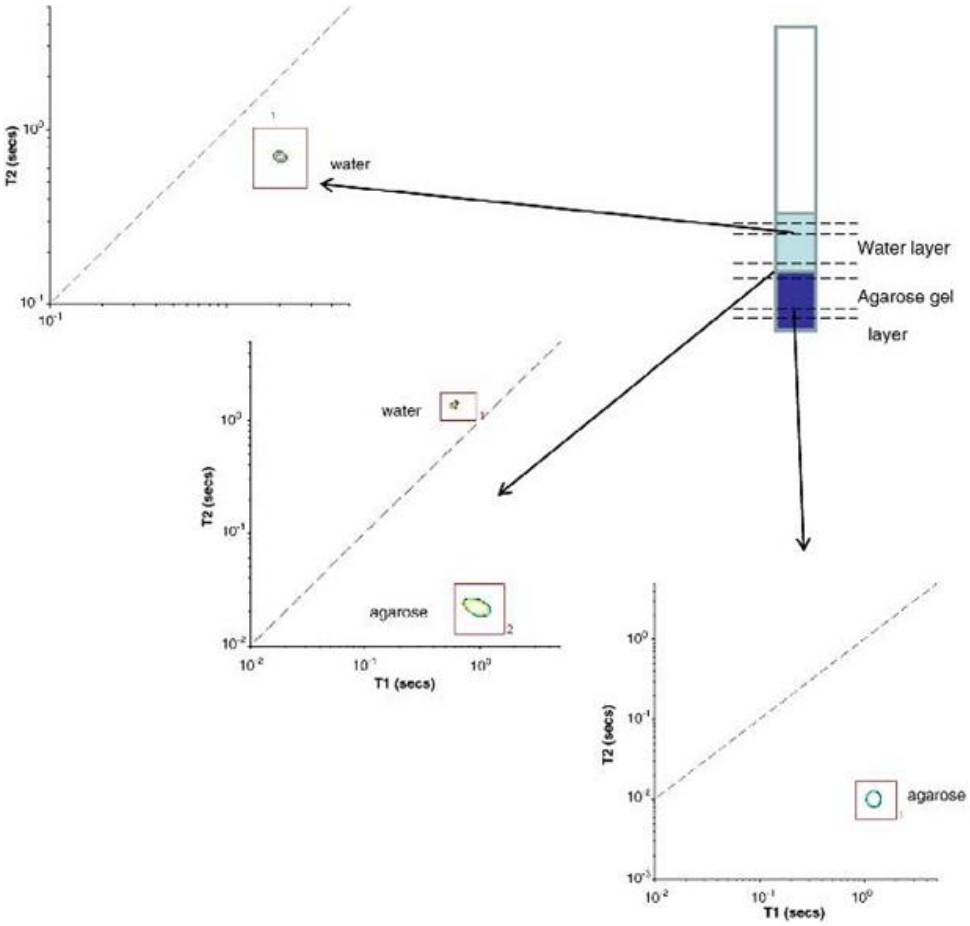

Figure 7.2 reproduced from (*133*). 2D T_1-T_2 relaxation profiles obtained using the inversion recovery-SPACE sequence on a 10mm wide NMR tube containing a layer of water resting on top of a layer of agarose.

A single peak is observed for each substance in the sample, resolved in both T_1 and T_2. Only the peak corresponding to either water or agarose is seen in the relevant slice selected scan while both are present in the boundary centred slice. The SPACE sequence provides a simple and effective method of volume selection and should be able to be inserted into the TR method at the end of the inversion recovery period, theoretically without slowing the sequence except when examining very low values of T_1. In this case if there were no room to include the volume selective step within the inversion recovery step then it could be placed before it, which should not cause problems as the recovery outside the VOI during this very short time should be minimal. In addition to the SPACE technique, a method has been proposed within the group to achieve volume selection through the use of the first 3 echoes of the CPMG sequence itself. Following the standard inversion recovery period the CPMG sequence is begun but, rather than going straight into hard 180 degree pulses and acquiring echoes, the first three 180 degree pulses are slice selective soft pulses performed in appropriate gradients so as to achieve volume selection. The rest of the CPMG is then

run as normal and echoes acquired to achieve the final 2D spectrum. This method also destroys magnetisation outside the VOI.

The use of multislice methods with these sequences, as discussed in chapter 6, would be more challenging from a programming standpoint as it would involve co-ordinating a single shot sequence so as to affect each slice in turn during the TR recovery period of the one before. In principle this is not a serious problem but would involve careful timing of each step and may require, at least initially, that a limited, and possibly fixed, number of slices be acquired so as to keep track of these precision timings. Each of these steps is currently in development under the name Clinical Ultrafast RElaxometry (CURE)[127].

7.2 CURE (Clinical Ultrafast RElaxometry)

The development of CURE does not just depend on implementation of the pulse sequence itself but also on its demonstrated ability as a practical biomarker in one or many clinical situations. In this thesis it has been shown that 2D relaxometry has the potential for differentiating diseased and healthy human articular cartilage in the context of osteoarthritis (chapter 4) as well as differentiating different mammalian tissues (chapter 3). This would seem to indicate that it has the potential to differentiate various tissue types as well as the condition of specific tissue types in various disease states, such as cancer formation or tissue degradation. Currently proposed projects include the differentiation of thermo-ablated liver tissue from the surrounding unaffected tissue. This is an important ability both clinically and in the development of thermo-ablation probes, as the technique is used to destroy regions of the liver large enough to include all observed tumours therein[135-138], and the border of destroyed tissue must be well established so as to achieve the stated goal with the minimum loss of healthy tissue. This characterisation is not easily achieved using currently available methods[139, 140].

Differentiation of the cortico-medullary border (the border between the cortex and medulla of the kidney), taken in clinical circles as a sign of kidney health[141-145], is another area that may warrant investigation. The specific reasons for the difference in image intensity, and the changes which lead to its loss, could be examined by 2D relaxometry, perhaps over time in a patient population, without the need to dissect or biopsy a sample.

Another potential application uses the CURE technique in the diagnosis of early stage prostate cancer. MRI is currently used to provide physical data on the size and location of tumour development[146-148] and quantitative T_2 mapping has shown a detectable difference between healthy and cancerous tissue[149, 150]. While interesting, this technique only uses a few (typically 16) data points to calculate an average T_2 exponential, falling far short of the information contained in a 2D T_1 -T_2 profile acquired with the CURE technique. It is hoped that CURE can act as a diagnostic biomarker in early stage prostate cancer as well as further utilising the information in the spectrum to quantitatively correlate its features with the biopsy based Gleason score (used to quantify the progress of the cancer)[151, 152] as well as finding correlations with the PSA (prostate serum antigen) level in the blood[148, 153].

On a less clinical front, projects proposed to the BBSRC include the examination of food in the gut. Currently the effect of food composition and microstructure on the digestive process is under close scrutiny in the food science field. Current methods for following food through the digestive system and examining its state at various points are not well developed and often include the use of experimental animals and their dissection at various digestive stages in order to get at the gut contents, or simply collection of faecal matter following complete digestion[154, 155]. Through the use of the CURE technique, food could be followed through the gut and 2D relaxometry performed to investigate its state and composition at each stage of the digestive process. This would improve our knowledge of in vivo digestion processes and physiological effects such as appetite control and allow the development of methods to improve bioavailability of nutrients from food matrices and targeted delivery of drugs.

7.3 Enhanced and computational characterisation enhancement

The potential of tissue characterisation has been demonstrated within this thesis with simple peak comparisons of a single peak's area, T_1 and T_2. The concept of using multiple peaks in this way was also discussed briefly with regards to statistical or probabilistic classification methods[86-88] such as principal component analysis (PCA)[89-91]. PCA involves a mathematical procedure to take a large set of possibly correlated variables and convert them into the same size or smaller set of linearly uncorrelated variables known as

principal components. The procedure is defined so as to make the first variable account for as much variation in the data as possible and the following variables, in order, account for as much of the remaining variability as possible while being orthogonal to (uncorrelated with) the existing variable. By reducing the variable space of our data (area, T_1 and T_2 for each peak) we may be able to identify clusters around tissue type and, ideally, large differences between specific tissue types or states that require distinction or categorisation.

Expert systems are computer systems designed to emulate the decision making abilities of a human expert[156-158]. An inference engine conducts logical reasoning based on a predefined set of rules known as "the rule base" or "knowledge base". This knowledge base can be expressed in natural language using IF, AND, OR, THEN, etc. In the case of human cartilage characterisation using only the main peak we might have;

"**IF** sample has a peak that has 85% area ± 15% **AND** that peak has T_1 of 870 ms ± 100 ms **AND** that peak has T_2 of 35 ms ± 22 ms **THEN** there is a strong probability that tissue is healthy cartilage"

This kind of rule could be expanded to include any number of peaks, looking at values of their peak area, T_1 and T_2 to establish the identity of the tissue. In the case of identifying T_1-T_2 spectra the data would likely be provided all at once but expert systems are also capable of acquiring data from the user as they go, refining and elaborating on the data set as the process goes on. Either way these systems rely on the knowledge base being correctly inputted and properly set up to achieve the decision making capabilities necessary for accurate diagnosis.

Many are trying to achieve the aims of expert systems using more adaptive technologies such as neural networks[159]. Neural networks in artificial intelligence and problem solving take inspiration from biological neural networks in that rather than using a single, set and designed network of computing modules and pathways, they are composed of artificial nodes or processing elements connected with each other in a complicated network like that of an biological neural net[160]. While the individual elements are simple, combined in this form they are capable of exhibiting complicated global behaviour. The neural net works with algorithms which alter the strength of the connections in the network to produce a desired output from a specified input. The distance from the desired output is assigned a

cost and so, over time the neural net will get better at producing the desired output. In this way it can be "trained"[161] to perform tasks such as those of an expert system[162].

7.4 MRICOM

The MRICOM[110] methodology provides ample future direction for investigation. Any pulse sequence that ODIN can model can be investigated and a library, not only of each sequence but, also of different parameters used with each sequence, would be needed to make it a truly generalizable method for the optimisation of image contrast. It would also require the acquisition of the 2D T_1 - T_2 relaxation profiles of each tissue to be examined. Under current experimental limitations this would require the extraction and scanning of tissue samples from each tissue type in vitro. This could be a shared research objective with the CURE project, which would itself require examination of many tissue types to establish its applicability. Furthermore, once the CURE protocol has been fully implemented, T_1 - T_2 relaxation profiles could be acquired from tissues in vivo, reducing the need for physical sample extraction and widening the range of available tissues, as any requiring removal via unnecessary biopsy would be essentially unavailable in an experimental setting. There is even the possibility that, given short enough computational times, T_1 - T_2 relaxation profiles could be acquired, via CURE, from a patient and the optimal contrast protocol established via MRICOM for immediate implementation. If this were to become common practice however, it would probably require the development of an algorithm to calculate final image intensities and contrasts automatically, so as to provide a list of the optimal imaging sequences and parameters without the clinical MRI practitioner being required to possess a detailed knowledge of the MRICOM methodology. This could be achieved using expert systems or neural networks.

7.5 Novel multidimensional spectroscopy sequences

All of these methods so far are based on the T_1 -T_2 relaxation spectrum which provides ample information of the relaxation behaviour of the sample. There are of course, many other 2D relaxometry options available to the NMR practitioner. As mentioned in previous chapters, the T_2-store-T_2 sequence, while previously used for peak assignment, can provide

additional information on the sample under examination[58]. The T_2-store-T_2 sequence allows the identification of additional exchange cross peaks due to magnetisation transfer between different proton pools. In a T_2-store-T_2 spectrum the standard peaks from a one dimensional T_2 spectrum are projected onto the diagonal between the two axes and, when the store time is comparable to the exchange lifetime between two peaks, cross correlation peaks appear in the spectrum. This allows exchange rates to be estimated but, on a qualitative basis, also provides another characteristic 'finger-print' profile of the sample. As with the T_1 - T_2 spectra, T_2 - store - T_2 spectra are an indication of the microstructure and composition of a sample and may be useful in differentiating tissues. The T_2 - store - T_2 sequence could be combined with volume selective methods so as to provide another clinically applicable biomarker to aid in diagnostic specificity. Multislice techniques[128] could also be used to increase its speed and therefore, its clinical applicability. T_2 - store - T_2 protocols would be difficult to combine with FLOP methods because the store period would change the steady state created by FLOP[129].

The T_2-D[23, 63] sequence was also used previously to aid in peak assignment and provides useful information about the sample. It allows examination of the diffusive properties of a T_2 peak in a certain direction. While this provides useful information in the lab, diffusion is already examined far more effectively in a medical context using DTI (Diffusion Tensor Imaging)[92, 163, 164]. In simple terms, the intensity of the image in a voxel is attenuated based on the direction and strength of an applied magnetic diffusion gradient. If greater diffusion occurs then the image intensity is more attenuated and by calculating based on a number of scans with different magnetic diffusion gradient directions, the complete diffusion profile of a voxel is established. The technique can be used to examine subtle pathology in complex regions such as the brain and the directional information can be used to examine its fine structure, even following specific neural tracts through the tissue. Whether the cross correlation between DTI and T_2 data provides additional valuable information remains to be investigated.

Another interesting parameter for study is the rotating-frame relaxation time, $T_{1\rho}$[20, 111]. Measurement of $T_{1\rho}$ involves the use of a technique known as spin locking in the rotating frame. Magnetisation is spin locked for a time τ by phase shifting the radio-frequency field of amplitude B_1 so that the effective field experienced by the spin is simply B_1 in parallel to the spin alignment. During this spin locked time τ the magnetisation relaxes in the B_1

field and following this period the signal is recorded as a standard FID (free induction decay, described in chapter 1). During the spin locked phase the resonant frequency of the spin is given by $\omega_1 = \gamma B_1$ and so the sample relaxes according to the time constant $T_{1\rho}(\omega_1)$. Longitudinal relaxation times, described previously in this thesis as T_1, are more accurately denoted as $T_1(\omega_0)$ wherein ω_0 is the main resonant frequency of the spin system. As the value of ω_1 approaches ω_0 the value of $T_{1\rho}(\omega_1)$ will approach the value of $T_1(\omega_0)$. Likewise as the value of ω_1 approaches 0 the $T_{1\rho}(\omega_1)$ value will approach that of T_2. We can now see that the $T_{1\rho}(\omega_1)$ frequency dispersion lies between that of T_1 and T_2 and contains dynamic information on the ω_1 frequency scale. Various 2D spectra could therefore be developed around rotating frame relaxation $T_{1\rho}$. Examples might include $T_{1\rho}$-T_2, $T_{1\rho}$-D, and T_1 -$T_{1\rho}$ which have not even been attempted on biological tissues in a lab setting. Work has also begun on a new 2D sequence to examine the fine micro-structure of inhomogeneous foams which could also be used to examine the structure of biological tissues. In its simplest form it comprises two concatenated CPMG sequences, the first with a long echo spacing so that it is sensitive to local susceptibility gradients, the second with a short echo spacing so it measures T_2. By utilising this sequence we can elucidate fine micro-structure too small for examination by conventional methods.

7.6 Conclusions

The examination of biological tissues using only the information provided by the two dimensional T_1 -T_2 relaxation pulse sequence has barely scratched the surface of what is possible[*(127)*]. Many tissue types have yet to be examined and acquisition and peak assignment of the spectra of these tissues in various healthy and diseased states may provide invaluable information on the composition of that tissue and the changes taking place within it at a microscopic level. Exploitation of this information, through the use of techniques such as MRICOM, are only in the testing and development phase but promise to greatly increase the efficiency and usefulness of existing clinical practices. The implementation of CURE holds the potential of introducing entirely new diagnostic testing possibilities through the use of 2D relaxation spectra as clinical biomarkers. Combination of CURE with expert systems and neural networks could provide clinicians with tissue and disease state classification methods for use in diagnosis and in development of medical technologies and procedures. All this is without examining the huge range of available 2D

sequences or the development and implementation of new ones, based on parameters such as $T_{1\rho}$. This thesis has examined some of this potential with a specific focus on possible medical applications, but the field of 2D cross correlation relaxometry is still a new and emerging one with vast amounts of potential both within the medical field and in many different basic science and laboratory settings.

8. References

1. P. Remplik, A. Stabler, T. Merl, F. Roemer, K. Bohndorf, Diagnosis of acute fractures of the extremities: comparison of low-field MRI and conventional radiography. *European radiology* **14**, 625 (Apr, 2004).
2. J. H. Ku, Y. S. Jeon, M. E. Kim, N. K. Lee, Y. H. Park, Is there a role for magnetic resonance imaging in renal trauma? *International journal of urology: official journal of the Japanese Urological Association* **8**, 261 (Jun, 2001).
3. E. Paakko, H. Reinikainen, E. L. Lindholm, T. Rissanen, Low-field versus high-field MRI in diagnosing breast disorders. *European radiology* **15**, 1361 (Jul, 2005).
4. M. A. Bredella *et al.*, Accuracy of T2-weighted fast spin-echo MR imaging with fat saturation in detecting cartilage defects in the knee: comparison with arthroscopy in 130 patients. *AJR. American journal of roentgenology* **172**, 1073 (Apr, 1999).
5. D. G. Disler *et al.*, Fat-suppressed three-dimensional spoiled gradient-echo MR imaging of hyaline cartilage defects in the knee: comparison with standard MR imaging and arthroscopy. *AJR. American journal of roentgenology* **167**, 127 (Jul, 1996).
6. B. P. Kreft *et al.*, Diagnostic value of MR imaging in comparison to CT in the detection and differential diagnosis of renal masses: ROC analysis. *European radiology* **7**, 542 (1997).
7. A. Abragam, *The principles of nuclear magnetism*. The International series of monographs on physics (Clarendon Press, Oxford,, 1961), pp. 599 p.
8. E. Merzbacher, *Quantum mechanics*. (Wiley, New York ; Chichester, ed. 3rd ed., 1998).
9. B. L. Cohen, *Concepts of Nuclear Physics*. (McGraw-Hill, [S.l.], 1971).
10. J. W. Rohlf, *Modern physics from a to Z*. (John Wiley, New York ; Chichester, 1994).
11. A. Das, T. Ferbel, *Introduction to nuclear and particle physics*. (J. Wiley, New York, 1993).
12. M. H. Levitt, *Spin dynamics: basics of nuclear magnetic resonance*. (John Wiley & Sons, Chichester, 2001).
13. A. H. Carter, *Classical and statistical thermodynamics*. (Prentice Hall, Upper Saddle River, N.J., 2001), pp. xvi, 432 p.
14. F. Bloch, W. W. Hansen, M. Packard, Nuclear Induction. *Physical Review* **69**, 127 (1946).
15. F. Klein, A. Sommerfeld, *Über die Theorie des Kreisels ... mit 143 Figuren im Text*. (B.G. Teubner, Leipzig,, 1897), pp. viii, 966 p.
16. F. Klein, A. Sommerfeld, R. J. Nagem, G. Sandri, *The theory of the top*. (Birkhäuser, Boston, 2008), pp. v <1-2>.
17. R. K. Harris, *Nuclear magnetic resonance spectroscopy: a physicochemical view*. (Pitman, London, 1983).
18. F. A. L. Anet, D. J. O'Leary, The shielding tensor. Part I: Understanding its symmetry properties. *Concepts in Magnetic Resonance* **3**, 193 (1991).
19. T. D. Scholz, S. R. Fleagle, F. C. Parrish, T. Breon, D. J. Skorton, Effect of tissue fat and water content on nuclear magnetic resonance relaxation times of cardiac and skeletal muscle. *Magnetic resonance imaging* **8**, 605 (1990).
20. B. Hills, *Magnetic resonance imaging in food science*. (Wiley, New York, 1998), pp. ix, 342 p.
21. WINDXP. (Resonance Instruments Ltd, Unit 31A, Avenue One, Station Lane, Witney, OX28 4XZ, UK), vol. Version 1.8.0.0.
22. J. Keeler, *Understanding NMR spectroscopy*. (Wiley, Oxford, ed. 2nd ed., 2010).
23. M. D. Hurlimann, L. Venkataramanan, Quantitative measurement of two-dimensional distribution functions of diffusion and relaxation in grossly inhomogeneous fields. *Journal of Magnetic Resonance* **157**, 31 (Jul, 2002).
24. Y. Q. Song *et al.*, T-1-T-2 correlation spectra obtained using a fast two-dimensional Laplace

inversion. *Journal of Magnetic Resonance* **154**, 261 (Feb, 2002).
25. N. A. Marigheto. (University of East Anglia 2007).
26. N. Marigheto, S. Duarte, B. P. Hills, NMR relaxation study of avocado quality. *Appl Magn Reson* **29**, 687 (2005).
27. N. Marigheto *et al.*, Methods for peak assignment in low-resolution multidimensional NMR cross-correlation relaxometry. *Journal of Magnetic Resonance* **187**, 327 (Aug, 2007).
28. R. R. Ernst, G. Bodenhausen, A. Wokaun, *Principles of nuclear magnetic resonance in one and two dimensions*. (Clarendon, Oxford, 1987).
29. R. Freeman, Selective Excitation in High-Resolution Nmr. *Chem Rev* **91**, 1397 (Nov, 1991).
30. A. N. Garroway, P. K. Grannell, P. Mansfield, Image formation in NMR by a selective irradiative process. *Journal of Physics C: Solid State Physics* **7**, L457 (1974).
31. *NMR : basic principles and progress*. (Springer, Berlin, 1969).
32. G. Woan, *The Cambridge handbook of physics formulas*. (Cambridge University Press, Cambridge, 2000).
33. P. C. Lauterbur, Image Formation by Induced Local Interactions - Examples Employing Nuclear Magnetic-Resonance. *Nature* **242**, 190 (1973).
34. S. R. Deans, *The Radon transform and some of its applications*. (Wiley, New York ; Chichester, 1983).
35. F. W. Wehrli, D. Shaw, J. B. Kneeland, *Biomedical magnetic resonance imaging : principles, methodology and applications*. (VCH, New York, 1988).
36. S. L. Smith, Nuclear magnetic resonance imaging. *Analytical chemistry* **57**, 595A (Apr, 1985).
37. A. Kumar, D. Welti, R. R. Ernst, Nmr Fourier Zeugmatography. *Journal of Magnetic Resonance* **18**, 69 (1975).
38. S. Ljunggren, A Simple Graphical Representation of Fourier-Based Imaging Methods. *Journal of Magnetic Resonance* **54**, 338 (1983).
39. D. B. Twieg, The K-Trajectory Formulation of the Nmr Imaging Process with Applications in Analysis and Synthesis of Imaging Methods. *Med Phys* **10**, 610 (1983).
40. R. J. Stafford, High field MRI - Technology, applications, safety, and limitations. *Med Phys* **32**, 2077 (Jun, 2005).
41. Y. Korogi, M. Takahashi, Cost containment and diffusion of MRI: oil and water?. Japanese experience. *European radiology* **7 Suppl 5**, 256 (1997).
42. R. Passariello, Cost containment and diffusion of MRI: oil and water?. The situation in Europe. *European radiology* **7 Suppl 5**, 259 (1997).
43. S. Crozier, D. M. Doddrell, In vivo localized H-1 spectroscopy of the rat eye at 7T: Preliminary studies. *Magn Reson Mater Phy* **3**, 137 (Sep-Dec, 1995).
44. Z. Ababneh *et al.*, Biexponential parameterization of diffusion and T-2 relaxation decay curves in a rat muscle edema model: Decay curve components and water compartments. *Magnet Reson Med* **54**, 524 (Sep, 2005).
45. S. J. Graham, M. J. Bronskill, MR measurement of relative water content and multicomponent T2 relaxation in human breast. *Magnetic resonance in medicine: official journal of the Society of Magnetic Resonance in Medicine / Society of Magnetic Resonance in Medicine* **35**, 706 (May, 1996).
46. G. Saab, R. T. Thompson, G. D. Marsh, Multicomponent T2 relaxation of in vivo skeletal muscle. *Magnetic resonance in medicine: official journal of the Society of Magnetic Resonance in Medicine / Society of Magnetic Resonance in Medicine* **42**, 150 (Jul, 1999).
47. P. C. Lin, D. A. Reiter, R. G. Spencer, Classification of degraded cartilage through multiparametric MRI analysis. *J Magn Reson* **201**, 61 (Nov, 2009).
48. M. D. Does, J. C. Gore, Compartmental study of T(1) and T(2) in rat brain and trigeminal nerve in vivo. *Magnetic resonance in medicine: official journal of the Society of Magnetic Resonance in Medicine / Society of Magnetic Resonance in Medicine* **47**, 274 (Feb, 2002).

49. W. Ling, R. R. Regatte, M. E. Schweitzer, A. Jerschow, Characterization of bovine patellar cartilage by NMR. *NMR in biomedicine* **21**, 289 (Mar, 2008).
50. J. Y. Zhou, B. Lal, D. A. Wilson, J. Laterra, P. C. M. van Zijl, Amide proton transfer (APT) contrast for imaging of brain tumors. *Magnet Reson Med* **50**, 1120 (Dec, 2003).
51. J. Y. Zhou, J. F. Payen, D. A. Wilson, R. J. Traystman, P. C. M. van Zijl, Using the amide proton signals of intracellular proteins and peptides to detect pH effects in MRI. *Nat Med* **9**, 1085 (Aug, 2003).
52. J. Y. Zhou, P. C. M. van Zijl, Chemical exchange saturation transfer imaging and spectroscopy. *Prog Nucl Mag Res Sp* **48**, 109 (May 30, 2006).
53. N. Marigheto, L. Venturi, B. Hills, Two-dimensional NMR relaxation studies of apple quality. *Postharvest Biol Tec* **48**, 331 (Jun, 2008).
54. J. T. S. a. M. D. Does, Compartmental Relaxation Measurements in a Graded Muscle Edema Model. *Proc. Intl. Soc. Mag. Reson. Med.* **17**, 1918 (2009).
55. P. T. Callaghan, S. Godefroy, B. N. Ryland, Use of the second dimension in PGSE NMR studies of porous media. *Magnetic resonance imaging* **21**, 243 (Apr-May, 2003).
56. RINMR. (Oxford Instruments Molecular Biotools, Tubney Woods, Abingdon, OX13 5QX, UK, (c) 1992-2007), vol. Version 5.4.0.0.
57. D. T. Guihéneuf. (RINMR User Manual (software release versions 4.1 and later), © Copyright Resonance Instruments Ltd 2002 2002).
58. B. P. Hills, The Proton-Exchange Cross-Relaxation Model of Water Relaxation in Biopolymer Systems. *Mol Phys* **76**, 489 (Jun 20, 1992).
59. M. D. Hurlimann, L. Venkataramanan, C. Flaum, The diffusion-spin relaxation time distribution function as an experimental probe to characterize fluid mixtures in porous media. *J Chem Phys* **117**, 10223 (Dec 8, 2002).
60. L. Frydman, T. Scherf, A. Lupulescu, The acquisition of multidimensional NMR spectra within a single scan. *P Natl Acad Sci USA* **99**, 15858 (Dec 10, 2002).
61. M. E. Furfaro *et al.*, Multidimensional NMR cross-correlation relaxation study of carrot phloem and xylem. Part I: Peak assignment. *Appl Magn Reson* **35**, 521 (May, 2009).
62. M. E. Furfaro *et al.*, Multidimensional NMR cross-correlation relaxation study of carrot phloem and xylem. Part II: Thermal and high-pressure processing. *Appl Magn Reson* **35**, 537 (May, 2009).
63. M. D. Hurlimann, L. Burcaw, Y. Q. Song, Quantitative characterization of food products by two-dimensional D-T-2 and T-1-T-2 distribution functions in a static gradient. *J Colloid Interf Sci* **297**, 303 (May 1, 2006).
64. G. Saab, R. T. Thompson, G. D. Marsh, P. A. Picot, G. R. Moran, Two-dimensional time correlation relaxometry of skeletal muscle in vivo at 3 tesla. *Magnet Reson Med* **46**, 1093 (Dec, 2001).
65. L. Venturi *et al.*, Multidimensional cross-correlation relaxometry of aqueous protein systems. *Appl Magn Reson* **33**, 213 (Apr, 2008).
66. E. Anoardo, G. Galli, G. Ferrante, Fast-field-cycling NMR: Applications and instrumentation. *Appl Magn Reson* **20**, 365 (2001).
67. D. H. Adams, B. Eksteen, Aberrant homing of mucosal T cells and extra-intestinal manifestations of inflammatory bowel disease. *Nat Rev Immunol* **6**, 244 (Mar, 2006).
68. L. Venturi, Università di Bologna (2008).
69. C. P. Slichter, *Principles of magnetic resonance*. (Springer, Berlin, ed. 2nd rev. and expanded ed., 1978).
70. G. D. Fullerton, I. L. Cameron, V. A. Ord, Frequency dependence of magnetic resonance spin-lattice relaxation of protons in biological materials. *Radiology* **151**, 135 (Apr, 1984).
71. R. F. Wolf *et al.*, The tissue hydration state in UW-preserved human donor livers. A clinical study of the relation between proton magnetic resonance relaxation times, donor condition, preservation procedure, and early graft function. *Transplantation* **57**, 1189

(1994).
72. P. Holzmueller, H. Reckendorfer, H. Burgmann, E. Moser, Viability testing of transplantation donor liver by 1H NMR relaxometry. *Magnetic resonance in medicine : official journal of the Society of Magnetic Resonance in Medicine / Society of Magnetic Resonance in Medicine* **16**, 173 (1990).
73. P. Holzmuller, E. Moser, H. Reckendorfer, H. Burgmann, M. Sperlich, Proton spin-lattice relaxation time as liver transplantation graft viability parameter. *Magnetic resonance imaging* **11**, 229 (1993).
74. T. Heye *et al.*, MR relaxometry of the liver: significant elevation of T1 relaxation time in patients with liver cirrhosis. *European radiology* **22**, 1224 (2012).
75. C. Hoad *et al.*, Quantitative magnetic resonance imaging (MRI) in the evaluation of the degree of steatosis, iron accumulation and fibrosis in chronic liver diseases (MRKER STUDY). *Gut* **60**, A55 (2011).
76. T. G. St Pierre, P. R. Clark, W. Chua‐anusorn, Single spin‐echo proton transverse relaxometry of iron‐loaded liver. *NMR in biomedicine* **17**, 446 (2004).
77. I. o. k. s. Piotr Michal Jaworski. (2006).
78. J. A. van der Hoeven, L. J. de Jong, R. F. Wolf, R. L. Kamman, R. J. Ploeg, Tissue hydration in kidneys during preservation: a relaxometric analysis of time-dependent differences between cortex and medulla. *Transplant International* **9**, S452 (1996).
79. K. Sievers, E. Löhr, T. Bauermann, MR relaxometry: Estimating overhydration in renal failure. *Computerized medical imaging and graphics* **19**, 219 (1995).
80. S. D. Wolff, R. S. Balaban, Magnetization transfer contrast (MTC) and tissue water proton relaxation in vivo. *Magnet Reson Med* **10**, 135 (1989).
81. Y. Huang *et al.*, Measurement and comparison of T1 relaxation times in native and transplanted kidney cortex and medulla. *Journal of Magnetic Resonance Imaging* **33**, 1241 (2011).
82. D. L. Parker, V. Smith, P. Sheldon, L. E. Crooks, L. Fussell, Temperature distribution measurements in two-dimensional NMR imaging. *Med Phys* **10**, 321 (1983).
83. Q. Liu, Y. Cai, W. Lin, G. H. Turner, H. An, A magnetic resonance (MR) compatible selective brain temperature manipulation system for preclinical study. *Med Devices* **5**, 13 (2012).
84. C. Birkl *et al.*, Temperature-induced changes of magnetic resonance relaxation times in the human brain: A postmortem study. *Magnetic resonance in medicine : official journal of the Society of Magnetic Resonance in Medicine / Society of Magnetic Resonance in Medicine* **28**, 24799 (2013).
85. N. Bloembergen, E. M. Purcell, R. V. Pound, Relaxation effects in nuclear magnetic resonance absorption. *Physical Review* **73**, 679 (1948).
86. R. A. Fisher, The use of multiple measurements in taxonomic problems. *Annals of Eugenics* **7**, 179 (1936).
87. R. A. Fisher, The statistical utilization of multiple measurements. *Annals of Eugenics* **8**, 376 (1938).
88. R. Gnanadesikan, *Methods for statistical data analysis of multivariate observations*. (Wiley, New York, NY ; Chichester, ed. 2nd ed., 1997).
89. S. Wold, K. Esbensen, P. Geladi, Principal component analysis. *Chemometrics and Intelligent Laboratory Systems* **2**, 37 (1987).
90. I. Jolliffe, in *Encyclopedia of Statistics in Behavioral Science*. (John Wiley & Sons, Ltd, 2005).
91. H. Abdi, L. J. Williams, Principal component analysis. *Wiley Interdisciplinary Reviews: Computational Statistics* **2**, 433 (2010).
92. M. A. Bernstein, K. F. King, *Handbook of MRI pulse sequences*. (Academic Press, Amsterdam ; Oxford, 2004).
93. O. Mougin, P. Gowland, in *Proc Intl Soc Magn Reson Med*. (2008), vol. 16, pp. 3083.

94. J. J. Hsu, I. J. Lowe, Spin-lattice relaxation and a fast T-1-map acquisition method in MRI with transient-state magnetization. *Journal of Magnetic Resonance* **169**, 270 (Aug, 2004).
95. S. H. Koenig, R. D. Brown, D. Adams, D. Emerson, C. G. Harrison, Magnetic-Field Dependence of 1/T1 of Protons in Tissue. *Invest Radiol* **19**, 76 (1984).
96. G. P. Arden, Total Knee Replacement. *Clinical Orthopaedics and Related Research* **94**, 92 (1973).
97. T. O. Smith *et al.*, Clinical and radiological outcomes of fixed-versus mobile-bearing total knee replacement: a meta-analysis. *Knee Surgery, Sports Traumatology, Arthroscopy* **18**, 325 (2010).
98. P. Beaufils *et al.*, Trochleoplasty in major trochlear dysplasia: current concepts. *Sports medicine, arthroscopy, rehabilitation, therapy & technology : SMARTT* **4**, 7 (2012).
99. S. T. Donell, G. Joseph, C. B. Hing, T. J. Marshall, Modified Dejour trochleoplasty for severe dysplasia: Operative technique and early clinical results. *The Knee* **13**, 266 (2006).
100. H. J. Mankin, A. Z. Thrasher, Water content and binding in normal and osteoarthritic human cartilage. *The Journal of bone and joint surgery. American volume* **57**, 76 (Jan, 1975).
101. J. Carballido-Gamio, X. Li, T. Link, S. Majumdar, in *Proc Intl Soc Mag Reson Med*. (2007), vol. 15, pp. 2661.
102. J. Carballido‐Gamio *et al.*, Feasibility and reproducibility of relaxometry, morphometric, and geometrical measurements of the hip joint with magnetic resonance imaging at 3T. *Journal of Magnetic Resonance Imaging* **28**, 227 (2008).
103. D. Binks *et al.*, Quantitative parametric MRI of articular cartilage: a review of progress and open challenges. *British Journal of Radiology* **86**, (2013).
104. M. Nissi *et al.*, Estimation of mechanical properties of articular cartilage with MRI-dGEMRIC, T2 and T1 imaging in different species with variable stages of maturation. *Osteoarthritis and cartilage/OARS, Osteoarthritis Research Society* **15**, 1141 (2007).
105. P. Julkunen, R. Korhonen, M. Nissi, J. Jurvelin, Mechanical characterization of articular cartilage by combining magnetic resonance imaging and finite-element analysis—a potential functional imaging technique. *Phys Med Biol* **53**, 2425 (2008).
106. E. Wiener, C. Pfirrmann, J. Hodler, Spatial variation in T1 of healthy human articular cartilage of the knee joint. *British Journal of Radiology* **83**, 476 (2010).
107. T. C. Dunn, Y. Lu, H. Jin, M. D. Ries, S. Majumdar, T2 Relaxation Time of Cartilage at MR Imaging: Comparison with Severity of Knee Osteoarthritis1. *Radiology* **232**, 592 (2004).
108. C. Stehling *et al.*, Patellar Cartilage: T2 Values and Morphologic Abnormalities at 3.0-T MR Imaging in Relation to Physical Activity in Asymptomatic Subjects from the Osteoarthritis Initiative1. *Radiology* **254**, 509 (2010).
109. T. H. Jochimsen, A. Schafer, R. Bammer, M. E. Moseley, Efficient simulation of magnetic resonance imaging with Bloch-Torrey equations using intra-voxel magnetization gradients. *J Magn Reson* **180**, 29 (May, 2006).
110. K. M. Wright *et al.*, MRICOM-MRI COntrast Modelling using 2D T1-T2 correlation spectra and relaxation signatures. *Magnetic resonance imaging* **28**, 661 (Jun, 2010).
111. B. Blümich, *NMR imaging of materials*. Monographs on the physics and chemistry of materials (Clarendon Press, Oxford University Press, Oxford, New York, 2000), pp. xxiii, 541 p.
112. J. Frahm, A. Haase, D. Matthaei, Rapid Nmr Imaging of Dynamic Processes Using the Flash Technique. *Magnet Reson Med* **3**, 321 (Apr, 1986).
113. J. P. Hornak. (Interactive Learning Software, Henietta, NY, 1996).
114. E M Escobedo *et al.*, Usefulness of turbo spin-echo MR imaging in the evaluation of meniscal tears: comparison with a conventional spin-echo sequence. *American Journal of Roentgenology* **167**, 1223 (1996/11/01, 1996).
115. K. Mudry, Biomedical Imaging. (2007).

116. P. Soyer *et al.*, Detection of focal hepatic lesions with MR imaging: prospective comparison of T2-weighted fast spin-echo with and without fat suppression, T2-weighted breath-hold fast spin-echo, and gadolinium chelate-enhanced 3D gradient-recalled imaging. *American Journal of Roentgenology* **166**, 1115 (1996/05/01, 1996).
117. K. J. Stevens, C. G. Wallace, W. Chen, J. K. Rosenberg, G. E. Gold, Imaging of the wrist at 1.5 tesla using isotropic three-dimensional fast spin echo cube. *Journal of Magnetic Resonance Imaging* **33**, 908 (2011).
118. R. F. Busse, H. Hariharan, A. Vu, J. H. Brittain, Fast spin echo sequences with very long echo trains: Design of variable refocusing flip angle schedules and generation of clinical T2 contrast. *Magnet Reson Med* **55**, 1030 (2006).
119. D. Gottlieb, C. Shu, On the Gibbs Phenomenon and Its Resolution. *SIAM Review* **39**, 644 (1997).
120. P. Le Roux, R. J. Gilles, G. C. McKinnon, P. G. Carlier, Optimized outer volume suppression for single-shot fast spin-echo cardiac imaging. *Journal of Magnetic Resonance Imaging* **8**, 1022 (1998).
121. T. H. Jochimsen, M. von Mengershausen, ODIN - Object-oriented development interface for NMR. *Journal of Magnetic Resonance* **170**, 67 (Sep, 2004).
122. S. Watanabe, *Pattern recognition: human and mechanical*. (John Wiley \\& Sons, Inc., 1985), pp. 570.
123. E. Waters, S. Wickline, Contrast agents for MRI. *Basic Res Cardiol* **103**, 114 (2008/03/01, 2008).
124. K. M. Ward, A. H. Aletras, R. S. Balaban, A New Class of Contrast Agents for MRI Based on Proton Chemical Exchange Dependent Saturation Transfer (CEST). *Journal of Magnetic Resonance* **143**, 79 (2000).
125. R. Bhattacharyya, A. Kumar, A fast method for the measurement of long spin-lattice relaxation times by single scan inversion recovery experiment. *Chem Phys Lett* **383**, 99 (Jan 1, 2004).
126. Y. Shrot, B. Shapira, L. Frydman, Ultrafast 2D NMR spectroscopy using a continuous spatial encoding of the spin interactions. *Journal of Magnetic Resonance* **171**, 163 (Nov, 2004).
127. J. Warner, S. Donell, K. Wright, L. Venturi, B. Hills, The characterisation of mammalian tissue with 2D relaxation methods. *Magnetic resonance imaging* **28**, 971 (Sep, 2010).
128. L. Venturi, J. Warner, B. Hills, Multisliced ultrafast 2D relaxometry. *Magnetic resonance imaging* **28**, 964 (Sep, 2010).
129. L. Venturi, B. Hills, The flipped longitudinal polarization sequence. *Magnetic resonance imaging* **28**, 957 (Sep, 2010).
130. L. Venturi, K. Wright, B. Hills, Ultrafast T-1-T-2 relaxometry using FLOP sequences. *Journal of Magnetic Resonance* **205**, 224 (Aug, 2010).
131. Y. Shrot, L. Frydman, Spatially encoded NMR and the acquisition of 2D magnetic resonance images within a single scan. *Journal of Magnetic Resonance* **172**, 179 (Feb, 2005).
132. V. Kumar, *Robbins and Cotran's pathologic basis of disease*. (Saunders, Philadelphia, Pa. ; London, ed. 8th ed. / Vinay Kumar., 2010).
133. L. Venturi, B. Hills, Spatially resolved multidimensional cross-correlation relaxometry. *Magnetic resonance imaging* **28**, 171 (Feb, 2010).
134. W. P. Aue, S. Muller, T. A. Cross, J. Seelig, Volume-Selective Excitation - a Novel-Approach to Topical Nmr. *Journal of Magnetic Resonance* **56**, 350 (1984).
135. T. Vogl *et al.*, Thermal ablation of liver metastases. Current status and prospects. *Radiologe* **41**, 49 (2001).
136. R. Lencioni *et al.*, Radio-frequency thermal ablation of liver metastases with a cooled-tip electrode needle: results of a pilot clinical trial. *European radiology* **8**, 1205 (1998).
137. H. Y. Akyildiz, J. Mitchell, M. Milas, A. Siperstein, E. Berber, Laparoscopic radiofrequency

thermal ablation of neuroendocrine hepatic metastases: Long-term follow-up. *Surgery* **148**, 1288 (2010).
138. E. Berber, M. Tsinberg, G. Tellioglu, C. Simpfendorfer, A. Siperstein, Resection Versus Laparoscopic Radiofrequency Thermal Ablation Of Solitary Colorectal Liver Metastasis. *J Gastrointest Surg* **12**, 1967 (2008/11/01, 2008).
139. H. Rhim, G. D. Dodd, Radiofrequency thermal ablation of liver tumors. *Journal of Clinical Ultrasound* **27**, 221 (1999).
140. M. J. L. W. L. Bowles B, et al., Safety and efficacy of radiofrequency thermal ablation in advanced liver tumors. *Archives of Surgery* **136**, 864 (2001).
141. J. Pattison, D. Goldsmith, B. Hartley, F. C. Fervenza, J. P. Grande, *Renal Medicine*. (Manson Publishing, 2004).
142. R. W. Schrier, *Diseases of the kidney & urinary tract*. (Lippincott Williams & Wilkins, Philadelphia, Pa. ; London, ed. 8th ed. / edited by Robert W. Schrier., 2007).
143. A. Greenberg, A. K. Cheung, *Primer on kidney diseases*. (Saunders, Philadelphia, Pa. ; London, ed. 5th ed., 2009).
144. G. Lund, J. Letourneau, D. Day, J. Crass, MRI in organ transplantation. *Radiologic clinics of North America* **25**, 281 (1987).
145. M. A. Neimatallah, Q. Dong, S. O. Schoenberg, K. J. Cho, M. R. Prince, Magnetic resonance imaging in renal transplantation. (1999).
146. D. Amsellem-Ouazana *et al.*, Negative prostatic biopsies in patients with a high risk of prostate cancer. Is the combination of endorectal MRI and magnetic resonance spectroscopy imaging (MRSI) a useful tool? A preliminary study. *European urology* **47**, 582 (2005).
147. K. Kagawa *et al.*, Initial clinical assessment of CT-MRI image fusion software in localization of the prostate for 3D conformal radiation therapy. *International journal of radiation oncology, biology, physics* **38**, 319 (1997).
148. B. Turkbey *et al.*, MRI of localized prostate cancer: coming of age in the PSA era. *Diagn Interv Radiol* **18**, 34 (2012).
149. Combined T2-Weighted and Diffusion-Weighted MRI for Localization of Prostate Cancer. *American Journal of Roentgenology* **189**, 323 (2007/08/01, 2007).
150. P. Gibbs, D. J. Tozer, G. P. Liney, L. W. Turnbull, Comparison of quantitative T2 mapping and diffusion‐weighted imaging in the normal and pathologic prostate. *Magnet Reson Med* **46**, 1054 (2001).
151. A. Partin *et al.*, The use of prostate specific antigen, clinical stage and Gleason score to predict pathological stage in men with localized prostate cancer. *The Journal of urology* **150**, 110 (1993).
152. C. A. Woodfield *et al.*, Diffusion-weighted MRI of peripheral zone prostate cancer: comparison of tumor apparent diffusion coefficient with Gleason score and percentage of tumor on core biopsy. *American Journal of Roentgenology* **194**, W316 (2010).
153. A. R. Padhani *et al.*, Dynamic contrast enhanced MRI of prostate cancer: correlation with morphology and tumour stage, histological grade and PSA. *Clinical radiology* **55**, 99 (2000).
154. P. J. Moughan, M. J. Birtles, P. D. Cranwell, W. C. Smith, M. Pedraza, The piglet as a model animal for studying aspects of digestion and absorption in milk-fed human infants. *World Rev Nutr Diet* **67**, 40 (1992).
155. A. J. Darragh, P. J. Moughan, The three-week-old piglet as a model animal for studying protein digestion in human infants. *J Pediatr Gastroenterol Nutr* **21**, 387 (1995).
156. R. G. Cowell, P. Dawid, S. L. Lauritzen, D. J. Spiegelhalter, *Probabilistic Networks and Expert Systems: Exact Computational Methods for Bayesian Networks*. (Springer, 2007).
157. D. Waterman, *A guide to expert systems*. (1986), pp. Medium: X; Size: Pages: 440.
158. E. Mira, A. Buizza, G. Magenes, M. Manfrin, R. Schmid, Expert Systems as a Diagnostic Aid

in Otoneurology. *ORL* **52**, 96 (1990).
159. H. Tirri, Implementing expert system rule conditions by neural networks. *New Gener Comput* **10**, 55 (1991/10/01, 1991).
160. M. Paliwal, U. A. Kumar, Neural networks and statistical techniques: A review of applications. *Expert Systems with Applications* **36**, 2 (2009).
161. F. Günther, S. Fritsch, neuralnet: Training of neural networks. *The R Journal* **2**, 30 (2010).
162. M. Karabatak, M. C. Ince, An expert system for detection of breast cancer based on association rules and neural network. *Expert Systems with Applications* **36**, 3465 (2009).
163. D. Le Bihan *et al.*, Diffusion tensor imaging: concepts and applications. *Journal of Magnetic Resonance Imaging* **13**, 534 (2001).
164. D. K. Jones, A. Leemans, in *Magnetic Resonance Neuroimaging*. (Springer, 2011), pp. 127-144.

9. Code appendix

All code presented here is my own work with varying levels of assistance from Kevin Wright. During composition, non-functioning code would be discussed and shown to Kevin who would make recommendations or direct edits to the code to fix problems and refine methods such as where an explicit programming loop could be replaced by a simpler MATLAB syntax of which I was not aware. Individual elements were harvested from older versions of code and existing programs in the lab's code library. Multiple versions of programs were passed back and forth with multiple edits and refinements at every stage.

Appendix to section 5.2.1

Appendix to section 5.2.1 is the first MATLAB simulation program developed for the "Virtual Sample Simulation" (VSS) method, with significant training and assistance from Kevin Wright. The code is documented throughout to denote the purpose of the various sections so as to be understandable for those with experience of MATLAB programming. Documentation and comments are shown in green. It is a simulation of a 1 dimensional stimulated echo imaging sequence (as shown in figure 5.1) with a simulated 1D phantom. The phantom used in the simulation consists of a 1D array of voxels containing vectors which can be given any magnitude and orientation required. Relaxation is applied according to the full 2D T_1-T_2 relaxation spectra of one or more tissue types. For efficiency of simulation this information is kept separate from the phantom and applied based on a voxels position in the phantom to simulate one tissue in one half and another in the other. The phantom begins at equilibrium and each pulse is simulated by affecting the vector in each voxel with a simulated radiofrequency field with set amplitude and time. Between pulses each voxel undergoes simulated relaxation by affecting the individual spins in the phantom by transverse or longitudinal relaxation for a set time and rotating them as they would during free procession. A random offset to the standard rotation rate is added to each spin to simulate T_{2*} effects over the entire phantom. Longitudinal and transverse relaxation is determined by the vectors orientation during the relaxation period and according to the relaxation values for the tissue being simulated, determined by the 2D relaxation spectrum. Simulated gradients and sinc pulses are used to achieve slice selective. Following the

simulated sequence the returned signal is obtained by summing the transverse magnetisation from each voxel. Following Fourier transformation the image profiles obtained from each of the slices can then be reassembled into a final intensity profile the sample and sequence.

```
% relstimechotestcon2.m
% Simulate a stimulated echo in a stepped X gradient
% ,now including relaxation
% FT the echo to get an image profile.
% Repeat using a series of frequency-selective RF pulses.
% by JFW on 27/09/07 from stimechotest10 KMW.

clear all;
close all;
scriptname = 'relstimechotestcon2';

% Set the NMR parameters.

T1 = 383;                %temporary fixed values of T1 and T2
T2 = 81;
T12 = 905;
T22 = 58;

tau = 2.6e-3;            % Time that gradient Gx_2 is switched on
t = 3.5e-3;              % Time of second 90 deg. pulse
T = 15e-3;               % Time of third 90 deg. pulse
TR = 10;                 % Time between successive scans
NN = 10;                   % Number of repeats(1 less than number of
scans)
hh=1;

%%%%%%%%%%%%%%%%%%%%%%%%%%%%%%%%%%%%%%%%%%%%%%%%%%%%%%%%%%%%%%%%%%%%%%%%%%%%%%%
%%%%%%%%%%%%%%%%%%%%%%%%%%%%%%%%%%%%%%%%%%%%
%%%%%selects and analyses first set of MAT files
% Get the data pathname and filename from a dialog box.
   [filename, pathname] = uigetfile({'*.batchdata*.mat', ...
                                     'CPMG-CPMG-Data Files
(*.batchdata*.mat)'; ...
                                     '*.*', ...
                                     'All Files (*.*)'}, ...
                                     'Select data file(s) created by
CPMG-CPMG-Calc', ...
                                     'MultiSelect','on');
   if isequal(filename,0) | isequal(pathname,0) % if cancel is pressed
      cd(originalpathname); % restore original directory
      fprintf(1,'*** Quitting *** : cancelled, or file not found.\n');
      return;
   end

   if iscellstr(filename) % if more than one file selected
      for nFile=1:length(filename) % assemble a cell array of full
filenames
         FileList{nFile} = fullfile(pathname, filename{nFile});
      end % for
   else % or for a single file
      FileList{1}=fullfile(pathname, filename);
```

```
   end % if

% display the filelist
fprintf(1,'The following file(s) will be processed:\n');
for nFile=1:length(FileList)
   fprintf(1,'    %s\n',char(FileList(nFile)));
end % for

% Find out if the user wishes to proceed?
if strcmp(questdlg('Ok to proceed?', ...
                   'relstimechotestcon2','Quit','Yes','Yes'),'Quit')
   return; % Quit
end

% with each file
for nFile=1:length(FileList) % with each batchdata file

   % decode the filename
   [pathname, filename, ext, versn] = fileparts(char(FileList(nFile)));
   filename=[filename ext];

   % change the current directory
   cd(pathname);

   load(filename); % load the saved workspace variables

   % extract the regularisation flags
   RegOpt=filename(end-6:end-4);

   % reconstruct original .txt datafile name
   filename=[filename(1:end-18) '.txt'];

   % (Re)Open a journal file to record text IO
   %diary([filename(1:end-4) '.Journal.txt']); % open a journal file to
recieve a copy of the text IO
   %diary on; % activate the journal file

   % tell the user whats going on
   fprintf(1,['\n*** relstimechotestcon2 *** %s ***\n\n' ...
              'Basic characteristics for %s ***\n'],datestr(now),
filename);
   pcFname=strrep(filename, '_', '-'); % a plot compatible version of
filename
end

[T1_dist, T2_dist, por, beta] = ComputeProjections(FEst, T1r, T2r);
% Save the SVD results
   %save([filename(1:end-4) '.batchres-
rel.mat'],'T1_dist','T2_dist','por','beta');


   T2i=0;                  %Sets selecting variable for T2 and creates
Mtconst at 0
   Mtconst = 0;
  %%%calculates normalising factor for T1 and T2 probability
distributions
TT1=0;
T1disttotal=0;
```

```
  while TT1 < length(T1_dist)  %follows loop for all values of T1_dist
and T1r

      TT1=TT1+1;
      T1disttotal=T1disttotal+T1_dist(TT1);

  end

 TT2=0;
T2disttotal=0;
  while TT2 < length(T2_dist)  %follows loop for all values of T1_dist
and T1r

      TT2=TT2+1;
      T2disttotal=T2disttotal+T2_dist(TT2);

  end
 %%%%%%calculates constants needed to correctly relax M

   disp('Mtconst=');
  while T2i < length(T2_dist)  %follows loop for all values of T2_dist
and T2r

      T2i= T2i+1;

      Mtconst = Mtconst + ((T2_dist(T2i)/T2disttotal)* exp(-t/T2r(T2i)));
      %Mtconst = Mtconst + (T2_dist(T2i)/T2disttotal);
      disp(Mtconst);

  end

  T1i=0;                    %Sets selecting variable for T1 and creates
MTconst at 0
  MTconst = 0;
  disp('MTconst=');
  while T1i < length(T1_dist)  %follows loop for all values of T1_dist
and T1r

      T1i= T1i+1;

      MTconst = MTconst + ((T1_dist(T1i)/T1disttotal)*(1-(exp(-(T-
t)/T1r(T1i)))));
      %MTconst = MTconst + (T1_dist(T1i)/T1disttotal);
      disp(MTconst);

  end

  %%%%%%%%%%%%%%%%%%%%%%%%%%%%%%%%%%%%%%%%%%%%%%%%%%%%%%%%%%%% TR relaxation constant
  TRi=0;                    %Sets selecting variable for T1 and creates
TRrelaxer at 0
  TRrelaxer = 0;
  disp('TRrelaxer=');
  while TRi < length(T1_dist)  %follows loop for all values of T1_dist
and T1r

      TRi= TRi+1;
```

```
      TRrelaxer = TRrelaxer + ((T1_dist(TRi)/T1disttotal)*(1-(exp(-
TR/T1r(TRi)))));

      disp(TRrelaxer);

  end

  %%%%%%%%%%%%%%%%%Selects and analyses second set of MAT files
% Get the data pathname and filename from a dialog box.
   [filename, pathname] = uigetfile({'*.batchdata*.mat', ...
                                     'CPMG-CPMG-Data Files
(*.batchdata*.mat)'; ...
                                     '*.*', ...
                                     'All Files (*.*)'}, ...
                                     'Select data file(s) created by
CPMG-CPMG-Calc', ...
                                     'MultiSelect','on');
   if isequal(filename,0) | isequal(pathname,0) % if cancel is pressed
      cd(originalpathname); % restore original directory
      fprintf(1,'*** Quitting *** : cancelled, or file not found.\n');
      return;
   end

   if iscellstr(filename) % if more than one file selected
      for nFile=1:length(filename) % assemble a cell array of full
filenames
         FileList{nFile} = fullfile(pathname, filename{nFile});
      end % for
   else % or for a single file
      FileList{1}=fullfile(pathname, filename);
   end % if

% display the filelist
fprintf(1,'The following file(s) will be processed:\n');
for nFile=1:length(FileList)
   fprintf(1,'    %s\n',char(FileList(nFile)));
end % for

% Find out if the user wishes to proceed?
if strcmp(questdlg('Ok to proceed?', ...
                   'relstimechotestcon2','Quit','Yes','Yes'),'Quit')
   return; % Quit
end

% with each file
for nFile=1:length(FileList) % with each batchdata file

   % decode the filename
   [pathname, filename, ext, versn] = fileparts(char(FileList(nFile)));
   filename=[filename ext];

   % change the current directory
   cd(pathname);

   load(filename); % load the saved workspace variables

   % extract the regularisation flags
   RegOpt=filename(end-6:end-4);
```

```
   % reconstruct original .txt datafile name
   filename=[filename(1:end-18) '.txt'];

   % (Re)Open a journal file to record text IO
   %diary([filename(1:end-4) '.Journal.txt']); % open a journal file to
recieve a copy of the text IO
   %diary on; % activate the journal file

   % tell the user whats going on
   fprintf(1,['\n*** relstimechotestcon2 *** %s ***\n\n' ...
              'Basic characteristics for %s ***\n'],datestr(now),
filename);
   pcFname=strrep(filename, '_', '-'); % a plot compatible version of
filename
end

[T1_dist, T2_dist, por, beta] = ComputeProjections(FEst, T1r, T2r);
% Save the SVD results
   %save([filename(1:end-4) '.batchres-
rel.mat'],'T1_dist','T2_dist','por','beta');


   T2i=0;                  %Sets selecting variable for T2 and creates
Mtconst at 0
   Mtconst2 = 0;
  %%%Calculates normalising factor for T1 and T2 probability
distributions
TT1=0;
T1disttotal=0;
  while TT1 < length(T1_dist)  %follows loop for all values of T1_dist
and T1r

      TT1=TT1+1;
      T1disttotal=T1disttotal+T1_dist(TT1);

  end

 TT2=0;
T2disttotal=0;
  while TT2 < length(T2_dist)  %follows loop for all values of T1_dist
and T1r

      TT2=TT2+1;
      T2disttotal=T2disttotal+T2_dist(TT2);

  end
 %%%Calculates constants needed to correctly relax M

   disp('Mtconst2=');
  while T2i < length(T2_dist)  %follows loop for all values of T2_dist
and T2r

      T2i= T2i+1;

      Mtconst2 = Mtconst2 + ((T2_dist(T2i)/T2disttotal)* exp(-
t/T2r(T2i)));
      %Mtconst2 = Mtconst2 + (T2_dist(T2i)/T2disttotal);
      disp(Mtconst2);
```

```
  end

  T1i=0;                    %Sets selecting variable for T1 and creates
Mtconst2 at 0
  MTconst2 = 0;
  disp('MTconst2=');
  while T1i < length(T1_dist)  %follows loop for all values of T1_dist
and T1r

      T1i= T1i+1;

      MTconst2 = MTconst2 + ((T1_dist(T1i)/T1disttotal)*(1-(exp(-(T-
t)/T1r(T1i)))));
      %MTconst2 = MTconst2 + (T1_dist(T1i)/T1disttotal);
      disp(MTconst2);

  end

%%%%%%%%%%%%%%%%%%%%%%%%%%%%%%%%%%%%%%%%%%%%%%%% 2nd TR relaxation constant
  TRi=0;                    %Sets selecting variable for T1 and creates
TRrelaxer2 at 0
  TRrelaxer2 = 0;
  disp('TRrelaxer2=');
  while TRi < length(T1_dist)  %follows loop for all values of T1_dist
and T1r

      TRi= TRi+1;

      TRrelaxer2 = TRrelaxer2 + ((T1_dist(TRi)/T1disttotal)*(1-(exp(-
TR/T1r(TRi)))));

      disp(TRrelaxer2);

  end

%%%%%%%%%%%%%%%%%%%%%%%%%%%%%%%%%%%%%%%%%%%%%%%%%%%%%%%%%%%%%%%%%%%%%%%%%%%%%%%
%%%%%%%%%%%%%%%%%%%%%%%%%%%%%%%%%%%%%%%%%%%%%%%%%%%%%%%%%%%%%%%%%%%%%%%%%%%%%%%


TD = 512;               % Points acquired in FID (must be >= SI)
SI = 512;               % Points used for FT of stimulated echo
                        % (ideally should be power of 2 for efficient FT)

DW = 10e-6;             % Dwell time, s (time step during acquisition)
AQ = SI*DW;             % Data acquisition time, s (for the stim. echo)
SW = 1/DW;              % Sweep width, Hz (using quadrature detection)
RES = SW/SI;            % Spectral resolution, Hz/pt
Gx1_Hz = 2e3;           % X field gradient, Hz/cm
Gx1_rad = 2*pi*Gx1_Hz;  % X field gradient, rad/s/cm
Gx2_Hz = 3e3;           % Second X field gradient, Hz/cm
Gx2_rad = 2*pi*Gx2_Hz;  % Second X field gradient, rad/s/cm

L = 20;                 % Sample length, cm
num_voxels = 5000;      % No. of spins (voxels) in sample
delta_x = L/num_voxels; % Voxel width, cm

% x-coordinates of the voxels in the phantom sample, in cm.
```

```
sample_x_axis = (-L/2):delta_x:(L/2-delta_x);

% x-coordinates of the voxels in the FT'ed image profile, in cm.
% This assumes that Gx_1 will be turned on during the acquisition,
% i.e. Gx_1 determines the calibration of the x-axis.

profile_x_axis = ((-SW/2):RES:(SW/2-RES))/Gx1_Hz;

% Set up a phantom sample profile. (Initialize the relative spin
% density for each of the voxels across the sample).

spin_density = [zeros(1,num_voxels/4) 2*ones(1,num_voxels/4) ...
     2*ones(1,num_voxels/4) ...
    zeros(1,num_voxels/4)];

% Find the integrated area of the sample profile (for normalization).

area = sum(spin_density);

% Plot the phantom sample profile vs. x.

figure;
plot(sample_x_axis,spin_density);
axis([-L/2 L/2 0 1.25*max(spin_density)]);
xlabel('x / cm');
ylabel('Relative spin density');
title('Original (phantom) sample profile');
drawnow;

% Set up the parameters for a 5-lobe sinc selective 90 deg. pulse.
% The subpulse amplitudes are returned in rad/s.
% This has to be done twice, because the second and third pulses
% are turned on when the gradient (Gx_2) is higher than for the
% first pulse (Gx_1). The gradient determines the pulse bandwidth.
% Here we assume the same slice thickness for all three pulses.

slice_thickness = 2; % cm
pulse_bandwidth_1 = slice_thickness*Gx1_Hz;
pulse_bandwidth_2 = slice_thickness*Gx2_Hz;
[rf_ampl_1,num_subpulses_1,subP90_1,P90_1] = ...
    selective_pulse(5,90,pulse_bandwidth_1);
[rf_ampl_2,num_subpulses_2,subP90_2,P90_2] = ...
    selective_pulse(5,90,pulse_bandwidth_2);

% Set the frequency offsets (in rad/s) of a series of selective 90 deg.
% pulses, designed to excite a series of slices across the sample.
% The pulses run from -6 to 6 cm in frequency space, in 2 cm steps.
% This is done twice, for the first of the three pulses at
omega_offset_1,
% and the second and third pulses at omega_offset_2.
% (These 2 arrays must be the same length).

omega_offset_1 = -Gx1_rad*[-6:2:6]; % rad/s
omega_offset_2 = -Gx2_rad*[-6:2:6];

% Find the frequency offset of spins in the X field gradient.
% Do this for both gradients Gx_1 and Gx_2.
```

```
grad_offset_1 = Gx1_rad*sample_x_axis; % rad/s
grad_offset_2 = Gx2_rad*sample_x_axis;

% Set up a random frequency offset (due to local magnetic field
% inhomogeneities) for each voxel, in rad/s. sigma is the standard
% deviation (in Hz) of a Gaussian distribution of frequencies.
% This should be much less than the spread due to applied field
gradients.

sigma = 0; % 1e1; % Hz
random_offset = 2*pi*sigma*randn(1,num_voxels);

% Initialize a series of image profiles (to be computed and saved later).

saved_profile = zeros(length(omega_offset_1),SI);

% Before starting the pulse program, check that we are trying to do a
% physically meaningful experiment.

% First, check that the acquired data array dimensions are sensible.

if SI>TD
    disp('Error: SI must be <= TD');
    % N.B. On DRX & Ultramaran spectrometers TD data are acquired and SI
    % data are transformed; SI >= TD, with SI > TD if zero filling is
used.
    % In this program, TD data are acquired, which may include spin
echoes
    % following the stimulated echo; the first SI data (the stimulated
    % echo) are extracted and transformed, so we must have SI <= TD.
    return
end

% Check that event times in the pulse program are in the correct order.

if 0 >= tau
    % The first pulse must occur before gradient Gx_2 is turned on
    disp('Error: 0 >= tau; tau must be positive');
    return
elseif tau >= t
    % Gradient Gx_2 must be turned on before the second pulse
    disp('Error: tau >= t; tau must be earlier than t');
    return
elseif t >= T
    % The second pulse must occur before the third pulse
    disp('Error: t >= T; t must be earlier than T');
    return
end

% Perform some checks on the parameters to ensure that the experiment
% can be done with the required delays; i.e. there are no negative time
% intervals in the pulse program.

if (tau-P90_1/2) <= 0
    disp('Error: delay tau-P90_1/2 is unphysical; increase tau');
    return
elseif (t-tau-P90_2/2) <= 0
    disp('Error: delay t-tau-P90_2/2 is unphysical; increase t');
```

```
    return
elseif (T-t-P90_2) <= 0
    disp('Error: delay T-t-P90_2 is unphysical; increase T');
    return
elseif (tau-AQ/2) <= 0
    disp(['Error: delay tau-AQ/2 is unphysical; increase tau' ...
        ' or decrease SI or DW']);
    return
end

% Is the difference in precession angle between adjacent spins equal
% to one or more cycles? If so, it will cause "rotary echo" artifacts.
% This assumes that Gx_1 will be turned on during the acquisition.

if Gx1_Hz*delta_x*TD*DW>=1
    disp('Error: rotary echoes will be formed during the acquisition.');
    return
elseif Gx1_Hz*delta_x*SI*DW>=1
    disp(['Error: rotary echoes will be formed during the acquisition'
...
        ' of the stimulated echo.']);
    return
end

% Loop over repetitions of the pulse sequence, with the selective pulses
% at a series of frequencies specified by omega_offset.


for r = 1:length(omega_offset_1)

    %------------------------------------------------------------------------
    % Start of the pulse sequence
    %------------------------------------------------------------------------

    % Zero the acquired signal.

    signal = zeros(1,TD);

    % Loop over all voxels in the sample, skipping the empty ones because
    % they cannot contribute to the signal.

    for s = 1:num_voxels

        if spin_density(s) == 0
            continue; % Empty voxel
        end

        % --- Initialization of the spin magnetization M ---

        % Initialize the Zeeman magnetization (at thermal equilibrium)
        % of the spin(s) in voxel s. The transverse components are
        % both zero, and the z-component is proportional to the spin
        % density in the voxel.
        % This is the situation prior to time -P90_1/2, when the first
        % selective 90 deg pulse begins.


        M=[0,0,spin_density(s)];
```

```
        %%%%%%%%%%%%%%takes the real value of M from zero to it's state
        %%%%%%%%%%%%%%after relaxation period TR
        if s<=(num_voxels/2)

            M = M*(TRrelaxer^NN);

        else

            M = M*(TRrelaxer2^NN);
        End

        % --- First selective 90 deg. pulse, centred at time 0. ---

        % Find the frequency offset (rad/s) of this spin during
        % the first selective pulse, in gradient Gx_1.
        % The RF frequency offset manifests as a z-component of
        % magnetization in the rotating frame.
        freq_offset =
random_offset(s)+grad_offset_1(s)+omega_offset_1(r);
        % First selective 90 deg. pulse about the x-axis, with its
maximum
        % RF amplitude defined as occurring at time 0.
        % The pulse starts at time -P90_1/2 and ends at +P90_1/2.
        % For each subpulse of the complete selective pulse...
        for p = 1:num_subpulses_1
            % The net B_eff is the resultant of rf ampl 1 and freq offset
            omega_eff = sqrt(rf_ampl_1(p)^2+freq_offset^2);
            % Direction cosines of net B_eff
            dir = [rf_ampl_1(p)/omega_eff; 0; freq_offset/omega_eff];
            % Rotate about the net B_eff for time subP90_1
            M = qrot(M,dir,omega_eff*subP90_1);
        end % of the loop over subpulses

        % ---- first relaxation period - transverse----------------------

         Minf = M;       %sets initial value of M as Minf for later use

        if s<=(num_voxels/2)
           M=[Minf(1)*Mtconst;Minf(2)*Mtconst;Minf(3)];%relaxs M
tranversely for t seconds
        else
            M=[Minf(1)*Mtconst2;Minf(2)*Mtconst2;Minf(3)];%relaxs M
tranversely for t seconds
        end

        %disp('first relaxation successful');


        % --- Free precession in gradient Gx_1 ---

        % Find the frequency offset (rad/s) during free precession
        % in gradient Gx_1.
        freq_offset = random_offset(s)+grad_offset_1(s);
        % Do free precession for time tau-P90_1/2.
        M = qrot(M,[0; 0; 1],freq_offset*(tau-P90_1/2));

        % --- Free precession in gradient Gx_2 ---
```

```
        % Find the frequency offset (rad/s) during free precession
        % in gradient Gx_2.
        freq_offset = random_offset(s)+grad_offset_2(s);
        % Do free precession for time t-tau-P90_2/2.
        M = qrot(M,[0; 0; 1],freq_offset*(t-tau-P90_2/2));

        % --- Second selective 90 deg. pulse ---

        % Find the frequency offset (rad/s) of this spin during
        % the second selective pulse, in gradient Gx_2.
        freq_offset =
random_offset(s)+grad_offset_2(s)+omega_offset_2(r);
        % Second selective 90 deg. pulse about the x-axis.
        % For each subpulse of the complete selective pulse...
        for p = 1:num_subpulses_2
            % The net B_eff is the resultant of rf ampl 2 and freq offset
            omega_eff = sqrt(rf_ampl_2(p)^2+freq_offset^2);
            % Direction cosines of net B_eff
            dir = [rf_ampl_2(p)/omega_eff; 0; freq_offset/omega_eff];
            % Rotate about the net B_eff for time subP90_2
            M = qrot(M,dir,omega_eff*subP90_2);
        end % of the loop over subpulses

        % ---- second relaxation period - longitudinal------------------
        if s<=(num_voxels/2)
            %uses M(t) and Minf to relax to M(T)
            M(1) = ((Minf(1) - M(1))*MTconst)+ M(1);
            M(2) = ((Minf(2) - M(2))*MTconst)+ M(2);
        Else
            %uses M(t) and Minf to relax to M(T)
            M(1) = ((Minf(1) - M(1))*MTconst2)+ M(1);
            M(2) = ((Minf(2) - M(2))*MTconst2)+ M(2);
        end
        %disp('second relaxation successful');

        % --- Free precession in gradient Gx_2 ---

        % Find the frequency offset (rad/s) during free precession
        % in gradient Gx_2.
        freq_offset = random_offset(s)+grad_offset_2(s);
        % Do free precession for time T-t-P90_2.
        M = qrot(M,[0; 0; 1],freq_offset*(T-t-P90_2));

        % --- Third selective 90 deg. pulse ---

        % Find the frequency offset (rad/s) of this spin during
        % the third selective pulse, in gradient Gx_2.
        freq_offset =
random_offset(s)+grad_offset_2(s)+omega_offset_2(r);
        % Third selective 90 deg. pulse about the x-axis.
        % For each subpulse of the complete selective pulse...
        for p = 1:num_subpulses_2
            % The net B_eff is the resultant of rf ampl 2 and freq offset
            omega_eff = sqrt(rf_ampl_2(p)^2+freq_offset^2);
            % Direction cosines of net B_eff
            dir = [rf_ampl_2(p)/omega_eff; 0; freq_offset/omega_eff];
            % Rotate about the net B_eff for time subP90_2
            M = qrot(M,dir,omega_eff*subP90_2);
        end % of the loop over subpulses
```

```
    % ---- third relaxation period - transverse----------------------

    if s<=(num_voxels/2)
       M=[M(1)*Mtconst;M(2)*Mtconst;M(3)];%%relaxs M(T) to M(T+t)
    else
        M=[M(1)*Mtconst2;M(2)*Mtconst2;M(3)];%relaxs M(T) to M(T+t)
    end



    % --- Free precession in gradient Gx_2 ---

    % Find the frequency offset (rad/s) during free precession
    % in gradient Gx_2.
    freq_offset = random_offset(s)+grad_offset_2(s);
    % Do free precession for time t-tau-P90_2/2.
    M = qrot(M,[0; 0; 1],freq_offset*(t-tau-P90_2/2));

    % --- Free precession in gradient Gx_1 ---

    % Find the frequency offset (rad/s) during free precession
    % in gradient Gx_1.
    freq_offset = random_offset(s)+grad_offset_1(s);
    % Do free precession for time tau-AQ/2.
    M = qrot(M,[0; 0; 1],freq_offset*(tau-AQ/2));

    % --- Data acquisition ---

    % Find the frequency offset (rad/s) during data acquisition,
    % in gradient Gx_1.
    freq_offset = random_offset(s)+grad_offset_1(s);
    % Do the data acquisition - loop over TD data in time steps DW.
    % Acquisition starts at time t+T-AQ/2.
    for j = 1:TD
        % Do free precession for time DW.
        M = qrot(M,[0; 0; 1],freq_offset*DW);
        % Acquire the jth point of the FID.
        signal(j) = signal(j)+complex(M(1),M(2));
    end % of loop over the acquired data.


end % of loop over voxels in the phantom sample.

%-----------------------------------------------------------------------
% End of the pulse sequence.
%-----------------------------------------------------------------------

% t_axis is the time scale for the data acquisition, starting at
% time t+T-AQ/2, where AQ=SI*DW.
% The stimulated echo should occur at the centre of the acquistion
% of the first SI data, at time t+T.

t_axis = (t+T-AQ/2+(0:DW:((TD-1)*DW)))*1e3; % Converted to ms

% If SI < TD, plot the normalized signal vs. time to show the whole
% of the acquired echo train, including any spin echoes that follow
% the stimulated echo. Then truncate the signal.
```

```
    if SI < TD
        figure;
        hold on;
        plot(t_axis,abs(signal)/area,'r-');
        plot(t_axis(1:SI),abs(signal(1:SI))/area,'b-');
        hold off;
        axis([t_axis(1) t_axis(end) 0 1.2*max(abs(signal))/area]);
        xlabel('Time / ms');
        ylabel('Relative abs(signal');
        title('Simulation of echo train');
        drawnow;

        % Truncate the signal to isolate the stimulated echo
        % (keep the first SI points and throw away the rest).

        t_axis = t_axis(1:SI); % ms
        signal = signal(1:SI);
    end

    % Plot the magnitude of the stimulated echo vs. time.

    figure;
    plot(t_axis,abs(signal)/area);
    axis([t_axis(1) t_axis(end) 0 1.2*max(abs(signal))/area]);
    xlabel('Time / ms');
    ylabel('Relative abs(signal)');
    title('Simulation of stimulated echo');
    drawnow;

    % Fourier transform the signal to get the image profile, and scale
    % it.
    % This assumes that gradient Gx_1 was on during data acquisition.
    % The scaling factor incorporates a factor of two to allow for the
    % stimulated echo being only the half the intensity of the initial
    % FID
    % (see Callaghan); and a factor of Gx1_Hz*delta_x/RES to allow for
    % the frequency equivalent of the voxel separation in the phantom
    % (Gx1_Hz*delta_x) being different, in general, to the spectral
    % resolution (RES) in the final profile. The scaling ensures that
    % the final profile has the same intensities (spin densities) as
    % the original phantom.

    profile = 2*(Gx1_Hz*delta_x/RES)*abs(fftshift(ifft(signal)));


    %calculate contrast from profile
I1=0;
I2=0;
L=length(profile);
if hh==1

conprof = zeros(1,L);
hh=hh+1;
end
for pro=1:L
    conprof(pro)=conprof(pro)+profile(pro);
end
```

```
    % Plot the image profile vs. x.

    figure;
    hold on;
    plot(sample_x_axis,spin_density,'k--');
    plot(profile_x_axis,profile,'b-');
    hold off;
    axis([0.5*profile_x_axis(1) 0.5*profile_x_axis(end) ...
        0 1.25*max(max(profile),max(spin_density))]);
    xlabel('x / cm');
    ylabel('Relative spin density');
    title('Image profile = FT of stimulated echo');
    drawnow;

    % Save the profile for the current selective pulse frequency

    saved_profile(r,:) = profile;

% End of loop over repeats of the pulse sequence

end

% Plot the complete series of profiles over a range of pulse frequencies.

figure;
hold on;
plot(sample_x_axis,spin_density,'k--');
for r = 1:length(omega_offset_1)
    if mod(r,2) == 0, col = 'r-'; else col = 'b-'; end % Alternate
colours
    plot(profile_x_axis,saved_profile(r,:),col);
end
hold off;
axis([0.5*profile_x_axis(1) 0.5*profile_x_axis(end) ...
    0 1.25*max(max(profile),max(spin_density))]);
xlabel('x / cm');
ylabel('Relative spin density');
title('Image profiles from a series of selective pulses');
drawnow;

% Save all the figures in .emf files.

savefigures_v3(scriptname);

%calculate contrast from final signal
    for xc = ((2*L)/6):((3*L)/6)
        xxc=round(xc);
        I1=I1+ (conprof(xxc)/(L/6));
    end

    for yc = ((3*L)/6):((4*L)/6)
        yyc=round(yc);
        I2=I2+ (conprof(yyc)/(L/6));
    end

    C=abs((I1-I2)/(I1+I2));
    disp('C = ');
    disp(C);
```

```
    disp('I1 = ');
    disp(I1);
    disp('I2 = ');
    disp(I2);
```

Appendix to section 5.2.2

Appendix to section 5.2.2 is the second MATLAB simulation program developed for the VSS) method, with significant training and assistance from Kevin Wright. The code is documented throughout to denote the purpose of the various sections so as to be understandable for those with experience of MATLAB programming. Documentation and comments are shown in green. It makes use of the same basic methods as the code in appendix 5.2.1 but implements these methods using a 2D phantom (created the same way as a complete matrix rather than a single row). The pulse program implemented with these methods is also change to be the turbo spin echo (TSE also known as fast spin echo, FSE) as shown in figure 5.3.

```
% --- simechotrain14.m

% SIMULATION OF A SPIN ECHO TRAIN,
% USING AN ARRAY OF SPINS WITH SMALL RANDOM FREQUENCY OFFSETS.
% needs readout - done
% needs relaxation - done
% needs to be split into 2d k space - done
% increase k space size to retreive enough voxels

% By JFW, 11 March 2008.

clear all;
close all;

%-------------------------------------------------------------------------
% Initialize NMR parameters
%-------------------------------------------------------------------------

tau = 10e-3;            % Time of first 180 deg. pulse (s)
t=tau;      % cpmg tau
T=1;        %
TR=10000000;       %recovery period
NECH = 32;%128;%256% Number of echoes in the CPMG
turbo_factor=4;%IMPORTANT: needs to be an even number!!!
TD = 512;               % Points acquired in FID

O1 = 2e3;               % Resonance frequency (Hz)
DW = 10e-6;             % Dwell time, s (time step during acquisition)
```

```
AQ = TD*DW;             % Data acquisition time, s
SW = 1/DW;              % Sweep width, Hz (using quadrature detection)

% Each echo must be acquired in the time interval (2*tau) between
% successive 180 pulses.
if AQ >= 2*tau
    disp('Error: AQ must be < 2*tau !');
    return
end


Gymax=20e4;%32e4;%          % Maximum Gy level
deltaGy=2*Gymax/(NECH);
Gy=-Gymax:deltaGy:Gymax-deltaGy;   % List of Gy values
TGy=1e-4;               % Duration of Gy phase encoding gradient

Gx =17*(TGy/AQ)*Gymax;%5e2; %2e4;%0.7e4;



%-------------------------------------------------------------------------
% Create sample profile
%-------------------------------------------------------------------------

disp('Generating sample profile...');

num_x_voxels =1024;% 512;              % No. of spins (voxels) along x
num_y_voxels = num_x_voxels;    % No. of spins (voxels) along y

total_num_voxels = num_x_voxels*num_y_voxels;   % Total no. of spins

Lx = 1;                         % Sample length along x, cm
Ly = Lx;                        % Sample length along y, cm
delta_x = Lx/num_x_voxels;      % Voxel width along x, cm
delta_y = Ly/num_y_voxels;      % Voxel width along y, cm

% x- and y-coordinates of the voxels in the phantom sample, in cm.

sample_x_axis = (-Lx/2):delta_x:(Lx/2-delta_x);
sample_y_axis = (-Ly/2):delta_y:(Ly/2-delta_y);

% Set up a phantom sample image. (Initialize the relative spin
% density for each of the voxels in the sample).
% Multiple versions of a phantom are presented with the active one not
% commented out

%Set up a series of boxes-------------------------------

% spin_density=[zeros(num_x_voxels/4,num_y_voxels); ...
%     zeros(num_x_voxels/8,num_y_voxels/8) ...
%     ones(num_x_voxels/8,num_y_voxels/8) ...
%     zeros(num_x_voxels/8,3*num_y_voxels/4); ...
%     zeros(5*num_x_voxels/8,num_y_voxels)];

% spin_density=[zeros(1*num_x_voxels/4,num_y_voxels); ...
%     zeros(num_x_voxels/4,1*num_y_voxels/4) ...
%     ones(num_x_voxels/4,num_y_voxels/4) ...
%     zeros(num_x_voxels/4,2*num_y_voxels/4); ...
```

```
%     zeros(2*num_x_voxels/4,num_y_voxels)];


% spin_density=[zeros(7*num_x_voxels/16,num_y_voxels); ...
%     zeros(num_x_voxels/8,7*num_y_voxels/16) ...
%     ones(num_x_voxels/8,num_y_voxels/8) ...
%     zeros(num_x_voxels/8,7*num_y_voxels/16); ...
%     zeros(7*num_x_voxels/16,num_y_voxels)];

% spin_density=[zeros(7*num_x_voxels/16,num_y_voxels); ...
%     zeros(num_x_voxels/8,6*num_y_voxels/16) ...
%     ones(num_x_voxels/8,num_y_voxels/4) ...
%     zeros(num_x_voxels/8,6*num_y_voxels/16); ...
%     zeros(7*num_x_voxels/16,num_y_voxels)];


spin_density=[zeros(6*num_x_voxels/16,num_y_voxels); ...
    zeros(num_x_voxels/4,7*num_y_voxels/16) ...
    ones(num_x_voxels/4,num_y_voxels/8) ...
    zeros(num_x_voxels/4,7*num_y_voxels/16); ...
    zeros(6*num_x_voxels/16,num_y_voxels)];

% spin_density=[zeros(3*num_x_voxels/8,num_y_voxels); ...
%     zeros(num_x_voxels/4,3*num_y_voxels/8) ...
%     ones(num_x_voxels/4,num_y_voxels/4) ...
%     zeros(num_x_voxels/4,3*num_y_voxels/8); ...
%     zeros(3*num_x_voxels/8,num_y_voxels)];

% spin_density=[zeros(num_x_voxels/2,num_y_voxels); ...
%     zeros(num_x_voxels/2,num_y_voxels/2)...
%     ones(num_x_voxels/2,num_y_voxels/2)];

% spin_density=[ones(num_x_voxels/8,num_y_voxels/8)...
%     zeros(num_x_voxels/8,7*num_y_voxels/8);...
%     zeros(3*num_x_voxels/8,num_y_voxels); ...
%     zeros(num_x_voxels/8,3*num_y_voxels/8)...
%     ones(num_x_voxels/8,num_y_voxels/4)...
%     zeros(num_x_voxels/8,3*num_y_voxels/8);...
%     zeros(2*num_x_voxels/8,num_y_voxels); ...
%     zeros(num_x_voxels/8,7*num_y_voxels/8)...
%     ones(num_x_voxels/8,num_y_voxels/8)];

%Set up a spot----------------------------------------

%     [x,y] = meshgrid(sample_x_axis,sample_y_axis);
%     Lfrac=8;
%     rad = Lx/Lfrac;%8; % Spot radius, cm
%     z5 = (x.*x + y.*y)   < rad^2;
%     spin_density = 1*z5;



% Find the integrated spin density of the phantom image
% (used for signal normalization).
integrated_spin_density = sum(sum(spin_density));

% Plot the spin density.
% figure;
```

```
% mesh(sample_x_axis,sample_y_axis,spin_density);
% axis([sample_x_axis(1) sample_x_axis(end) ...
%     sample_y_axis(1) sample_y_axis(end) 0 1.1]);
% drawnow;


% figure;
% checky=((fft2(spin_density)));
% %checky=abs(fftshift(fft2(spin_density,512,512)));
% mesh(abs(checky));
% %mesh(abs(fftshift(fft2(spin_density,512,512))));
% title('fft2spin_density');
% drawnow


% figure;
% checkyy=((fft2(checky,256,256)));
% %checkyy=abs(fftshift(fft2(checky,512,512)));
%
% mesh(abs(checkyy));
%
% title('spin_density');
% drawnow

%return;


% Set up a random frequency offset for the spins
sigma = 2e2; % Standard deviation of normal distribution of frequencies,
Hz
random_offset = 2*pi*sigma*randn(num_x_voxels,num_y_voxels); % rad/s

disp('...completed.');

%-------------------------------------------------------------------------
% Test for rotary echos ------------
%-------------------------------------------------------------------------


tot=2*AQ;%tau;%*NECH;

        if tot> 1/(Gx*delta_x*1.5)%*2)
            disp('Gx error: Rotary echos will be formed');
            return;
        end

        disp('No rotary echos formed');
        %return;

%%%%%%%%%%%%%%%%%%%%%%%%%%%%%%%%%%%%%%%%%%%%%%%%%%%%%%%%%%%%%%%%%%%%%%%%%%%%
%%%%%%%%%%%%%%%%%%%%%%%%%%%%%%%%%%%%%%%%%%%%%%%%%%%%%%%%%%%%%%%%%%%%%%%%%%%%

% set values of Mtconst and Mtconst2 used for speed during development%

Mtconst=0.5928;

Mtconst2=0.4022;
```

```
%%%%%%%%%%%%%%%%%%%%%%%%%%%%%%%%%%%%%%%%%%%%%%%%%%%%%%%%%%%%%%%%%%%%%%%%%%%%
%%%%%%%%%%%%%%%%%%%%%%%%%%%%%%%%%%%%%%%%%%%%%%%%%%%%%%%%%%%%%%%%%%%%%%%%%%%%

Mtconst = single(Mtconst);
Mtconst2 = single(Mtconst2);

disp('Mtconst=');
disp(Mtconst);
disp('Mtconst2=');
disp(Mtconst2);

turboremover=single(1/(Mtconst^(2*turbo_factor)));
turboremover2=single(1/(Mtconst2^(2*turbo_factor)));
disp('turboremover=');
disp(turboremover);
disp('turboremover2=');
disp(turboremover2);
%return;
%%%%%%%%%%%%%%%%%%%%%%%%%%%%%%%%%%%%%%%%%%%%%%%%%%%%%%%%%%%%%%%%%%%%%%%%%%%%
%%%%%%%%%%%%%%%%%%%%%%%%%%%%%%%%%%%%%%%%%%%%%%%%%%%%%%%%%%%%%%%%%%%%%%%%%%%%

%-----------------------------------------------------------------------
% Start of pulse sequence
%-----------------------------------------------------------------------

disp('Beginning pulse sequence...');

signal = zeros(1,NECH*TD);   % Zero the signal. Leave space for NECH
echoes

% Loop over all voxels
disp('x pos=');
for j=1:num_x_voxels
    disp(j);
    for k=1:num_y_voxels

        % Skip empty voxels
        if spin_density(j,k) == 0
            continue;
        end
           turbo=1;
        % Begin with transverse magnetization after 90x pulse
        M=[0; spin_density(j,k); 0];

        % Find the frequency offset (rad/s) during free precession
        freq_offset = 2*pi*O1 + random_offset(j,k);
        % Find gradient effect
        Gy_effect =2*pi*Gy*sample_y_axis(k);%
        Gx_effect =2*pi*Gx*sample_x_axis(j);


        % Do free precession about z for time tau.
        M = qrotz(M,freq_offset*(tau));


        % Find the precession angle during time DW including Gx.
        theta = (freq_offset+Gx_effect)*DW;
        c = cos(theta);
        s = sin(theta);
```

```
% Repeat 180-(tau-AQ/2)-AQ-(tau-AQ/2)-, NECH times
for m=1:NECH

    % Do transverse relaxation for time tau.
    if j<(num_x_voxels/2)
    M=[M(1)*Mtconst;M(2)*Mtconst;M(3)];%*Mtconst];
    else
    M=[M(1)*Mtconst2;M(2)*Mtconst2;M(3)];%*Mtconst2];
    end

    % 180x pulse
    M=[M(1); -M(2); -M(3)];

    % Do free precession about z for time tau-AQ-TGy,
    % then for during Gy, then for during Gx
    M = qrotz(M,freq_offset*((tau-AQ)-TGy));
    M = qrotz(M,(freq_offset+Gy_effect(m))*(TGy));
    M = qrotz(M,(freq_offset-Gx_effect)*(AQ/2));

    % Do transverse relaxation for time tau.
if j<(num_x_voxels/2)
    M=[M(1)*Mtconst;M(2)*Mtconst;M(3)];%*Mtconst];
else
    M=[M(1)*Mtconst2;M(2)*Mtconst2;M(3)];%*Mtconst2];
end


    % Do the data acquisition - loop over TD data in time steps
    % DW.
    % (qrotz is not used, because the precession angle stays the
    % same throughout acquisition, and this speeds up
    % calculation.)
    for n = 1:TD
        % Acquire the nth point of the mth FID.
        nn = n+(m-1)*TD;
        signal(nn) = signal(nn)+complex(M(1),M(2));
        % Do free precession about z for time DW.
        M = [c*M(1)+s*M(2); -s*M(1)+c*M(2); M(3)];
    end % of loop over the TD acquired data

    % Do free precession about z for time tau-AQ/2.
    M = qrotz(M,freq_offset*((tau-AQ)-TGy));

    M = qrotz(M,(freq_offset-Gy_effect(m))*(TGy));
    M = qrotz(M,(freq_offset-Gx_effect)*(AQ/2));


    %%%%%%%%%%%%%%%%%
    %turbo factor
    %%%%%%%%%%%%%%%%%
%     disp('turbo=');
%     disp(turbo);
    turbo=turbo+1;
    if turbo>(turbo_factor)
       turbo=1;
% Begin with transverse magnetization after 90x pulse
M=[0; spin_density(j,k); 0];
```

```
        % Find the frequency offset (rad/s) during free precession
        freq_offset = 2*pi*O1 + random_offset(j,k);
        % Find gradient effect
        Gy_effect =2*pi*Gy*sample_y_axis(k);%
        Gx_effect =2*pi*Gx*sample_x_axis(j);


        % Do free precession about z for time tau.
        M = qrotz(M,freq_offset*(tau));


        % Find the precession angle during time DW including Gx.
        theta = (freq_offset+Gx_effect)*DW;
        c = cos(theta);
        s = sin(theta);
            end

        end % of loop over the echoes
    end % of y voxel loop
end % of x voxel loop

disp('...completed.');

%------------------------------------------------------------------------
% Plot the spin echo train
%------------------------------------------------------------------------

figure;
plot((0:(length(signal)-1)),real(signal)/integrated_spin_density);
axis([0 length(signal) -1.1 1.1]);
xlabel('Points');
ylabel('Real(Normalized signal intensity)');
title(['Signal acquired during ' num2str(NECH) ' spin echoes']);
drawnow;

figure;
plot((0:(length(signal)-1)),abs(signal)/integrated_spin_density);
axis([0 length(signal) 0 1.1]);
xlabel('Points');
ylabel('Abs(Normalized signal intensity)');
title(['Signal acquired during ' num2str(NECH) ' spin echoes']);
drawnow;

%------------------------------------------------------------------------
% split the echo train into a 2d k space
%------------------------------------------------------------------------

signal2D=zeros(NECH,TD);
for kplacement = 1:NECH

        for ifff=1:TD
            signal2D(int16(kplacement),ifff)=signal(((kplacement-
1)*TD)+ifff);
        end

end

%
```

```
% figure;
% mesh(real(signal2D));
% title('real-signal2D');
%
% figure;
% mesh(imag(signal2D));
% title('imag-signal2D');

figure;
mesh(abs(signal2D)/integrated_spin_density);
title('abs-signal2D');


finalmap = fftshift(fft2(signal2D),2);%,512,512));

% figure;
% mesh(real(finalmap));
% title('real-finalmap');
%
%
% figure;
% mesh(imag(finalmap));
% title('imag-finalmap');

figure;
mesh(abs(finalmap));
title('abs-finalmap');


%calculate contrast from final signal multiple versions included.
%Final to be selected based on phantom used
I1=0;
I2=0;
 testtest=1;%%%%%%%%%%%%%%%%%%%%%%%%%%%%%%%%%%%%%%%%%%%%%%%%
%     for xc = (TD/2)-(TD/(2*Lfrac)):TD/2
%         xxc=round(xc);
%         %disp(xxc);
%         for xxxc=1:6
%           %disp(xxxc);
%         I1=I1+ (finalmap((round(NECH/2)+3-xxxc),xxc)/(TD/Lfrac));
%
%         cont(xxxc,testtest-1)= (finalmap((round(NECH/2)+3-
xxxc),xxc)/(TD/Lfrac));%%%%%%%%%%%
%
testtest=testtest+1;%%%%%%%%%%%%%%%%%%%%%%%%%%%%%%%%%%%%%%%%%%%%%%%%%%%%%
%%%%%%%%%%
%         end
%     end
%
%     for yc = TD/2:(TD/2)+(TD/(2*Lfrac))
%         yyc=round(yc);
%         for yyyc=1:6
%         I2=I2+ (finalmap((round(NECH/2)+3-yyyc),yyc)/(TD/Lfrac));
%
%         cont(yyyc,testtest-1)= (finalmap((round(NECH/2)+3-
yyyc),yyc)/(TD/Lfrac));%%%%%%%%%%%%%%%%%%
%
%
testtest=testtest+1;%%%%%%%%%%%%%%%%%%%%%%%%%%%%%%%%%%%%%%%%%%%%%%%%%%%
%         end
```

```
%     end

testtestx=1;%%%%%%%%%%%%%%%%%%%%%%%%%%%%%%%%%%%%%%%%%%%%%%%%%%%%%%%%%%%%%%%%
qwert=((TD/10)+(TD/16))/2;
    for xc = (TD/2)-(TD/(10)):(TD/2)-(TD/(10))+qwert
    %for xc = (TD/2)-(TD/(10)):TD/2
        xxc=round(xc);
        %disp(xxc);
        testtesty=1;%%%%%%%%%%%%%%%%%%%%%%%%%%%%%%%%%%%%%%%%%%%%%%%%%%%%%%%%%%%%
        for xxxc=(NECH/2)-(NECH/16)+1:(NECH/2)+(NECH/16)+1
            xxxxc=round(xxxc);
            I1=I1+ finalmap(xxxxc,xxc);

cont(testtesty,testtestx)=finalmap(xxxxc,xxc);%%%%%%%%%%%%%%%%%%%%%%%%%%%%%%
%%%%
            testtestx=testtestx+1;
            testtesty=testtesty+1;
        end
    end

    for yc = (TD/2)+(TD/16)-qwert:(TD/2)+(TD/16)
    %for yc = TD/2:(TD/2)+(TD/16)
        yyc=round(yc);
        testtesty=1;%%%%%%%%%%%%%%%%%%%%%%%%%%%%%%%%%%%%%%%%%%%%%%%%%%%%%%%%%%%%
        for yyyc=(NECH/2)-(NECH/16)+1:(NECH/2)+(NECH/16)+1
            yyyyc=round(yyyc);
            I2=I2+ finalmap(yyyyc,yyc);

cont(testtesty,testtestx)=finalmap(yyyyc,yyc);%%%%%%%%%%%%%%%%%%%%%%%%%%%%%%
%
            testtestx=testtestx+1;
            testtesty=testtesty+1;
        end
    end

figure;%%%%%%%%%%%%%%%%%%%%%%%%%%%%%%%%%%%%%%%%%%%%%%%%%%%%%%%%%%%%%%%%%%%%%
    mesh(abs(cont));%%%%%%%%%%%%%%%%%%%%%%%%%%%%%%%%%%%%%%%%%%%%%%%%%%%%%%%%

title('cont');%%%%%%%%%%%%%%%%%%%%%%%%%%%%%%%%%%%%%%%%%%%%%%%%%%%%%%%%%%%%%

    C=abs((I1-I2)/(I1+I2));
    disp('C = ');
    disp(C);
    disp('I1 = ');
    disp(I1);
    disp('I2 = ');
    disp(I2);
```

Appendix to section 6.2

Appendix to section 6.2 is the Turbo Pascal pulse program and MATLAB controller for the TR method of fast T_1 - T_2 acquisition. As the labs expert on both programming methods, Kevin Wright was consulted about each program but was far less involved in the conception and implementation of these programs. The idea to acquire data in a single shot

was entirely my own, devised when trying to fix the problem with variable timings based on Windows' lack of ability to properly time its various processes.

Turbo Pascal pulse program

The turbo Pascal pulse program (INVCPMGS) is written in a form that is readable to the DRX console in the lab. The sequence is based on an initial attempt to conduct saturation recovery which was then expanded to perform full inversion recovery experiments. The code is documented throughout to denote the purpose of the various sections so as to be understandable for those with experience of Turbo Pascal and pulse sequence programming. The version of Pascal implemented on the DRX console lacks certain functions of Turbo Pascal which required some improvisation in achieving certain goals. Documentation and comments have been changed to green for clarity in distinguishing from the code itself.

```
PROGRAM INVCPMGS;
{BASED ON SATRECL1 and CPMG VERSION 1.1 26 MAY 98 FOR MARAN ULTRA}
{ FOR DRX CONSOLE WITH DRESSLER POWER AMP.          }
{ THIS VERSION BY JFW, 14/01/10    }
{ Does full INVCPMG sequence as single shot }
{ Suggest low tau to reduce steady state longitudinal recovery }
{ steady state worse at low T1 }
{ Modified By JFW, 14/01/10 to insert a P90 to destroy long mag after the cpmg}
{ Check that lowest Tconst value is greater than the FID following CPMG }

{ SUGGESTED D9=20us FOR DRESSLER TxEnable }
{ ALWAYS USES 1us FOR TxDisable          }

{ SUGGESTED PHASE LISTS: }
{ PH1=0213             }
{ PH2=0213             }
{ PH3=1122             }
```

```
{$I COMPILE.INC }

USES
{$I UNITSDIG.INC }

VAR {sets variables for use in the pulse sequence}
 AcqTime     : REAL;              { Define Total Acquisition Time     }
 PreAcqTime  :        DOUBLE;          { Define Time Pre-Acquire          }
 PostAcqTime :        DOUBLE;          { Define Time Post-Acquire         }
 Tconst : DOUBLE;                    { Define constant relaxation delay  }
 n : LONGINT;
 testvar : LONGINT;
 F1:Text;
 x:REAL;

PROCEDURE Sequence;

BEGIN
 AcqTime:=SI*DW;                          { Total Acquire Time }
 PreAcqTime:=Tau-Dead2-(P180/2)-(AcqTime/2)+GroupDelay;{ Time Pre-Acquire   }
 PostAcqTime:=Tau-(AcqTime/2)-(P180/2)-GroupDelay-D9;  { Time Post-Acquire  }
 Tconst:=C4;{3000000;the recovery time TR is defined here as internal variable C4}
 { Set Up The Variable Delay List }
 { D1 Is The Initial Value; D2 Is The Linear Increment }
 { The t1 list (t1 is denoted D1 in the program) must be set up in this way as this version }
{of turbo pascal cannot import a text file to retrieve the list. The exponential factor of }
{2.302585 is necessary as this version of turbo pascal cannot perform 10^x operations}

 FOR n:=1 TO (C1-1) DO
 BEGIN
 SetDurationList(n,exp(2.302585*(D1+(((D2-D1)/(C1-1))*(n-1)))));
 END;
```

```
{ Initialize }
Duration(1,0);
ZeroTime;
Duration(1,0);


{ 90 pulse with T(x) wait  puts tissue in required starting condition}
Duration(D9,TxEnable);                  { D9 us To Enable Dressler    }
Duration(P90,RF(PH1));                  { 90 Pulse, Tx CH1=PH1        }
Duration(Tconst,TxDisable);                     { Wait For Tx               }


{ Loop Over C1 Echo Trains. Inversion recovery section begins }
StartLoop(C1-1);


{180 pulse with D1 wait}
Duration(1,0);
Duration(D9,TxEnable);                  { D9 us To Enable Dressler Tx }
Duration(P180,RF(PH1));                 { 180 Pulse, Tx CH1=PH1       }
Duration(1,TxDisable);                  { Disable Tx                  }
Duration(10,NextVariable);    { Increment Variable Delay List Pointer }
Duration(Variable,0);                { Wait For Variable Delay From List }


{ CPMG section begins}
Duration(D9,TxEnable);                  { D9 us To Enable Dressler    }
Duration(P90,RF(PH1));                  { 90 Pulse, Tx CH1=PH1        }
Duration((Tau-(P90+P180)/2-D9),TxDisable); { Wait For Tau              }
Duration(D9,TXEnable);                  { Enable Tx CH1 For First 180 }
StartLoop(NumEchoes);                   { Start Echo Train            }
  Duration(P180,RF(PH3));               { 180 Pulse, Tx CH1=PH3       }
  AcquireEx(PreAcqTime,SI,PH2);           { Delay Then Acquire Echo     }
```

```
  Duration(PostAcqTime,0);              { Post-Acquire Delay        }
  Duration(D9,TxEnable);                { Enable Tx CH1 For Next 180  }
EndLoop; { over NumEchoes }

Duration(P90,RF(PH1));                  { 90 Pulse, Tx CH1=PH1      }

{ Disable Tx and wait for T(x)}
Duration(Tconst,TxDisable);

EndLoop; { Over C1 }

{ Increment The Phases Then Repeat Everything For NS Scans }
Duration(20,Next(PH1)+Next(PH2)+Next(PH3));

END;

BEGIN
Run(Sequence);
END.
```

MATLAB controller

The MATLAB controller (INVCPMGSS.m) was composed by me based on an older MATLAB template written by Kevin Wright. This program provides the parameters for the inversion recovery CPMG experiment and controls the RINMR program which in turn runs the pulse program INVCPMGS.PAS. The code is documented throughout to denote the purpose of the various sections so as to be understandable for those with experience of MATLAB programming. Documentation and comments are shown in green.

```
% InvCPMGSS.m
% Template for Matlab/RINMR inter-process communication.
% By JFW, 16/02/09 from template by KMW, 12/12/08.
clear all;
close all;
```

```
%pathname='C:\Users\INVCPMGSS data';
pathname='C:\Documents and Settings\warnerj\Desktop\temp';
cd(pathname);
% Declare Resonance Instruments NMR parameter names as global variables.
useridata; % See separate file useridata.m
% Use RINMR as an ActiveX server.
% Starts RINMR if necessary and communicates with it.
% h is a handle to the RINMR process.
h=actxserver('rinmr.nmr');

  C1=64; %number of points in the t1 dimension
  NECH=8192;%number of echoes in the CPMG section, points in the t2
                                                              dimension
  FinalData = zeros((C1+1),(NECH+1));
  Tconst=1000;%the recovery period TR
  D1=2;% the start of the t1 list is 10^D1
  D2=7.3;% the end of the t1 list is 10^D2
  TAU=200;


    % Typical method to execute an RINMR command without parameters,
    % e.g. switch spectrometer to acquisition mode.
    invoke(h,'Execute','~AMODE');

    pulseprog='INVCPMGS';

    invoke(h,'Execute',['LOAD ' pulseprog]);

        invoke(h,'Execute',['PH1 ' 0]);
        invoke(h,'Execute',['PH2 ' 0]);
        invoke(h,'Execute',['PH3 ' 1]);
        invoke(h,'Execute',['PH4 ' 0]);
        invoke(h,'Execute',['PH5 ' 0]);


% Set and display some parameters.

invoke(h,'Execute',['C4 ' num2str(Tconst)]);
disp(['Tconst = ' num2str(Tconst)]); % Display the value Tconst
NS=1; % number of phase encoded steps
invoke(h,'Execute',['NS ' num2str(NS)]);
disp(['No. of scans NS = ' num2str(NS)]); % Display the value NS
SI=1; % number of points per echo =SI
invoke(h,'Execute',['SI ' num2str(SI)]);
disp(['No. of points per echo SI = ' num2str(SI)]); % Display the value
SI
invoke(h,'Execute',['NECH ' num2str(NECH)]);
disp(['No. of echoes NECH = ' num2str(NECH)]); % Display the value NECH

invoke(h,'Execute',['TAU ' num2str(TAU)]);
disp(['TAU = ' num2str(TAU)]); % Display the value TAU
RGinit=str2double(invoke(h,'GetParameter','RG')); % gets initial RG from
                                                                  RINMR
disp(['Receiver gain RG = ' num2str(RGinit) ' %']); % Display the value
RG
C1sent=C1+1;
invoke(h,'Execute',['C1 ' num2str(C1sent)]);
disp(['No. of echo trains C1 = ' num2str(C1)]); % Display the value C1
```

```
RD=100000000; %RD value is not used but must be set to "trick" RINMR to
run
invoke(h,'Execute',['RD ' num2str(RD)]);
disp(['Relaxation delay RD = ' num2str(RD) ' us = ' ...
    num2str(RD*1e-6) ' s']); % Display the value RD
%%%%%%%%%%%%%%%%%%%%%%%%%%%%%%%%%%%%%%%%%%%%%%%%%%%%%%%%%%%%%%%%%%%%%%%

for n=1:(C1) %%% creates the t1 (Dlist) list from D1 and D2
    Dlist(n)=exp(2.302585*(D1+(((D2-D1)/(C1-1))*(n-1))));

end
 % Display the value 1st and last values of the t1 list
disp(['1st delay in list = ' num2str(Dlist(1)) ' us']);
disp(['64th delay in list = ' num2str(Dlist(C1)) ' us = ' ...
    num2str(Dlist(C1)*1e-6) ' s']);

     invoke(h,'Execute',['D1 ' num2str(D1)]); % Display the value D1
    disp(['First delay = ' num2str(Dlist(1)) ' us']);

invoke(h,'Execute',['D2 ' num2str(D2)]); % Display the value D2
disp(['Log(step in us) = ' num2str(D2)]);

% Run the pulse program. N.B. 'Execute' not needed!
disp(['Running ' pulseprog ' ...']);
invoke(h,'GO');

% Write the data to an RINMR format data file.
filename='TEST';
% invoke(h,'Execute',['WR ' filename]);
drawnow;
% Manipulate the acquired data, e.g. do a baseline correction.
%invoke(h,'Execute','BC');

% Typical method to retrieve an NMR parameter from the RINMR data, e.g.
RG.
RG=str2double(invoke(h,'GetParameter','RG'));
disp(['Receiver gain RG = ' num2str(RG) ' %']); % Display the value RG
% Get the data from RINMR.
% Extract the real (A) and imaginary (B) data components.
% (must stay EXACTLY as it is)
a=get(h,'DataA'); A=zeros(length(a),1); for j=1:length(A); A(j)=a{j}; end
b=get(h,'DataB'); B=zeros(length(b),1); for j=1:length(B); B(j)=b{j}; end
% Optional: make the data into a complex fid.
fid=complex(A,B);
% Process the fid as required...
drawnow;
% Plot the fid
figure;
hold on;
plot([1 NECH*SI],[0 0],'k-');
plot(real(fid(1:(NECH*SI))),'y-');
plot(imag(fid(1:(NECH*SI))),'g-');
plot(abs(fid(1:(NECH*SI))),'r-');
hold off;
title([filename ' (first CPMG only)']);

% Plot the full echo train
figure;
hold on;
plot(real(fid),'y-');
```

```
plot(imag(fid),'g-');
plot(abs(fid),'r-');
hold off;
title([filename ' (complete CPMG train)']);
drawnow;

    finalmult=1;

% convert the data to a matrix
for c=1:(C1)
        for nn=1:(NECH*SI)

        FinalData(c+1,nn+1)=FinalData(c+1,nn+1)+(fid(((c-
1)*(NECH*SI))+nn));

        end
end
 % add table axes to data for use in data processing
for n=1:(C1)
    FinalData(n+1,1)=Dlist(n);
end
for nn=1:(NECH*SI)
    FinalData(1,nn+1)=2*nn*TAU;
end

invoke(h,'Execute','~AMODE');
invoke(h,'Execute',['RG ' num2str(RGinit)]);
RG=str2double(invoke(h,'GetParameter','RG'));
disp(['Receiver gain RG = ' num2str(RG) ' %']);
disp(['RG int = ' num2str(RGinit)]);

% saves the data acquired as a .txt file ready for data processing
absFinalData=abs(FinalData');
save absFinalData.txt absFinalData -ascii;
disp('absFinalData saved');
% Release the ActiveX server.
release(h);
```